

ABSTRACT

KAROUI, ABDENNACEUR. Nucleation and Growth of Defects in Nitrogen doped Silicon. (Under the direction of Professor George A. Rozgonyi)

Ultra high purity silicon is advantageously modified by as low as $5 \times 10^{14} \text{ cm}^{-3}$ nitrogen. Such a doping level was proved to drastically impact grown-in and process-induced defects, enhances the denuded zone intended for making devices, improves impurity gettering, and increases the gate oxide integrity in metal oxide silicon devices. Interestingly, with such a low nitrogen level wafer toughness is significantly increased. However, nitrogen doping alters standard wafer heat treatment processes through the modification of the early stages of point defect clustering dynamics.

In this thesis, the basic interactions of light element impurities, particularly N and O, with point defects and crystal defects in silicon are scrutinized in order to understand the mechanisms of extended defect nucleation and growth in N doped silicon. Experimental data are used with molecular dynamics and quantum mechanics calculations for modeling defect formation. Various thermal annealing have been utilized to produce diverse conditions for defect interactions. Defect type, size distribution, nanoscale and atomic structure, and composition have been determined with emphasis on the depth dependence. Nanoscale analysis of defects probed at different depths allowed to build models of point defect dynamics from the extended defect formation history. Defect nucleation during crystal growth was qualitatively discussed and defect precursors were mapped on the crystal hot zones showing point defect clustering stages during solidification. This was based on results from the atomistic modeling of atomic structure of chemical complex ground states, the thermodynamic parameters close to the melting point, and the adsorption/desorption of point defects by stable chemical complexes. It was found that N_2 is a stable mobile species, VN_2 is an active metastable complex, and V_2N_2 is an immobile stable nucleus for oxygen precipitation but not for vacancy clustering. The formation energy of VN_2 was found positive by DFT calculations, which negates the spontaneous formation of isolated complex. However, the formation energy is reduced to about $k_{\text{B}}T/2$ near the melting point by coupling to one oxygen atom, which activates the formation of VN_2 , while weakly bound to the oxygen. The calculated thermal stability of a wide range of prominent chemical complexes was cross-checked with the signature of experimentally proven viable ones. Furthermore, IR absorption line intensities in annealed wafers were obtained as a function of depth by high spatial resolution synchrotron FTIR, which allowed having N-V-O depth profiles. These appeared in good agreement with that of the oxynitride precipitate profiles by OPP and SIMS. Such an agreement represents a strong support for both chemical complex spectroscopic identification and calculated thermodynamic parameters.

At the macroscopic level, nitrogen appeared to slowly athermally segregate under compressive stresses to dislocations and wafer surface; the segregation is accelerated at high temperature. In addition, nitrogen was found to couple with oxygen to form oxynitride zones and it segregates to precipitate interfaces making N-rich shells. Finally, silicon mechanical properties measured by nanoindentation of a variety of substrates appeared to well correlate with the dislocation pinning by light elements such as N, O, and C. The locking mechanism was correlated to dislocation interaction with impurity atmospheres simulated using elasticity theory, the size effect model, and Tersoff inter-atomic potential.

Nucleation and Growth of Defects in Nitrogen doped Silicon

by

Abdennaceur Karoui

A dissertation submitted to the Graduate Faculty of

North Carolina State University

In partial fulfillment of the

Requirements for the degree of

Doctor of Philosophy

In

Materials Science and Engineering

Raleigh, NC

(2004)

Approved by:

Prof. Carl Koch

Prof. Jagannadham Kasichainula

Prof. Jerry L. Whitten

Prof. Thomas B. Gunnoe

Prof. George A. Rozgonyi,
Chair of Advisory Committee

*For always being supported, I dedicate
this thesis to Am Said, his daughter Faouzia,
my parents, my brothers, my sisters,
Sondes, and Mohamed Fateh.*

BIOGRAPHY

Abdennaceur Karoui completed in 1975 his high school studies in Mathematics with engineering option. He received his first university diploma in Mathematics and Physics in 1978, then his Bachelor of Science in Physics in 1980. Thereafter, he visited University of Pierre Marie Curie in Paris where he conducted research for his Master degree in Condensed Matter Physics, which he obtained in 1982. While he was research assistant at the Institut National de Recherche Scientifique et Technique (INRST) in Tunisia, he visited the Inter-University Micro-Electronics Center (IMEC) in Belgium to carry out research on solar cell optical and electrical characterization and modeling of the electronic transport. He obtained his Ph.D. in Physics in 1987. Thereafter, he headed the Department of Physics and Energy at INRST, in Tunis, where he participated in a number of research projects on semiconductor materials and devices. In 1995, he obtained a two year Fulbright award to visit North Carolina State University (NCSU). He joined the Microelectronics Materials research group of Professor George A. Rozgonyi. Then he extended his visit, and after two years he decided to do a Ph.D. in Materials Science. At NCSU, his experimental work dealt with (i) photovoltaic materials sponsored by NREL, AstroPower, and BP Solar, (ii) MeV ion implantation and impurity gettering with Micron Technology, (iii) Rapid Thermal Processing with Mattson Technology, (iii) charge carrier lifetime in semiconductor materials and Injection Level Spectroscopy for low level impurity detection in semiconductors, sponsored by NREL, (iv) molecular dynamics and first principles calculations for materials atomic engineering sponsored by SiWEDS, and (v) “ultra-thin SiGe layer virtual substrate” for strained silicon, sponsored by Texas Instrument and SiWEDS. His present research orientation is on nanoscale materials and systems.

ACKNOWLEDGEMENTS

This dissertation was possible thanks to the valuable support of Professor George A. Rozgonyi, my advisor and chair of my thesis committee. His open-minded relation have been the basis for our long standing scientific relation, I am indebted to his continuous help.

I am grateful for my thesis committee, Prof. Carl Koch and Prof. Jagannadham Kasichainula both from the Department of Materials Science and Engineering and Prof. Jerry L. Whitten and Prof. Thomas B. Gunnoe both from the Department of Chemistry.

I acknowledge the strong interaction and moral support of Dr Faouzia Sahtout Karoui.

The Silicon Wafer Engineering and Defect Science (SiWEDS) has provided me with a good subject to investigate, financial support to this research, and a unique forum for top notch science and engineering dialogue with university and industry colleagues.

I value the collaboration with National Renewable Energy Lab., CO (NREL) and the three-year sponsorship that allowed me to acquire special silicon materials for this research, and I am thankful to Dr Ted Ciszek, Dr Richard Mattson, and Dr Bob McConnell, all from NREL for their valuable collaboration.

Dr Deren Yang from Zheijang University, in China, is thanked for his cooperation and for sending specially grown silicon wafers.

I greatly appreciate the efforts of Professor Koji Sueoka from Okayama University in Japan and Dr Masataka Hourai from Sumitomo-Sitix for the sponsorship and the interesting discussions during our collaboration in a joint project.

I am grateful to Professor Naohisha Innoue from Osaka University and his students for the close relation we have established that has enabled us to solve some of the FTIR work.

For the OPP measurements I would like to thank Dr S. Umeno from Sumitomo Sitix, and Mrs Pamela Flesher from High Yield Technology, Santa Clara, CA.

With Dr Alex Kvit I obtained significant useful results on HRTEM and related techniques; our collaboration was fruitful, pleasant, and friendly.

Many thanks to Dr. Rainier Losen for obtaining high resolution coupled SIMS imaging.

I would like to thank Dr Michael Martin and Mr Tonio Buonassisi both from the Advanced Light Source at Berkeley National Laboratory for collaboration on the Synchrotron-FTIR.

Many thanks to Dr Sergey Yarmalenko from the Department of Mechanical Engineering, NC A&T University at Greensboro, who helped me in performing the nanoindentation work.

Rene Gielen from the SiWEDS and Edna Deas from the Department of Materials Science and Engineering administration are also acknowledged, they were instrumental in providing a valuable source of technical support and advice.

Special thanks to my old friends and colleagues, Dr John M. Glasko for his support and useful discussion, Dr Kiman Bae with whom I started this work, Mr T. Sasaki from Nippon Steel Corp. for providing me with some samples, and Toshiaki Ono who initiated the joint project with his company Sumitomo Sitix.

Most of all, I am grateful to my family for the long and hard sacrifices they have made with me. I extend special thanks to my wife and my children. I owe a debt of gratitude to my parents, for their unfailing faith and their continual support and encouragement.

TABLE OF CONTENT

LIST OF FIGURES	ix
LIST OF TABLES	xiii
OUTLINE	1
Chapter I	8
INTRODUCTION	8
1. Problem Statement	8
1.1. Grown-in Defects in Float Zone and Czochralski silicon	8
1.2. Process Induced Defects in Czochralski silicon wafers	12
1.3. Nitrogen in CZ and FZ silicon.....	13
1.3.1. Control of Silicon Defects by N Doping	13
1.3.2. Dislocation Control by Nitrogen doping	16
2. Research Motivation	17
3. Objectives of the Thesis	19
Chapter II	23
EXPERIMENTAL STUDY OF DEFECTS IN NITROGEN DOPED SILICON	23
1 Introduction	23
2 Experimental Procedure	24
3 Results and Discussion.....	26
3.1. Defect Nucleation Mechanisms in N-CZ Si	36
3.2. Defects in N-CZ Silicon Wafers.....	38
3.3. Nitrogen and Oxygen Interactions and Co-Segregation to the Surface.....	39
3.4. Composition of Sub-Surface Defects in N-CZ Wafers	42
3.5. Nitrogen and Oxygen Coupling.....	46
3.6. Nitrogen and Oxygen Interactions in the Bulk	47
4 Summary	48
Chapter III	52
GROWTH MECHANISMS OF EXTENDED DEFECT IN N-CZ SILICON WAFERS.....	52
1. Introduction.....	52
2. Experimental procedure	52
3. Results and Discussion.....	53
3.1. Macroscopic Model of SF formation.....	53
3.2. Defect Structure and dynamics of point defect clustering	56
3.2.1. Subsurface Defects.....	56
3.2.1.1. Structure of Subsurface Octahedra –Like Oxynitride Precipitates.....	57
3.2.1.2. Microscopic Model of Subsurface SF Formation.....	61
3.2.2. Structure of thePrecipitates in the “Denuded Zone”	62
3.2.2.1. Precipitate Platelets	62
3.2.2.2. “Dragon-Fly” Defect	63
3.2.3. Bulk Defects beyond the Denuded Zone.....	64
3.2.3.1. The Umbrella Defect (in the Bulk).....	64
3.2.3.2. Point defect and N- and O- Complex Dynamics for the Umbrella Defect	67
3.3. Effects of Nitrogen Segregation on Precipitation Mechanisms.....	69
4. Summary	70

Chapter IV.....	73
POINT DEFECT INCORPORATION AND COMPLEXING IN NITROGEN DOPED CZOCHRALSKI SILICON	73
1. Processes of Point Defect Incorporation during Crystal Growth.....	73
1.1. Introduction	73
1.2. Melt/Solid Equilibrium Interface and Crystal Growth	74
1.3. Impurities and Point Defect Introduction	76
1.3.1. Oxygen Incorporation.....	77
1.3.2. Vacancy and Self-Interstitial Creation	78
2. Point Defect Redistribution and Extended Defect Nucleation.....	78
3. Basic model for Oxygen and Vacancy Agglomeration in CZ Si	82
4. Prominent complexes in CZ and N-CZ Si	84
4.1. Model for Defect Precursors in N-CZ Si Ingot	84
4.2. Space-Temperature Map of Defect Precursors within N-CZ Si Ingot.....	86
 Chapter V.....	 91
FIRST PRINCIPLES CALCULATIONS OF V-N-O COMPLEX FORMATION, THERMAL STABILITY, AND EQUILIBRIUM CONCENTRATION.....	91
1. Introduction.....	91
2. Atomic Structure, Formation Energy and Stability of N-Pairs and N-O-V complexes at the Ground State	94
2.1. Atomic Structure	94
2.2. Energy of Formation of N-Related Defects.....	96
2.3. Results and Discussion	97
3. Thermal Stability of N-Pairs and Equilibrium Concentration of VN ₂ : Semi-Empirical and Statistical Thermodynamic Calculations.....	101
3.1. Introduction	101
3.2. Thermal Stability	102
4. Equilibrium concentration of VN ₂ defects	102
5. Trapping of Oxygen and Vacancy by N-pairs	108
5.1. Introduction	108
5.2. Results and Discussion	109
6. Conclusion	113
 Chapter VI.....	 115
FIRST PRINCIPLES CALCULATIONS OF THE VIBRATIONAL SPECTRA OF V-N-O COMPLEXES AND EXPERIMENTAL IDENTIFICATION BY SYNCHROTRON FTIR	115
1. Vibrational Spectra of N-V and N-V-O Defects in Nitrogen Doped Silicon Using Density Functional Theory.....	115
1.1. Introduction	115
1.2. Computational Method.....	115
1.3. Vibrational Spectra of N ₂ , VN ₂ and V ₂ N ₂ Complexes	116
1.4. Vibrational Spectra of N ₂ O _n , VN ₂ O _n , V ₂ N ₂ O _n Complexes (n=1,2)	117
2. Identification of Chemical Complexes in Subsurface of Annealed N-CZ Silicon Wafers Using Synchrotron FTIR.....	120
2.1. Introduction	120
2.2. Experimental Method	121
3. Results and Discussions	122
3.1. Nitrogen and Oxygen Segregation in N-CZ Heat Treated Wafers	122
3.2. Nitrogen Complexes in As-Grown N-FZ	124
4. Conclusion	126

Chapter VII	129
CHARACTERIZATION OF OXYGEN AND NITROGEN EFFECTS ON MECHANICAL PROPERTIES OF SILICON USING NANO-INDENTATION.....	129
1. Introduction.....	129
2. Samples and Experimental Procedure.....	130
3. Results.....	133
3.1. Single Point Indentations.....	133
3.2. Indentation Arrays.....	134
3.3. Load controlled Nano-scratch Tests.....	134
4. Discussion.....	137
5. Summary.....	143
 Chapter VIII.....	 146
INTERACTION OF LIGHT ELEMENTS WITH DISLOCATIONS IN SILICON.....	146
1. Introduction.....	146
2. Model Used for Dislocation-Impurity interactions.....	147
3. Calculation of dislocation-impurity Binding Energy.....	151
4. Simulation Results and Discussion:.....	152
4.1. Atomic Structure of the Used Specimen.....	152
4.2. Atomic Structure of the Core of an Edge Dislocation.....	152
4.3. Impurity Distributions Within The Dislocation Atmosphere.....	155
4.3.1. Oxygen.....	155
4.3.2. Nitrogen.....	156
4.3.3. Carbon.....	156
4.3.4. Germanium.....	157
4.4. Impurity-dislocation binding energy and shear stress for dislocation separation.....	158
4.4.1. Effect of the impurity Type.....	158
4.4.2. Effect of the Impurity Concentration.....	159
4.4.3. Temperature Effect on the dislocation atmosphere.....	161
5. Conclusion.....	162
 Chapter IX.....	 164
SUMMARY AND GENERAL CONCLUSIONS.....	164
 LIST OF PUBLICATIONS RELATED TO THE THESIS.....	 169
1. Structural Properties / Defect Size Distribution in N-CZ Si.....	169
2. Thermodynamics of chemical complexes in N-CZ Si.....	169
3. Identification of Chemical complexes in N-CZ by Spectroscopy Methods.....	170
4. On Aspects of Nucleation and Stimulated Defects in N-CZ.....	170
5. Point Defect Clustering in N-CZ.....	171
6. Mechanical Properties.....	171
7. Optical Properties.....	171
8. Manuscripts Submitted (or to be submitted).....	172
9. Patent Disclosures (based on our studies on nitrogen in silicon).....	172
 REFERENCES.....	 173

LIST OF FIGURES

Fig. 1: Basic chemical reactions for extended defect formation in CZ silicon.....	11
Fig. 2: Contact induced defects in RTP wafer at T= 1150 C for 30 s.....	13
Fig. 3: Contact induced defects in a 300 mm wafer cycled in an RTP system that uses two support rings at the wafer rim and at a radius equal to 0.6 that of the wafer. RTP wafer for 10 s at 1200°C.....	13
Fig. 4 : Sequence of defect formation in N-CZ Si crystals versus N-free CZ Si.	14
Fig. 5: Defects variations in N-CZ Si as a function of v/G , the Voronkov ratio, where v is the pulling rate and G is the temperature gradient maintained across the ingot during cooling.....	15
Fig. 6: Defect morphology variations in N-CZ Si in relation with the Voronkov ratio v/G and the N doping level.....	16
Fig. 7: X-ray topographic images of dislocations in CZ, undoped FZ, and nitrogen doped FZ wafers following scribing and two cycles of thermal annealing at 1150°C.....	17
Fig. 8: Nomarski micrographs of Wright-Jenkins etched samples:	27
Fig. 9: (a) OPP determined defect size-distributions at 30 μm depth in as-grown N-CZ silicon, in 1G wafer, and in heat treated wafers with Lo-Hi (1L8) and with Hi-Lo-Hi (1H8).....	28
Fig. 10: Measured OPP defect depth distributions in N-CZ wafers from Set 1, as-grown (1G) and cycled with Lo-Hi (1L8) and with Hi-Lo-Hi (1H8).....	28
Fig. 11: Nomarski micrograph in (110) cleavage plane of a sample from 1L8 Wright-etched for 2 min, sample was polished after cleavage.....	29
Fig. 12: Near-surface etch pit density profile.....	30
Fig. 13: Oxygen and nitrogen SIMS profiles obtained in as-grown and heat treated N-CZ Si samples in argon in near surface (a), and in the bulk of 3L8 (b) and 3L64 (c) specimens.....	31
Fig. 14: Nomarski micrograph of a bulk region in a cleaved (110) face showing a high density of etch pits related to small SF and precipitates.	32
Fig. 15: Sequence of O and N SIMS images obtained from adjacent positions that are 200 μm separated, on a 2° beveled surface of a sample from wafer 3L8 (Lo-Hi cycled N-CZ Si).	33
Fig. 16: High resolution O and N SIMS depth profiles (sample 3L8). Dashed lines indicate local background and as-grown bulk levels.	34
Fig. 17: Ratio of oxygen and nitrogen concentration depth profiles for near-surface region (a) and for the bulk region (b) and for the three regions in wafer 3L64 (c).	35
Fig. 18: Cross-sectional TEM image of near-surface region in 3L8 (Lo-Hi cycled N-CZ Si wafer).....	36
Fig. 19: STEM image in Z-contrast mode of a defect region similar to type 1, shown in Fig. 18 for 3L8 wafer. Note that the wafer surface is on the left and is not shown in the picture.....	45

Fig. 20: Low resolution STEM image of near surface precipitate and SF(s) in 3L8 wafer.....	45
Fig. 21: Stacking faults profiles in wafers 1L8 and 1H8 obtained by etching. Note that the distribution starts at the bottom edge of the LDZ, no SFs were observed in the LDZ in both Lo-Hi and Hi-Lo-Hi N-doped CZ samples.....	55
Fig. 22: Model for nitrogen pair diffusion and segregation to the surface.	56
Fig. 23: TEM image of the near-surface region (two-beam conditions) from TEM foil S.	56
Fig. 24: HRTEM micrograph of commonly observed precipitate in the subsurface of N-CZ Si Lo-Hi treated wafer 3L8 (i.e., TEM foil S), and (b) sketch depicting its facet planes.....	57
Fig. 25: High Resolution TEM micrograph from foil S (from a Lo-Hi treated N-CZ silicon wafer 3L8 described in Chapter II). It shows a commonly observed sub-surface precipitate.....	59
Fig. 26: HRTEM micrograph of a precipitate Type 1, in sample S.....	59
Fig. 27: (a) HRTEM micrographs of a precipitate in sample S of 3L8 N-CZ Si wafer (Lo-Hi treated, as described in Chapter II).....	60
Fig. 28: (a) High-resolution Z-contrast image of a typical defect system (precipitates connected to SF) found in the wafer initial sub-surface (TEM foil S);.....	61
Fig. 29: Model for defect growth dynamics. Precipitate and SF final boundaries are represented with dashed and dotted lines, respectively.	62
Fig. 30: HRTEM image of an elongated pyramid-like precipitate (Type 3) found in the bottom of sample S, i.e., at 3 μm from the surface.	63
Fig. 31: (a) HRTEM image of a platelet precipitate, so-called “Dragon fly-like” defect, found in the “DZ”, i.e., TEM foil D10.	64
Fig. 32: Type 4 bulk defect in B30, which is an assembly of a precipitate with a self interstitial wavy zone, so-called “Umbrella-like” defect.	65
Fig. 33: (a) Low magnification STEM Z-contrast image of an oxynitride precipitate in sample B3 at 30 μm from the original wafer surface,.....	66
Fig. 34: Schematic of the suggested model for Umbrella defect growth.	69
Fig. 35: Radial vacancy profiles in CZ crystal ingot subsequent to lateral diffusion, for different cooling rates and times.....	79
Fig. 36: X-ray topography image of OSF-Ring of a 200 mm copper decorated CZ wafer.	80
Fig. 37: A schematic sequences of ring-OSF structure formation in CZ crystals as the crystal cools.	82
Fig. 38: Basic mechanism of extended defect formation in CZ-Si based on the model of “V-O clustering pathways” by K. Bae.....	83
Fig. 39: Suggested multi-pathways model of clustering mechanisms in the N-CZ.....	86
Fig. 40: Correlation of point defect and complex thermal histories during N-CZ Si crystal growth with subsequent extended defect in heat treated wafers. Hatched area represents the nucleation and growth temperature zone in the Si crystal.....	87

Fig. 41: Diffusivity of substitutional N, and N ₂ interstitial, compared to V.....	92
Fig. 42 : Relaxed geometries of neutral (a) N ₂ , (b) VN ₂ , and (c) V ₂ N ₂ complexes in Si with DFT.....	95
Fig. 43 : Atomic structure of the three classes of N-O complexes in (a) N ₂ O.....	96
Fig. 44: Calculated Gibbs free-energy change versus temperature of chemical reactions described by equations (18), (19), (20) leading to N-V complexes in N-CZ Si.....	103
Fig. 45: Equilibrium concentration of VN ₂ as a function of [V] for [N ₂] = 1x10 ¹⁵ cm ⁻³	106
Fig. 46: Ratio of [VN ₂] over [V] versus nitrogen pair concentration [N ₂].....	106
Fig. 47: Equilibrium concentration of VN ₂ as a function of temperature when the formation energy of VN ₂ deviates slightly from the calculated value of 2eV; [N ₂] = 1x10 ¹⁵ cm ⁻³ , [V] = 5x10 ¹³ cm ⁻³	107
Fig. 48: VN ₂ defect temperature of formation versus [V] for several levels of VN ₂ concentration, [N ₂] = 10 ¹⁵ cm ⁻³	108
Fig. 49: Supercell used for the calculation of the potential well for vacancy adsorption by V ₂ N ₂ defect. In this figure, most of the silicon atoms were removed to improve the visibility of the defects.....	110
Fig. 50: Variation of the interaction potential energy of (a) O and (b) V and N ₂ , as a function of the separation distance point defect-complex (i.e., V or O atom - N ₂ center) which is along [110].....	111
Fig. 51: Variation of the potential energy during (a) O and (b) V migration towards a VN ₂ defect.....	111
Fig. 52: Variation of the potential energy during (a) O and (b) V migration towards a V ₂ N ₂ defect.....	112
Fig. 53. (a) and (b) N ₂ complex and its IR active frequencies (779 cm ⁻¹ and 986 cm ⁻¹); (c) VN ₂ defect ; (d) V ₂ N ₂ defect.....	116
Fig. 54: ν_1 (symmetric stretching, 1203 cm ⁻¹), ν_2 (symmetric bending, 517 cm ⁻¹), ν_3 (asymmetric stretching, 1136 cm ⁻¹) normal modes of Si ₂ O.....	118
Fig. 55: (a) Defect depth distribution by OPP in Lo-Hi cycled wafer.....	122
Fig. 56: Intensity of absorption lines (measured from the base) of annealed N-CZ Si wafer.....	123
Fig. 57: XRT of N-FZ wafer. Circles indicate defect rings. Color coded map shows variations of the intensity if IR absorption line (extracted from the FTIR spectra).....	125
Fig. 58: Load vs. time during indentation tests used in single point and array indentations.....	132
Fig. 59: (a) SPM of a 5 μm x 5 μm area in which a 5000 μN indent was performed with Berkovich tip on the initial surface of N-CZ sample.....	133
Fig. 60: Array of indents used in the analysis of N-CZ sample.....	135
Fig. 61: A 15 μm scan of 2000 μN scratch made with a conical indenter on the surface of the N-CZ Si Hi-Lo-Hi material (N-CZ sample). Zoomed area is about 3 μm in length.....	136
Fig. 62: Data from 2000 μN scratch on the initial surface of N-CZ sample with conical tip.....	136
Fig. 63: Friction ratio for the load controlled scratch.....	137
Fig. 64: Hardness vs. Contact Depth for the individual indents on each of the five samples; one indent each on the first four samples and fourteen indents on N-CZ sample.....	138
Fig. 65: Reduced Modulus versus Contact Depth for indents on each of the five samples; one indent	

each on the first four samples and fourteen indents on N-CZ sample.....	138
Fig. 66: Hardness vs. Contact Depth for the indentations from Grid 1 on N-CZ sample.....	139
Fig. 67: Reduced Modulus vs. Contact Depth for the indentations from Grid 1 on N-CZ sample.	139
Fig. 68: Hardness vs. Contact Depth for the indentations in Grids 2, 3, and 4 on N-CZ sample.....	139
Fig. 69: Reduced Modulus vs. Contact Depth for indentations in Grids 2, 3, and 4 on N-CZ sample....	140
Fig. 70: Plots representing hardness and reduced modulus of Grid 4 indents compared along respective X and Y axes as laid out in Fig. 60.	143
Fig. 71: Models for elastic shape deformation of atoms during interactions with dislocations.	149
Fig. 72: Large interstitial octahedral sites in FCC and in BCC structures, and the used dislocation configuration.	150
Fig. 73: Silicon sample that has an edge dislocation in its center. Crystal oz orientation is $[\bar{1}10]$, see (b). The red points and segments are immobile H atoms and the green ones are mobile silicon.	153
Fig. 74: Core of the edge dislocation visible with the penta-ring connected to a septa-ring, (a) guessed structure, and (b) relaxed structure.	153
Fig. 75: Energy and stress force variations over time during a geometry optimization of a silicon sample without any dislocation in (a) and (b) and with an edge dislocation in its center in (c) and (d). The unit cell is shown in Fig. 73.	154
Fig. 76: Oxygen distribution in a 90° dislocation field at $T=300^\circ\text{K}$. In this case the O content around the dislocation is $x=10^{-4}$. The energy of the system after relaxation is -2.403565 eV. The numbers (5) and (7) are labels for the penta- and septa-rings, respectively, located in the dislocation core.	155
Fig. 77: Nitrogen distribution in 90° dislocation field at $T=300^\circ\text{K}$, shown in $(\bar{1}10)$ plane. Like oxygen in Fig. 76, the N content is taken $x=10^{-4}$	156
Fig. 78: Carbon distribution in a 90° dislocation field at $T=300^\circ\text{K}$, shown in $(\bar{1}10)$ plane. Again, the C content is taken $x=10^{-4}$. The energy of the system after relaxation is -2.023677 eV.	156
Fig. 79: Germanium distribution in a 90° dislocation field at $T=300^\circ\text{K}$, shown in $(\bar{1}10)$ plane. Like in previous cases, the Ge content is taken $x=10^{-4}$	157
Fig. 80: (a) Distribution of various type of impurities in a 90° dislocation field at $T=300^\circ\text{K}$. The impurity content is taken $x=10^{-4}$	158
Fig. 81: Interaction energy of edge dislocation with nitrogen vs. N fraction (in the atmosphere),	160
Fig. 82: Binding energy versus N content, and (b) fitting curves of binding energy vs. [N].	160
Fig. 83: Interaction energy gradient calculated as $G = \frac{E_{\max} - E_{\min}}{E_{\max} + E_{\min}}$	161
Fig. 84: Effect of the N concentration on (a) the interaction energy impurity-dislocation for an edge type (b) and the shear stress.	162

LIST OF TABLES

Table I: List of samples with thermal cycles they have undergone. All annealing were done in argon.....	24
Table II: Nitrogen and oxygen concentrations in the low density defect zone (LDZ) and at the surface of as-grown and Lo-Hi heat treated wafers from Set 2.	31
Table III: Formation energy of N-pairs and V-N-O complexes as calculated by quantum mechanics DFT-LDA on 64 Si atom supercells.	99
Table IV: Geometry parameters of relaxed V-N core defects by DFT-LDA calculations on 64 atom supercells.....	100
Table V: Geometry parameters of relaxed N-V-O defects by DFT-LDA calculations.	101
Table VI: Geometry parameters of relaxed N-V-O ₂ defects by DFT-LDA calculations.	101
Table VII: Calculated vibrational spectra for N-pairs and N-O complexes. Infra-red and Raman active modes are labeled IR and RA, respectively.....	119
Table VIII: Analysis of the absorption line intensity and assignment to chemical complexes.	124
Table IX: Published friction and hardness of silicon bulk and films.	130
Table X: Description of the material tested by nanoindentation and load controlled nanoscratches.	132
Table XI: Summary of results from single indentation tests made with Berkovich indenter on the five samples. All indents were done using a trapezoidal load function, see Fig. 58.....	134
Table XII: Summary of the data obtained with various indentation grids on the cross-section of N-CZ silicon sample.	141
Table XIII: Main results obtained for different regions of Hi-Lo-Hi cycled N-CZ Si sample.	141
Table XIV: Basic parameters necessary for modeling the dislocation atmosphere (covalent radius, i.e, half bond length) for prominent impurities.	152
Table XV: Energy terms and the total energy of the cylindrical silicon sample (with 29610 Si atoms and terminated with 4942hydrogen atoms; the sample has 56759 bonds).	155
Table XVI: Dislocation-impurity binding energy due to size effect, for a number of prominent impurities in silicon at 10 ⁻⁴ . The type of the considered dislocation is edge.	159

OUTLINE

In recent years, nitrogen doping of silicon has been receiving much technological and academic attention [1]. Pioneering research on nitrogen doping of silicon enlists many benefits of lightly doping silicon with nitrogen primarily allowing the control of a wide range of defects. It has been shown, indeed, that Czochralski (CZ) and Float Zone (FZ) as well as polycrystalline silicon are advantageously modified by as low as $5 \times 10^{14} \text{ cm}^{-3}$ average nitrogen level. Specifically, nitrogen doping of CZ silicon (N-CZ Si) drastically changes the type, size, and distribution of most of the defects known in N free silicon. As a consequence, it enhances the denuded zone [2] and increases the gate oxide integrity in metal oxide silicon (MOS) devices. In addition, impurity gettering is improved [3] by nitrogen, where a high density of small oxygen precipitates act as efficient gettering centers grown in the bulk. Furthermore, N doping offers a unique solution for toughening modern large silicon wafers for integrated circuit (IC) technologies and thin ones for photovoltaic (PV) . The wide range of properties, recently uncovered, is distinctive to the interactions of nitrogen with point defects and impurities in silicon, especially vacancy and oxygen atoms. The mechanisms of nucleation, defect growth, interaction of point defects with extended defects, and the surface are strongly controlled by nitrogen atoms, thus need to be thoroughly understood to enable new applications.

One of the main objectives of this work is to scrutinize the basic interactions of point defects, i.e., silicon interstitial (Si_i , abbreviated as I) and vacancy (Si_v , abbreviated as V) with light element impurities in silicon, particularly O, N, and C. To this end, a validation methodology has been developed. The thesis research project has been started by studying the size distribution of as-grown and thermal anneal induced extended defects in silicon. The focus was on two types of annealing that are used conventionally for denuded zone formation in N-free CZ silicon. The defect type was analyzed by chemical etching and transmission electron microscopy (TEM) and the size distribution by oxygen precipitate and defect profiler (OPP) [4]. The detailed atomic structure of these defects was determined principally by high resolution TEM (HRTEM) and related Z-contrast imaging technique. Point defects and clusters are identified using spectroscopy techniques, namely micron-resolution synchrotron Fourier transform IR spectroscopy (FTIR), grazing angle FTIR [5], spectroscopic ellipsometry [5], and

cathodoluminescence [5]. Unique data obtained from the three last techniques are not discussed in this thesis and will be published elsewhere.

In this work, the experimental facts are linked to theoretical models that were built-up based on atomistic calculations, which used quantum mechanics, molecular mechanics, and molecular dynamics. Detailed studies of the ground state and thermal stability at high temperature (up to melting point) were brought to reality using semi-empirical atomistic calculations. Emphasis was placed on identification of N- and O-related complexes. The identification was done by matching FTIR data to the calculated IR vibrational spectra by semi-empirical quantum mechanics calculations. Chemical complex formation and their thermal stability were discussed in relation to the FTIR based identification and detection of N- and O-related species. A set of self-consistent conclusions have been reached then employed to develop macroscopic physical models for defect formation.

Finding the thermodynamic properties of active species enabled building macroscopic models for the nucleation and extended defect formation mechanisms. However a quantitative assessment of the precipitation in presence of a large number of species has not been reached for N-CZ Si defects. A continuum model is planned and will be based on the idea of multi-component homogenous nucleation of defects in nitrogen doped oxygen-rich silicon. It will be solved by chemical rate equations for small clusters (RE) and Fokker Planck equation (FPE) for precipitates coupled with point defect continuum equations (CE). Previously, we have developed a RE/FPE/CE parallel code that runs on supercomputer for solving point defect clustering for N-free CZ silicon, the code was exploited for a number of annealing conditions [6]. The base physical model was the mono-component homogenous nucleation.

The physical models of defect nucleation and growth in N-CZ are complicated by the wide range of chemical complexes induced by nitrogen doping. Moreover, these complexes transform in a variety of species at high temperature, at various stages of crystal growth and wafer annealing. The combination of experimental data and extensive numerical simulation using high performance computation was ultimately found necessary. The entire high performance computation (HPC) has been carried out in our laboratory. The HPC resources were made available to us through a user grant award received by Dr F. Sahtout Karoui from North Carolina Supercomputer Center. Sumitomo Sitix has sponsored part of our theoretical

investigation effort, in the framework of a Silicon Wafer Engineering and Defect Science (SiWEDS) research project.

The material used in the experimental studies was offered by the Key Laboratory at Zhejiang University in China and Nippon Steel Corp., in the framework of the SiWEDS research program, and the National Renewable Energy Lab., CO. Two sets of N-CZ silicon wafers were annealed with various annealing cycles. In contrast to N-free CZ Si, small oxygen precipitates were found in the as-grown N-CZ Si. Furthermore, these grown-in defects appeared to resist to high temperature annealing and could not be dissolved, unlike in the N-free silicon. Theoretical studies [7, 8] suggested that V_2N_2 complexes are very stable at wafer processing temperature range and higher. The split-interstitial N_2 is also stable but mobile, as it is thought to be the vehicle of nitrogen diffusion, but can form vacancy complexes either as VN_2 , or in later stage, as V_2N_2 . These complexes tie up vacancies at high temperature (during ingot cooling). They reduce the formation of voids by delaying the onset temperature of void formation [3]. It is known that precipitate growth rate and size in CZ silicon are controlled by diffusion of oxygen and point defects (at high temperature), whereas in N-CZ they appeared diffusion-reaction limited, involve many more species, and the point defect clustering is shifted towards lower formation temperatures [3, 9].

Oxygen out-diffusion is found experimentally, strongly altered by N dopant. The latter prevents oxygen from evaporation, which results in a formidable pile up of N and O species at the surface, hence forming an oxynitride shallow layer with a large density of precipitates and sub-micrometer stacking faults. This indicates a change in the boundary conditions by N, while the coupling of O with N modifies the nucleation mechanisms. Two decoupled precipitation domains, separated by the so-called denuded zone (DZ), were found in annealed N doped silicon wafers, i.e., the bulk and the sub-surface. These domains are characterized by different types of extended defects and distributions. Each involves species and specific mechanisms of formation, boundary and initial conditions, and clustering processes spanning over different scales. The reason stems from the fact that (i) point defect clustering in N-CZ produces at high temperature many more species than in N-free CZ silicon, (ii) the early stage of clustering is the dominant process (due to a significant reduction of the critical radius by nitrogen, i.e., most nitrogen grown-in defects were found very stable), and (ii) in the nucleation early stages N and O couple.

The precipitate nucleation modes consistently appeared distinct from that in N free silicon and faster as seen from the nucleation time lag reduction by nitrogen.

First principles calculations, i.e., Density Functional Theory (DFT), are used to account for chemical complex formation and molecular dynamics (MD) as basis for the clarification of nucleation mechanisms in N-CZ silicon. The ground state and temperature dependent equilibrium atomic structures complexes in silicon (formed of nitrogen and oxygen atoms and silicon vacancies, i.e., $N_1O_mV_n$) were established. The viability of a “guessed species” is deduced from its stability at ground state and at high temperature. The thermodynamics was cross-correlated with results from the identification of chemical complexes based on FTIR spectroscopy data. The latter consisted in calculating the IR absorption lines and comparing them to the measured FTIR lines. The identification led to selection of the viable candidates that are effectively detected in as-grown or heat treated materials. The studied basic nitrogen complexes are N-pairs (i.e., interstitial N_2 or substitutional pairs VN_2 or V_2N_2) which can be coupled to oxygen (i.e., N-O and N-O-V, generic notation for $N_1O_mV_n$ in silicon crystal matrix). The main result of these calculations is that N_2 and V_2N_2 appeared to be very stable, while VN_2 has a much lower stability. Nevertheless, at high temperature VN_2 plays an important intermediary role for forming the more stable V_2N_2 or the mobile and stable N_2 . Energy of formation calculation, by quantum mechanics, showed that VN_2 spontaneously forms only when activated by an oxygen atom, which is a likely conclusion in view of the high concentration of oxygen. For this important early stage species (i.e., VN_2), the equilibrium concentration required the calculation of the configurational entropy (by thermodynamics statistical analysis) and the vibrational entropy by semi-empirical calculations. To facilitate the interpretation of the defect clustering, the adsorption of V and O by N pairs in the bulk material was investigated by first principles calculations and MD. It was found that (i) VN_2 does not attract V and O atoms, but it may capture a vacancy rendering it the very stable V_2N_2 , and (ii) both N_2 and V_2N_2 can attract V and O atoms. Although carried out by different levels of theories and calculation methods, the IR absorption, the thermal stability, the thermodynamic statistics, the enthalpy of formation, and the adsorption potential were self-consistent. For instance they showed that V_2N_2 is (i) a stable complex, (ii) detectable species in the silicon matrix, and (iii) plays the principal role in oxygen precipitate nucleation, while it reduces the void formation. In addition, this set of methods showed that the concentration of the precursor VN_2 is in line with the measured N- and O-rich

domains density obtained by high resolution SIMS depth profiles, suggested to be almost the majority of nuclei. Their density appeared to correspond to that of high hardness phases detected by μN load controlled nano-scratches. The calculated characteristics of interaction of chemical complexes with the point defects and O atoms are in line with the experimental observations on the enhancement of oxygen precipitation and the delay of void formation.

The effects of light elements (N, O, C, and B) on wafer mechanical properties were also studied by atomistic calculations by molecular mechanics using Tersoff three-body potential. This allowed accounting for dislocation locking by the creation of impurity atmosphere. The impurity size effect is implemented using the method developed by Johnson [10], which merges the continuum elasticity theory with the atomistic assessment of impurity interaction with the dislocation core, namely the stress field. These calculations allowed obtaining the binding energy (BE) and the separation shear stress of the dislocation from its impurity atmosphere. We found that the strongest locker of edge dislocation is oxygen, followed by nitrogen, and then carbon. Other impurities have been tested as well. For instance germanium appeared not to bind with dislocation, the reason for which threading dislocations appear in SiGe heterostructures in addition to the high density of misfit dislocations. Phosphor atoms are totally transparent to dislocation. In addition, the correlation of mechanical properties with the local composition as well as the average, the nature of chemical complexes, and second phases was sought. This was done by nano-indentation and load controlled nano-scratches. These tests have been carried out at the Dept. of Mechanical Engineering, NC A&T University at Greensboro.

The end result of this thesis is a handful of models and theories of defect formation in ultra pure silicon containing two impurities (N and O) which have large differences in the transport properties and strongly interact. The clarification of various issues was published in a number of papers (listed at the end of this report) and were channeled into practical applications which were filed for patents. To name three, (i) the application of N and O co-segregation to the fabrication of nano-electronics and quantum devices (quantum dots made of SiGe and GaN) by application of thermo-mechanical stresses [11], (ii) the modification of the silicon surface by ion beam [12], and (ii) the implementation of precursors by AFM indentation with ultra small load (pico-Newton), co-precipitation of N and O, and dislocation healing by H-based forming gas annealing [13].

The first chapter introduces the problem of crystal growth and defects in as-grown and annealed wafers, the benefits of nitrogen doping for silicon, and the draw backs with the means to circumvent them. In Chapter II, experimental observations on nitrogen doped as-grown and annealed silicon wafers with and without annealing are presented. Emphasis was made on the depth dependence of defect nature, size distribution, atomic structure, composition, and stoichiometry. In Chapter III nanoscale analysis by high resolution TEM and STEM are discussed for a number of defects probed at different depths of annealed N-CZ silicon wafer. Z-contrast imaging and EELS analysis allowed clarification of the N and O interactions. The detailed defect structure and composition were used to develop models of point defect dynamics and extended defect formation. Physical models of defect nucleation were qualitatively discussed in Chapter IV and defect precursors were mapped on the crystal body to show the growth and transformation stages during solidification. Chapter V is dedicated to (i) defect atomistic modeling at ground states, (ii) chemical complex thermodynamics at high temperature, (iii) characteristics of N-related nuclei, (iv) interactions of point defects (i.e., V, and interstitial O_i) with the recently uncovered nuclei, and (v) discussion of the impact of the interaction potentials on extended defect formation. In Chapter VI, chemical complexes were identified based on their IR absorption signature calculated by quantum mechanics with reference to IR lines (from measured FTIR spectra) of as-grown and heat treated materials. The established signatures of chemical complexes were verified by the viability of the complex candidate (deduced from the calculated thermal stability). Depth profiles of IR line peak intensities of annealed wafers were obtained by high spatial resolution synchrotron FTIR. Depth distributions of N-V-O complexes have been deduced. These appeared in agreement with oxynitride precipitate and continuum defect depth profiles detected by the combination of SIMS, OPP and etching of bevel polished samples from the same wafer. This confirmed the validity of the IR absorption based identification results while cross-checking the calculated chemical complex thermodynamics. In Chapter VII, silicon mechanical properties measured by nanoindentation and nanoscratches on a variety of substrates were compared and correlated to the dislocation pinning discussed in Chapter VIII. In the latter, the benefits of nitrogen are further explored by simulation of the dislocation locking by light element atmospheres. Additionally, for comparison purposes, a wide range of elements have been studied. The last chapter was dedicated to global discussion, conclusions, and recommendations needed for using nitrogen in silicon.

1		
Chapter I.....		8
INTRODUCTION		8
2 Problem Statement		8
2.1 Grown-in Defects in Float Zone and Czochralski silicon		8
2.2 Process Induced Defects in Czochralski silicon wafers		12
2.3 Nitrogen in CZ and FZ silicon		13
2.3.1 Control of Silicon Defects by N Doping.....		13
2.3.2 Dislocation Control by Nitrogen doping.....		16
3 Research Motivation.....		17
4 Objectives of the Thesis		19

Chapter I

INTRODUCTION

1. Problem Statement

1.1. Grown-in Defects in Float Zone and Czochralski silicon

In high purity silicon impurities particularly, oxygen in CZ, react in a myriad of ways giving rise, to a wide range of extended defects. These have become detrimental for and for giga scale integration (GSI) applications and sub-micrometer electronic devices. Electrical properties are controlled by the doping concentration; likewise they are very sensitive to impurities inevitably incorporated during crystal growth and during wafer processing. Crystal defects also negatively affect the electrical properties since they trap/release impurities, particularly the harmful transition metals. The undesirable effects of impurities are minimized by removing them from the device zone by internal gettering (IG). Hence, an impurity denuded zone (DZ) is created at the near-surface region of the substrate and used for device fabrication. Oxygen precipitation, in the range of tens of nanometers, grown away from the DZ (tens of micrometers deep in the bulk), can be used for IG. In addition to the efficient IG function realized by oxygen precipitates in the bulk, oxygen has been used to control the mechanical strength of silicon. This enables tailoring the wafer toughness to be compatible with the production of ICs and devices. Designing the gettering during complex annealing cycles requires a detailed knowledge of the size and number of oxygen precipitates inside the wafer. The origins of oxygen precipitation and the defect formation inherent to the high content of oxygen in CZ silicon are of high interest for both IC technology and for fundamental studies on point defects and their interactions. Voids near the surface of the wafers known as D-defects or crystal originated particles (COP), are known to appear in CZ Si annealed wafers, mainly in the central part of the wafer. Giant octahedral voids can be annealed-out by hydrogen at high temperature, around 1200°C [14]. Two techniques dominate the production of single crystal Si that meet the requirements of the microelectronic device technology, low metal concentration, reasonable defect density and size and rarely extended defects like ingot core, OSF ring... One technique is zone melting (FZ)

method and the other is a pulling method Czochralski (CZ) [15]. The CZ process with quartz crucible is the most widely used technique for efficiently producing pure silicon. However, the used quartz crucible reacts with the silicon melt introducing a high amount of oxygen into the crystal, in amount approaching the solubility limit at melting point. Today's GSI technology faces new challenges due to the large amount of oxygen thus demanding reduction of oxygen, higher material quality, and larger wafers. Large diameter Czochralski crystals contain a central zone with vacancy related faults known as "D-defects" [16]. The D-defect zone is surrounded by an annular ring containing oxygen precipitates and oxidation-induced stacking faults (OSF ring defect). The radial position of the OSF-ring is strongly dependent on the pull rate; slower pull rates result in a small ring diameter. Outside the ring an essentially defect-free region exists. Initially the OSF-Ring formation process was described based on an axial point defect diffusion model introduced by Voronkov [17, 18], which states that either the Si vacancy (Si_v also referred to as V) or self-interstitial (Si_i also referred to as I) can dominate depending on v/G , where v is the crystal pull rate and G is the axial temperature gradient. The OSF-Ring was proposed to form at the boundary separating the vacancy/self-interstitial rich regions. This implies that the self-interstitial and vacancy concentrations are of comparable magnitude. However, there is evidence that the vacancy concentrations may exceed that for self-interstitials by a significant amount over the entire crystal solidification and cooling temperature range. Also, as reported by Suhren et al [19], the OSF-Ring is strongly dependent on the boron concentration indicating that chemical/electronic interactions are also operative and the OSF-Ring can not be explained by a simple vacancy/self-interstitial boundary reaction. Thus, the complex interactions between vacancies, oxygen, and dopants determine the formation of voids, oxygen precipitates, and the position of the OSF-Ring.

A-defect [20, 21], and D-defect [22] have been identified in FZ crystals as the major grown-in crystal imperfections. A-defect always occurs in a striated pattern, and that striations are well correlated to impurity micro-segregation. In the 1970s the nature of A-defects was determined by TEM to be an interstitial-type dislocation loop [21]. These observations lead to the conclusion that the self-interstitial was the dominant point defect in silicon. However, in 1981 it was proposed that D-defects delineated in rapidly grown crystals were agglomerates of supersaturated vacancies and not distributed in a striated pattern [22]. It was therefore widely believed that self-interstitials were dominant for slow pulled crystals and vacancies for fast

pulled crystals; even though the origin and formation mechanisms of either the A- or D-defect were still not understood clearly. Subsequently, Chikawa [23], studying the crystal growth data produced by Miyamoto et al [24], suggested that A-defects are actually secondary defects requiring precipitation-induced self-interstitials. In Miyamoto's work, high purity, multi-pass, float-zone purified crystals were found to be free of A-defects, indicating that these extrinsic dislocation loops only appear following impurity precipitation which is coupled to their striated distribution. Thus, Chikawa speculated that vacancies are the dominant point defect over the entire range of pull rates and temperature gradients. Taking as a starting point Chikawa's proposal [23] that the vacancy is the dominant source for FZ silicon grown-in defects, and the CZ observation by Sadamitsu et al [25] that dislocation loops outside the OSF-Ring can be traced to a precipitation source. One can then build a unified V based model that describes the entire defect spectrum in the OSF defect system. An entire temperature-time-spatial sequence for formation of the D-defect and OSF-Ring was proposed [26], see Fig. 1. It was shown that vacancies dominate in the central region of the ingot, and the radius of that region depends on cooling rate. In the proposed model oxygen out-diffusion is not significant, relative to the vacancy, due to oxygen much lower diffusivity. However, the interaction between vacancies and oxygen generates a common nucleus for either the D-defect in the ingot core region or the oxygen precipitate region (OSF ring), depending on the radial vacancy profile. It is important to note that, since no extended defects are available to act as heterogeneous nucleation sites, supersaturated point defects and impurities (interstitial oxygen, O_i , carbon, and dopant atoms) will interact with each other to reduce their unstable supersaturated and lattice stressing state by forming complexes. Considering the opposite stress fields of oxygen atoms and silicon vacancies and the mobility of the latter, they can easily form a pair in the solid phase, as early as in the under-cooled interface. It has been proposed that vacancy supersaturation reduces the critical nuclei radius of oxygen precipitates, thus enhancing oxygen precipitation [27]; whereas the self-interstitial supersaturation suppresses oxygen precipitation. Similarly, aggregation of a supersaturated concentration of vacancies will be enhanced by a local increase in oxygen concentration. Thus, we have proposed that the primary defect complex present as a silicon crystal cools is a lattice stress compensating vacancy-oxygen agglomerate. These agglomerates then act as a precursor or nucleus for either an octahedral void or an oxygen precipitate to form according to the following reaction pathways proposed by Kiman Bae et al [28]:

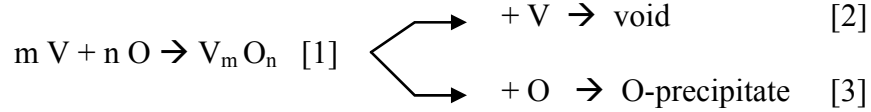


Fig. 1: Basic chemical reactions for extended defect formation in CZ silicon [28].

The V-O based model together with the radial vacancy diffusion dominance, have been verified by simple diffusion calculation of the point defect [26]. The cooling rate was taken variable, and the point defect equilibrium concentrations at the MP were considered as initial concentration values. At each level of the ingot, the equilibrium concentration at the corresponding temperature is considered as a boundary condition. It appears that the vacancy/oxygen complex controls the type and spatial distribution of voids and precipitates in the OSF ring. The model is consistent with a large body of experimental evidence and amenable to thermodynamic considerations of point defect and impurity behavior, as described in more detail below. To the simple physical model based on the V-O complex and the strong radial component of vacancy diffusion [26], Sinno and Brown supported the model of point defect axial diffusion [18, 29]. The primary silicon defect that is the VO complex can be artificially generated by irradiating a Si substrate at room temperature. The absorbed kinetic energy separates the produced Frenkel pairs into mobile vacancies and interstitials. The former trap interstitial oxygen atoms yielding VO complexes [30] (known also as A-centers) and the latter most often produce dislocation loops. The A-centers form irrespective to any type of irradiation method be it by electrons, protons, neutrons, α -particles, γ -rays, etc. Electron paramagnetic resonance (EPR) [31] and studies on uniaxial stress effects on the local vibrational mode have shown that the structure of the negatively charged centre and the neutral form are similar. Umerski and Jones demonstrated that an O atom bridging a pair of Si neighbors of the vacancy is energetically favorable [32]. The defect has FTIR vibrational modes at 836 cm^{-1} for the neutral form [33] and 885 cm^{-1} for the negatively charged form. The lines are broad and no ^{29}Si isotope shift has been detected [34]. The strained Si-Si bond between the other pair of Si atoms bordering the vacancy induces an acceptor level at $E_c-0.17 \text{ eV}$, associated with the VO center. Their migration barrier is $1.46 \pm 0.29 \text{ eV}$ [35] (also given as 1.86 eV [36, 37]), allowing them to migrate at lower temperatures than O_i .

Thermodynamics of point defect agglomeration during crystal growth has been discussed by several authors. Voronkov and Falster suggested that small voids form at high temperature between 1400-1150°C [17, 38], whereas oxygen precipitates form at lower temperature, around 1050°C. Precipitation was investigated experimentally for silicon annealed wafers and by diffusion and diffusion-reaction limited clustering modeling in relation to Si_I and Si_V exchange and creation/annihilation. In this context, computer simulation has been performed for calculating the number and size of oxygen precipitates and void defects in thermally treated silicon crystals [6, 39, 40, 41, 42]. This allowed suggesting models of grown-in defects in CZ silicon (i.e., small O precipitates and V agglomerates) .

1.2. Process Induced Defects in Czochralski silicon wafers

Heat treatments of wafers for advanced microelectronics use RTP-based high temperature, short time, and single wafer processing. Unfortunately, RTP treatments often produce extended defects via stress relaxation, particularly at wafer contact points, as shown in Fig. 2. Also, whenever a large thermal gradient exists across the wafer diameter, dislocations and slip lines typically appear at the wafer edge, or at any location where a stress riser exists, as shown in Fig. 3. These defects then act as gettering sites and locally perturb the minority carrier lifetime. Options for supporting large wafers in production RTP, as well as in vertical furnaces include either an annular perimeter support ring or a series of quartz pins. In principle, the ring concept offers a lower average local stress across the wafer. However, during high temperature processing, a large deflection can occur for 300 mm wafers due to their weight and make them susceptible to plastic flow, particularly if a temperature gradient exists across the wafer diameter. Also, it is difficult to eliminate localized stress risers along the contact surface of the annular ring as can be seen in the XRT close to the support ring for a wafer treated at 1150 C for 30 sec [44].

The processed material is subject to gravitational stresses, which generally induce friction and various contact forces, particularly the impact force at the contact instant. These various mechanical components, associated with the thermal stress, account in the dislocation formation, distribution and movement. A wide range of dislocation configurations has been observed, while large contact surface and slow handling exhibited a minimum dislocation depth extension. Wafers processed with extremely slow up and down lifting and introduction on the hot zone, has led to dislocation-free contact regions.

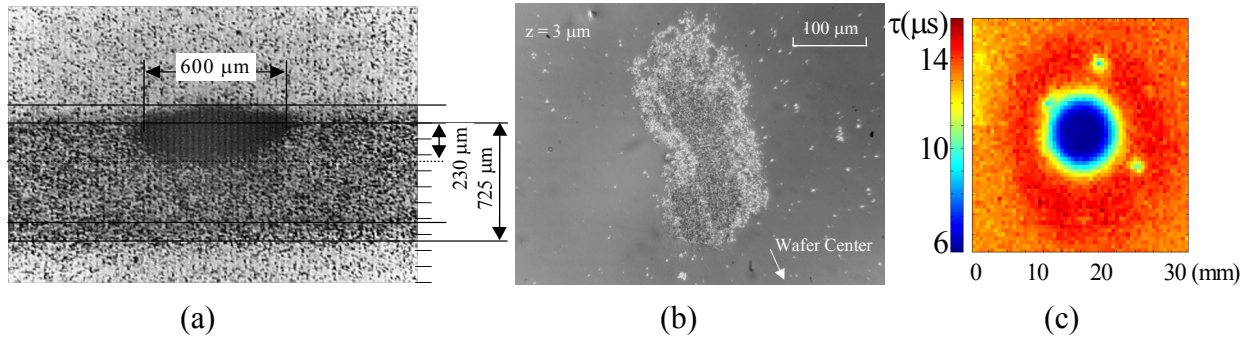


Fig. 2: Contact induced defects in RTP wafer at $T= 1150\text{ C}$ for 30 s .

- (a) XRT cross section
- (b) Nomarski micrograph of Secco Etched sample cut at the contact point
- (c) μ PCD minority carrier recombination lifetime variations at the contact point; the shown area is cut from whole wafer map. Degradation is about 1/3 outside the damage and more than one order of magnitude at the dislocation array.

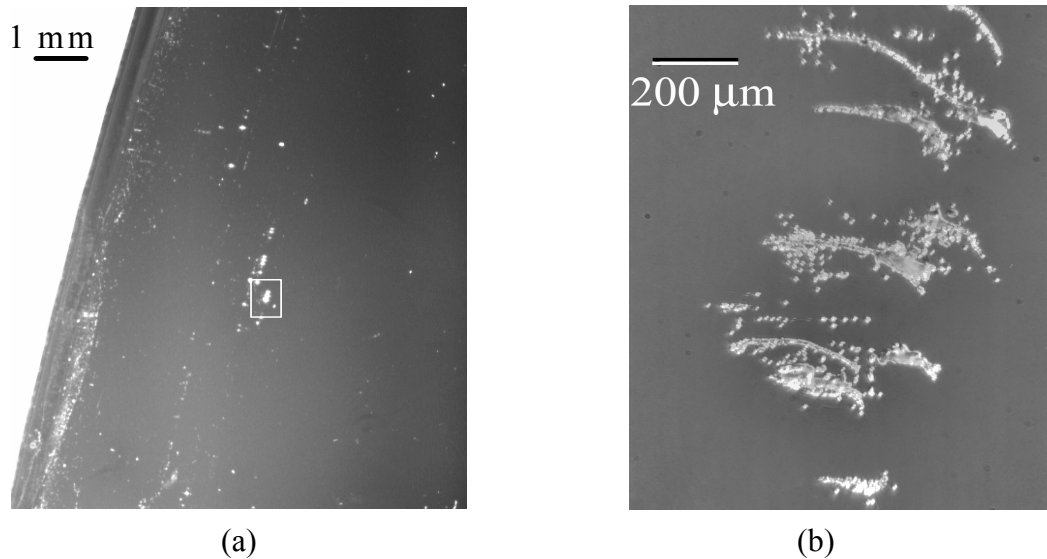


Fig. 3: Contact induced defects in a 300 mm wafer cycled in an RTP system that uses two support rings at the wafer rim and at a radius equal to 0.6 that of the wafer. RTP wafer for 10 s at 1200°C .

- (a) Portion at the wafer rim of a plane view transmission XRT image
- (b) Nomarski micrograph of Secco Etched of the in-boxed area in (a).

1.3. Nitrogen in CZ and FZ silicon

1.3.1. Control of Silicon Defects by N Doping

The primary thrust of nitrogen doping is its strong influence of nucleation of oxygen precipitates via the formation of N-V complexes and the reduction of void size to below detection limits. The interaction of nitrogen with vacancies and interstitials greatly impacts the

size and density of precipitates as well as the nucleation and motion of dislocations. Another strong benefit of N doping is the compensation of hardness loss in the needed low oxygen ingots. Large wafers (300 mm diameter and more) can be toughened in order to reduce material volume thus their weight, which results in a better handling and increase of the yield. The adjustment of oxygen and nitrogen contents can be used in connection to a variety of growth conditions (crystal growth rate, temperature growth, ambient,...) and wafer annealing cycles. These parameters of prime importance adjust the point defect balance and interaction during cooling.

Ohashi and Nakai showed that a delay in the void formation sequence occurs during growth of N-CZ crystals [3, 45]. Void defect formation temperature shifts toward lower temperature, as shown in Fig. 4. Frozen vacancies which could not form void defects (as it happen in N free CZ silicon) are carried over into the onset temperature of oxygen precipitation. Enhanced oxygen precipitation leads to as-grown precipitates.

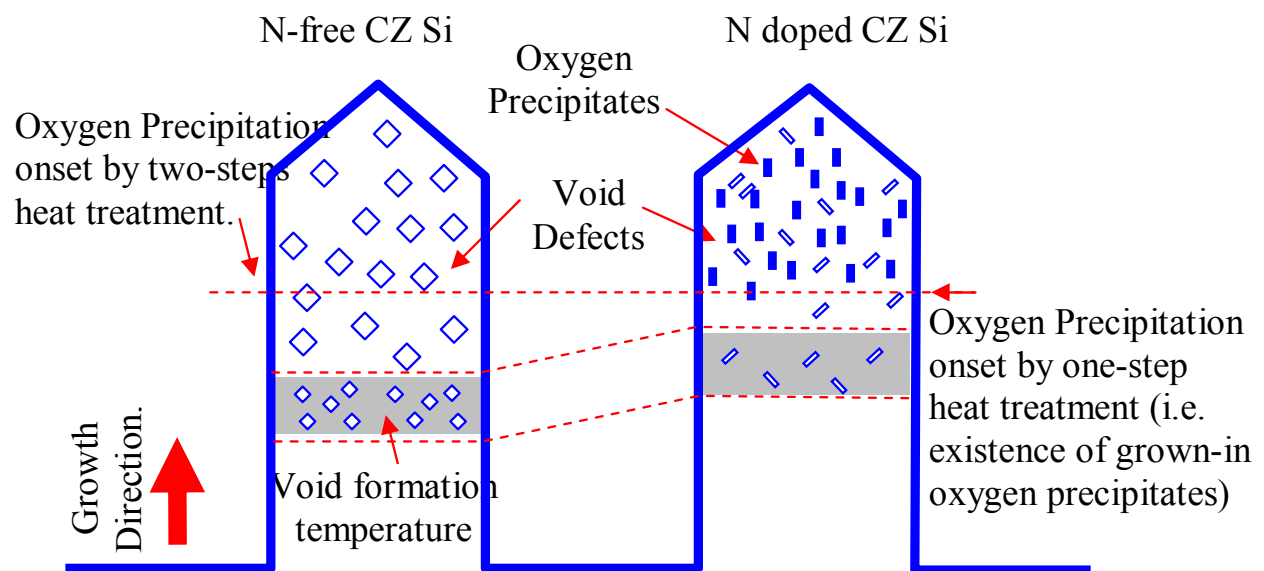


Fig. 4 : Sequence of defect formation in N-CZ Si crystals versus N-free CZ Si [45].

The radial distribution of defects changes with v/G in N doped wafers, and the defect nature is modified across the OSF region, as shown in Fig. 5. It is possible to remove the void by either by using a slow pulling rate or by applying a high temperature gradient. Both allow V defects to out diffuse to the ingot boundary at high temperature, before stages of complex formation with impurities. High v/G , reduces the precipitation zone.

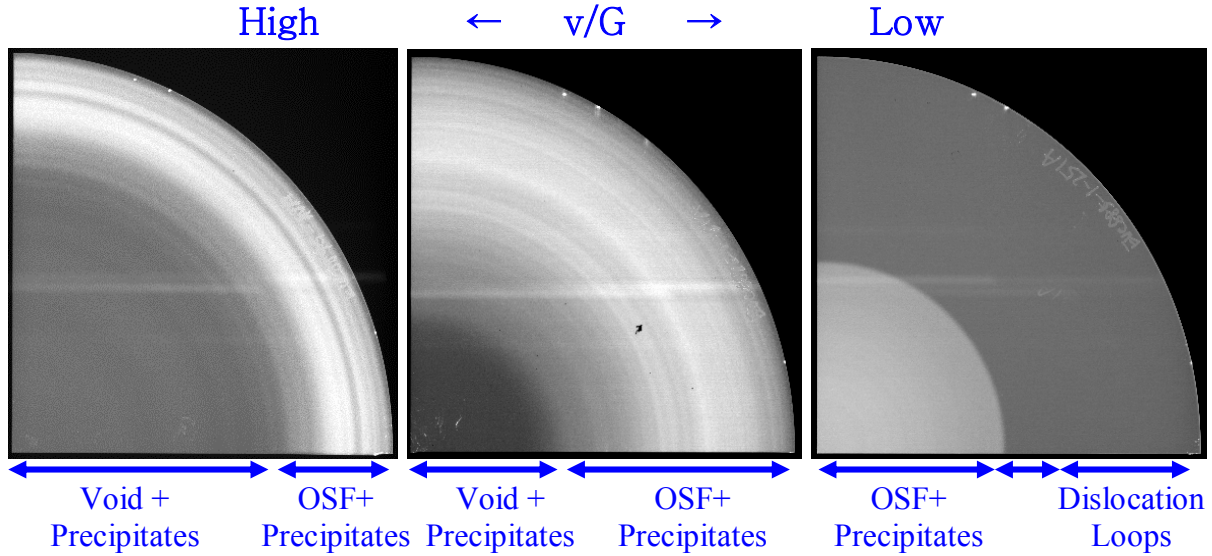


Fig. 5: Defects variations in N-CZ Si as a function of v/G , the Voronkov ratio, where v is the pulling rate and G is the temperature gradient maintained across the ingot during cooling [45].

Conventional high pulling rate in CZ grown crystals, leads to V rich ingots, which then have V clusters and voids. These are detrimental for devices, and can be annihilated at crystal growth by N doping. The effect of N doping and v/G ratio on defect morphology in wafers is coarsely depicted in Fig. 6. The defect nature is modified from basically octahedral shaped voids to strain-free precipitate platelets and to strained precipitates with a high shape ratio. This figure clearly shows that:

1. Grown-in defects in nitrogen doped CZ-Si crystals are plate shape triclinic voids of volume density $10^7/\text{cm}^3$ and oxygen precipitates of volume density $10^9/\text{cm}^3$.
2. When the nitrogen concentration is low the morphology of voids takes indefinite octahedral shape. When the nitrogen concentration is high, voids annihilate and oxygen precipitates becomes major grown-in defects. The shape of plate shape triclinic void is not susceptible to the cooling rate of the crystal, only the size increases when the cooling rate decreases.
3. Nitrogen doped and argon annealed wafers accomplished remarkable surface zone defect annihilation to form COP-DZ and a high Bulk Micro-Defect (BMD) density simultaneously. They also showed excellent electric performance; Gate Oxide Integrity (GOI) and impurity gettering ability.

Images in Fig. 6 show the large variety of defect morphologies in annealed N-CZ Si in relation with the N doping level and the crystal growth conditions (expressed with the Voronkov ratio

v/G). This shows the large choices for defect control and engineering by slightly doping silicon with nitrogen.

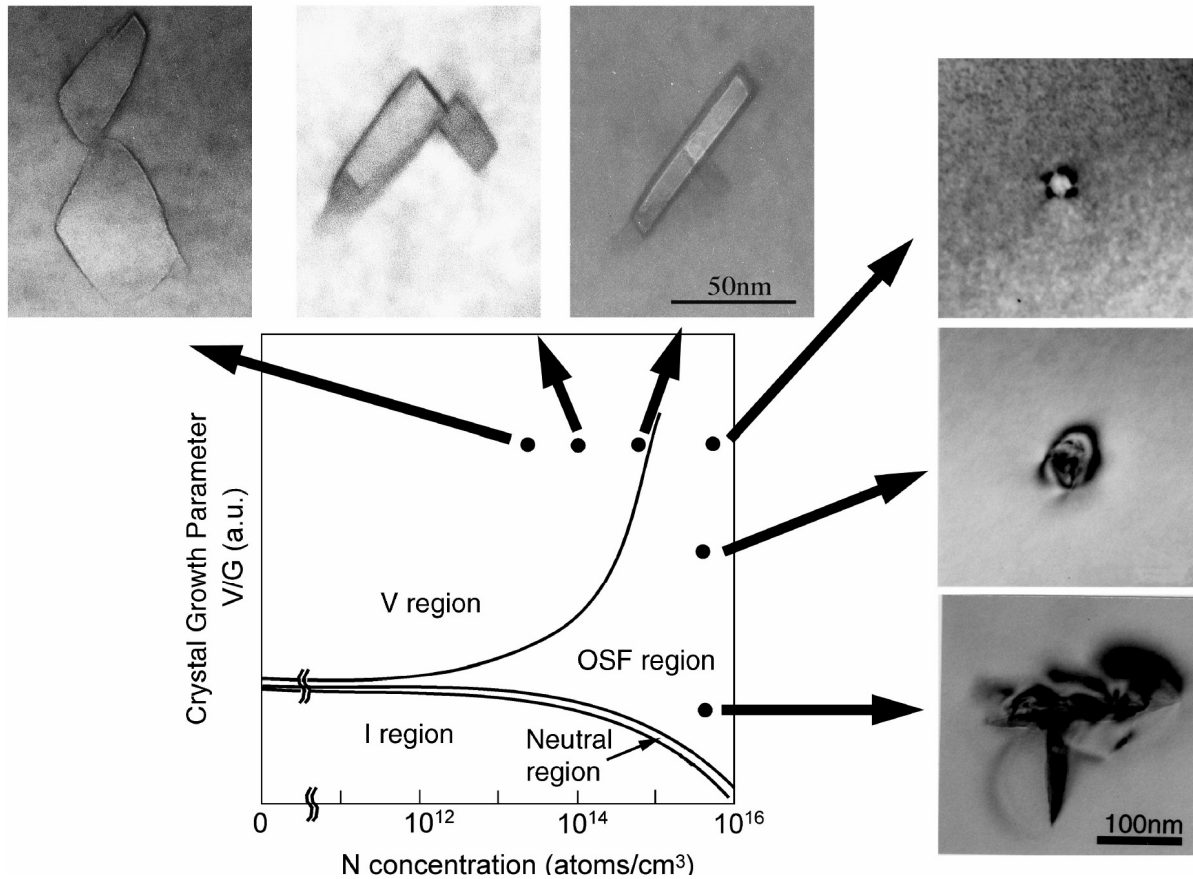


Fig. 6: Defect morphology variations in N-CZ Si in relation with the Voronkov ratio v/G and the N doping level, after Ohashi [57].

1.3.2. Dislocation Control by Nitrogen doping

Float zone crystals are known to be more vulnerable than CZ to the generation and movement of dislocations, as illustrated in the x-ray topographic(XRT) images presented in the upper pair of scribed wafers in Fig. 7 (from the work of Abe, et al [47]), following a single or double thermal cycle of 1150C. An FZ crystal strengthened by nitrogen doping to $4 \times 10^{14} \text{ cm}^{-3}$, as shown in the lower pair of XRT in Fig. 7, is dramatically improved to the point where the N doped FZ wafer is actually more resistant to dislocation formation than the undoped but higher O content CZ wafer. It has been shown that nitrogen atoms and their related defect complexes are effective in enhancing the nucleation of oxynitride precipitates which produce a dislocation locking action that is about 100 times more effective than that provided by oxygen precipitation [48].

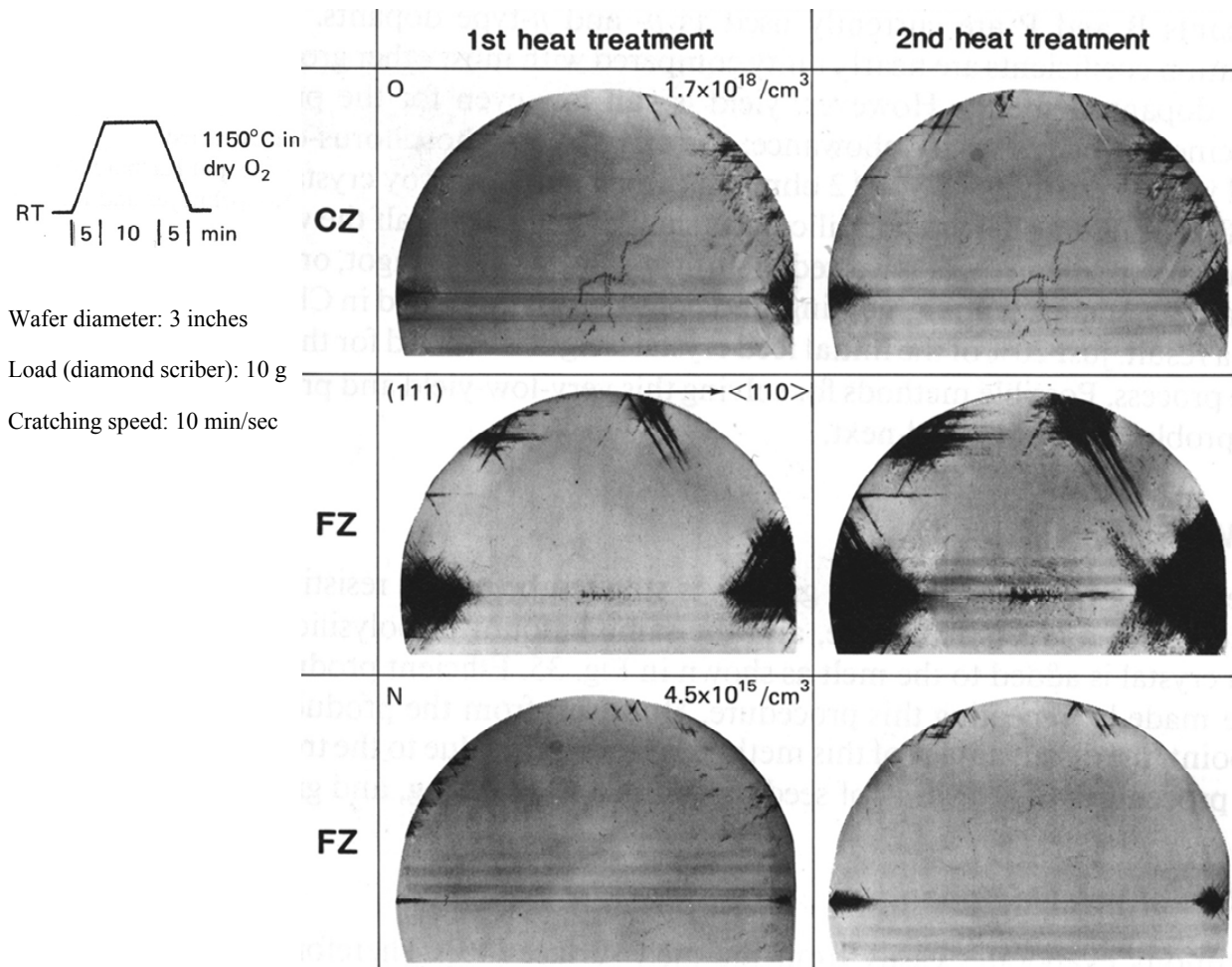


Fig. 7: X-ray topographic images of dislocations in CZ, undoped FZ, and nitrogen doped FZ wafers following scribing and two cycles of thermal annealing at 1150°C [47].

2. Research Motivation

For modern low oxygen concentration CZ crystals, obtained by reduced dissolution of quartz crucibles, nitrogen doping enables impurity gettering to occur by forming oxynitride precipitates. This is currently a very active area of study for IC wafer production [49] for two reasons. First, the low oxygen translates into lower levels of metallic impurities. Second, nitrogen, coupled with vacancies during ingot cooling, greatly reduces the size and density of void defects, which are a serious IC yield limiting crystal defect. This point is crucial to our interest in creating defect engineering options for PV applications which will depend on balancing the vacancy/interstitial nitrogen and oxygen concentrations and to activate/deactivate

inter-reactions such that the defects are reduced, wafers are strengthened and the charge carriers have a longer lifetime.

The denuded zone and impurity internal gettering (IG) techniques used in CZ silicon technologies are being re-engineered with two different approaches. In the first method, the material properties are modified during wafer processing via a controlled injection of point defects, e.g. vacancies (V). This is possible because the as-grown defects are exposed to a large open surface, and unlike crystal growth, can more easily exchange V and/or Si_I with the surface, depending on the ambient. This offers a strong advantage for defect engineering, provided that adequate fluxes of appropriate point defects are supplied in the right sequence. In this category, R. Falster et al has developed the Magic Denuded Zone (MDZ) process [50, 51, 52] which potentially provides a “real DZ” as deep as 60 to 80 μm, in which no defects were detected by etching. In principle, the MDZ does not depend neither on the wafer position relatively to the L- or P- bands [53], nor on the radial position within the wafer. More important, the MDZ is not sensitive to the initial point defect distribution but to the installed vacancy profile.

In the second method, the post wafer processing defect size is scaled down by changing oxygen precipitate (OP) and void growth mechanisms. This is achieved by modifying the nuclei type, size, and density during crystal growth. This is achieved by the control of chemical complex formation kinetics and the point defect supersaturations. As a consequence, the defect growth phases are significantly changed during both crystal growth and wafer processing. To reach this goal, practically one can dope the crystal for instance with nitrogen [54, 55] or carbon [56, 57].

Nitrogen doping has recently made a renewed drive for silicon manufacturing as it allows efficient control of extended defects. While oxygen concentration of $5 \times 10^{17} \text{cm}^{-3}$ is required for wafer strengthening [58] by locking dislocations with O atoms [59, 60], nitrogen can induce the same effect with 2 to 3 orders lower concentration [61, 62]. Therefore, N doping option is suitable for next generation large wafers [63]. In addition, carrier lifetime can be improved by reducing the O amount, while lightly doping with N maintains high material toughness [64, 7]. Prior work of Sun and co-authors [65] reported that N cancels the C effects during internal gettering (IG) cycling. However, they also found that N degrades the denuded zone. More recent works have shown a feasible approach for defect control in C-free CZ Si by low N-doping [3, 66, 67]. At concentrations in the order of 10^{15}cm^{-3} or less, nitrogen efficiently reduces micro-

defects such as A-defects, D-defect, [68, 69, 70, 71] and enhances oxygen precipitation [66, 55 72, 73, 74] by increasing the precipitate concentration while reducing their size. These phenomena are interrelated and are affected by the high concentration of stable grown-in nuclei induced by nitrogen [66, 75]. The retardation of void formation was suggested to be due to a shift of the nucleation temperature during crystal growth [3, 66, 76]. The defect type and concentration were suggested to be determined by the nitrogen concentration and v/G Voronkov ratio [3, 66, 67].

In order to understand and model oxygen precipitation mechanisms in N-doped Si, the kinetics of point defect reactions during crystal growth and during subsequent wafer annealing need to be thoroughly clarified. Extended defects are examined before and after wafer thermal cycling that are used in conventional DZ processing of N-free CZ Si. Our focus was on the newly found effects of N doping on the DZ. Precipitate size distributions and concentrations depth profiles are discussed in connection to N and O concentration profiles, along with the defect structure and chemical composition. Models are suggested to describe N-rich oxygen precipitate formation based on N related chemical complex interactions, N-O coupling, and nitrogen and oxygen segregation to the surface.

A more general motivation stems from the means provided by modern crystal growth technologies for understanding the mechanisms of defect nucleation and growth. The co-doping is a strong means for material control and provides new horizons for modern devices, especially nanoscale devices. The “atomic engineering” is made possible by silicon, since it is the most pure semiconductor material and has unique properties. It is expected that a full control of grown-in defects via nitrogen doping of CZ-Si crystals will enable tremendous options for both micro and point defect engineering.

3. Objectives of the Thesis

The primary thrust of this work is to examine the influence of nitrogen on the nucleation of oxygen precipitates via the formation of N-V complexes. The interaction of nitrogen with vacancies and oxygen interstitials will greatly impact the size and density of precipitates, as well as the nucleation and motion of dislocations. The intent is to vary the oxygen content as a means to reduce oxygen precipitate size, which are becoming the major problem for submicrometer and

nanoscale IC technologies. The use of CZ and FZ crystalline silicon with low oxygen concentration has clear benefit for the electrical function of the device, but degrades the mechanical properties of the substrate. Low nitrogen level appears to improve the hardness of both systems. Another parameter of prime importance is the variation in crystal growth rate given the fact that it adjusts the point defect balance during cooling. These special materials were made available to this research through the Silicon Wafer Engineering and Defect Science (SiWEDS) consortium. This center research program included modeling and simulation of point defects in nitrogen doped CZ and investigation of precipitate nature (formation, morphology, and composition) and their impact on the wafer.

The end goal of this work is to gain knowledge on the control of extended defects useful for (i) extended defect control, (ii) metal impurity gettering by precipitates, (iii) use the dopant to alter individual and bunched dislocation/grain boundary environments, (iv) enhance the mechanical properties in addition to the functional electrical and optical properties (v) engineer new applications for nanoscale technologies by manipulating light element impurities (N, O, and the main dopant: B) and crystal point defects. An extremely important consideration is the dynamic state of point defects in specific wafer regions (subsurface device zone as well as the neighboring regions i.e., DZ and the bulk). Although defects and impurities in silicon are usually specified to have a certain density or concentration, it is often the point defect balance that fundamentally dictates the quality of a crystal/wafer during growth/processing. Thus, the balance between lattice vacancies and interstitials and their mutual interaction with various dopants as well as their condensation into dislocations/voids will also be examined in this study. It is also believed that it would be valuable for (i) the hydrogenation/passivation community, and (ii) for self organized atomic structure, to have access to the produced expertise in point defect control.

The different phases involved can be broken down into the following:

1. Experimental assessment of the Lo-Hi and Hi-Lo-Hi annealing, conventionally used for making DZ.
2. Physical modeling of defect formation/annihilation, in order to describe the nucleation processes and the clustering mechanisms. Historically, the clustering has been investigated first with CZ Si, but with the rise of N-CZ silicon the nucleation has become a key issue that needs clarification.

3. Computer simulation. It has become necessary to use multiscale modeling of physical point and extended defects processes. Therefore we merge:
 - First principles methods, molecular dynamics and crystal defect visualization,
 - Spectroscopic signature of N-related defects, as a means of identification and analysis of the acting species, and
 - Phenomenological description of clustering phenomena.
4. Correlation of the multi-scale simulation with the macroscopic material properties, namely:
 - dislocation interaction with N chemical elements, with
 - the mechanical properties (material elasticity and hardness)

These topics are interconnected and scale in different ranges. The multi-scale numerical methods describe each stage of defect formation, i.e., atomic interactions, complex formation, clustering problem. Clearly the size of each of these problems requires supercomputing to insure convergence in tolerable computation times.

Chapter II	
Experimental Study of Defects in Nitrogen Doped Silicon.....	23
1 Introduction	23
2 Experimental Procedure	24
3 Results and Discussion.....	26
3.1 Defect Nucleation Mechanisms in N-CZ Si.....	36
3.2 Defects In N-CZ Silicon Wafers	38
3.3 Nitrogen and Oxygen Interactions and Co-Segregation to the Surface	39
3.4 Composition of Sub-Surface Defects in n-cz Wafers	42
3.5 Nitrogen and Oxygen Coupling	46
3.6 Nitrogen and Oxygen Interactions in The Bulk.....	47
4 Summary	48

Chapter II

EXPERIMENTAL STUDY OF DEFECTS IN NITROGEN DOPED SILICON

1 Introduction

In order to comprehend and model oxygen precipitation mechanisms in N-doped Si, the kinetics of point defect reactions during crystal growth and during subsequent wafer annealing need to be thoroughly clarified. In this chapter, we present investigations on extended defects in N-CZ Si via wafer thermal cycling that are used in conventional DZ processing of N-free CZ Si. We focus on the newly found effects of N doping on the DZ. Precipitate size distributions and concentrations depth profiles are discussed in connection with N and O concentration profiles, along with the defect structure and chemical composition. Physical models are suggested to describe N-rich oxygen precipitate formation based on N related chemical complex interactions, N-O coupling, and nitrogen and oxygen segregation to the surface.

Nitrogen doping of CZ silicon, even at relatively low concentration of $5 \times 10^{14} \text{ cm}^{-3}$, fundamentally modifies vacancy (V) clustering [55, 78, 79] and oxygen precipitation mechanisms [3, 80, 82], both at the early stages, during crystal growth, and subsequent wafer heat treatments [83, 84]. One of the goals of this chapter is to present a set of experimental observations that are useful to depict the basic mechanisms of defect formation in heat-treated N-CZ Si wafers in the context of N related complex diffusion-reaction. This is approached by determining the composition of oxygen precipitates, the proportions of N and O dissolved in the Si host crystal, and by considering stress effects. Analysis of N and O co-precipitation mechanisms in N-CZ Si are based on measured [O] to [N] ratio profiles. The precipitate chemical composition with the atomic structural information and strain distribution are used to discuss the O and N coupling and segregation.

2 Experimental Procedure

Two sets of boron-doped wafers from Si ingots grown in different environments were examined, see Table I. The wafers of the first set were 75 mm in diameter, [111] oriented, and grown in a nitrogen ambient which allowed incorporation of nitrogen at a concentration of $\sim 10^{15} \text{ cm}^{-3}$ close to the ingot tail. The concentration was estimated by FTIR and spreading resistance evaluation of N-related shallow thermal donors. The as-grown oxygen concentration was found to be $1.1 \times 10^{18} \text{ cm}^{-3}$ using the 1107 cm^{-1} absorption line by FTIR with a calibration factor of $3.14 \times 10^{17} \text{ cm}^{-2}$. Wafer 1H8 was subjected to a Low-High (Lo-Hi) thermal cycle at 650°C for 8 hours followed by 1050°C for 16 hours, while wafer 1G is left as-grown for reference. Prior to the Lo-Hi heat treatment, wafer LH8 underwent a pre-anneal at 1250°C for 1 hour, which, in effect, dissolves grown-in defects in N free CZ Si [85]. All annealing were done in argon rather than the often used nitrogen ambient, in order to avoid incorporation of ambient nitrogen so as to correlate defect formation kinetics in the near-surface region with grown-in nitrogen. The "reference" nitrogen-free CZ Si wafer paired with Set 1 N-CZ wafers, were obtained from an ingot grown under identical thermal conditions and pulling rate, but in argon ambient. As shown in Table I, these wafers were labeled 2G for as-grown and 2L8 and 2H8 for Lo-Hi, and Hi-Lo-Hi cycled wafers, respectively.

Table I: List of samples with thermal cycles they have undergone. All annealing were done in argon.

Set 1 (111) $[\text{O}_i]=1.1 \times 10^{18} \text{ cm}^{-3}$ $[\text{N}]=1 \times 10^{15} \text{ cm}^{-3}$ $\phi=75 \text{ mm}$	N-CZ	As-grown	1G	Hi: 1250°C for 1 hrs Lo: 650°C for 8 hrs Hi: 1050°C for 16 hrs
		Lo-Hi	1L8	
		Hi-Lo-Hi	1H8	
	CZ	As-grown	2G	
		Lo-Hi	2L8	
		Hi-Lo-Hi	2H8	
Set 2 (100) $[\text{O}_i]=8.4 \times 10^{17} \text{ cm}^{-3}$ $[\text{N}]=5 \times 10^{14} \text{ cm}^{-3}$ $\phi=150 \text{ mm}$	N-CZ	As-grown	3G	Hi: 1250°C for 1 hrs Lo: 750°C for X hrs Hi: 1050°C for 16 hrs X=8, 64 h
		Lo-Hi	3LX	
	CZ	Lo-Hi	4L8	
Hi-Lo-Hi		4H8		
$\phi=200 \text{ mm}$				

Set 2 test wafers were acquired from another source; they are larger (i.e, 150 mm in diameter) and [100] oriented. This material is characterized by lower N and O concentrations than Set 1. The N was incorporated by introducing oxynitride in the melt; its concentration was estimated by FTIR to be about $5 \times 10^{14} \text{ cm}^{-3}$. The oxygen concentration is about $8.5 \times 10^{17} \text{ cm}^{-3}$, according to Japan Electronic Industry Association (JEIDA) standard. These wafers were labeled 3G for as-grown, and 3L8 and 3L64 for Lo-Hi annealed wafers with a Lo step duration equal to 8 and 64 h, respectively. The Lo-Hi thermal cycle was similar to the one used for Set 1, except that the low step annealing was done at 750°C. For Set 2 wafers, N-free Si material from the same vendor was used for reference, hereafter referred to as 4L8 for Lo-Hi and 4H8 for Hi-Lo-Hi.

Samples from these wafers were etched in preferential Wright-Jenkins solution with different observation planes, i.e., (100), (110) and (111), to characterize the defect structure. Using a scanning bright field infra-red interferometer known as Optical Precipitate Profiler (OPP) [86, 87, 88], the defect size distributions were measured in the as-grown and the heat treated wafers after the last annealing step (i.e., growth step). The y-scan mode was used to obtain the defect size distributions in the bulk (at 30 μm from the surface) and the z-scan mode to obtain the defect concentration profiles up to a depth of 60 μm . The size distributions were found by averaging the OPP signal from 36 spots distributed over a cross, parallel to [110] and $[\bar{1}\bar{1}0]$ directions. For each spot, three y-scans were averaged, each is 128 μm long. The defect concentration depth profiles were constructed from the OPP signal acquired in the z-scan mode by averaging OPP y-scan. In this case, the y-scan lines are separated by 3 μm and distributed within a horizontal cell of 1000 μm x 1000 μm area. The measurement cell was stepped from the wafer surface to a 60 μm depth in increments of 0.7 μm , which corresponds to the diameter of the excitation volume.

The calibration of the OPP voltage signal as a function of the defect size was based on precipitate sizes determined by Transmission Electron Microscope (TEM) using samples from 1L8 wafer. The smallest detected OPP signal marked with the line (α) in Fig. 9 (a), and the largest value at the size distribution tail, line (δ), were converted into equivalent radii of the smallest and the largest precipitates, respectively; these were determined by TEM. Similarly, the signal at the distribution peak, indexed with (β), was assigned to the most frequent TEM

determined sizes. The size-voltage correlated value designated as (γ), was added from Ref. 89, obtained with the same procedure and the same OPP tool. The ghost images generated within the detected images were filtered out using the procedure developed by Nakai et al [88].

Nitrogen and oxygen concentration depth profiles were measured for Set 2 samples using Cameca IMS-6f SIMS apparatus. Nitrogen ion implanted FZ Si samples were used as standards to calibrate N and O concentrations. Negative secondary ions were acquired through a 60 μm diameter optically gated area, with the sample biased at -4.5 kV, and $^{28}\text{Si}^{14}\text{N}^-$ ions were counted. Also nitrogen and oxygen concentration images as a function of depth were obtained for the 3L8 sample. A series of SIMS images were acquired simultaneously every 200 μm along a 2° bevel. These images were obtained by rastering a cesium beam across a sampling area of 200 μm x 200 μm . The beam diameter was smaller than 1 μm and the sputtering depth was about 65 nm, measured by an optical profilometer. The same detection method and calibration procedures were used as for the depth profiling but with higher sputtering rate and shorter integration time. In addition to these image pairs, N and O profiles were produced between 20 and 30 μm depth, with a lower sputtering rate and longer integration time, which resulted in a depth resolution of 40 nm. High-resolution cross-sectional (HRTEM) imaging was done in order to examine defect structure in near-surface and bulk regions. Scanning TEM (STEM) images in the Z-contrast mode was done to delineate the phases within small precipitates, while Electron Energy Loss Spectroscopy (EELS) was used to identify impurities within precipitate phases and to estimate the [N] to [O] concentration ratio. The field emission JEOL 2010 STEM can reveal local variations in atomic number and has a lateral resolution below 2Å.

3 Results and Discussion

The defect structure for samples cut from heat-treated wafers after 2 min Wright-Jenkins etching is shown in the Nomarski micrograph in Fig. 8. The first micrograph is taken at about 20 μm from the surface of Lo-Hi treated 1L8 N-CZ Si wafer from Set 1 (see Table I); this sample was bevel polished to 5° off the (111) plane (i.e., initial wafer surface). The two other micrographs pertain to etched samples from 4L8 and 4H8 N-free CZ Si wafers of Set 2 that were cycled respectively with Low-High (Lo-Hi) and Hi-Lo-Hi thermal annealing. The samples were (110) cleaved and polished prior to etching. The magnification of the first image in Fig. 8 (a) is

about three times higher than the images in Fig. 8 (b) and (c); the etch pits are therefore smaller and much denser than in the similarly heat treated N-free CZ wafer 4L8 shown in Fig. 8 (b). Note that the larger and brighter pits in Fig. 8 (a) are due to very small stacking faults (SF). The nitrogen-free wafer 4L8, similarly treated with Lo-Hi exhibits much larger SF(s) , see Fig. 8 (b), with a lower density $\sim 5 \times 10^4 \text{ cm}^{-2}$, whereas no SF appear in similar wafer 4H8 that was pre-annealed with a Hi step prior to Lo-Hi heat treatment, see Fig. 8 (c). Furthermore, the etch pits in 4H8 appear smaller and less dense than those in the N-free Si Lo-Hi treated wafers 4L8, see Fig. 8 (b), and in 1L8 Lo-Hi N-doped CZ sample, see Fig. 8 (a).

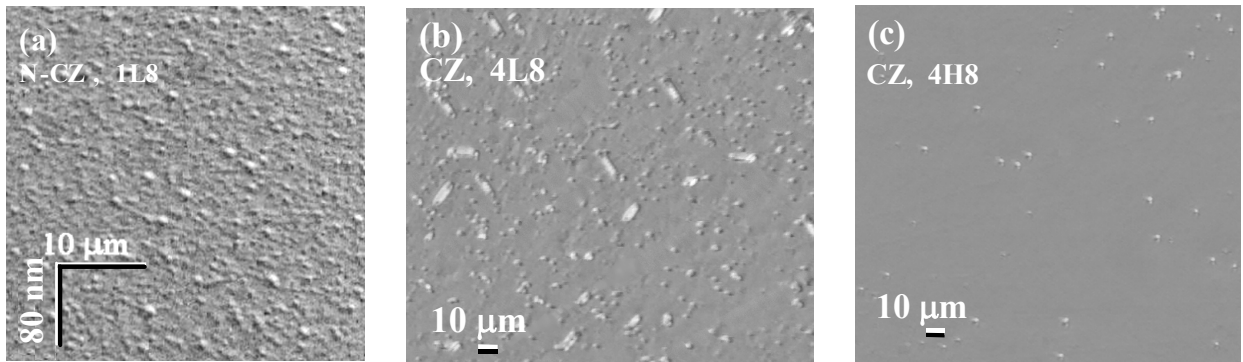


Fig. 8: Nomarski micrographs of Wright-Jenkins etched samples:

- (a) bevel polished at 5° off (100) plane of a N-CZ-Si sample cycled with Lo-Hi (1L8).
- (b) (110) cross section CZ-Si sample cycled with Lo-Hi (4L8), and
- (c) (110) cross section CZ-Si sample cycled with Hi-Lo-Hi (4H8).

Figure 9 (a) shows the OPP determined defect size distribution at $30 \mu\text{m}$ depth in the as-grown N-CZ Si wafer 1G, and annealed 1L8 and 1H8 wafers, after precipitate growth step. Likewise, Fig. 9 (b) shows the defect size distribution in N-free Si wafers (i.e., 2L8 and 2H8) at the same depth. Note that in Fig. 9 (a) the defect size distributions measured at $30 \mu\text{m}$ from the surface, for Hi-Lo-Hi and Lo-Hi N-CZ Si wafers are almost identical. In contrast, in similarly heat treated N-free CZ Si, the defect density is one order of magnitude lower after Hi-Lo-Hi cycle, for all defect sizes, see Fig. 9 (b). In addition, a reduced population of small defects were found in as-grown N-CZ (1G) wafer, see Fig. 9 (a), whereas we were not able to detect by OPP any grown-in defects in as-grown N-free CZ Si wafers (i.e., 2G).

Defect concentration depth profiles in the N-doped wafers 1G, 1L8, and 1H8 are given in Fig. 10. The integration of the size distribution, measured at $30 \mu\text{m}$, over all defects gives their concentration at the same depth, which is $2.5 \times 10^{10} \text{ cm}^{-3}$ for both heat treated samples, see Fig. 11. This supports the nearly equal size distributions for these two samples. Note the unusual

OPP peaks within the first 2 μm from the surface that appear in the subsurface (region I) in both heat treated and as-grown wafers. In the low density defect zone (LDZ), region II, the defect level is above $1 \times 10^9 \text{ cm}^{-3}$, which shows that the near-surface region in N-doped Si significantly deviates from the conventional denuded zone in N-free CZ Si. Approaching the bulk zone (region III), there is a large defect concentration peak just at the bottom edge of the LDZ, indicated by arrows labeled L and H. Aside from the oscillations, the bulk defect concentration below 30 μm for Hi-Lo-Hi and Lo-Hi wafers are almost identical. The three regions are further illustrated in the Nomarski micrograph (see Fig. 11) of a cleaved sample from wafer 1L8, polished, and Wright etched for 2 min.

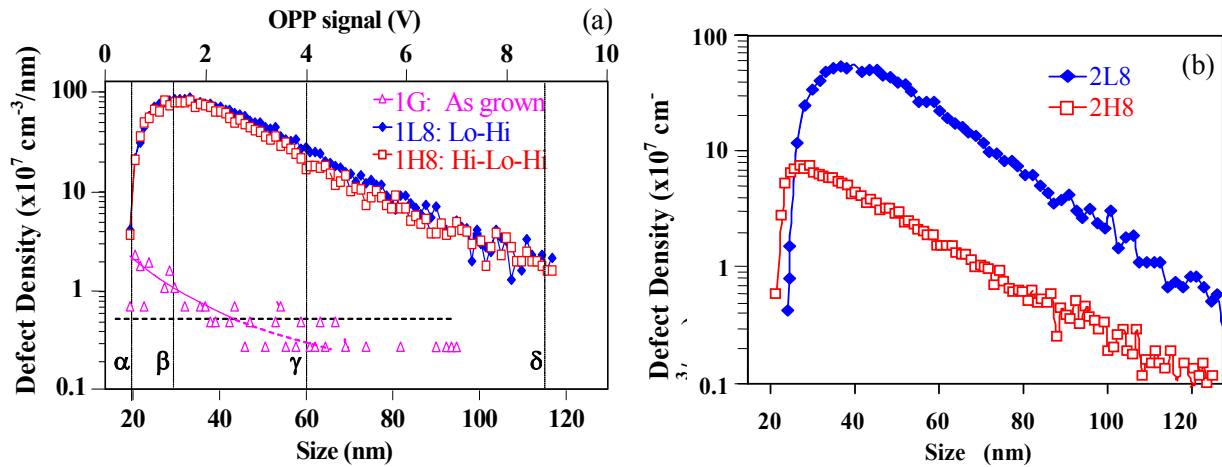


Fig. 9: (a) OPP determined defect size-distributions at 30 μm depth in as-grown N-CZ silicon, in 1G wafer, and in heat treated wafers with Lo-Hi (1L8) and with Hi-Lo-Hi (1H8). Calibration using TEM is illustrated with the lines α , β , δ (this work) and γ , [89] (b) OPP determined defect size-distributions in N-free CZ (2L8 and 2H8). Note the large differences in the defect concentrations, which is about two orders at all defect sizes.

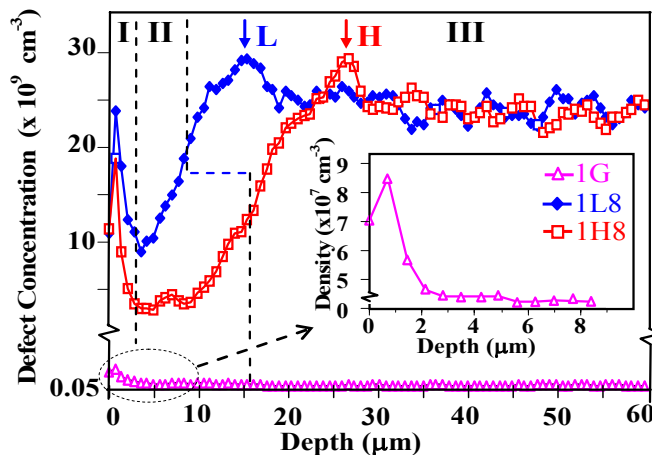


Fig. 10: Measured OPP defect depth distributions in N-CZ wafers from Set 1, as-grown (1G) and cycled with Lo-Hi (1L8) and with Hi-Lo-Hi (1H8).

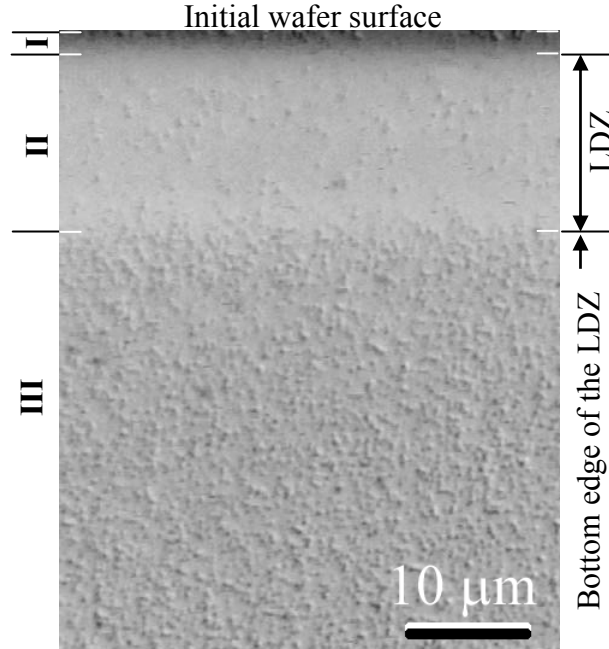


Fig. 11: Nomarski micrograph in (110) cleavage plane of a sample from 1L8 Wright-etched for 2 min, sample was polished after cleavage. It shows clearly the near-surface defect (region I), the low-density defect zone (region II), and the bulk (region III).

The etch pit density profile in the near-surface zone of sample 3L8 shown in Fig. 12 (a), is calculated from the micrograph in Fig. 12 (b) which depicts clearly the defects in region I. The etching result confirms the OPP subsurface defect concentration peak observed in Fig. 10 and extrapolates more reliably the defect depth profile at the subsurface where the OPP is imprecise. Indeed, the OPP depth resolution is degraded close to the surface by the excitation volume and the strong refractive index gradient caused by the strain gradient in the near surface region as revealed by STEM, as shown in Fig. 19. Consequently, the OPP peak is broadened by at least the excitation volume size, which is $\sim 0.7\mu\text{m}$. The surface etch pit density is estimated to about $2 \times 10^7 \text{ cm}^{-2}$ and there is a rapid defect density decay occurring essentially within the first 300 nm. Beyond that depth, the decay slows and begins to join the OPP defect profile in region I. It is safe to consider that the etch pits depict most of the surface defects since the etched layer is shallow ($< 1 \mu\text{m}$) and the etch pit overlap is limited. This approximation leads to a near surface defect concentration of about $\sim 2 \times 10^{11} \text{ cm}^{-3}$. It is important to note that the newly found etch pits appear only in the near surface of N-CZ heat-treated wafers (i.e. 1L8, 1H8, 3L8, and 3L64) but neither in the as-grown N-CZ (i.e. 1G and 3G8) nor in the N-free CZ wafers.

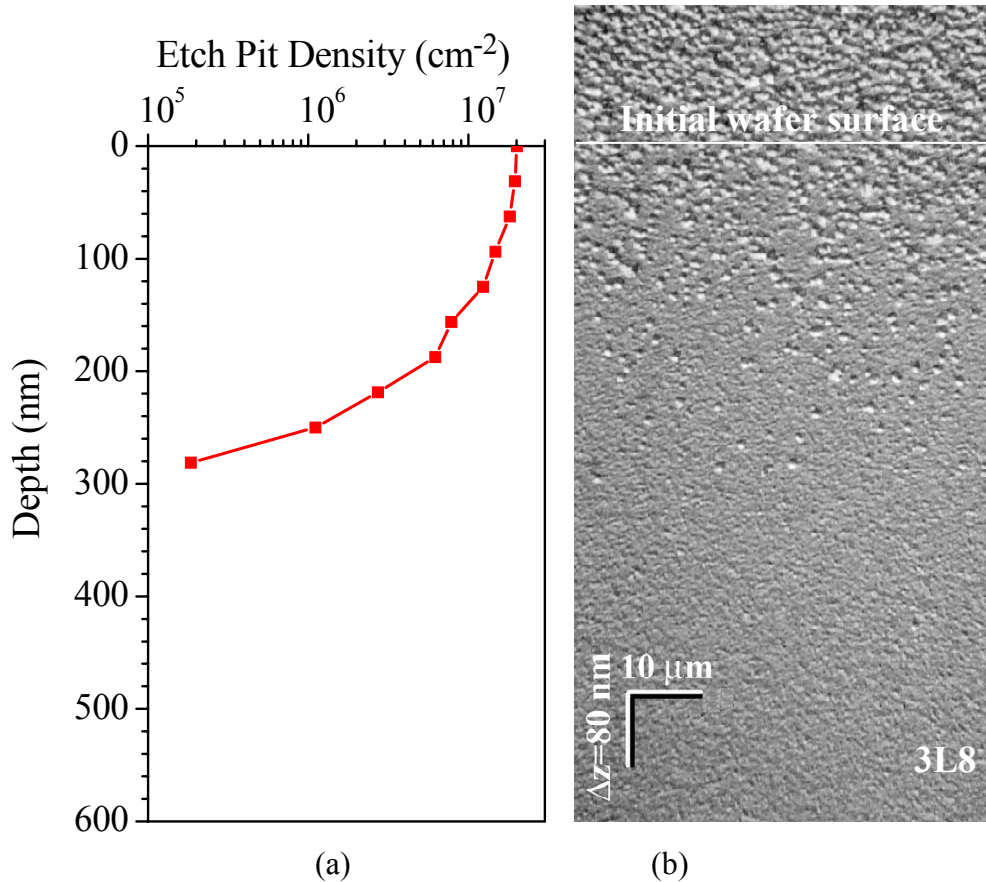


Fig. 12: (a) Near-surface etch pit density profile.
 (b) Nomarski micrograph showing pits in a 2 min Wright-etched of a bevel-polished sample from 3L8 wafer; the bevel angle was 34'.

As can be seen in the SIMS profiles of as-grown and Lo-Hi heat treated wafers from Set 2 in Fig. 13 (a), both O and N appear to pile-up close to the surface and the near-surface decays are confined to a depth of about 0.5 μm . Table II lists the O and N total concentrations obtained from the SIMS profiles in Fig. 13 (a). The concentrations at the surface were obtained by extrapolation of the near-surface SIMS peak omitting the peak nearest to the surface. The values at the LDZ were obtained by averaging the concentration of the tails of the SIMS profile given in Fig. 13 (a). The concentrations right at the wafer surface (see arrows in Fig. 13 (a)) were obtained by extrapolation of the near-surface parabolic curve, omitting the SIMS peaks nearest to the surface which could be artifacts. The total O and N concentrations in the “as-grown” sample (i.e., 3G) are 1.1×10^{18} and $5.6 \times 10^{15} \text{ cm}^{-3}$, respectively, which are close to the background concentrations, while at the surface they reach 4.7×10^{18} and $3.4 \times 10^{16} \text{ cm}^{-3}$. In the SIMS profiles of samples 3L8 and 3L64 in Fig. 13 (b), in Fig. 13 (c), the oscillations are not noise but due to

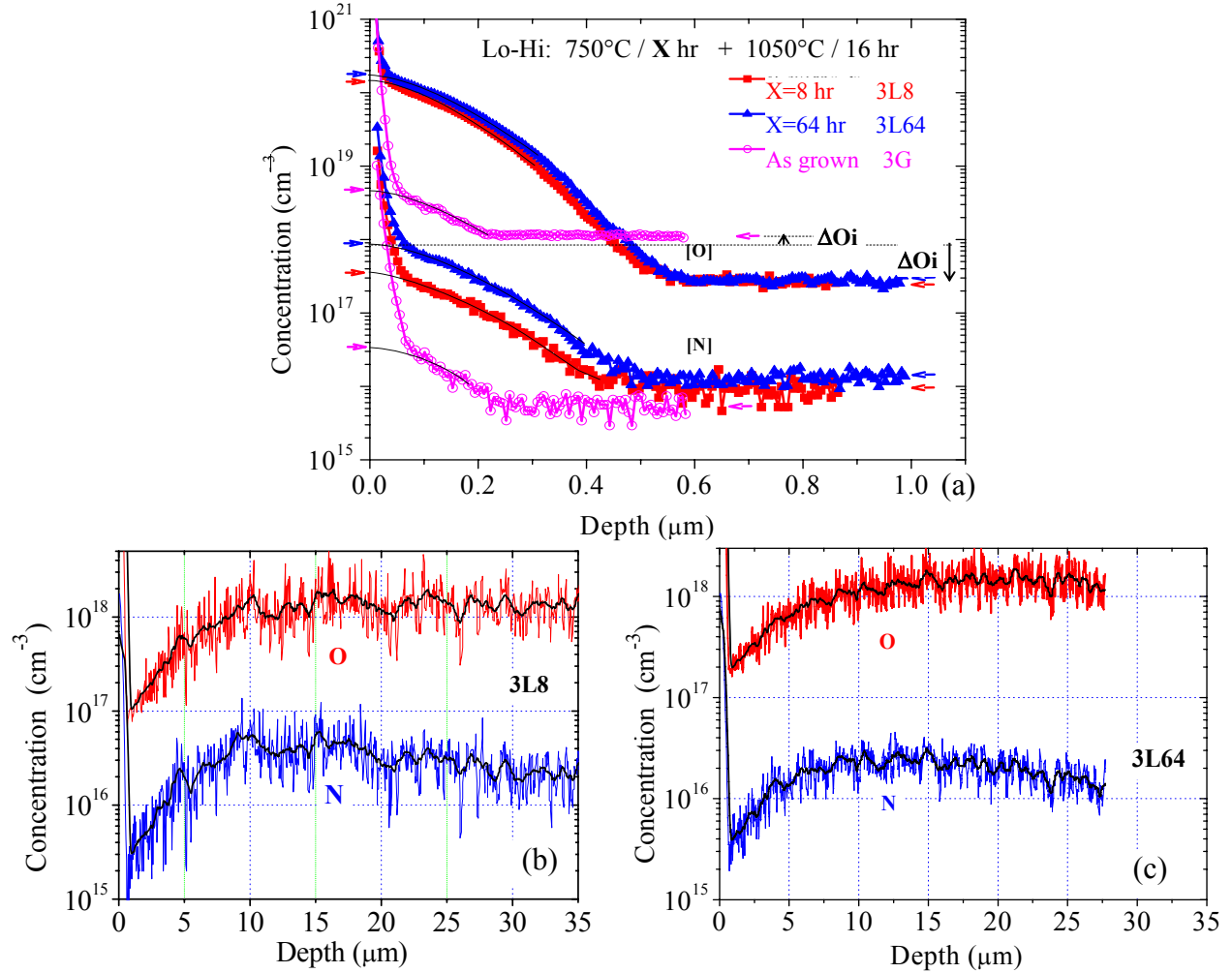


Fig. 13: Oxygen and nitrogen SIMS profiles obtained in as-grown and heat treated N-CZ Si samples in argon in near surface (a), and in the bulk of 3L8 (b) and 3L64 (c) specimens. precipitates. The N and O oscillations of the two samples are similar and their magnitude depends on the duration of the Lo heat treatment step. Note the resemblance with the OPP depth profile (see 1L8 profile in Fig. 10), although the OPP and SIMS profiles pertain to samples from Set 1 and Set 2, i.e., different N-CZ materials and slightly different Lo temperatures.

Table II: Nitrogen and oxygen concentrations in the low density defect zone (LDZ) and at the surface of as-grown and Lo-Hi heat treated wafers from Set 2.

	Concentrations at the LDZ (cm ⁻³)			Concentrations at the surface (cm ⁻³)		
	3G	3L8	3L64	3G	3L8	3L64
[N]	(5.6±1)x10 ¹⁵	(9.4±1.5)x10 ¹⁵	(1.4±0.2)x10 ¹⁶	3.4x10 ¹⁶	3.6x10 ¹⁷	8.6x10 ¹⁷
[O]	(1.1±0.03)x10 ¹⁸	(2.9±0.5)x10 ¹⁷	(3.1±0.8)x10 ¹⁷	4.7x10 ¹⁸	1.5x10 ²⁰	1.7x10 ²⁰

The Nomarski micrograph in Fig. 14 (a) shows etch pits in a cleaved sample from the Lo-Hi wafer 3L8. The area shown is located in the bulk and precisely in the bottom of region II (LDZ). The SF(s) in that region have a very high density and are rather small, less than $3.5 \mu\text{m}$. Although we were not able to count SF etch pits at the surface because of their small size, making them difficult to distinguish from precipitate etch pits, we were able to detect them with STEM in Z-contrast mode as shown in Fig. 14 (b). In this image, the contrast is formed because of the increased mass density due to Si_I condensates. The size of these near-surface SF(s) is in the order of 100 nm . We also could not detect SFs in the LDZ with both etching and Nomarski optical microscopy and Z-contrast imaging. Starting from the bottom edge of the LDZ (i.e., top of region III), the SF(s) detected by etching have a density as high as $4 \times 10^5 \text{ cm}^{-2}$, which vanishes beyond a depth of $100 \mu\text{m}$. The Hi-Lo-Hi sample 1H8 has a broader SF distribution and $20 \mu\text{m}$ deeper than that of the Lo-Hi sample 1L8.

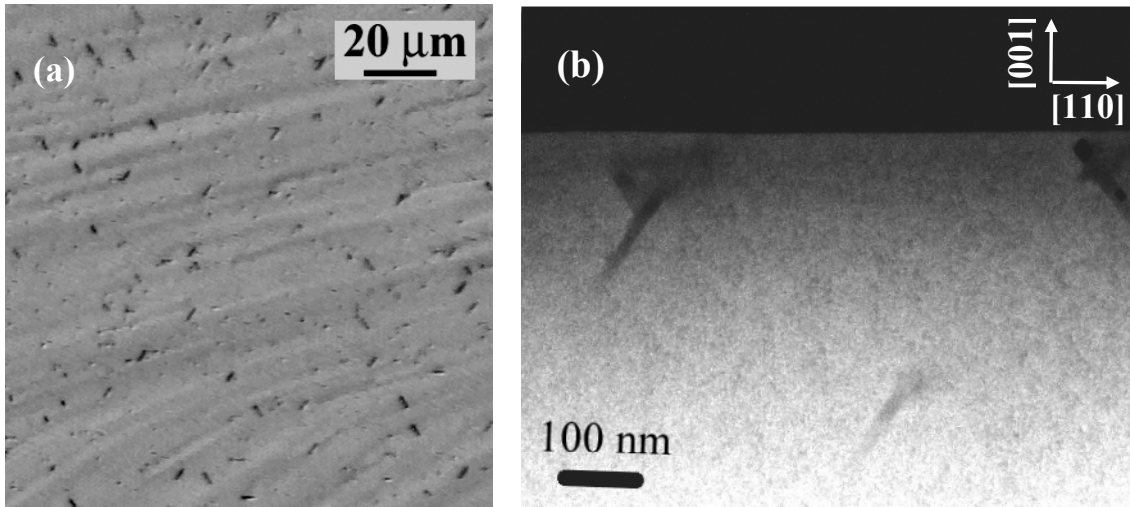
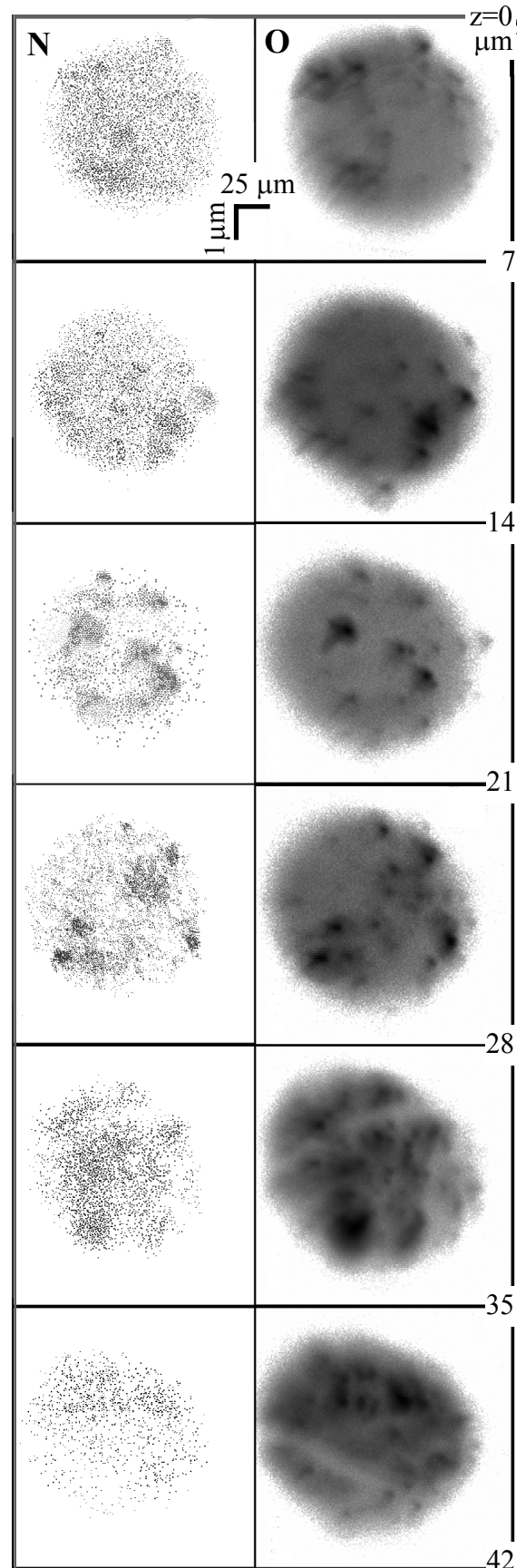


Fig. 14: (a) Nomarski micrograph of a bulk region in a cleaved (110) face showing a high density of etch pits related to small SF and precipitates. The sample was cut from 3L8 Lo-Hi treated wafer, and Wright etched for 1 min.
 (c) High density of nanoscale stacking faults in the same sample visualized by STEM in Z-contrast mode.

The depth-dependent oxygen and nitrogen SIMS image pairs in Fig. 15 acquired for the N-CZ wafer 3L8 show the spatial distribution of N and O at discrete depths within the crystal. The O background concentrations appear much higher than that of N at all depths. The N and O concentration images reveal a one to one correlation between locations of a number of dark spots in each pair of SIMS images, which indicate the presence of elevated impurity concentration.

Fig. 15: Sequence of O and N SIMS images obtained from adjacent positions that are 200 μm separated, on a 2° beveled surface of a sample from wafer 3L8 (Lo-Hi cycled N-CZ Si). The grey scale, corresponding to impurity concentration, is logarithmic.

Since the used gray scale is the same for each image column, noticeable differences appear in the nitrogen background concentrations along the depth; this holds true for the oxygen images as well. Note that the dark spots in the paired N and O images have the same shape and size; their spatial correlation suggests that they are originated from the same single or group of precipitates. Within these features, nitrogen concentration appears lower than that of oxygen. Since the average distance between large precipitates is much higher than the SIMS probe size ($<1 \mu\text{m}$), individual precipitates can be resolved. The density of the SIMS features detected within 65 nm layer corresponds to those precipitates detected by oxygen precipitate profiler (OPP), see Fig. 10. Smaller precipitates as well as N and O chemical complexes contribute to the SIMS image background. In the center of the first image pair the N and O background concentrations are $9 \times 10^{15} \text{ cm}^{-3}$ and $3 \times 10^{17} \text{ cm}^{-3}$, respectively. Both nitrogen and oxygen SIMS contrasts increase similarly as we go deeper in the bulk up to the contrast peak (between 14 and 21 μm depth), then the O contrast becomes constant while the N contrast gradually decreases



and fades. This is in agreement with the trends observed in both N distribution in 3L8 wafer and OPP defect density profile in wafer 1L8. Although these two samples pertain to different sets, the observed phenomena are fundamentally and uniquely related to the N dopant rather than growth conditions.

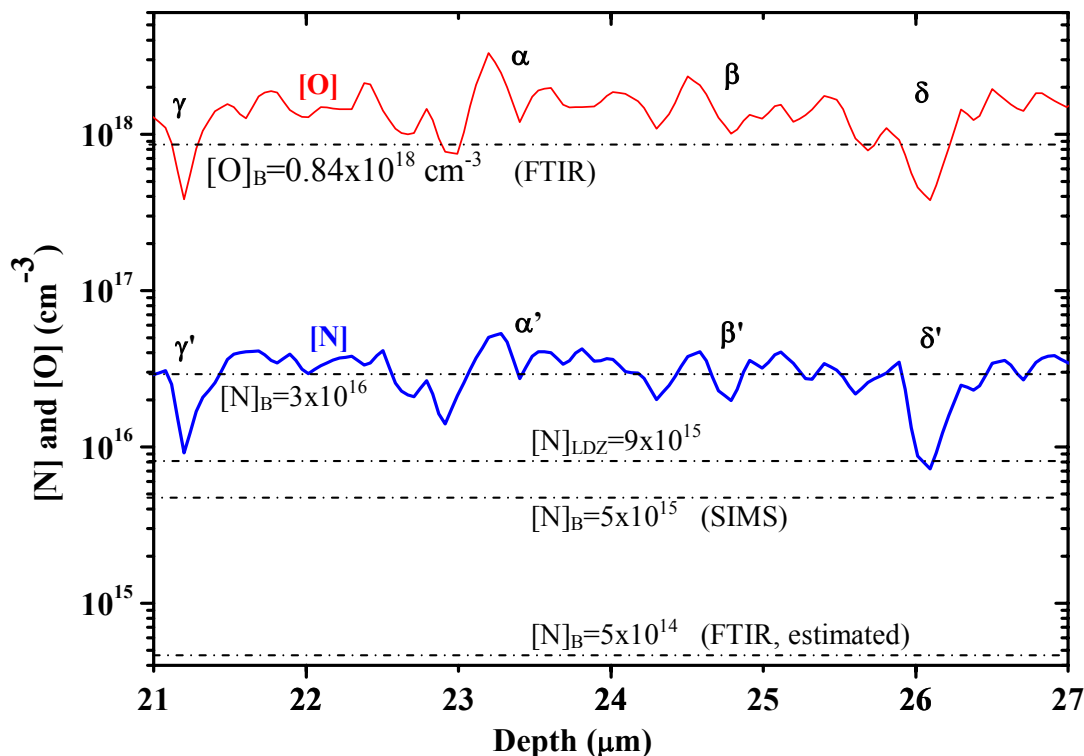


Fig. 16: High resolution O and N SIMS depth profiles (sample 3L8). Dashed lines indicate local background and as-grown bulk levels.

In Fig. 16, the high resolution nitrogen and oxygen SIMS depth profiles of heat treated N-CZ Si wafer 3L8, which start at 21 μm depth, show that the fluctuations in the $[\text{N}]$ and $[\text{O}]$ are strongly correlated, thus are suggested to be originated from the same precipitates. Using a 1.5 μm average separation distance between O peaks and the 70 nm sputtering depth, the detected precipitate concentration appears in the order of $6 \times 10^{12} \text{ cm}^{-3}$. This is two orders of magnitude higher than the OPP determined defect concentration at 20 μm depth, refer to Fig. 10. The difference indicates that SIMS probed an entire small defect population that was not detected by OPP. Depth dependent $[\text{N}]$ to $[\text{O}]$ ratios in as-grown sample 3G, and in Lo-Hi cycled wafers 3L8 and 3L64 are presented in Fig. 17. They were calculated from the SIMS profiles provided in Fig. 13. All stoichiometry ratios throughout region I, II and III are higher than 0.2%, corresponding to as grown stoichiometry in region III. Deeper than 0.4 μm , the ratio profiles of heat-treated

samples in Fig. 17(a), match the corresponding ratio profiles in Fig. 17(b). At this depth, the [N] to [O] stoichiometry ratios have sharp transitions, which signifies an abrupt increase in the N content relatively to O. The low defect density (LDZ) is N-lean as compared to the subsurface and the transition LDZ-region III. Beyond 35 μm depth the N amount is reduced and the [N] to [O] ratio approaches the value in the LDZ, see Fig. 17(c), with on one hand a smooth stoichiometry profile in region I and region II and on the other hand the oscillating profile in region III, illustrates the differences in the nature of the constituents of the near surface and bulk regions.

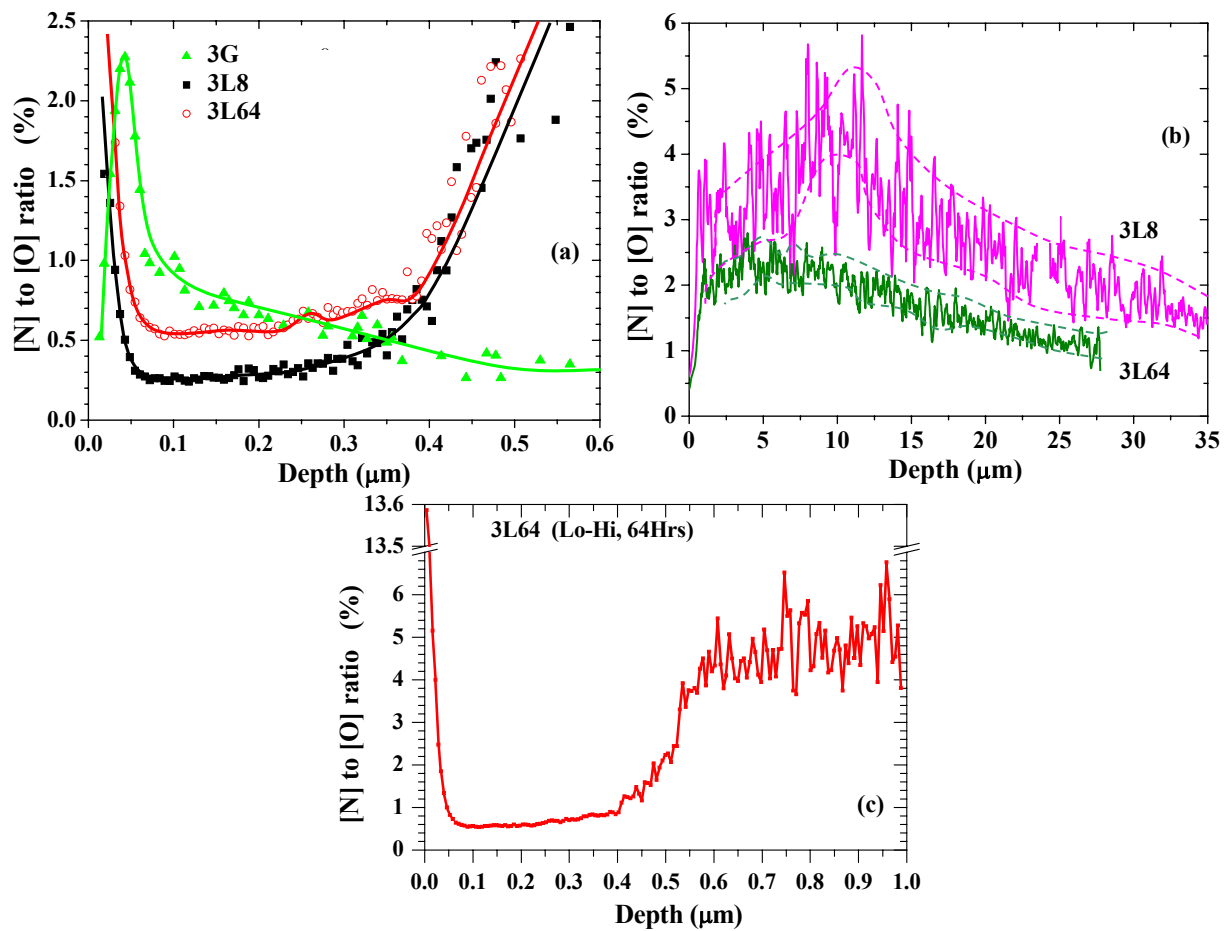


Fig. 17: Ratio of oxygen and nitrogen concentration depth profiles for near-surface region (a) and for the bulk region (b) and for the three regions in wafer 3L64 (c).

Figure 18 shows conventional bright field TEM micrograph taken at the near surface region of the N-CZ heat-treated wafer 3L8. It reveals a band parallel to the wafer surface with strong strain related contrast variations from dark to gray. A number of representative defects found close to the surface are numbered in that figure; these were further examined by HRTEM.

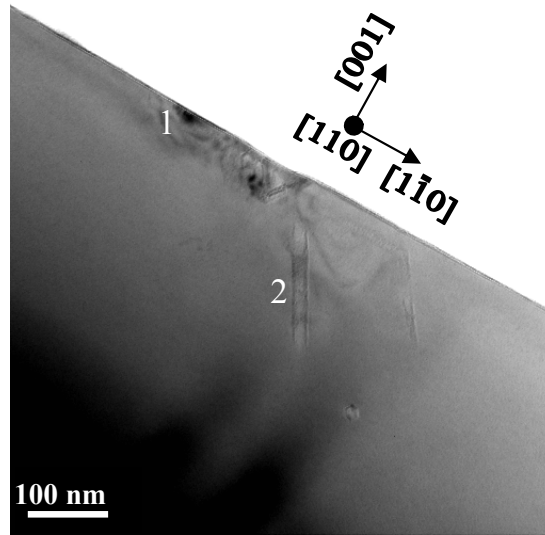


Fig. 18: Cross-sectional TEM image of near-surface region in 3L8 (Lo-Hi cycled N-CZ Si wafer).

3.1. Defect Nucleation Mechanisms in N-CZ Si

It is well accepted, based on etching, light scattering thomography (LST), and Oxygen Precipitate and defect Profiler (OPP) data and the classical theory of homogenous nucleation that during the Lo step in the Lo-Hi heat treatment of N-free CZ Si wafers, defect nuclei are formed and those that are larger than the critical radius grow during the Hi step [90, 91, 92]. These observations have been correlated with point defect and chemical complex formation models [93, 9, 95], diffusion limited phenomenological models of these species and verified with computer simulations [40, 97, 6]. The well accepted defect formation mechanisms of Hi-Lo-Hi annealing are drastically altered by N doping, as clearly illustrated in the comparative data in Fig. 8-5. Indeed, Fig. 8 readily illustrates the different nucleation regimes, where one can see large differences in the etch pit structure and density. The OPP defect profiles in Fig. 10 show a clear modification of the denuded zone by N and a high bulk defect concentration, independent of the annealing cycle be it Lo-Hi or Hi-Lo-Hi, thus unaffected by the so-called dissolution step. This fact appears also in the corresponding OPP defect size distributions measured away from the LDZ (at 30 μm depth), see Fig. 9 (a), which exhibit little differences in the 40 to 80 nm size range. The similarity of the two size distributions is in agreement with the identical trend of defect density depth profiles starting from 30 μm depth (see Fig. 9). Therefore, unlike in N-free CZ silicon, the “dissolution” pre-anneal at 1250°C does not dissolve grown-in nuclei in N-CZ Si, because they are bigger than the critical size at 1250°C. This supports earlier arguments of

Shimura and Hockett [55] that grown-in defects in N-CZ Si are highly stable at high temperature. It is important to note that a defect concentration of $\sim 8 \times 10^7 \text{ cm}^{-3}$ in the subsurface of the as-grown wafer 1G has been detected by OPP, see Fig. 10, in contrast to the as-grown N-free wafers (2G).

In strong contrast with nitrogen-free CZ Si, stable nuclei (against 1250°C anneal) were found in N-CZ as-grown wafers, which suggests that N-related clusters are the cause, chiefly N-O complexes. Likewise, these complexes reinitiate the formation of small clusters during the Lo wafer annealing at much higher rate than in N-free CZ Si. The new mechanisms of precipitation, which is clearly driven by nitrogen, vary with the depth due to its intense segregation, coupling with O, and interaction with point defects. Although low concentration of nitrogen was introduced ($\sim 5 \times 10^{14} \text{ cm}^{-3}$ for Set 2 wafers), nitrogen totally controls the complex formation processes and O clustering during the nucleation stages.

The nitrogen local average concentration in the SIMS profiles, see in Fig. 13 (b) and Fig. 13 (c), follows the same trend as the OPP profile, then slowly decays starting from the lower edge of the LDZ. Similarly, oxygen local average concentration follows the OPP defect concentration trend but deviates from it, starting from the bottom edge of the LDZ, where it remains nearly constant. The strong correlation of SIMS [N] and OPP defect profile suggests that nitrogen complexes control the nuclei generation and distribution. Therefore, N related nuclei distribution can be visualized by scaling nitrogen depth profile. The type of N complexes involved at early stages dictates the extended defect nature and their size distribution. For instance, it was reported that platelet and octahedral precipitates are generated between 700-1000°C and 1000-1100°C, respectively [79, 3, 81]. Precipitates grown at high temperature are suggested to be $\text{N}_2\text{V}_2\text{O}_x$ and those grown at around 750°C to be N_mO_n [99, 68, 101].

Nitrogen doped wafers that were Lo-Hi cycled with variable Lo time have shown that the OPP defect size distributions stabilize above 16 h [102] whereas in N free CZ Si with exactly the same heat treatment, defects grow larger for Lo times up to 64 h [89, 26, 6, 35] meaning that the nuclei growth regime in N-CZ Si saturates in a much shorter annealing time than in N free CZ Si. The rapid saturation of the nucleation regime in N-CZ silicon is inherent to the high stability of grown-in defects and the high reactivity of N. In contrary, in N-free CZ Si wafers cycled with Hi-Lo-Hi, where mono-component homogeneous nucleation occurs and is driven exclusively by

the O supersaturation; the nucleation has very long time lag [104, 105] . The removal of nuclei and the low O diffusivity [106] in N-free silicon are the factors for the small size of precipitates and the low strain in the surrounding Si matrix. In contrast, stable nuclei are plenty in N-CZ Si and nitrogen enhances O diffusion [3 81, 68 100], thereby speeding up the growth. We suggest that for N-CZ Si, the Lo annealing step acted more as a consolidation step of existing nuclei instead of a nucleation step. The nuclei consolidation is similar to aging process and consists on stress relief, transformation of the chemical complexes, and selective growth of grown-in embryos in connection to wafer boundary conditions, including the ambient. The nucleation itself occurs earlier during crystal growth.

3.2. Defects in N-CZ Silicon Wafers

1. *Near surface oxynitride zone (Region I)*: Etching data given in Fig. 12(a) and (b) corroborate the near-surface OPP peaks appearing in region I, within the first 1 to 2 μm from the surface (see Fig. 10) in both Lo-Hi and Hi-Lo-Hi N-CZ samples, and rules out considering them as artifacts. These OPP peaks represent an unusual superficial and shallow defect band. It is noticeable that these peaks decay similarly within the region extending from the surface to the LDZ (region II), especially their width is independent of the type of heat treatment, whether Lo-Hi or Hi-Lo-Hi. Likewise, the near surface nitrogen and oxygen SIMS profile widths do not depend on the heat treatment as it clearly appears in Fig. 13 (a). These features are unique to N doping of silicon. The near-surface OPP defect concentration shown in Fig. 10 for Set1 wafers appears three times wider than that given by SIMS for Set 2 wafers, see Fig. 13 (a). The main factors responsible for that apparent excess are: (i) the N concentration in Set 1, which is twice higher than in Set 2 wafers, (ii) lower Lo step temperature, and iii) the OPP peak broadening by refraction at the subsurface.

2. *Low density defect zone (Region II)*: The defect concentration in the LDZ (i.e., region II) is four times higher in the Lo-Hi processed wafer (1L8) than in the Hi-Lo-Hi wafer (1H8). While the defects in the LDZ are very small, their concentration, which depends on the heat treatment, is still relatively high compared to N free CZ silicon, but one order of magnitude lower than in the bulk. The LDZ width is in the same range as that of the DZ in N-free Si [107]; it doubles when a dissolution step is applied prior to Lo-Hi heat treatment. These facts signify that oxygen out-diffusion remains over all effective in presence of N. However, the O out-diffusion is more complex than in N-free CZ Si.

In view of (i) the observed high stability of N related nuclei deep in the bulk and at the surface, (ii) the independence of the bulk defect mechanism from the Hi pre-anneal step, (iii) the variations of the LDZ width with the Lo time, and (iv) the lower [N] in the LDZ, it appears that the oxygen out-diffusion through the LDZ is strongly effected by the subsurface via a strong exchange of point defects and the mobility of N pairs and N-O complexes.

3. Oxygen precipitates in the bulk, underneath LDZ (Region III): The defect disparities in Fig. 8 show that the formation mechanisms in the N-doped Si fundamentally differ from the N-free case. The dominant defect size in Hi-Lo-Hi cycled N-free sample 2H8 is 25 nm, and reaches 40 nm if no dissolution step is applied, see 2L8 defect profile in Fig. 9 (b), whereas, it is only 28 nm for N-doped Lo-Hi cycled 1L8 sample, see profile in Fig. 9 (a). These results confirm that N-doping considerably reduces precipitate sizes (without dissolution step), however it increases their concentration [79, 3, 81, 99].

It is remarkable that the bulk N and O SIMS profiles of 3L64 (i.e. Lo step for 64 h) have smaller oscillations than 3L8. The reduction in the oscillations of the N and O SIMS profiles in the bulk region of specimen 3L64 with the long “Lo” anneal step is due to smaller precipitates and/or a reduction in the depletion of N and O species from immediate surrounding of precipitates during the Hi growth phase. It is also remarkable that the [N] peak of 3L8 is 5 μm shallower than the OPP of 1L8 sample, such a difference is mainly attributed to the differences in the initial N level and the temperature of the Lo annealing step (750°C versus 650°C). Higher N level (sample 1L8) has caused an increase in the LDZ width, as compared to 3L8 sample. The control of O out-diffusion and precipitation could be by modification of O diffusion mechanisms in this zone.

3.3. Nitrogen and Oxygen Interactions and Co-Segregation to the Surface

The closely correlated N and O SIMS profiles of as grown and heat treated samples shown in Fig. 13 (a), clearly corroborate the N and O segregation to the surface. From mass conservation, the large amount of N found in the LDZ bottom edge and in the subsurface of argon annealed wafers comes from the bulk. Such long range segregation appears in the slow decay of the SIMS nitrogen profile. An inversion of N level beyond $\sim 100 \mu\text{m}$ is expected, for which [N] becomes slightly lower than the initial bulk concentration.

The correlated OPP and SIMS peaks demonstrate that N and O together piled up at the surface. In the subsurface region of heat-treated wafers the concentrations of N and O greatly

exceed their respective solubility limit at temperature just shy of the melting point (Fig. 13 (a)), which is for oxygen between $2 \times 10^{18} \text{ cm}^{-3}$ [108] and $3 \times 10^{18} \text{ cm}^{-3}$ [109] and for nitrogen $4.5 \times 10^{15} \text{ cm}^{-3}$ [110]. The N and O concentrations at the surface of 3L8 and 3L64 wafers are 3.6 to $8.6 \times 10^{17} \text{ cm}^{-3}$ for N and 1.5 to $1.7 \times 10^{20} \text{ cm}^{-3}$ for O, see Fig. 13 (a), which are much higher than the initial concentration levels. Starting from the surface, the N concentration decays then stabilizes in the LDZ at concentrations of $0.9 \times 10^{16} \text{ cm}^{-3}$ (3L8) and $1.4 \times 10^{16} \text{ cm}^{-3}$ (3L64), which is almost independent of the L_0 time. While exactly mimicking the shape of the N profile, the O concentration profiles decay from $\sim 1.7 \times 10^{20} \text{ cm}^{-3}$ (at the surface) to $\sim 3.1 \times 10^{17} \text{ cm}^{-3}$ (at 0.6 μm depth) and become constant in region II.

The presence of the small near-surface OPP peak found in the as-grown 1G sample, see insert in Fig. 10, is well correlated with the N and O SIMS profiles of as-grown 3G sample, although these data pertain to different materials with different initial N concentrations (1G has higher initial [N]). In spite of O and N accumulation in the near surface of the as-grown samples, Wright-Jenkins etching and TEM did not reveal extended defects (e.g., oxide or oxynitride precipitates). The N and O segregation to the surface resulted in strain/refractive index gradients which profiles should mimic the [N] and [O] profiles. Therefore, the OPP signal peak in as-grown wafer is purely caused by segregated N and O point defects and complexes dissolved in the matrix, rather than extended defects. It has been reported that N pairs aggregate on strained regions [111], scratches [112], indents [113] and along dislocations [112, 114]. Therefore, the newly observed phenomenon in our as-grown N-CZ samples must have occurred uniformly over the wafer surface during slicing and polishing, as a consequence of the mechanical stress applied at the surface. The latter caused the observed O and N piling up at the surface. It has been reported that VN_2 complexes, a major mediating species in N-CZ silicon, induce local tensile stress and can couple into more stable V_2N_2 if it traps a vacancy in which case the tensile stress increases (this issue will be discussed in Chap. V). In contrast, N_2 and N_2O complexes generate local compressive strain (see Chap. V). Therefore, while the matrix is under compressive strain during wafer mechanical processing, complexes that can create local tensile strain (such as VN_2) segregate to the surface to balance the applied stresses, and to form V-N-O complexes. Also nitrogen can be easily trapped by dislocation as demonstrated by Itoh and Abe [111] and by simulation as discussed in Chapter VIII. Therefore, micrometer size dislocation

loops and nanoscale loops created during material silicing and polishing, respectively can also be the cause for N accumulation at the sub-surface during material wafering.

At annealing temperature other mechanisms can be involved in the N and O pile up. We suggest that the mobile N atoms segregated to the surface while can couple intermittently to O atoms during diffusion steps, as evidenced by the residual N and O concentrations which were found by SIMS profiling to track one another. Thus, it is possible that the simultaneous segregation of N and O could have occurred by diffusion of N-O complexes at high temperature, or that mobile interstitial nitrogen pairs drag interstitial O atoms (not necessarily the same ones) known to be coupled but not directly bonded [101, 115].

In the LDZ of as-grown wafer 3G the SIMS determined O level appears higher than the level measured by FTIR. The difference is due to difficulty in measuring O concentration with only the 1107 cm^{-1} band in N-CZ Si, since O small clusters and Si-O bonds within grown-in precipitates have several other lines. Therefore, the difference between the SIMS and FTIR determined values can be attributed to grown-in precipitates and small O clusters. In both Lo-Hi heat treated 3L8 and 3L64 wafers, the O concentration appears to be lower than the initial total O content measured by SIMS and the O_i level by FTIR. This difference is mainly due to out-diffused oxygen; only portion of which has precipitated right at the surface and another contributed to making the near surface continuum defect. Accumulated O doses in the subsurface (between the surface and $0.6\mu\text{m}$ depth) are found equal to 2.0×10^{15} and $2.4 \times 10^{15}\text{ cm}^{-2}$ for 3L8 and 3L64 wafers, respectively. These values were obtained by integration of the SIMS profiles, which were extrapolated to the surface. Integrated out-diffused oxygen for these wafers (omitting the subsurface zone) is 92% of the piled up dose. The small shortage is due to a limitation in the SIMS profile depth extension. However, this result infers that O does not escape from the surface of nitrogen doped silicon wafers.

In contrast to oxygen, nitrogen levels have increased in the LDZ from $5.6 \times 10^{15}\text{ cm}^{-3}$ in both 3L8 and 3L64 wafers, to 1×10^{16} and $1.4 \times 10^{16}\text{ cm}^{-3}$, respectively. The nitrogen accumulation in the near-surface region (500 nm deep) with up to two orders increase in the concentration shows the strength of N segregation to the surface. It also supports that Si-N-O chemical complexes are not volatile species, in contrast to SiO. In N free Si, all out-diffused oxygen atoms escape from the surface (at annealing temperature) by sublimation of SiO compound formed right at the

surface. The difference between the two cases shows that stable Si-N-O complexes are strongly bound to the surface at annealing temperature. This thermodynamic equilibrium leads to near surface N and O concentrations largely in excess of their respective bulk equilibrium concentrations. Last, the established N-O correlation in the near-surface region in terms of [N] to [O] ratio and distribution profiles (shape and width) applies also throughout the explored bulk volume. This can be seen in the SIMS average O and N concentrations (SIMS profiles in Fig. 13 (b) and Fig. 13 (c) given for the LDZ up to 30 μm depth range) as well as in the correlated oscillations of both profiles which perfectly track each other. Both N and O distributions in wafer treated with long L_o time (i.e. 64 h, 3L64) have smaller oscillations than in wafer treated with a shorter L_o time (i.e. 8 h, 3L8). The average relative deviation is 0.18 % versus 0.33 %. The large N and O profile oscillations are due to large oxynitride precipitates and/or a deep depletion of N and O from the precipitate surrounding. These show the range of N and O interactions during the precipitate formation.

3.4. Composition of Sub-Surface Defects in N-CZ Wafers

Both annealed 3L8 and 3L64 and as grown 3G samples have much higher O and N concentrations at the surface than the corresponding bulk solubility limits at annealing temperature (i.e., 1050°C) and melting point (MP). The N closest concentration to the reported solubility limit at MP is slightly higher 10% and is found away from the subsurface zone. The N concentration excess in annealed wafers comes from a depleted region, as deep as 100 μm , estimated by extrapolation of the SIMS profile reported in Fig. 13. It should be noted that Itoh and Abe [116] reported nitrogen SIMS depth profiles of heat treated nitrogen doped float zone (N-FZ) Si, and discussed only the out diffusion of N pairs, but no any near surface effect in float zone silicon. It is conceivable that, unlike in N-CZ Si, the low oxygen content in N-FZ Si was not favorable for N and O accumulation at the surface. This depicts the different behaviors of N pairs and V-N complexes in N-FZ as compared to N-CZ [117], where in addition N-O complexes are involved.

At the wafer surface, the N and O stoichiometry ratio reaches a maximum value of 4% and 13.6% for 3L8 and 3L64 sample, respectively, as shown in Fig. 17(a) and (c). The differences in the [N] to [O] ratio peaks in region I of heat treated samples as compared to the as grown illustrate different regimes of N segregation to the surface. The maxima, which show that

more N accumulates at the surface, appear to depend on the Lo anneal duration. The integrated concentration of precipitated oxygen in sample 3L64 between the surface and 100 nm depth, where the majority of precipitates are confined (as shown in Fig. 12) is found to be $1 \times 10^{17} \text{ cm}^{-3}$. Etching depth profile and TEM determined precipitate average size were employed for this estimation. Since the average N fraction is 6% in this zone, the precipitated N concentration is about $6 \times 10^{15} \text{ cm}^{-3}$. However, the total [O] and [N] integrated from SIMS profiles (over the same depth range) is found to be 2×10^{20} and $4 \times 10^{18} \text{ cm}^{-3}$, respectively. This shows that only small fractions of about 1 per 2000 of O and 1 per 1000 of N have precipitated within the 100 nm subsurface region. This limited precipitation, in spite of the high O and N supersaturation, is attributed to N, V and O interactions and the nuclei density in the near-surface zone. The [N] to [O] ratio, in Fig. 17(c), readily illustrates the character of near-surface defects; the smooth part is mainly due to the continuum component, while the oscillations pertain to heavy precipitation in region III. In the subsurface precipitation zone no oscillation appear in the N to O ratio, as illustrated in Fig. 17(c), because precipitates are confined within 100 nm depth, as revealed by the TEM image in Fig. 18 and by the etch pit depth profile cutoff in Fig. 12 (a). Most of N and O in the $0.6 \mu\text{m}$ deep zone are dissolved in the matrix, most likely forming non-detectable precipitates and chemical complexes at a concentration in the order of the local N pair concentration. The strong continuum defect component in the near-surface was inferred from the large N and O concentrations (and high supersaturation), the smoothness of the depth profiles of [N], [O], and stoichiometry ratio as compared to their counterparts in region III. The defect size distribution of annealed N-free silicon was calculated by clustering theory using rate equations, Fokker Planck and point defect continuity equations for CZ Si [6, 118]. A distinct population of stable precipitates (larger than the critical size) appeared to rise apart from the much higher concentration of small clusters grown from an initial distribution of O monomers and dimers [40, 6]. The latter, being in N-free silicon and at early stages of formation are instable. Nitrogen doping reduces the precipitate critical size and smaller ones become more stable forming the continuum defect.

Between $0.05 \mu\text{m}$ and $0.4 \mu\text{m}$ depth, the short Lo annealing time (8 hr) gave rise to a nearly constant [N] to [O] ratio that is equal to the average ratio observed in the "as-grown" material, i.e., away from the surface. Sample 3L8, subjected to a longer Lo annealing time (64 hr), had a ratio that is about double of the as-grown bulk's ratio. This infers that for long Lo

time a significant change in the average stoichiometry occurs before the growth step. The short L_0 time anneal (sample 3L8) has most likely lead to less N-O complexes, which resulted in smaller defect size distribution, as found by OPP. The process of N-O accumulation is controlled by the high reactivity of nitrogen and the pile up at the surface. These being slower diffusers, their effects is higher during longer L_0 time anneal. The involved point defects originated at the surface control the observed strong depth dependency of the oxynitride composition.

In the as-grown sample, the [N] to [O] ratio decays abruptly, starting from its peak (located at ~40 nm) to 200 nm depth, then linearly decreases, see Fig. 17(a). Beyond 600 nm depth, the ratio becomes constant (~0.3 %), this level represents the real as-grown bulk stoichiometry ratio. Although the stoichiometry ratio peak in the near-surface of as-grown 3G wafer correlates well with the OPP small peak in 1G wafer, their origin is not obvious. It is proposed that small dislocations (generated during wafer slicing) and the surface thermo-mechanical stresses (applied during polishing) induced migration of N to the subsurface and an easy coupling of O with N leads to their accumulation within 0.6 μm (for this set of wafers). The shape of the ratio depth distribution (mainly the increase from 0.6 μm up to the peak at 40 nm) may indicate that the N species are not injected from the exterior but migrated from the near surface zone. The peak at 40 nm, can not be explained with oxygen out-diffusion at low temperature, but one has to consider an athermal diffusion of N induced by the stress and the reaction of N with V and O.

The effect of N and O on near-surface precipitates and continuum defects is further investigated by STEM in Z-contrast mode. Figure 19 shows a Z-contrast image of Type 1 defect (Fig. 18). It shows notable variations from dark to light, from the surface towards the bulk, as well as from the precipitate center to its interfaces. The lighter contrast in the region nearer to the surface in the TEM image of Fig. 18 is ascribed to a strain gradient induced by the N- and O-rich sub-surface region. This gradient band is correlated to the STEM Z-contrast image of Fig. 19. The dark band indicates the presence of lighter elements or a lower mass density of the continuum defect with respect to silicon. The interpretation of the Z-contrast gradient dark band correlates with the gradual pile-up of N and O established by SIMS profiling (Fig. 13 (a)). It should be noted that optical infra-red birefringence microscopy imaging of cross-sectional samples from the same 3L8 wafer has shown a strain spreading over 1.5 μm depth from the surface [119]. The disparity in the depth range is inherent to differences in the signal nature and detection levels.

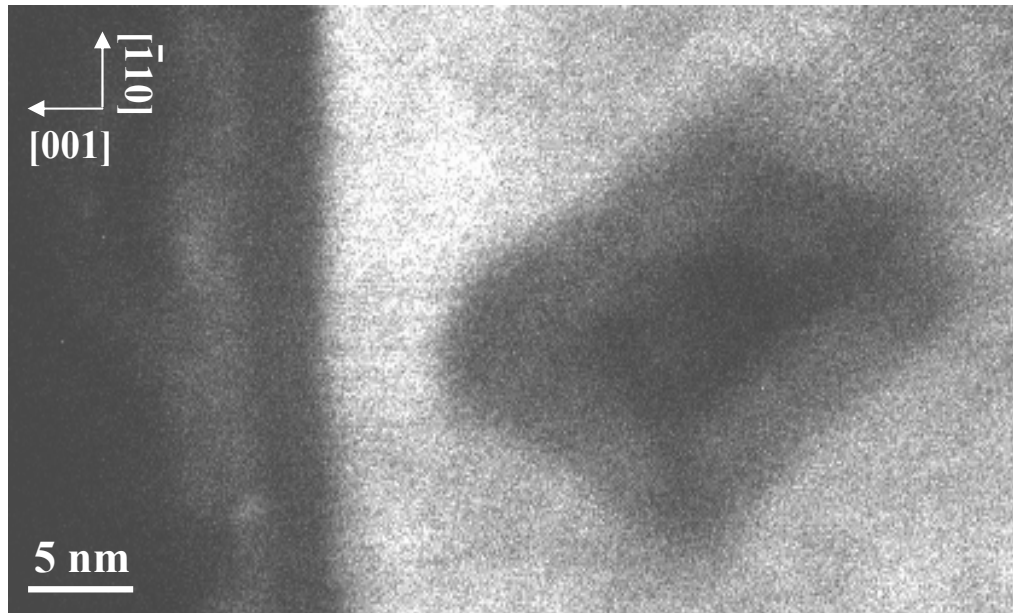


Fig. 19: STEM image in Z-contrast mode of a defect region similar to type 1, shown in Fig. 18 for 3L8 wafer. Note that the wafer surface is on the left and is not shown in the picture.

Figure 20 (a) is a low magnification Z-contrast micrograph of a typical precipitate to which a SF is physically connected. The EELS spectrum shown in Fig. 20 (b) was acquired from the area indicated by arrow A in Fig. 20 (a). Note the pronounced absorption edge due to oxygen and the weaker one related to nitrogen. The EELS spectrum provides quantitative assessment of the amount of N present within the precipitates. Both N and O absorption K-edges appear in the spectra. The integration of the peaks allows evaluation of the N and O contents.

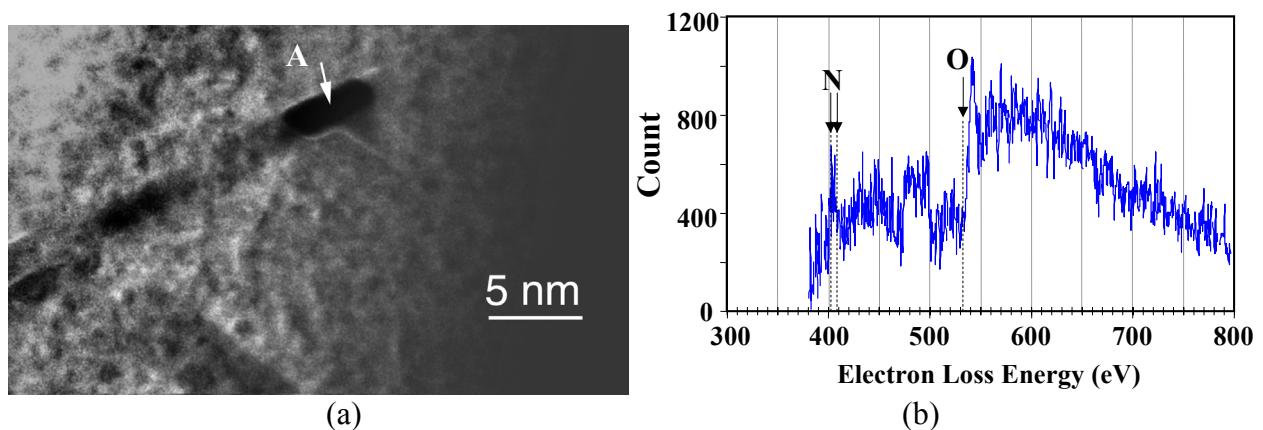


Fig. 20: (a) Low resolution STEM image of near surface precipitate and SF(s) in 3L8 wafer. (b) EELS spectra, from which the background signal was subtracted. It was acquired inside the precipitate, in the location shown with the arrow in (a). Note the absorption N-K edge at 401 eV and the O-K edge at 532 eV.

First principles atomistic calculations showed that N-O complexes generate significant local strain extending up to 10 and 15 Å distance (see Chap. V), which certainly causes the trapping of more O atoms. Also molecular dynamics (Chap. V) calculations predicted potential wells of about 20 Å full width for adsorption of oxygen by N pairs. For 3L8 wafer, starting from the surface to 0.1 μm depth, [N] to [O] ratio decreases from ~14 to 0.3 %, in the same fashion as the strain gradient. One can speculate that, starting from the surface groups of 7 to 300 oxygen atoms associated to each nitrogen atom, without being bonded. This may occur via composition fluctuation and/or local strain. The first O atom couple to the N center via the adsorption potential well. As more O atoms are added, the adsorption potential well spreads and decays, simultaneously the local strain is relieved. At 0.1 μm depth, there is an equivalent of $\sim 10^{18} \text{ cm}^{-3}$ single N-O complexes distributed uniformly (one every 36 sites in a row). Starting from the surface, as the N and the associated O concentrations decrease with the depth, one expects that NO distribution decreases similarly. The latter with additional O atoms cause the continuous strain gradient revealed by TEM and STEM imaging in near surface region.

3.5. Nitrogen and Oxygen Coupling

It is known from FTIR studies that nitrogen and oxygen are not directly bonded [115, 121]. The N₂-O bond is characterized by a binding energy of -0.8 eV, see Chap. V but the atomic configuration is actually favorable for diffusion. Driven by N₂, the N₂O diffusion leads to a higher mobility of interstitial oxygen in N-CZ than in N-free CZ silicon. The exact spatial correlation of O and N features (in the SIMS image pairs of Fig. 15) clearly indicates the strong coupling of the two species. At a given location the N and O background levels reflect the proportion at which these species are dissolved in the matrix. Likewise, the intensity of the SIMS features in Fig. 15 reflects the N and O coupling within precipitates. The pairing of O with N inhibits escaping from the surface, but in the absence of nitrogen, out diffusing oxygen evaporates as SiO. On the other hand, according to the data reported on FZ Si [116], with low oxygen, nitrogen is barely adsorbed at the surface. Therefore, the high supersaturation of O in the near-surface zone could not occur without the intimate coupling with N atoms, forming chiefly small stable V-N-O clusters. It is reported that N-O can form at 700°C and are stable upon cooling [68, 123, 124], therefore, the long Lo anneal step saturates the host crystal matrix with further N-O complexes (in addition to the grown-in ones). The subsurface continuum defect

(formed by dissolved N pairs, interstitial O atoms, and N-O small chemical complexes) is induced by (i) the N and O interactions moderated by the exchanged V with the surface, and (ii) the chemical potential defined by N distribution.

The nitrogen and oxygen SIMS depth profiles reveal that (i) oxygen concentration fluctuates above and below the bulk as-grown concentration, depending on whether one points to a precipitate or a depleted zone, (ii) most of the N and O peaks and dips appear strongly correlated, and (iii) the average ratio of N to O concentrations fluctuates between 1.5 and 2.5 % in the explored depth. The correlated N and O peak pairs denoted (α , α') and (β , β') likely represent big precipitates, whereas the dip pairs (γ , γ') and (δ , δ') result from N and O local depletion. The O concentrations at the peaks well exceed the background concentration in the bulk material which is $\sim 0.84 \times 10^{18} \text{ cm}^{-3}$. In contrast to oxygen, anywhere in the probed range the concentration of nitrogen is largely higher than the initial concentration (i.e., $5 \times 10^{14} \text{ cm}^{-3}$, estimated by FTIR). The local background concentration in the explored depth range is $3 \times 10^{16} \text{ cm}^{-3}$, that is about two orders of magnitude higher than the N doping level. Surprisingly, N concentration remains right above the LDZ background level (i.e., $9 \times 10^{15} \text{ cm}^{-3}$, see Table II), which denotes a sort of equilibrium of [N] between the LDZ, the subsurface, and the bulk region III. At the profile dips, which most likely are the precipitate interfaces, both oxygen and N concentrations decrease similarly up to 3 times below local background levels. The correlated deep depletion of O and N demonstrates that nitrogen caused an additional driving force for oxygen segregation towards precipitates. In addition, a smaller amount of N and O segregate from far field (as interstitials and small chemical complexes) and enrich the subsurface region. These two segregation components support the strong coupling of N and O in N-CZ, such an effect does not appear in N-FZ silicon.

3.6. Nitrogen and Oxygen Interactions in the Bulk

In the bulk, N to O stoichiometry ratio of the long Lo time sample (i.e., 3L64) is about half of that of 3L8, see Fig. 17(b), in contrast to the near-surface region where it is twice higher. Such a difference is the effect of the “Lo” anneal time, 8 hrs versus 64 hrs. Actually, it is the total [N] that is reduced by a factor of two in the bulk, whereas the average [O] is rather constant, as shown by the SIMS profiles in Fig. 13. The ratio decay shows a monotonic decrease of the average N concentration, which is believed to stabilize at around 100 μm depth. In addition, the

stoichiometry peak of the 3L64 sample is broader than that of 3L8 and is shifted ~ 7 μm closer to the surface, see Fig. 17(b).

The density of oscillations is the same in both samples, consistent with the OPP defect density in the bulk of Lo-Hi and Hi-Lo-Hi cycled N-CZ wafers. However, the oscillations are smaller for 3L64 (as compared to 3L8) indicating smaller precipitates (as compared to 3L8) and/or a homogenization of the concentration fluctuations. More importantly, they show that the involved N amount, thus the N-O complexes, are smaller in 3L64 precipitates, due to a possible change in the composition of nitrogen related chemical complexes in the matrix. This includes the decomposition of V-N complexes and production of mobile interstitial N pairs which segregate to the surface throughout the 100 μm depth range, as discussed above in the model of N pair diffusion and V production.

Oxygen nucleation in N-CZ appeared to have a short time lag [125], as the clustering initiated by N is fast, thus the 64 hrs Lo anneal in fact allowed time for nuclei consolidation. Furthermore, active chemical complexes (N-O and/or V-N) are transformed and/or become in equilibrium with the host crystal leading to a total relaxation of the nuclei prior to the growth annealing step. Therefore, it is likely that at the end of the 64 hrs Lo annealing step, the N related complexes and the stable nuclei take up the configuration yielding the lowest free energy. As a result, the nuclei cross-section for trapping O atoms is reduced in the long Lo time sample (3L64) and precipitate growth rate is lowered during the final Hi thermal step. In short, the stoichiometry profile changes with the Lo annealing time is suggested to be caused by (i) a short range redistribution of nitrogen, and/or (ii) a modification of the V-N-O complexes in the bulk.

4 Summary

The distribution of oxygen precipitates in nitrogen doped and nitrogen free CZ Si wafers subjected to typical oxygen denuded zone cycling were studied. Defect formation kinetics and consequently defect size distributions in N-CZ silicon largely differ from similarly heat treated N-free CZ Si wafers. Specifically, OPP determined bulk defect densities were almost identical in Lo-Hi and Hi-Lo-Hi cycled wafers; a newly found property unique to N doping. In addition, defects are smaller and denser when compared to conventional N-free CZ Si. The first Hi step known to dissolve grown-in defects in N free CZ Si wafers appeared ineffective in N doped CZ

Si. Nitrogen SIMS depth profiles mimic exactly the OPP defect depth profiles and strongly correlates with the oxygen profiles. Defect thermal history showed that N and O are intimately coupled during crystal cooling stages and the Lo-Hi and Hi-Lo-Hi wafer annealing. Nitrogen appeared to segregate to the near-surface region and to the bottom edge of the LDZ where the concentration was found greatly in excess of the solubility limit at annealing temperature. It clearly appeared that nitrogen segregates to the surface athermally under mechanical stress. The segregation process is accelerated at high temperature. We detected a near-surface oxynitride layer of 0.5 to 2 μm in polished as-grown N-CZ Si wafers as well as cycled wafers with either Lo-Hi or Hi-Lo-Hi cycles. In addition, the latter have small precipitates nucleated at the surface and small SF(s) confined within the 250 nm from the surface. The presence of nitrogen in CZ Si results in the formation of very stable grown-in defects detectable by OPP and SIMS, in contrast with the nitrogen-free CZ Si. It is suggested that the nucleation mechanism is essentially controlled by nitrogen, which establishes the nuclei distribution, independent of any high temperature pre-annealing. Extended defects and N and O distributions show that the Lo annealing step in the Hi-Lo-Hi cycle drives in N-free Si a mono-component homogeneous nucleation of oxygen precipitates, while this mechanism is strongly modified in presence of nitrogen. Correlation of nitrogen and oxygen concentration depth images with precipitate density profiles and nano-scale structure and composition analysis were used to clarify defect formation mechanisms in N-CZ Si wafers. The N segregation to the surface occurs while it is coupled to O. Both phenomena lead to a great change of the oxygen out-diffusion mechanisms in silicon; as a consequence, O and N solubility in region I and in the beginning of region III largely exceeded the known limits. Out-diffused N and O mutually prevent their evaporation at the surface by pairing. As a result, near surface N- and O-rich continuum defect is formed, while during heat treatment co-precipitation occurs. It is remarkable that most of the N and O detected in the subsurface did not precipitate, in spite of exceeding their respective solubility limits. The long Lo annealing causes a modification of chemical complexes thereby strongly effecting the composition of subsurface oxynitride layer, as well as the precipitates. Precipitates in the subsurface appeared faceted and have two distinct oxynitride amorphous phases, configured in a core and a shell, the latter being richer in nitrogen. Their position from the surface, and their morphology reminds the D-defects and the voids with oxidized walls in N free CZ Si.

It is suggested that the precipitation at the subsurface is dictated by the high density of N-related nuclei and by V and N interactions at the surface. The V-N complexes contribute to precipitation enhancement by increasing the density of stable complexes such as substitutional nitrogen pair V_2N_2 ; such an increase reduces precipitate ripening. Within more than 100 μm depth range the grown-in V-N complexes can dissociate and form mobile species which then outdiffuse. While reacting with interstitial O, the N mobile species lead to modulation of the three regions or to aggregation right at the surface, depending on the available point defects and nucleation sites

GROWTH MECHANISMS OF EXTENDED DEFECT IN N-CZ SILICON WAFERS	52
1. Introduction	52
2. Experimental procedure	52
3. Results and Discussion	53
3.1. Macroscopic Model of SF formation	53
3.2. Defect Structure and dynamics of point defect clustering	56
3.2.1. Subsurface Defects.....	56
3.2.1.1. Structure of Subsurface Octahedra –Like Oxynitride Precipitates	57
3.2.1.2. Microscopic Model of Subsurface SF Formation	61
3.2.2. Structure of thePrecipitates in the “Denuded Zone”	62
3.2.2.1. Precipitate Platelets.....	62
3.2.2.2. “Dragon-Fly” Defect.....	63
3.2.3. Bulk Defects beyond the Denuded Zone	64
3.2.3.1. The Umbrella Defect (in the Bulk)	64
3.2.3.2. Point defect and N- and O- Complex Dynamics for the Umbrella Defect	67
3.3. Effects of Nitrogen Segregation on Precipitation Mechanisms	69
4. Summary	70

Chapter III

GROWTH MECHANISMS OF EXTENDED DEFECT IN N-CZ SILICON WAFERS

1. Introduction

The analysis of the structure of as-grown defects is useful for depicting the dynamics of N, O, and point defect early stage interactions, the nucleation, and the mechanism of void cancellation in N-CZ Si, while the atomic resolution structure of post-anneal defects is relevant for elucidating oxynitride precipitate growth during annealing. Hence, nanoscale and atomic analysis of extended defects leads to the a comprehensive understanding of the early stage mechanisms of point defects and related chemical complex formation. It has been shown, in previous chapter that N doping induces a high density of small grown-in defects whose size distribution are detectable by Optical Precipitate and defect Profiler (OPP). This is in contrast to N-free CZ Si, where no defects could be found by OPP [75, 127] and evidently by TEM coupled to MOS-capacitor breakdown [79]. The N related grown-in defects play the role of stable nuclei during wafer annealing. Examination by high resolution TEM (HRTEM), Scanning TEM (STEM) in the Z-contrast mode, and Electron Energy Loss Spectroscopy (EELS) is ultimately a fortunate combination and efficient method to decipher their mechanism of formation. In this chapter we discuss precipitate composition, morphology, and strain at the interface in terms of point defect and local stress distributions.

2. Experimental procedure

A suite of methods were used for atomic- and nano-scale characterization of precipitate structure and composition as well as the induced strain at defect interface and in the bulk or near surface of annealed N-CZ Si wafer. Three types of TEM foils were prepared from nitrogen doped Czochralski silicon (100) wafers which were annealed with Lo-Hi oxide nucleation-growth cycle. The annealing cycle was at 750°C for 8 hrs and then at 1050°C for 16 hrs. The as-grown oxygen concentration was $8.5 \times 10^{17} \text{ cm}^{-3}$ and the N was estimated by FTIR to be about $5 \times 10^{14} \text{ cm}^{-3}$. The first TEM foil was labeled S, it was obtained by thinning and ion milled from the backside leaving the "as-annealed" original mirror polished surface as is. This specimen

includes a high density sub-surface defect zone, which was described in Chapter II, and referred to as region I. The defect density was measured non-destructively by OPP and found to be $\sim 3 \times 10^{10} \text{ cm}^{-3}$. The second specimen was intended for examining the so called denuded zone (“DZ”) that is in fact a low defect density zone estimated by OPP to be 20 μm deep. Thus, a 10 μm thick layer was first removed from the original top surface before thinning from the back side to obtain the TEM foils. This specimen is referred to as D10. Similarly, a 30 μm layer was first removed from the surface of the third specimen here referred to as B30, which is intended for studying defects in the bulk region. The used TEM is a field emission JEOL-JEM 2010; in the STEM Z-contrast mode; it reveals local differences in atomic number with a spatial resolution of 2 Å.

3. Results and Discussion

3.1. Macroscopic Model of SF formation

HRTEM in Z-contrast mode and preferential etching of Lo-Hi heat treated N-CZ 1L8 and Hi-Lo-Hi 1H8 wafers showed that N-doping significantly changes the mechanism of SF formation. In the upper part of region III the SF average size is reduced to less than 3.5 μm , while their density is up to two orders higher than in the similarly heat treated N-free CZ silicon (2L8 and 4H8). In the near surface region the SF size is about 150 nm or less, see Fig. 28 (b). This infers that the interstitial condensation formation dynamics significantly differ from N-free CZ Si. One must note that during crystallization the coupling of V with N (in stable complexes) reduces the vacancy-interstitial recombination and results in an excess of Si_i relative to N-free CZ Si (higher Si_i supersaturation than in N free CZ Si). The grown-in interstitials along with those emitted during annealing while precipitates grow, condense when their concentration exceeds a threshold. The observed high density of small SFs underneath the LDZ infers that most of the produced interstitials condense locally and are not supplied from far field.

To explain the confinement of the measured SF distribution to the surface and to the 100 μm band below the LDZ, HRTEM and STEM Z-contrast studies have been done [129]. In some regions around precipitates conglomerate of Si_i mixed with O and N are formed, which result in large compressive strain of the Si matrix [130]. In this condition no SF can form but rather highly strained Si_i conglomerate. The N-V complexes are likely source for N within such

conglomerates, because they are attracted by Si_i , while they drag O atoms. We proposed that local strain compensation and O depletion thus N removal are two major requirements for SF formation in N-CZ Si. This condition is fulfilled in other regions, where single vacancies recombine with some of the ejected interstitials, thus compensating the excessive strain in the vicinity of Si_i condensate while O and N drift away; so to allow the self-interstitials condensate to form SF(s).

The large difference in the SF sizes, $\sim 0.1 \mu\text{m}$ in the surface versus $3 \mu\text{m}$ underneath the LDZ, indicates that at the surface a large portion of self-interstitials may have coupled with the out-diffused single O (not bonded with N) and evaporated as SiO. Such a process could be accelerated by the recombination with injected V from the free surface (not oxidized). Frigeri et al [131] interpreted the absence of SF in the near surface in their annealed CZ Si samples, as being due to recombination of Si_i with injected V. In N-CZ Si single vacancies (or V-N) can adjust Si_i excess and the local stress. However, if V-N complexes are involved O will be trapped and N-O- Si_i conglomerate defects are formed rather than SF(s). The SF density depth profiles shown in Fig. 21(a) mimic the profile edges of those self-interstitials and vacancies responsible on the SF creation. As sketched in Fig. 21(b), the concentration profile of the self-interstitials is related to precipitate density, thus tracks the OPP depth profile along the bottom edge of the LDZ, compare the OPP profile in Fig. 10 of Chapter II and Fig. 21(a). The injected vacancies are the result of a size mismatch of the N atoms adsorbed at the wafer surface, which imposes a surface reconstruction, as discussed for carbon adsorption on silicon by Kelires and Tersoff [132]. The recombination of injected vacancies with Si_i reduces the excess of Si_i and provides a strain relief mechanism necessary for SF formation. The proposed V profile in Fig. 21(b) is similar to that measured by Falster and Voronkov for CZ Si annealed wafers in N atmosphere at 800°C for 4 hr and 1000°C for 16 hr. Although we expect a higher V concentration as a consequence of the higher N concentration in the near-surface region of our N-CZ samples, the depth profile is nonetheless likely to be similar and extending up to the same depth range ($100 \mu\text{m}$). Fuma et al [133] have used DLTS to profile vacancies-nitrogen complexes in n-type silicon and come up with an error function profile. A proposed scheme for the interstitial-substitutional Turnbull process for N diffusion during annealing starts by moving a substitutional N pair in interstitial position and liberating a vacancy, as shown in the following chemical reaction:



In a subsequent step, N_2 diffuses toward either (i) the surface where it can be adsorbed and coupled with O, which results in injection of a V, or (ii) to the bulk where it may trap a V and goes back to substitutional position. As shown in Fig. 21, this process generates two vacancies. The first is emitted from N-V decomposition and the second from the surface, which then diffuses to the bulk volume.

The V depth distribution in Fig. 21(b) corresponds to both the end of SF range and the N segregation range from the bulk. One should notice that the required vacancy distribution for the magic denuded zone (MDZ) formation in N-free CZ Si determines the defect depth range (below the MDZ). Similarly in N-CZ Si, the injected vacancies along with the piled up oxygen atoms determine the limits of the LDZ, while in conjunction with the self-interstitial distribution they determine the SF depth profile. In the LDZ, the density of the produced Si_I is low and overwhelmed by the injected V, thus the recombination is dominant and not enough Si_I were left to form SF(s). Upon decomposition of V-N complexes, vacancies are emitted back and spread over 100 μm depth at an average concentration of $8 \times 10^{13} \text{cm}^{-3}$, while the liberated N accumulates as oxynitride precipitates within the top 0.25 μm (with an average N concentration of $3 \times 10^{17} \text{cm}^{-3}$). The remaining nitrogen is dissolved in the supersaturated continuum defect band as

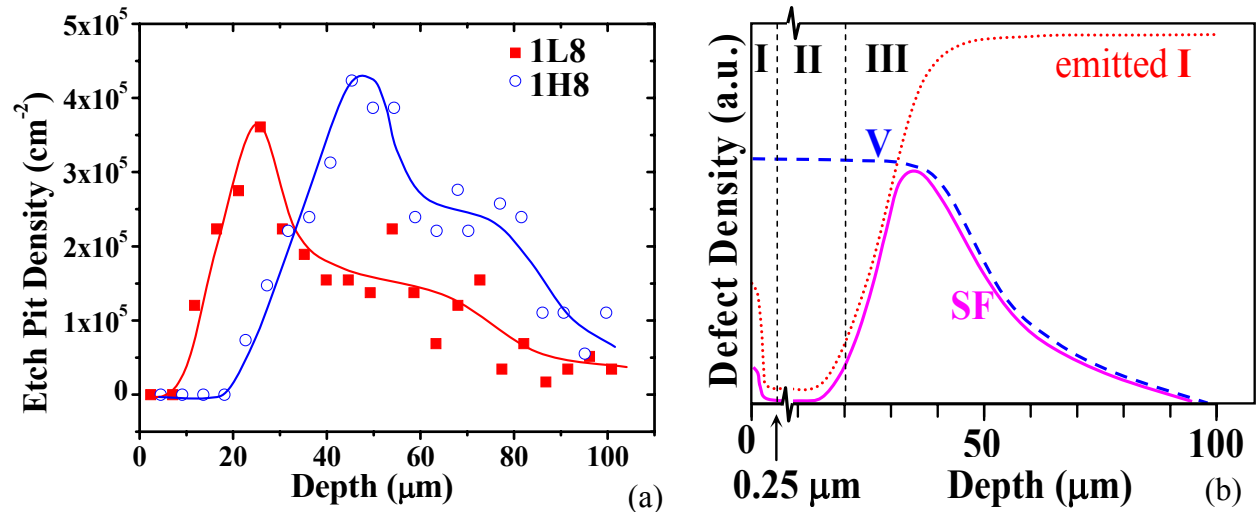


Fig. 21: (a) Stacking faults profiles in wafers 1L8 and 1H8 obtained by etching. Note that the distribution starts at the bottom edge of the LDZ, no SFs were observed in the LDZ in both Lo-Hi and Hi-Lo-Hi N-doped CZ samples.

(b) Model for SF formation and distribution in heat treated N-CZ Si wafers.

N-O complexes at a concentration between 10^{16} and $8 \times 10^{17} \text{ cm}^{-3}$, as revealed by SIMS. The V concentration of $8 \times 10^{13} \text{ cm}^{-3}$ is considered in the range of the measured value by Voronkov, who argued that only single V are considered in his platinum decoration experiment. The $100 \mu\text{m}$ depth corresponds to the range of vacancies produced by V-N decomposition. The $0.25 \mu\text{m}$ depth is the SF range somewhat revealed by etching and clearly seen in the TEM imaging.

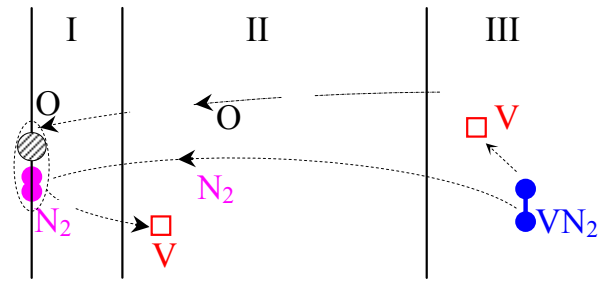


Fig. 22: Model for nitrogen pair diffusion and segregation to the surface.

3.2. Defect Structure and dynamics of point defect clustering

3.2.1. Subsurface Defects

First one has to note that no defects were detected in the as-grown samples examined by TEM using both two-beam and high-resolution imaging, consistent with the fact that they have an extremely low density ($\sim 5 \times 10^6 \text{ cm}^{-3}$ as obtained by OPP) and their size is small making it difficult to find them. Extended defects observed in the subsurface region, relative to the initial wafer surface (Lo-Hi annealed sample S) are typically similar to those shown in Fig. 23.

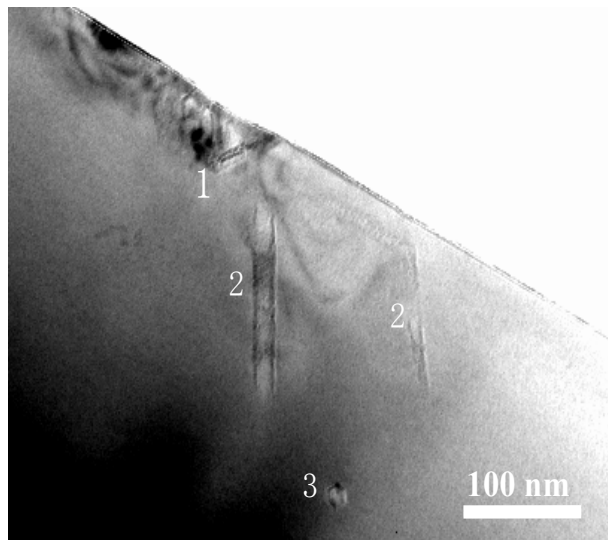


Fig. 23: TEM image of the near-surface region (two-beam conditions) from TEM foil S.

3.2.1.1. Structure of Subsurface Octahedra –Like Oxynitride Precipitates

Figure 24 shows HRTEM images of precipitates from type 1 defect as indicated in Fig. 23. Orientation of specific atomic planes and crystalline directions shown in Fig. 24 (b), allow the identification of the precipitate facets. The dark and bright contrasts inside this small precipitate are associated with variations in residual stress magnitude and type. It is to be noted that no stress is seen to spread out in the Si matrix, implying that the stress is confined entirely within the oxide precipitate and that the interface is fully relaxed. Type 2 defects were identified to be stacking faults (SF). The peripheral contrast band within the precipitate is analyzed by indexing the precipitate/matrix interfaces. Fourier transform of these images showed that the major boundaries of the precipitate indeed coincide with the host Si crystal $\{111\}$ habit planes [134]; in agreement with previous work on N free CZ Si precipitates [135]. The $\{111\}$ planes represent the most energetically favorable planes for SiO₂/Si interface (i.e., for OP growth) [136], and is known to provide higher oxide growth rate [137, 138].

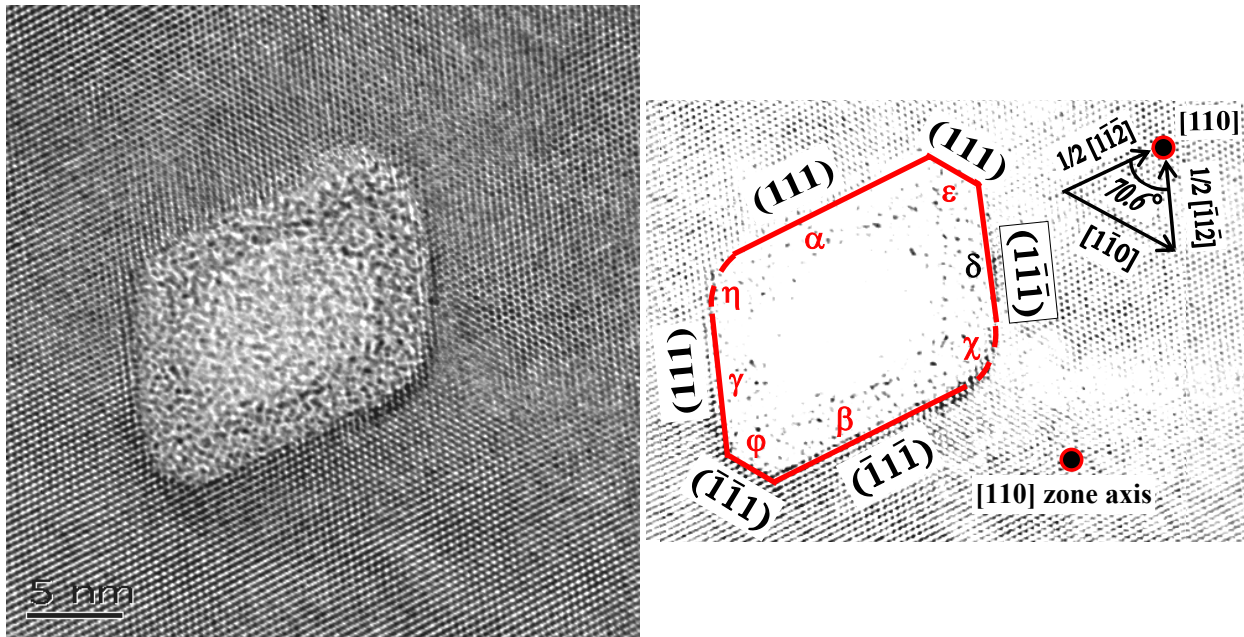


Fig. 24: (a) HRTEM micrograph of commonly observed precipitate in the subsurface of N-CZ Si Lo-Hi treated wafer 3L8 (i.e., TEM foil S), and (b) sketch depicting its facet planes.

The TEM image of Fig. 24 suggests that the majority of the subsurface precipitates nucleated right at the surface and grew within 100 nm or less, while SFs extended in their habit planes up to 250 nm depth. This is in line with the etching defect depth profile provided in

Chapter II, and indicates that the tail of that profile is chiefly due to SF(s). The HRTEM image of octahedral-like precipitate in Fig. 24 is in [110] zone axis. First, note that the χ and γ sides in the sketch shown in Fig. 24 (b), are basically rounded and no unique crystal plane appears. In accordance with the angle relationship between the Si atomic rows, the precipitate-bulk interface sides α , β , γ , and δ are suggested to belong to vertical planes (perpendicular to the image plane (110)), whereas ε and φ sides belong to $\{111\}$ inclined planes. Sides α and δ are suggested to belong to $(\bar{1}\bar{1}\bar{1})$, β and γ to $(1\bar{1}\bar{1})$, and ε and φ sides to (111) and $(\bar{1}\bar{1}\bar{1})$ planes, respectively. As a consequence, all major facets of the precipitate are vertical and so are the inner interfaces of the peripheral band. Therefore, the high contrast constitutes a shell, that is a distinct amorphous phase within the precipitate, and is not a TEM artifact from inclined facets. The origin of the contrast is due to differences in atomic structures of the amorphous zones and in composition, namely N and O concentrations. Indeed the high resolution STEM Z-contrast image of Fig. 28 provides evidences of composition variation. The Z-contrast image in Fig. 14 (b) and Fig. 19 clearly show composition contrasts to the shell and the core relative to the host crystal. The dark region of the precipitate (core) contains elements lighter than Si, namely O and N; the gray apparent shell contains more N than the core. The EELS spectrum shown in Fig. 33(c) provides quantitative assessment of the amount of N present within precipitates, that supports the shell and core model of N-rich oxygen precipitates.

For all precipitates examined in the subsurface region, the major facets of the two-phase precipitates (the interface with the Si host crystal) had $\{111\}$ habits, and appeared ordered and coherent. As a consequence, the surrounding Si matrix to the sub-surface precipitates appears under minimal stress. This is unique to N doping and reflects the absorption of a high amount of incoming vacancies (from the continuum and eventually from the surface) for the stress relief along with ejection of a large number of Si_i. We found that the [N] at the interface of a precipitate is about 18 %, which then implies that about 9 % of the involved V are trapped at the interface, assuming that the involved complexes are VN₂. This is in contrast with N free Si, where the involved V fraction does not exceed 2 % [139, 140, 141].

The HRTEM image in Fig. 27: shows a polyhedron platelet precipitate, found at the bottom edge of the LDZ of the same sample (i.e., 3L8). It has a main body (A) that is extended by region (B), see sketch in Fig. 27: (b). Note that unlike the precipitates shown in Fig. 24, Fig. 25: and

Fig. 26 which are directly exposed to the electron beam, this one is almost totally embedded in the matrix, as indicated by the ordered Si thin layer on top of it.

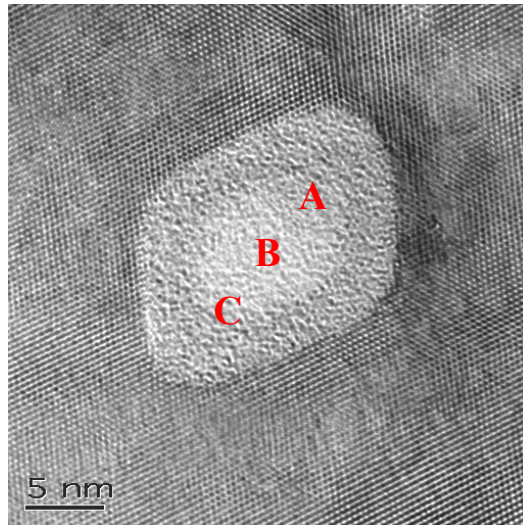


Fig. 25: High Resolution TEM micrograph from foil S (from a Lo-Hi treated N-CZ silicon wafer 3L8 described in Chapter II). It shows a commonly observed sub-surface precipitate.

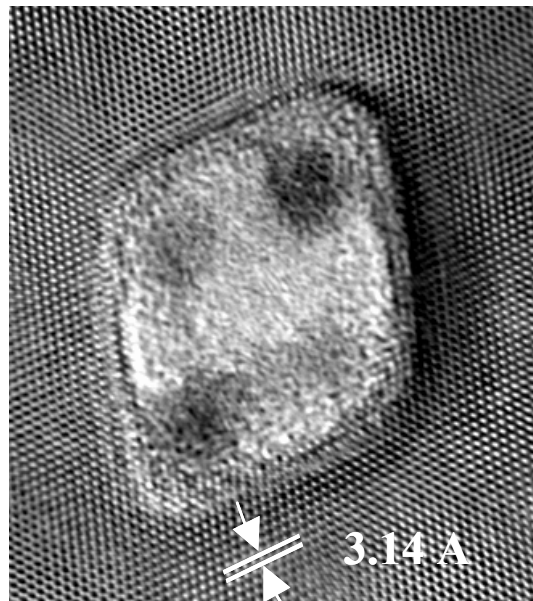


Fig. 26: HRTEM micrograph of a precipitate Type 1, in sample S.

It should be noted that because of the strong bonding of N to Si and the N coupling with O, the observed N-rich shell acts as a diffusion membrane for O migrating from the matrix into the precipitate core, i.e., creates a barrier for O out-diffusion from the precipitate core to the Si matrix. This constitutes a model for cancellation of precipitate dissolution by N doping. The “oxynitride diffusion membrane” clarifies the stability of N related nuclei leading to high density

of small precipitates in N-CZ Si heat treated wafers, as well as why the first high temperature annealing step in the Hi-Lo-Hi cycle is not efficient in dissolving grown-in precipitates. It suggests also that in N-CZ Si, the nuclei do not compete for growing and the known picture of big precipitates growing at the expenses of smaller ones is shifted to “concurrent growth” [142].

Figure 28 shows a STEM Z-contrast image of a typical near-surface defect system. The reason for a dark contrast faceted object is twofold: first, lighter (lower-Z) elements are involved in the precipitate’s composition and, second, the amorphous nature of the precipitate scatters electrons channeled in the host Si crystal matrix oriented in the zone axis, in our case [001]. Type 2 defects appear as distinct gray bands running from and terminating at adjacent precipitates. The gray band b is perfectly oriented along one of the $\{111\}$ planes. Likewise defect feature c shows some facets parallel to other $\{111\}$ planes. The atomic-scale sharpness of the stacking fault contrast is clearly demonstrated in Fig. 28 (b), which is a high-resolution STEM Z-contrast intensity profile obtained along the line indicated in Fig. 28 (a). The SFs gave rise to an intensity ramp modulated with a periodic pattern reflecting the existence of steps that are $\sim 6.75 \text{ \AA}$ spaced on average.

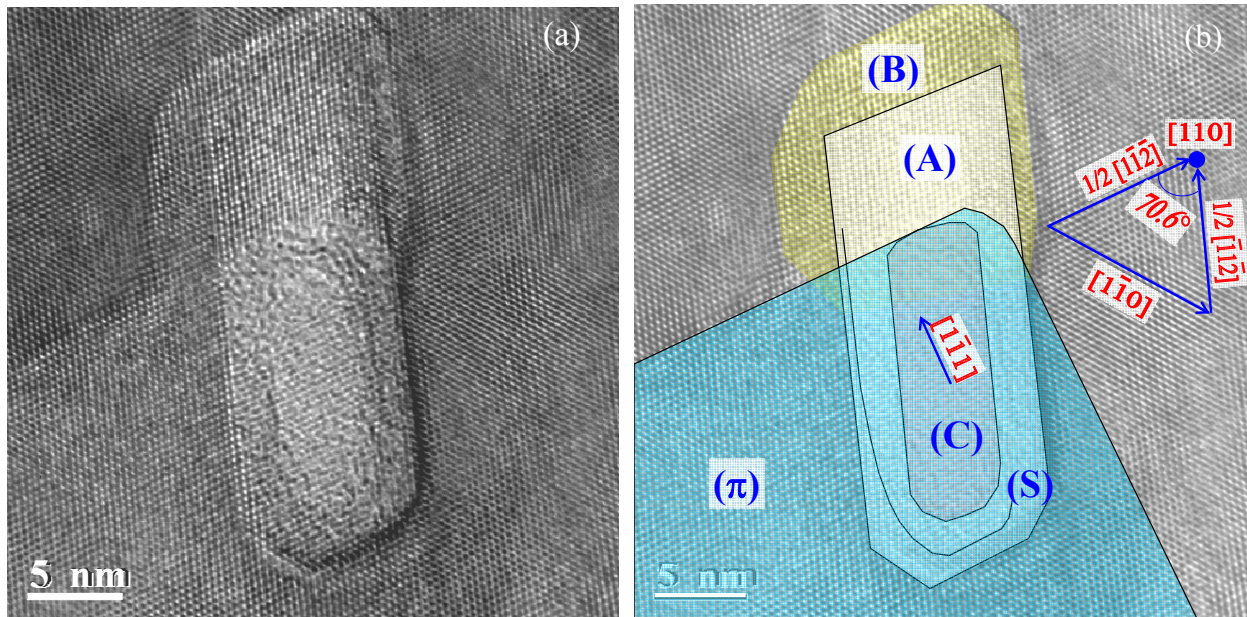


Fig. 27: (a) HRTEM micrographs of a precipitate in sample S of 3L8 N-CZ Si wafer (Lo-Hi treated, as described in Chapter II).

(d) Sketch delineating the different zones within the precipitate in (a); the pictorial cut plane which is parallel to a SF is labeled (π).

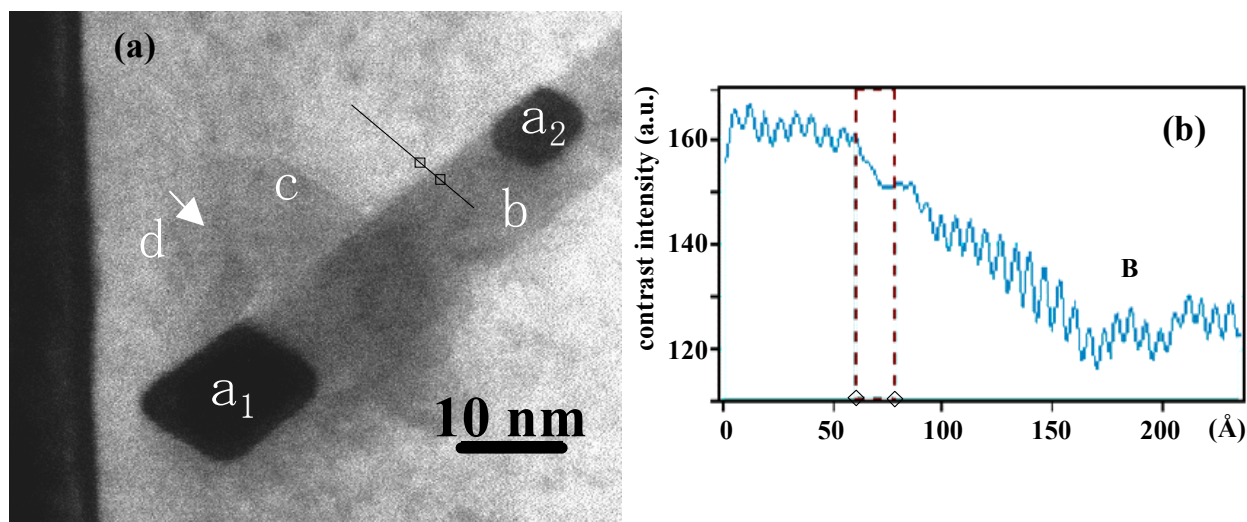


Fig. 28: (a) High-resolution Z-contrast image of a typical defect system (precipitates connected to SF) found in the wafer initial sub-surface (TEM foil S); (b) Z-contrast profile along the line A across defect b.

3.2.1.2. Microscopic Model of Subsurface SF Formation

It is known that oxygen precipitation in N free silicon is accompanied with emission of one self-interstitials (Si_i) per two oxygen atoms. Therefore, the interrelated precipitate-SF assembly shown in Fig. 28, is consistent with the known mechanism of precipitate growth in the bulk, although the absence of lattice strain is not common. The existence of SFs connected to precipitates points to a unique near-surface defect growth environment driven by N, which largely involves V and/or V-N complexes. Note that precipitate (a_1) and (a_2) appear perfectly lined up with one edge of the SF (b) and that the SF projected width is equal to that of precipitate (a_1). These features readily infer a correlation of the three defects. Note also that (a_1) is much bigger than (a_2). We suggest that (a_1) nucleated first and then in the process of growth it gave rise to SF (b) by condensation of the emitted Si_i in one of the $\{111\}$ habit planes. At a certain point during the first or the second annealing (a_2) nucleated at the edge of stacking fault (b), as shown in Fig. 29, thereafter the three defects continue to grow simultaneously. The difference in size between precipitates (a_1) and (a_2) suggests that (i) the latter nucleated on the edge of the SF, and (ii) the nucleation processes for (a_1) and (a_2) were differed. The SF and precipitate size relationship and orientation infer that the self-interstitial condensation process occurs as the precipitates grow. It is likely that during the second annealing the SF growth continued without disturbing the condensation order and that the condensation requires a growth front.

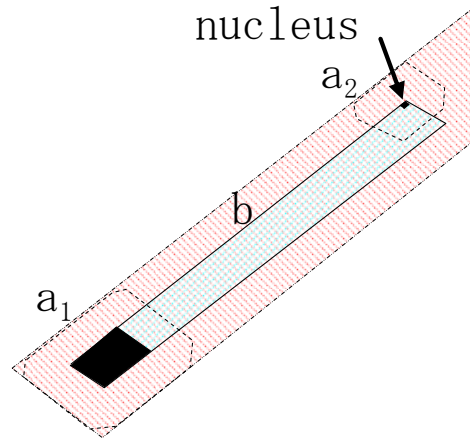


Fig. 29: Model for defect growth dynamics. Precipitate and SF final boundaries are represented with dashed and dotted lines, respectively. At the end of first stage (i) precipitate a_1 grew up to the size shown as a dark area, (ii) SF (b) extended over an area with the same projected width as precipitate (a_1) from which it was originated, and (iii) a nucleus is formed at the edge of the SF. During the second annealing the two precipitates grew further and similarly in preferential directions. SF (b) width is the same as the projected width of precipitate (a_1); their growth interfaces are lined.

In conclusion, the depicted SF growth sequence implies that precipitate nucleation was not limited to the Lo anneal. It suggests that in such N-V rich matrix nucleation proceeds even during the Hi step anneal (known as growth step in N free CZ silicon).

3.2.2. Structure of the Precipitates in the “Denuded Zone”

3.2.2.1. Precipitate Platelets

While Type 1 and 2 defects are more frequent, fewer defects of Type 3 were found at the bottom of sub-surface region, lying $3\ \mu\text{m}$ from the surface. Detailed structure of this defect appears in the HRTEM image of Fig. 30. This defect is a large platelet that has pyramid-like shape at both sides of the major facet that is parallel to a $\{110\}$ plane, indicated by the dashed line. As opposed to the defect structure of the near-surface region, no SFs are present in this case while the precipitate has generated stress in the surrounding Si matrix, appearing as a white diffuse halo. This is attributed to ejected Si_i from the precipitate interface for every precipitating O pair. It is worthwhile noting that in N-free Si, on average, only a fraction between 0.04 and 0.08 of V contributes to the compensation of the misfit strain for every precipitated SiO_2 molecule [143, 6] meaning that the stress is mainly relieved by Si_i ejection. In N-CZ Si this

situation is modified in the bulk by N atoms which reach the precipitate interface while coupled with vacancies. Moreover, in the near surface region this mechanism is enhanced by additional vacancies from the surface coupled to N.

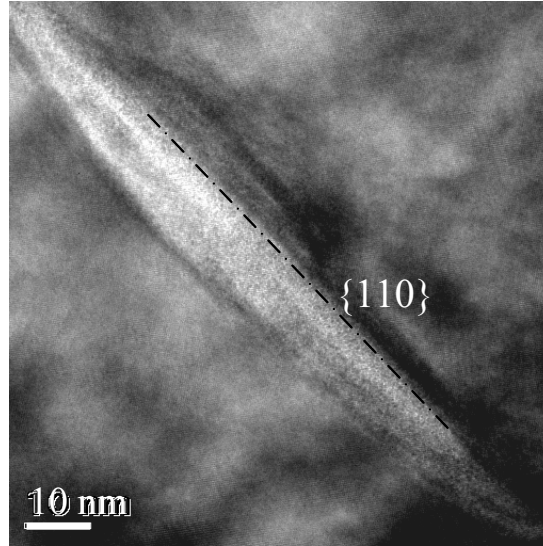


Fig. 30: HRTEM image of an elongated pyramid-like precipitate (Type 3) found in the bottom of sample S, i.e., at 3 μm from the surface.

3.2.2.2. “Dragon-Fly” Defect

The “dragon-fly” like defect shown in Fig. 31 is typically found in sample D10. It is basically an oxygen platelet surrounded by two largely strained zones. Using EELS analysis, the platelet boundary was found N-rich. Components of the platelet (1)-(3) are defined relatively to its main axis LL. Since the precipitate is highly symmetric, in contrast to the “Umbrella Defect” that will be discussed in the next section, it is suggested that the nucleation occurred at the defect center (1) and the growth has proceeded from the two principal growth interfaces made of $\{111\}$ facets. The configuration of the stress is such that its apex starts in region A of the platelet, and propagates along the transverse axis TT.. In this case the stress relief mechanism occurs by a distribution of the strain over a very large zone in the matrix. We suggest that in zone A high stress raises at the precipitate interface because of a high amount of Si_I ejected during precipitate growth. The strain sign contrast in the wavy region (“wings”) varies alternatively. It most probably encompasses zones of high concentration of Si_I . The accumulation of ejected Si_I from region A close to the interface (in the neck of the stress contour) reduces the growth rate and results in a thinner platelet. The stress exerted at the interfaces that are parallel to the main axis reduces the transverse growth rate (i.e., R_T small), while the longitudinal growth rate (R_L) is

high, about six times higher prone. Therefore, for this type of defect the strain and self interstitial accumulation are the controlling factors of the growth rate.

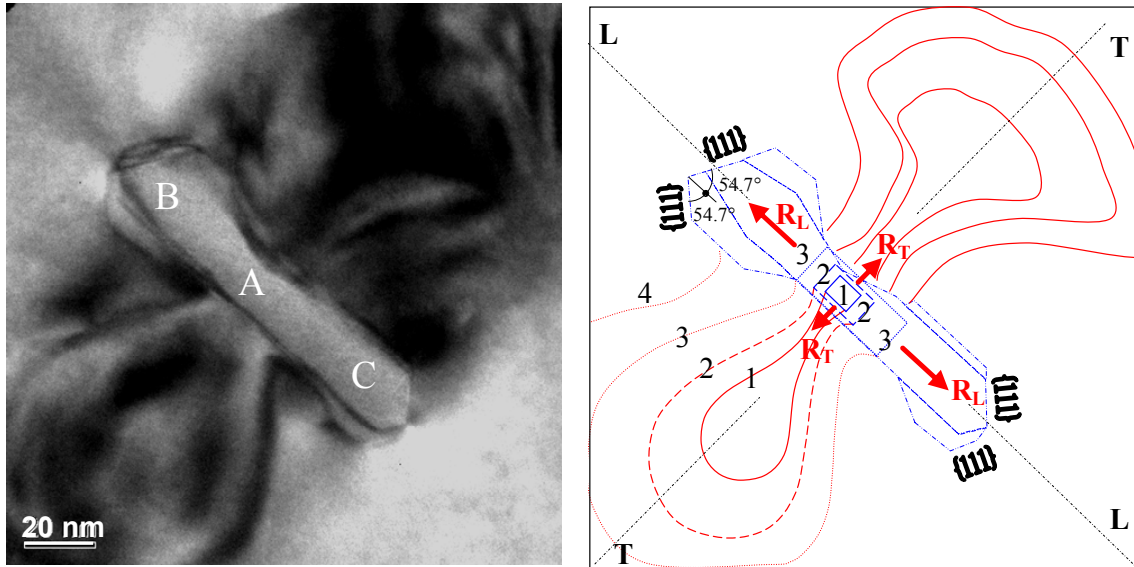


Fig. 31: (a) HRTEM image of a platelet precipitate, so-called “Dragon fly-like” defect, found in the “DZ”, i.e., TEM foil D10.

(b) Sketch of the major parts of the dragon-fly defect system.

3.2.3. Bulk Defects beyond the Denuded Zone

3.2.3.1. The Umbrella Defect (in the Bulk)

The umbrella-like defect (Type 4), shown in Fig. 32, which is commonly found in sample B30, i.e., at 30 μm from the original wafer surface, was identified as a platelet precipitate (i.e., stem) with a condensate of Si_I , O and N at one side (i.e., canopy). Below and above the interstitial zone a large compressive strain is observed (dark area). Part of the interstitials where the strain is minimum tends to line up in a $\{111\}$ plane for which the trace $[110]$ is indicated with an arrow in Fig. 32. In the strained dark areas, the stress is high and reaches a maximum at the curved lines where the interstitials are thought to condense mostly. However, the stress is much lower than the dislocation yield stress, since no dislocations could be detected. Apparently, the high strain prevented the formation of SFs, because the system reduces its energy by expanding the boundary of interstitial rich-zone into a series of curved surfaces. The thermal sequence and the Si_I excess were not favorable to achieve the organization of the emitted Si_I in SF. Most likely, the nucleation in planarly ordered extrinsic SF was altered in the bulk by the mix of N and O with Si_I and the lack of free V that could reduce the high stress by recombining

the excess interstitials. This is in contrast to the near surface zone; i.e., SF and octahedral precipitates in sample S. We believe that the stress build-up increases the energy of the $\{111\}$ habit planes in this region by straining them, thus making SF nucleus domains instable and inadequate for extrinsic SF formation.

Figure 33(a) and (b) show Z-contrast image and a scan profile along line A, indicated in Fig. 33(a) at the thin section of the umbrella defect stem [145]. The line-scan, shows notable intensity variations within the precipitate. The high intensity close to the precipitate peripheral zone edges (B) and (D), in Fig. 33(b), implies the existence of a lighter element, thus one expects the precipitate boundaries to be richer in nitrogen than the center. The EELS spectra given in Fig. 33(c) provides quantitative assessment of the amount of N present within precipitates. The EELS spectrum taken in the center of line A and at the interface of the precipitate platelet are shown in Fig. 33. Both N and O absorption K-edges appear in the spectra. The oxygen absorption edge (O-K) overwhelms the spectra in the inner zone, whereas it is significantly attenuated at the interface and becomes comparable to the nitrogen absorption edge

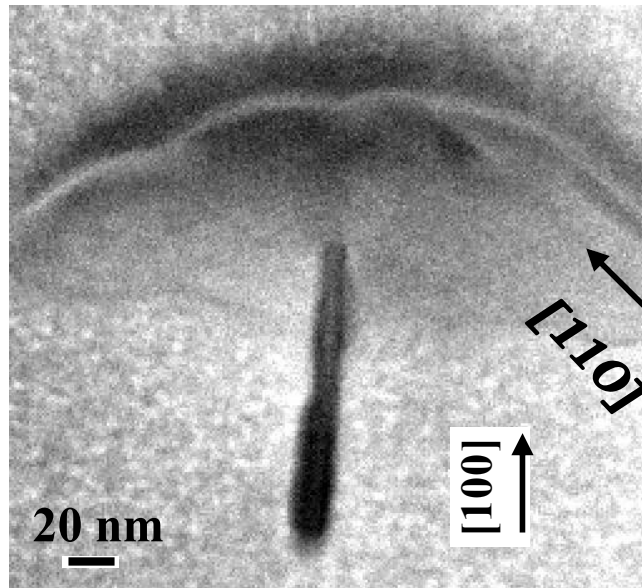


Fig. 32: Type 4 bulk defect in B30, which is an assembly of a precipitate with a self interstitial wavy zone, so-called “Umbrella-like” defect.

(N-K), but still significantly higher and wider. The fine structure lines in the O-K edge, indicated with arrows, infer the existence of a variety of Si-O bonds in the precipitate center, each being characterized by specific absorption lines. This implies that within the precipitate there is either a variable stoichiometry, thus a non-homogenous oxide phase or a variable strain

both of which effect the Si-O bond giving rise to a series of absorption sub-edges. Usually such sub-edges are correlated to variations in the electronic density of states. It is worth noticing that the N-related absorption edge exhibits sub-edges. Using high spatial and energy resolution EELS analysis for $\text{SiO}_2/\text{Si}_3\text{N}_4/\text{SiO}_x\text{N}_y/\text{Si}$ stack Sekigushi et al [146] correlated variations of the nitrogen K-edge with composition change along the depth. They related the core-loss edge at 401 eV to the Si-N bonds in stoichiometric nitride Si_3N_4 . They found that the presence of N-O bonds in SiO_xN_y shifts the edge to higher energies, i.e., 401.6 eV, and they suggested that is due to higher electro-negativity of O with respect to N. The core loss energy of N in SiO_2 shifts the edge to lower energy, i.e., 400.6 eV. Therefore there are at least two bonding states of N in the

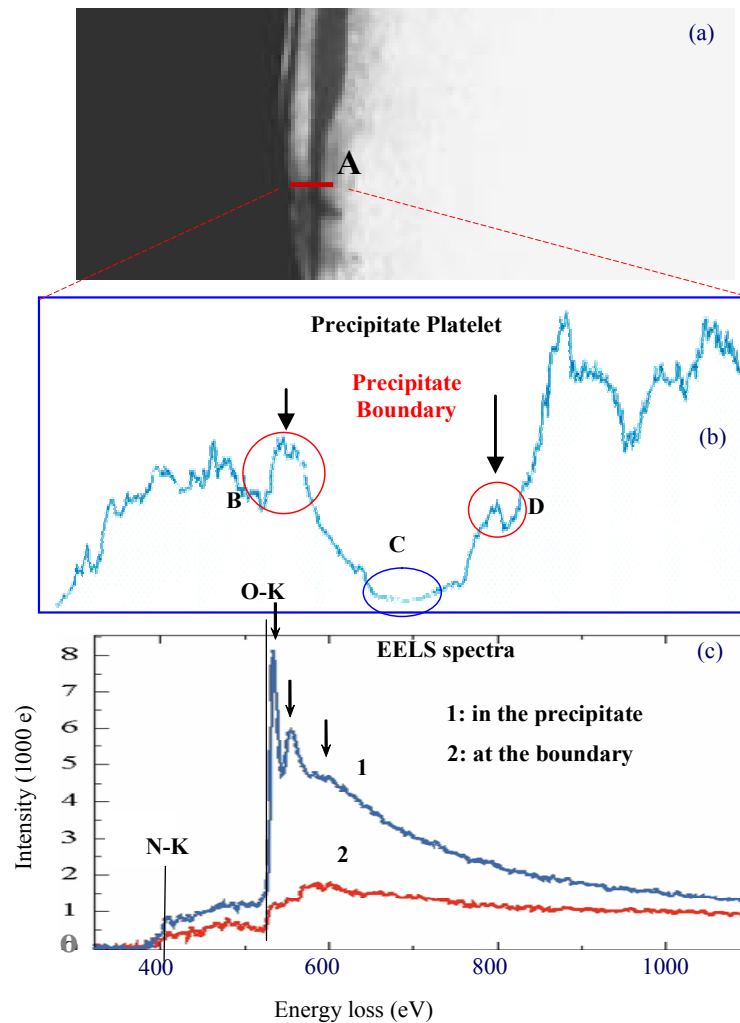


Fig. 33: (a) Low magnification STEM Z-contrast image of an oxynitride precipitate in sample B3 at 30 μm from the original wafer surface,
 (b) Z-contrast line-scan along line A running across the precipitate (50 nm),
 (c) EELS spectra acquired in the precipitate center and at the boundary.

dual phase precipitates we explored. The integration of the energy absorption edges provided the N content in the precipitate, estimated to be 6% of the [O] in the core region. With a similar measurement we have also found a ratio of 17 % in the shell region [129]. This value is in the same range as that found at the wafer near-surface by SIMS and denotes that similar fluxes of complexes have been exchanged, and similar mechanisms are involved regardless of whether it is wafer surface or precipitate interface.

The N to O concentration ratio is calculated by deconvolution of the EELS spectra then integration of the specific absorption edges. The ratio reaches its maximum at the interface ($\sim 17\%$), whereas in the center it is about 2%. The abruptness of the edges B and D in the Z-contrast profile in Fig. 33(b) infers that N ceases to exist outside the oxygen precipitate boundaries and the surrounding regions are deeply depleted of N. The N pileup at the precipitate/silicon matrix interface is consistent with that found in the near-surface by SIMS depth profiling; where we found that N segregation leads to a concentration up to 8 orders of magnitude above the initial background level. In addition, the N pile-up is always accompanied with O pileup with an identical depth profile shape and twenty times higher O concentration. As will be discussed in Chapter VI, first principle and semi-empirical calculations of N-O complex IR absorption lines in silicon suggested that N and O atoms are strongly coupled without being directly bonded and form a continuum of interstitially coupled dimers with five to fifty oxygen per nitrogen atom. FTIR depth profiling of the near surface oxynitride continuum in similarly heat treated material, confirmed that O and N form N-O complexes.

3.2.3.2. Point defect and N- and O- Complex Dynamics for the Umbrella Defect

It is widely agreed that N atoms pair with vacancies [148] at very early stage of crystal growth in stable and less stable forms [149, 7, 151]. The V-N species increase the total concentration of V to an extent that concentration of stored V largely exceeds that in N-free CZ Si. As a result the interstitial condensation mechanism is modified by recombination with V-N complexes, or by the strain induced by N complexes. The former produces mobile interstitial N pairs and results in a fully relaxed matrix, while the latter perturbs the ordered condensation of self-interstitial into SF resulting in umbrella type defect. Unlike the dragon fly defect which is closer to the surface, the mechanism that drove the interstitials to one region was a sustained strain induced transport of Si_I during the platelet growth.

The N and O found in the condensate (“canopy” region) is gettered by the migrating Si_I and the stress build up (stress induced segregation). Note that away from the surface the precipitate size is about the same, only defect morphology changes with the depth. In all cases the small dimension is in the range of 20 nm, while the long side is six times larger. The lateral growth is believed to be due to O adsorption from the sides while repulsive stress is high at the bases. The growth occurs in two stages, during the first V are consumed, interstitial are ejected from the two larger faces where the stress builds up and consequently the growth at these facets is reduced while it proceeds laterally, as shown schematically in Fig. 31 (b). Rate reduction is also seen in the umbrella defect in the stem zone that is close to interstitial condensate.

Figure 34 is a schematic of a suggested model for the growth of the Umbrella Defect. The combination of Z-Contrast line scan with EELS at the neck of the precipitate (Umbrella stem) has shown that the [N]/[O] ratio is high (~17%) at the precipitate interface while it is minimum (about 2%) at the the precipitate core. The average nitrogen to oxygen stoichiometry ratio is about 6%. Like the precipitates found in the wafer subsurface, the interface region forms a shell that is N rich. The Z-contrast in the canopy’s white ridges are heavily dominated by Si_I . Energy Loss Near Edge Spectroscopy (ELNES) in the “canopy region” showed that O and N content are also high. It is believed that the curved regions are highly stressed. During the defect the stress was reduced by increasing the condensation region and developing curved zones. We suggest that the sequence of defect formation are:

- 1) the nucleation of the platelet started from the bottom at a nitrogen stable complex such as V_2N_2 ,
- 2) the growth rate is biased towards a region that most likely has initially tensile stress (created either by N and/or V supersaturation)
- 3) the growth interface, made of {111} steps, moved away from the nuclei location
- 4) the oxygen flux comes essentially from the region between the growth interface and the canopy (O source)
- 5) the growth regime is first reduced by necking the platelet at the growth interface then is stopped when the O supersaturation in the O source region is totally reduced.

The morphology of the platelet depends on the initial conditions of nuclei position in regard to the neighboring strained region that becomes later a condensation zone (canopy).

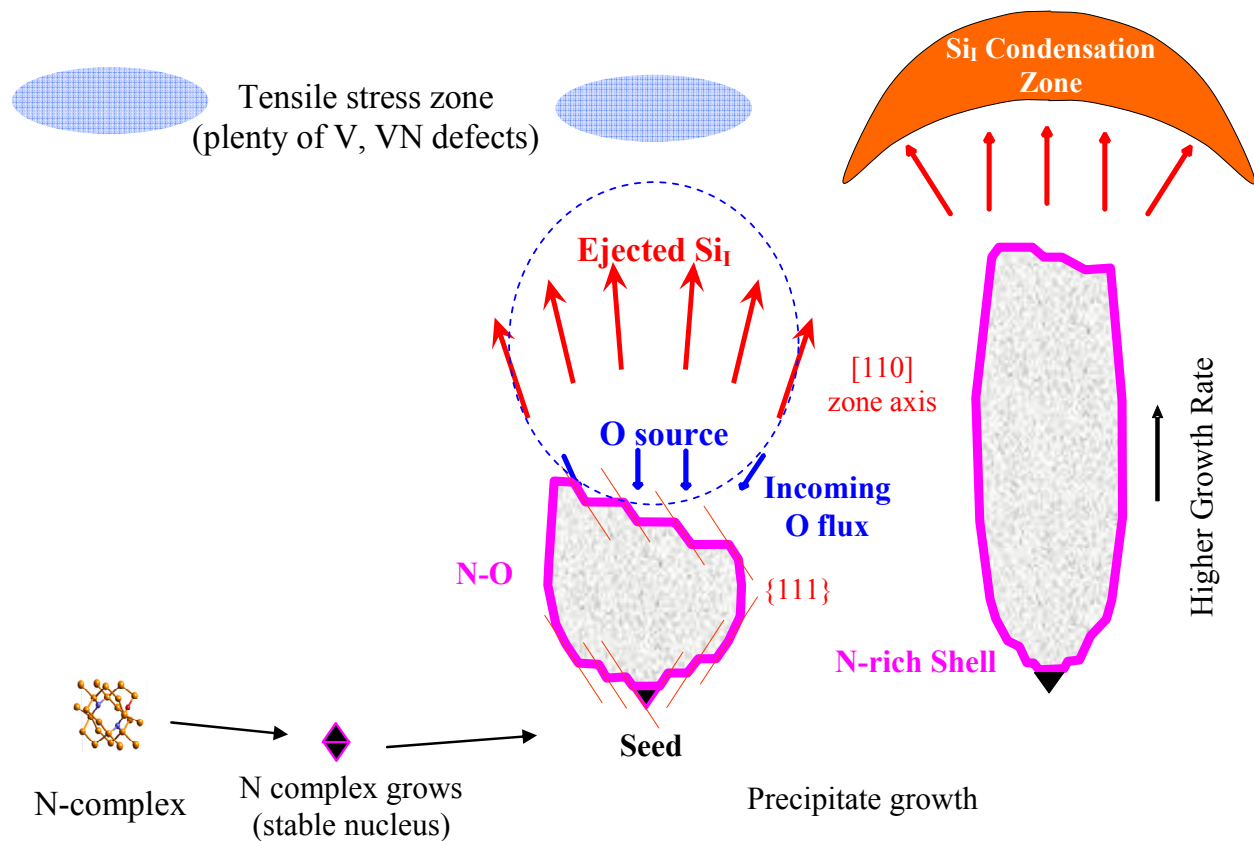


Fig. 34: Schematic of the suggested model for Umbrella defect growth.

3.3. Effects of Nitrogen Segregation on Precipitation Mechanisms

Despite the initial low nitrogen level in our samples, nitrogen consistently segregates in a large proportion in the peripheral areas of precipitates [152], or piles up at the surface. Both effects are analogous to what happens during growth of thin film oxynitrides, where N segregates to the interfaces [153] and results in V injection [154]. The N segregation leads to concentrations much higher than the solubility limits. This occurs in the subsurface and less dramatically in region III, but not in region II. Such a strong pile up, which at the subsurface reaches three orders higher than the initial concentration, does not occur without strong O-N coupling and the surface effects. This is consistent with data from Itoh and Abe on N-FZ. The coupling controls the O out-diffusion while it changes the precipitation mechanism in the bulk and induces co-precipitation at the free surface.

From the observed precipitate structure we suggest that in a first stage, a second phase of oxynitride is formed which acts, as a nucleus when its radius exceeds the critical radius at

annealing temperature. During growth stages, as the defect gets bigger, the second phase of the oxynitride breaks up and the N segregates to the interface and adiabatically generates a third phase which is richer in nitrogen. This occurs by a simultaneous out-diffusion of N from the core to the interface while N species from the continuum keep on sinking into the precipitate boundaries. While N segregates to the precipitate interface, oxygen diffuses across the oxynitride shell towards the core region and gets trapped. The proposed mechanism accounts for the cancellation of precipitate dissolution at 1250°C. These processes are facilitated by the fact that N coupled to V sink at the precipitate interface, while self-interstitials are emitted in the matrix. Both mechanisms contribute to the relief of strain induced by precipitate-matrix volume misfit, with the dominance depends on the depth. In particular, at the surface, V and V related complex driven mechanisms are dominant and the precipitates are equilibrium defect type, whereas in the bulk precipitates have more complicated interface and appear highly stressed [142]. The nuclei high density and the N induced local stresses suggest that in N-CZ Si nuclei do not compete for growing. The known picture of big precipitates in N-free CZ, grow at the expenses of smaller ones is shifted in N-CZ to “concurrent growth” [155]. Quantum mechanics calculations of the energy of formation of N pairs combined with statistical mechanics allowed prediction of nuclei concentration.²⁵ The proposed range of N-based nuclei concentration in the bulk is between 10^{12} and 10^{13} cm^{-3} , which is one to two orders lower than the N pair concentration at annealing temperature.²⁵ This range appears in the order of the precipitate concentration ($6 \times 10^{12} \text{ cm}^{-3}$) estimated by correlation of N and O SIMS profiles.

4. Summary

Annealed nitrogen doped silicon showed a variety of depth dependent precipitate and stacking fault nucleation and growth modes. The composition and the morphology of these defects appeared as unique devices for probing the interplay of point defects and chemical complexes and for singling out the role of local stress in the control of extended defect growth mechanisms. The effect of the surface conjugated with N species is striking since the defect type is shifted from stress free octahedral oxynitride (with two phase precipitate coupled with stacking faults) to a variety of platelets with a point defect condensate. The structure of these platelets depends on the depth and the orientation of emitted interstitial fluxes. Local stresses and/or flux of ejected interstitials reduce locally the precipitation rate forcing the growth to

proceed in opposite or perpendicular direction. The platelet growth rate reached six times higher than in the slow direction. Large local stress in the umbrella defect drives a large flux of Si_I aside from the platelet and prevents SF formation.

Vacancies and thus stress appear to control the interstitial stream and condensation which correlate with precipitate morphology. Various depth dependent modes were singled out:

- close to the surface where plenty of V exist, they contribute to the formation of precipitates to which very small SF are connected in stress-free matrix. Vacancies are either injected from the surface or grown-in as single point defect or paired with nitrogen atoms,
- in the “DZ” where the V concentration is reduced, Si_I form a halo around precipitate platelets, and no SF could form,
- at 10 μm depth, and
- in the bulk, with an extremely reduced V contribution, precipitate platelets grow even thinner. Due to the large N induced stress, the ejected Si_I segregate and condense in the N-lean side of the precipitate, forming an umbrella defect system. Interstitial stream reduces the growth rate and produces a neck in the precipitate platelet.

Chapter IV

POINT DEFECT INCORPORATION AND COMPLEXING IN NITROGEN DOPED

CZochralski Silicon	73
1 Processes of Point Defect Incorporation during Crystal Growth	73
1.1 Introduction	73
1.2 Melt/Solid Equilibrium Interface and Crystal Growth	74
1.3 Impurities and Point Defect Introduction	76
1.3.1 Oxygen Incorporation	77
1.3.2 Vacancy and Self-Interstitial Creation	78
2 Point Defect Redistribution and Extended Defect Nucleation	78
3 Basic model for Oxygen and Vacancy Agglomeration in CZ Si	82
4 Prominent complexes in CZ and N-CZ Si	84
4.1 Model for Defect Precursors in N-CZ Si Ingot	84
4.2 Space-Temperature Map of Defect Precursors within N-CZ Si Ingot	86

Chapter IV

POINT DEFECT INCORPORATION AND COMPLEXING IN NITROGEN DOPED CZOCHELSKI SILICON

1. Processes of Point Defect Incorporation during Crystal Growth

1.1. Introduction

The knowledge of defect thermal history, a cumulative parameter, represents a major issue for crystal growth and wafer processing. It has been addressed in different ways in order to allow a correct understanding of extended defect formation in N-CZ Si (including generation of chemical complexes and nuclei). It is complicated by the cumulated effects of the sequence of thermally activated point defect chemical reactions, which involve critical temperatures for the reaction to occur, the diffusion lengths, and the concentration of the reacting species. A limited number of temperature ranges can be singled out for both crystal cooling and wafer heat treatments. Likewise, a limited (although large) number of chemical complex types are created for which the behavior of already formed complexes can change. These temperature ranges, with the point defect concentrations (which vary depending whether the boundary conditions are related to the crystal or wafer surfaces) control the subsequent defect growth stages.

During crystal cooling, vacancies and self-interstitials become supersaturated. Their actual concentrations (at the cooled zone temperature: T) remain close to their equilibrium concentrations at the melting temperature (T_m), while they are actually higher than their respective equilibrium concentrations at T . The major part of the free energy is lowered by removal of the excess amount of both point defects. This can occur either by (i) recombination, (ii) out-diffusion to the lateral surface of the crystal, or (iii) point defect complex formation and precipitation. Generally, recombination and lateral out-diffusion take place prior to precipitation, since precipitation requires significant supersaturation to overcome the energy barrier for nucleation, which is fulfilled at lower temperature. It is evident that lateral out-diffusion to the crystal perimeter or wafer edge will take a longer time than recombination, since the recombination energy barrier is expected to be small at high temperature and recombination will occur due to the high vacancy and self-interstitial concentrations. The equilibrium concentration

of vacancies in CZ Si is reported to be more than one order of magnitude higher than that for self-interstitials.[156] Thus, as the temperature decreases from the melting point, recombination becomes the most effective mechanism for the annihilation of excess self-interstitials. As a consequence, the vacancy remains not only in a supersaturated state but also as the dominant point defect. Therefore, in subsequent stages self-interstitials in CZ Si can be captured without a significant reduction in vacancy concentration. The excess vacancies are then free to diffuse laterally until the temperature reaches a critical value (T_c) at which vacancy complexing with oxygen impurities occurs and void nucleation is initiated.

In this chapter, the main issues of crystal growth, i.e., point defect incorporation and pairing at high temperature are presented for the O-rich CZ silicon. The model developed by Kiman Bae et al [26] that is based on the vacancy dominance for crystal defect formation and which favors the radial diffusion, and the numerical simulation that I have done as a starting point for this work are briefly described. Thereafter, the generation of N and O related complexes in N-CZ is discussed and a tentative map showing the defect generation history during N-CZ crystal growth is suggested.

1.2. Melt/Solid Equilibrium Interface and Crystal Growth

Ideal crystal pulling rate: Silicon crystal growth is accompanied by phase change at different moments of the growth from 1412°C down to 1200°C, i.e., at various levels of the ingot, starting from the interface solid-liquid. The atomic structure changes successively, from disordered to locally ordered at the interface to a stressed and defected crystalline structure. The change of the symmetry does not proceed continuously, but at specific thermodynamic conditions [158], thus defines specific defect zones within the crystal. Considering the equilibrium region of the liquid and solid, the Gibbs free energy balance $G_L = G_S$ at the Liquid-Solid interface can be written as:

$$\Delta G = \Delta H - T\Delta S = 0 \quad (2)$$

For a small deviation from this equilibrium, we have:

$$\begin{aligned} \Delta G &= \Delta H \frac{(T_E - T)}{T_E} \\ &= \Delta S \cdot \Delta T \end{aligned} \quad (3)$$

where $\Delta T = T_E - T$ represents the undercooling of the material close to the interface. The

internal free energy, the enthalpy and the entropy have discontinuity for the change of the material thermodynamic state, which is of first order. Due to the temperature fluctuation, the transformation can not be homogeneous, thus the solidification will advance or recede. The liquid temperature is maintained slightly above the melting point T_m and growth at a constant crystal diameter is achieved by maintaining the solidification isotherm in a vertical position [159] and a flat melt surface. The solidification rate is a function of temperature and limited by the heat removal rate at the crystal interface. Crystallization involves the supply of thermal energy to the melt coupled with the removal of the latent heat of solidification from the crystal. The energy transfer results in a limitation in the crystal pulling rate. Assuming no radial temperature gradient the maximum pulling rate is:

$$\begin{aligned}
 V_p|_{\max} &= \frac{K_c}{\rho_c \Delta H} \left(\frac{dT}{dz} \right)_c & (4) \\
 &\propto \left| \left(\frac{dT}{dz} \right)_c - \left(\frac{dT}{dz} \right)_m \right| \\
 &\approx \left(\frac{d^2T}{dz^2} \right)_{\text{interface}}
 \end{aligned}$$

K_c , ρ_c are the thermal conductivity and density of the silicon, respectively. This expression shows that a flat surface rather imposes a null pulling rate; in reality the interface is maintained parabolic to get a constant pulling rate.

Fluctuations at the interface: The macroscopic pulling rate is always greater than the ideal growth rate and limited by the fact that the melt drops at a threshold level. The microscopic growth rate differs from the macroscopic growth rate due to the deviation of the thermal center of symmetry from the crystal rotation axis, which results in periodic thermal fluctuations at the growth interface. The thermal fluctuation is roughly periodic and related to the relative rotation speed of the ingot and the crucible ($\omega_s - \omega_c$). The growth rate is then expressed as follows:

$$V_G = V_P - \frac{2\pi\Delta T_i \omega}{(dT/dz)_m} \cos(2\pi(\omega_s - \omega_c)t) \quad (5)$$

When the cosine becomes negative, there is no growth and the some newly solidified parts of the interface remelt [160]. The local remelt enhances the formation of point defect clusters [161], due to excess of interstitials and vacancies apart [162]. In addition to the heat flow, the growth rate depends on the structure of the interface, whether it is smooth or rough, affecting the

introduction of atoms into the solid. The macroscopic growth rate depends on the macroscopic undercooling decided by the puller geometry, thermal transfer and ambient conditions [163]. In parallel, the microscopic growth rate depends on the microscopic undercooling, which in turn depends locally on the interface roughness [164]. When a high fluctuation causes a transient increase in the interface temperature, remelt occurs, therefore the pulling rate must be lowered until the solidification restarts. A major problem associated with high pulling rates, required in production, of heavily doped silicon crystals, is the loss of single-crystalline structure due to excessive impurity introduction [165].

Facet growth: The pulling rate for $\langle 111 \rangle$ oriented Si crystals is slow because the growth rate direction has a slow growth rate (in this case normal to the plane $\{111\}$) since it is the most closely packed in the diamond structure, whereas growth by lateral extension of the $\{111\}$ plane is favored. The preferred directions of lateral growth in the (111) plane are $[2\bar{1}\bar{1}]$, $[\bar{1}2\bar{1}]$, $[\bar{1}\bar{1}2]$ and are associated to 3 habit lines. While the $\langle 111 \rangle$ presents the facet growth problem in addition to the isotherm stability, crystals grown along $\langle 100 \rangle$ do not have the problem of facet growth, therefore they have a better crystal melt interface stability. Therefore, growing silicon along $\langle 100 \rangle$ direction is easier, and possibly faster, because it is only dominated by the solidification isotherm curvature.[166] The solidification process initiation requires a substantial undercooling.[167] The faceting problem is associated with a local deformation of the interface.

The facet layer growth start first at the crystal peripheral, because of the concavity of the solidification isotherm, which makes the $\{111\}$ facets grow laterally toward the center rapidly. This is a fast but very selective process (because of the well defined crystal orientation), thus sensitive to the variation of the solidification process isotherm and the solid-melt interface. The mismatch creates “growth striations” which locally have different impurity dopant concentrations [168]. Also oxygen content is known to fluctuate laterally and axially [169].

1.3. Impurities and Point Defect Introduction

The relation between the shape of the crystal melt interface, the crystal defects and the impurity distribution is well documented [170, 171, 172]. The non uniform impurity distribution is attributed to a difference in segregation coefficient at the flat portion versus the curved portion of the interface as well as the differential time for growing equivalent atomic planes inherent to the curvature of the interface. The melt flow pattern also affects the interface shape [173] and

dominates the incorporation of the impurities including oxygen dissolved from the crucible quartz walls. Such an idea is implemented in the magnetic CZ (MCZ) process for growing silicon with reduced O content (1 order lower than CZ).

1.3.1. Oxygen Incorporation

Regardless of the oxygen level in CZ Si, macroscopic properties of the material are greatly affected by oxygen [174] such as the material mechanical strength via dislocation locking, and the electrical properties via impurity gettering. The impurity segregation phenomena contributes to a local variation of the melting point at the interface. Most impurities in silicon lower the melting point of silicon, because they form an eutectic system with silicon, thus they present a segregation coefficient lower than one, except the oxygen [175]. This means that oxygen is dissolved easily, with higher concentration in the solid than in the liquid and that oxygen tends to increase the melting temperature of silicon, thus contributing to the development of the interface inhomogenities. The oxygen atoms incorporated form the silicon melt, occupy interstitial sites in the crystal with average positions midway between two neighboring silicon atoms along one of the four equivalent directions $[111]$, $[1\bar{1}\bar{1}]$, $[\bar{1}\bar{1}1]$, and $[\bar{1}11]$ [176]. The oxygen interstitial bonding model suggests that the Si-Si bond is broken into Si-O-Si with six possible equivalent positions for diffusion [177], which results in a low activation energy for the transition from one site to the neighboring sites. Oxygen diffusion does not involve point defects (i.e. V and I) like other impurities, but rather occurs by maintaining one bond, breaking the other bond and switching it to form a new bond with a close neighbor silicon atom [178]. The oxygen diffusivity is given below as:

$$D_{O_i} = 0.13 \exp\left(-\frac{2.53}{kT}\right) \text{ (cm}^2\text{/s)} \quad (6)$$

This expression is well supported by various experimental data from various measurement techniques. However, some techniques show a small discrepancy at 450°C, originated by thermal donors (chemical complexes involving oxygen) formation/dissociation [179]. In addition, the point defect creation during crystal growth or during device fabrication processes changes drastically the impurity diffusivity [180]. The solubility of oxygen is around $3 \times 10^{18} \text{ cm}^{-3}$ at Tm and drops two orders of magnitude at 900°C, most common long annealing and driving-in temperature. With such a high supersaturation, oxygen precipitates at temperature ranges of conventional wafer processing, such as Lo-Hi and Hi-Lo-Hi denuded zone cycles.

1.3.2. Vacancy and Self-Interstitial Creation

“Today, silicon technology faces two main defect challenges, neither of which can be solved simply by increasing the level of crystal *purity*, as was the case in the transition-metal problem.” [181]. The authors referred to the control of (1) the intrinsic point defects vacancy and self interstitials and (2) the extrinsic oxygen impurity. Interstitial and vacancy produce two types of defects microdefects (A/B swirl defects) and vacancy-type (“D”) defects, respectively. A threshold growth rate (v_t) defines a change from A or B defects to D defects. Such threshold was found to be proportional to the near interface axial temperature gradient G [17, 183]. Swirl defects are formed if v/G is below ξ_t associated with the threshold growth rate v_t , and D defects are formed otherwise. The rule based on the Voronkov ratio “ v/G ” holds both for float-zone and Czochralski grown crystals [184], independent of oxygen content. This simple rule translates the fact that the type of defect is determined by the transport phenomena (diffusion, convection, recombination, and generation) of the intrinsic point defect at the sub-interface thin zone. In turn, the incorporated point defects are controlled by the parameter v/G , in the vicinity of the interface.

2. Point Defect Redistribution and Extended Defect Nucleation

The thermodynamic equilibrium between the driving forces for point defect incorporation into the crystal and the supersturation (consequent to temperature decrease) is achieved by the reduction of the point defect concentrations. This occurs forcefully by recombination and point defect pairing close to the liquid-solid interface and in later stages by outdiffusion. However, constrains in the evacuation of point defects by outdiffusion are imposed in the axial direction by the forbidden melt-solid interface and the remote and cooled necking region. These two conditions reduce the significance of the axial component for point defect reduction. Therefore the lateral outdiffusion was suggested to be dominant [185]. Vacancy lateral out-diffusion has been calculated [157] using cylindrical coordinates, where the z-component (axial crystal direction) is negligible, i. e., practically, there is no abrupt change in growth rate even with stop-growth tests. The three-dimensional V distribution in the silicon ingot can be obtained as a series of Bessel functions [186]:

$$\frac{C_V - C_V^{eq}(T_m)}{C_V^{eq}(T_c) - C_V^{eq}(T_m)} = 1 - \frac{a}{2} \sum_{n=1}^{\infty} \frac{e^{-D_V \alpha_n^2 t} J_0(r \alpha_n)}{\alpha_n J_1(a \alpha_n)} \quad (7)$$

where $C_v^{eq}(T)$ and $D_v(T)$ used for this calculation are from Ref.187. Results of the calculation are shown in Fig. 35 where longer times (to cool from T_m to T_c .) correspond to a slower pulling rate. Grown-in defect distribution found by x-ray topography of copper decorated CZ Si wafer proposed to explain observed oxygen precipitation behavior, see Fig. 36. It is important to note at this point that oxygen induced stacking fault (OSF) ring is a defect system that is a result of point defect transport and interactions with oxygen, since no extended defects are available to act as heterogeneous nucleation sites, supersaturated point defects and impurities (interstitial oxygen, carbon, dopant atoms) will interact with each other to reduce their unstable supersaturated and lattice stressing state by forming complexes. Note that although the lateral vacancy out-diffusion can be significant, see Fig. 35, the vacancy concentration remains close to its initial value in the central core region, and its supersaturation is sufficient for void nucleation to be initiated at T_c .

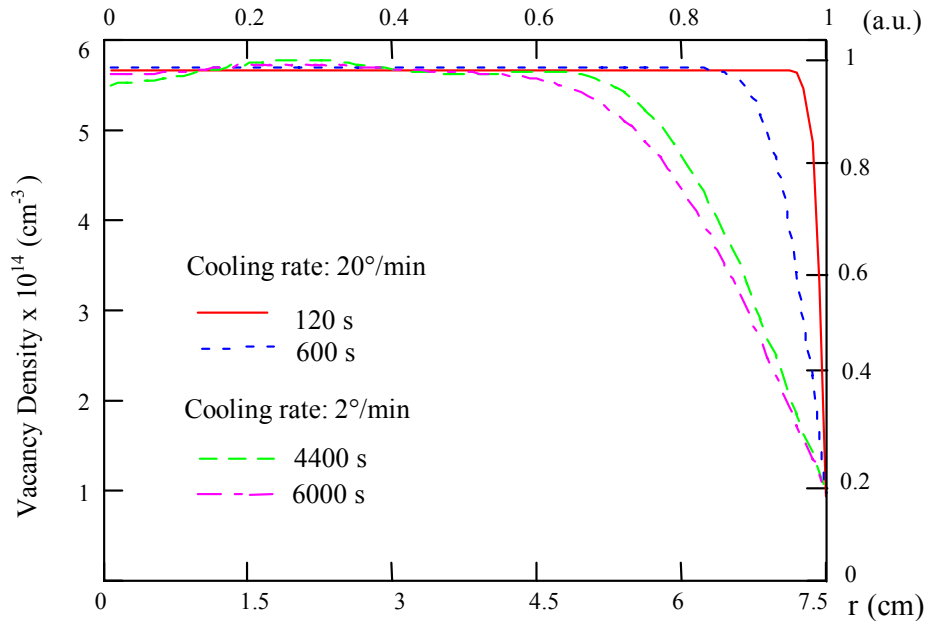


Fig. 35: Radial vacancy profiles in CZ crystal ingot subsequent to lateral diffusion, for different cooling rates and times.

Thus, the extent of the central D-defect region, or equivalently, the diameter of OSF-Ring depends on the cooling rate and is consistent with lateral vacancy out-diffusion. The pull rate strongly affects the crystal cooling history and slower pull rates can result in a collapsing of the OSF-Ring; whereas, fast pull rates allow the ring to extend to the outer wafer edge, enabling the D-defects to be distributed over the entire wafer.



Fig. 36: X-ray topography image of OSF-Ring of a 200 mm copper decorated CZ wafer.

A possible mechanism is suggested to be a sequence of defect interaction during cooling from the crystallization temperature. First, recombination or pairing of intrinsic and extrinsic point defects occur uniformly in the near-interface zone. Second, point defect diffusion occurs farther (from solidification front) in regions where diffusivity is still high. This results in central vacancy rich region and outer interstitial rich region. As crystal cools down, both point defects become more and more supersaturated. When critical temperature is reached, vacancy and interstitial can nucleate new defects at regions above critical supersaturation. Subsequent to nucleation, the growth above critical radius starts (both being driven by the point defect supersaturation).

An entire temperature/time/spatial sequence for formation of the D-defect and OSF-Ring was proposed by K. Bae [157, 185]; an enhanced version is presented in Fig. 37. Note that at the

ingot outer surface (wafer edge) the V and I concentrations are taken equal to their equilibrium concentration; these evolve with the temperature of the considered ingot zone. Stages (a) and (b) essentially describe that vacancies dominate and the D-defect region radius depends on cooling rate. Frame (b) depicts the intermediate region where vacancy and interstitial balance each other, and result in a defect-free zone at vacancy rich region whose supersaturation is low for void nucleation. Grown-in oxide nuclei in (a) is believed to be formed by homogeneous nucleation which is enhanced by the residual vacancy environment, and strongly affected by the initial oxygen concentration. Note that relative to the vacancy profile, oxygen out-diffusion is not significant due to its much lower diffusivity, see Fig. 37 (b); however, the interaction between vacancies and oxygen generates a common nucleus for either the D-defect core region or the oxygen precipitate (OSF-Ring) region, depending on the radial vacancy profile.

As the crystal cools down, oxygen precipitation in the Ring-OSF band follows in sequence the void nucleation. Internal wall oxidation will occur earlier than nucleation since it provides favorable condition for oxide of larger lattice parameter. Small oxide will completely filled with oxide and eventually transformed into oxygen precipitates. At lower temperature, oxygen cluster on already formed nuclei, but remain sensitive to the incoming vacancies as it constitutes the mechanism of stress relief, thus strongly affected by the local vacancy concentration. The stress generated by the second phase formation is due to volume mismatch of SiO_2 as compared to that of the host crystal.

In the anomalous oxygen precipitation (AOP) region, which is at the edge of the vacancy profile, still contains high vacancy concentration, oxygen nucleation will take place here. Since in the AOP there are no stacking faults, the precipitate size should be smaller than the one in Ring-OSF band. In the periphery zone, as the radial concentration is reduced, a relatively small amount of vacancies is available for agglomeration, so that voids remain small and practically not detectable.

Note that in stage (b) of Fig. 37, the double hatched area above the critical level for precipitation have been used essentially for void formation and for ring OSF for O precipitation. The simple-hatched zone condensate in extrinsic dislocation loops.

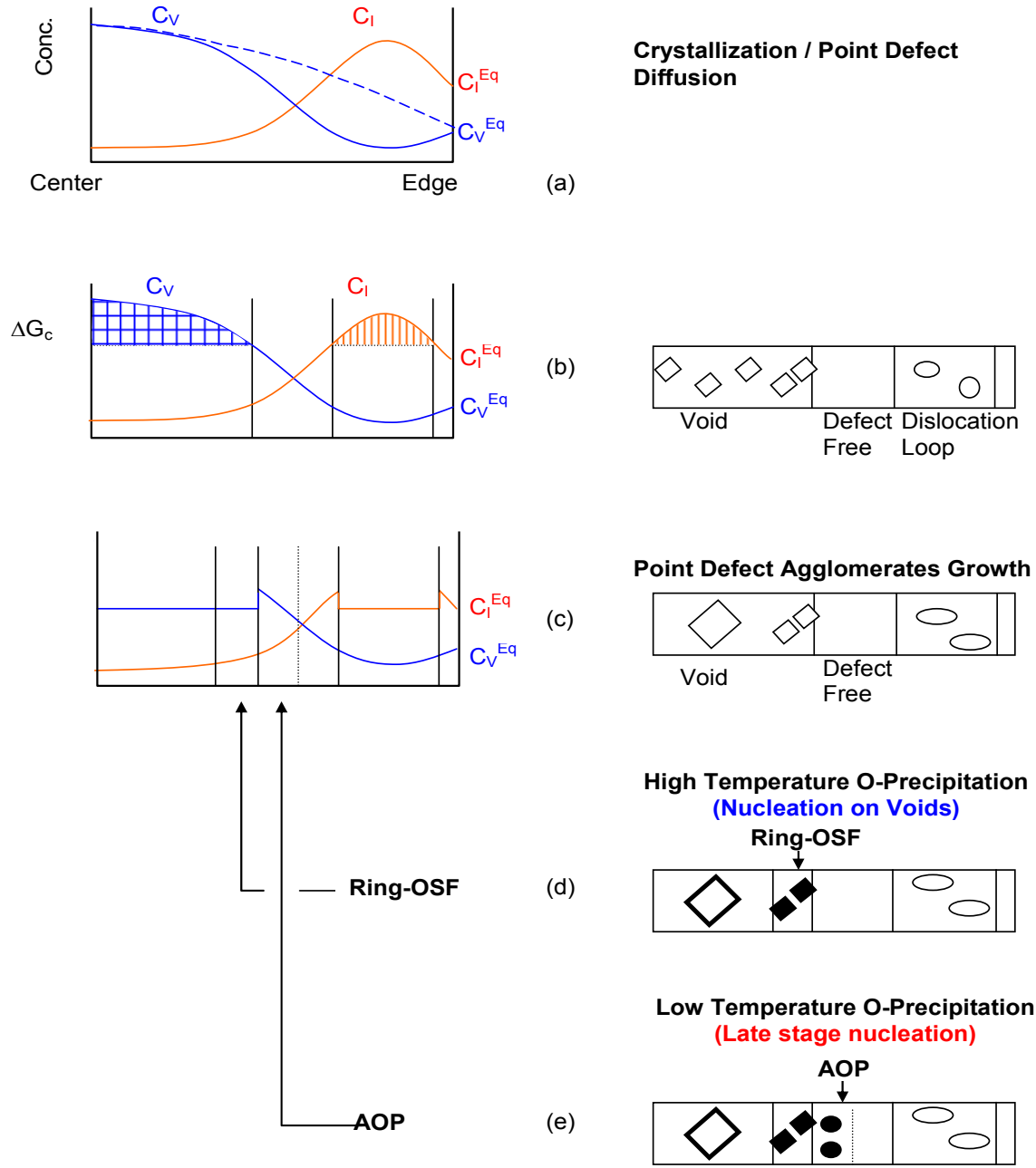


Fig. 37: A schematic sequences of ring-OSF structure formation in CZ crystals as the crystal cools from (a) to (d). Dashed curves in (a) shows the vacancy profile with out-diffusion only, and the solid line includes both out-diffusion and recombination with self-interstitials, adapted from Ref. 157.

3. Basic model for Oxygen and Vacancy Agglomeration in CZ Si

Considering the opposite stress fields of oxygen and vacancies in the Si lattice, it is highly probable that they form agglomerates during crystal cooling. Previously, the point defect

interaction with oxygen in silicon lattice has shown [27] that a vacancy supersaturation will reduce the critical nuclei radius of oxygen precipitates, thereby enhancing oxygen precipitation; whereas the self-interstitial supersaturation suppresses oxygen precipitation. Similarly, aggregation of a supersaturated concentration of vacancies will be enhanced by a local increase in oxygen concentration. Thus, a lattice stress compensating vacancy-oxygen agglomerate have been proposed, [157, 185] which is a primary defect complex, that is present at the top layers of the silicon ingot as the crystal cools. The V-O complex is a major species in N-free silicon, it acts as a precursor or nucleus for either voids or an oxygen precipitates, according to the reaction pathways shown in Fig. 38. If they trap vacancies, they act as precursor for octahedral voids (with or without internal oxidized walls) if they receive oxygen atoms an oxygen precipitate develops,.

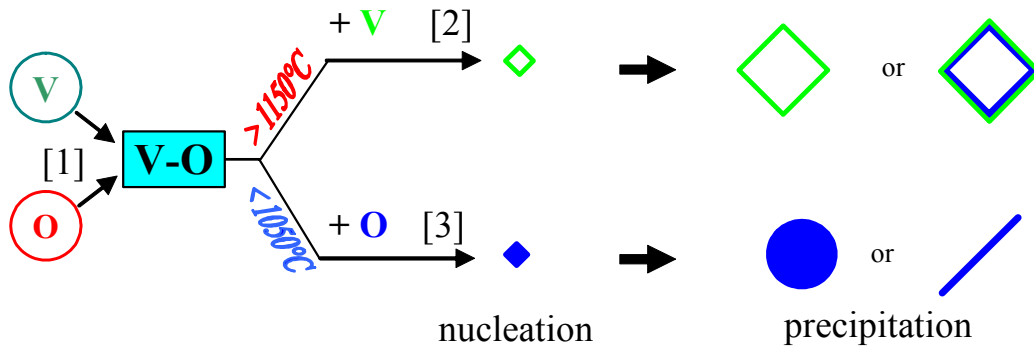


Fig. 38: Basic mechanism of extended defect formation in CZ-Si based on the model of “V-O clustering pathways” by K. Bae [157, 185].

Void formation precedes oxygen precipitation, since the vacancy is more supersaturated than interstitial oxygen and is a faster diffuser. Note that activation energy of 2.66 eV for vacancies and 1.52 eV for oxygen obtained from the slopes of solubility in the C_v^{eq} and C_o^{eq} diagrams. Figure 37 (c) illustrates how the crossover of the lateral vacancy profile with the critical temperature, T_c , dictates the extent of the inner crystal region where the initial vacancy/oxygen nuclei form and the vacancy dominant reaction in path [2], shown in Fig. 38, is operative for producing D-defects. Whereas, in the outer region, the vacancy supersaturation is low due to lateral out diffusion, thus nuclei and void can not form. As the crystal continues to cool, see Fig. 37 (d), the excess vacancies in the inner core region diffuse to the nuclei and grow into octahedral voids until equilibrium vacancy concentration is reached. After void formation, at the radius, r , a localized bump in the vacancy concentration appears due to the discrete void

formation in the inner region and continued out diffusion toward the surface. As the crystal cools further, see Fig. 37 (e), at about 1050°C, large vacancy-oxygen agglomeration occurs at the bump (within a finite annular ring) driven by the greatly reduced vacancy supersaturation, thereby providing new V-O nuclei at which oxygen precipitation occurs (according to path [3] of Fig. 38). The available heterogeneous sites for oxygen include the facet walls of large voids in the core region, and vacancy-oxygen complexes within or closer to the OSF-Ring band. Finally, the volume expansion of the precipitates provides the basis for OSF nucleation and growth defining the annular OSF-Ring. Outside the ring there are no V-O nucleation sites due to the reduced vacancy concentration, requiring oxygen precipitates to nucleate homogeneously. This requires significant supercooling at which point the diffusion barrier becomes too large. Thus, an essentially defect-free region results in the region outside the OSF-Ring.

4. Prominent complexes in CZ and N-CZ Si

4.1. Model for Defect Precursors in N-CZ Si Ingot

The endeavor of determining the chemical complex early formation stages and their distributions is the most complicated task in crystal growth. It is not possible to experimentally characterize these complexes immediately after formation. The only possible experiments are done on extended defects. In this situation, theory becomes unavoidable. Models for chemical complexes have been proposed these last two decades based on experimental observations. Stein found by IR absorption analysis that nitrogen is left in the material as pairs [189]. In addition he found that at 1100°C N-N have higher diffusivity than oxygen [190]. Diffusion experiments indicate that N-N pairs are stable at least up to 1270°C [191], in argument with first principles by Jones [192], Kageshima [151], and Sawada [194] predicted that $V N_2$ and $V_2 N_2$ stable with $V_2 N_2$ more stable (has a larger enthalpy of formation).

Von Ammon suggested that the suppression of vacancy aggregation by [195] the following reaction:



and that of interstitial by the following reaction:

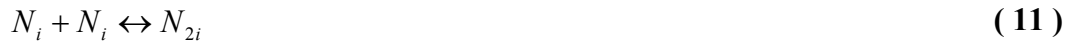


The fact that N reduces free vacancy concentration it also reduces the aggregation temperature. Ohashi [196], Nakai [3] reported a 50°C temperature decrease of the aggregation onset of both voids and precipitates in N-CZ. At a fixed [O] level void size decreases when increasing [N]. Von Ammon suggested that at low temperature VN₂ complexes can form again and the above decomposition reaction are reduced subsequent to the reduction of the point defect diffusion.

Nitrogen effects on precipitation, is reduced by a factor of ten in CZ as compared to FZ [198]. In high oxygen concentration [O]=3-8x10¹⁷ cm⁻³ he suggested that the formation of N₂ is reduced by the reaction :



The incorporation of nitrogen at M.P. mostly occurs via interstitial positions and only 10% of N can occupy interstitial sites [199, 200]. Von Ammon suggests for FZ, 7% can be incorporated as single N interstitial close to melting point. Either highly mobile nitrogen pairs form from two N_{int}



or a VN₂ complex from one single interstitial and one substitutional nitrogen atom according to the following equation:



Therefore N effect on vacancy is important from the early stages of complex formation: N tigh up vacancies. In addition the strong and likely coupling of N with O strongly reduces the vacancy aggregation in CZ crystals. The complex NO was predicted by Gali [201] and the complex N₂O was found stable up to 700°C by Wagner and confirmed by Wagner [124] and Qi [123]. At high temperature the NO is decomposed into O interstitial and nitrogen interstitial pair N₂ according to the following reaction [204]:



Interstitial nitrogen pair N₂ can not exist close to MP (because of the high [O_i] and high diffusivity of N₂) but nitrogen couples with oxygen with the following reactions:



or decompose, during diffusion, as:



At lower temperature NO is produced, but much less NO left after precipitation (below 650°C), these are detected as nitrogen related thermal donors [205]. Von Ammon proposed that NO

complexes are formed in CZ in high temperature region [204]. Indeed the NO complexes must form earlier and easier than N-V complexes, it is expected though their formation temperature ranges must overlap (they can form simultaneously but the NO formation represents a stronger component).

Model for defect formation in N-CZ material is suggested in Fig. 39 as an extension of that proposed by Bae et al [157] in agreement with other authors [184]. The modification was based on this work, which encompasses studies on chemical complex formation, thermal stability, and identification supported by experimental validations. The present extended model merges the defect formation mechanisms in N-free CZ with the strong modification forced by nitrogen doping. However, the V-O complex contribution competes with N-O. We will demonstrate in the course of the following chapters that V-O contribution is strongly reduced in some areas of an annealed wafer, whereas N-O is largely dominant, as seen from spatially resolved FTIR spectroscopy.

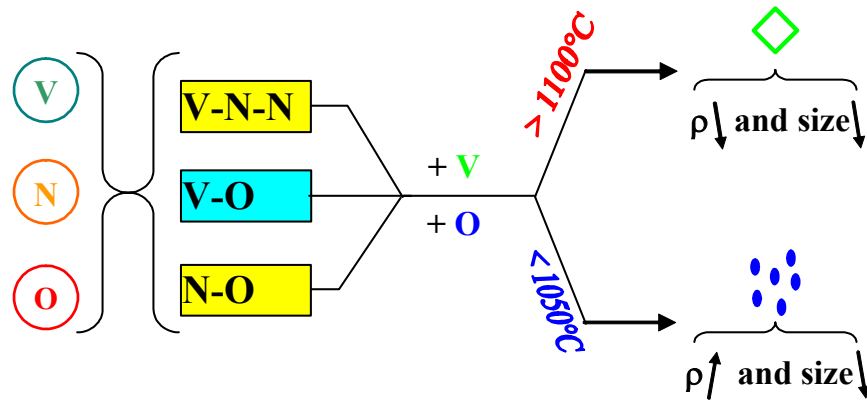


Fig. 39: Suggested multi-pathways model of clustering mechanisms in the N-CZ.

4.2. Space-Temperature Map of Defect Precursors within N-CZ Si Ingot

The characteristic temperature ranges for complex formation, the evolution of operative chemical complexes and their concentrations as well as that of point defects are mapped to the crystal ingot, as suggested in Fig. 40. How the nuclei form will depend also on (i) the point defect diffusion lengths (ii) the concentrations of stable complexes (such as V_2N_2), (iii) their chemical potential for adsorption of supersaturated species (such as O_i) which changes as the nuclei grows bigger, (iv) the nuclei size and constitution, and (v) in a later stages (e.g., wafer

heat treatments) how the chemical complexes and point defects contribute to the growth or dissolution of precipitates.

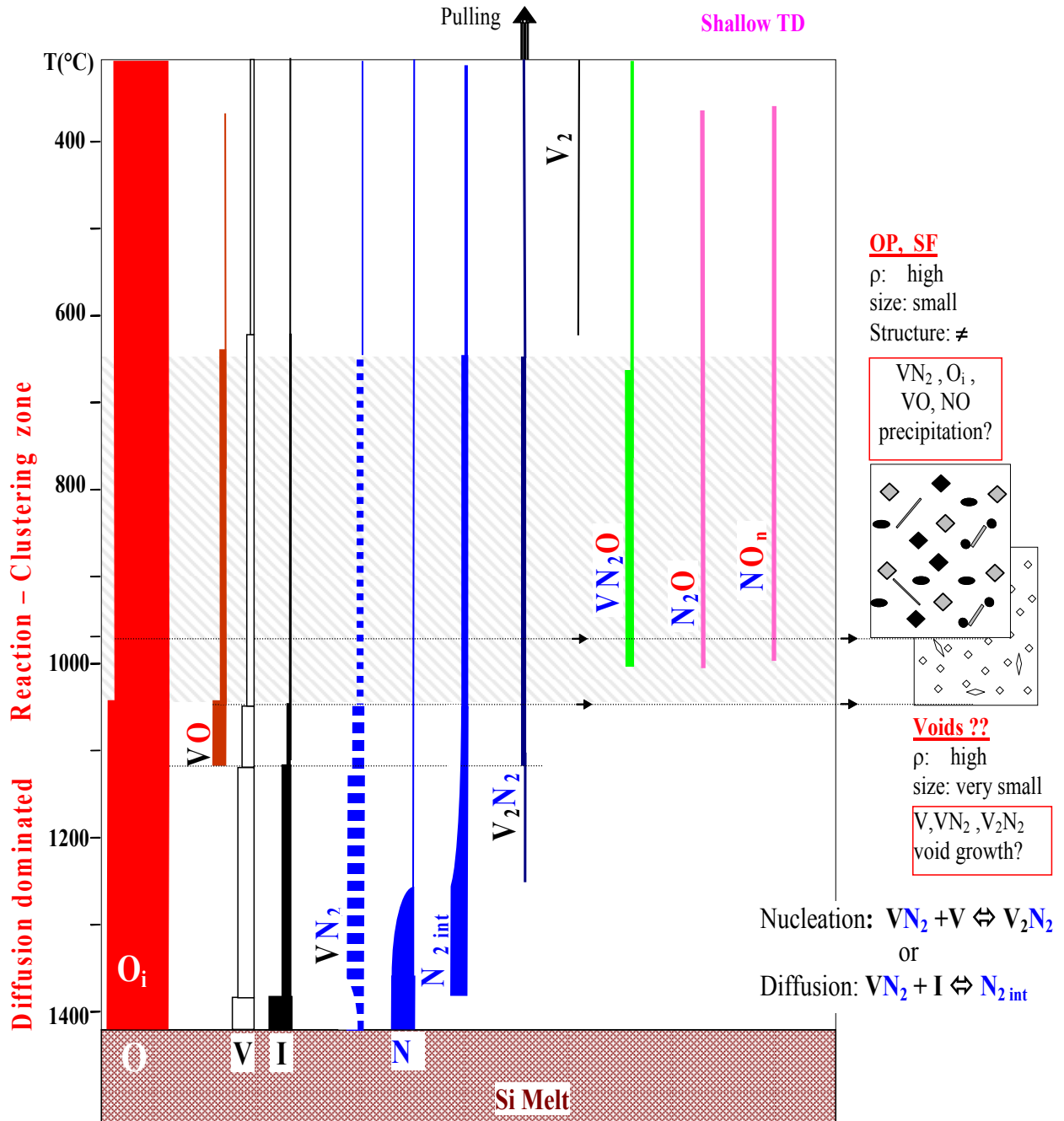


Fig. 40: Correlation of point defect and complex thermal histories during N-CZ Si crystal growth with subsequent extended defect in heat treated wafers. Hatched area represents the nucleation and growth temperature zone in the Si crystal.

In Fig. 40, the thickness of the lines mimics the species concentration, and the broken lines symbolize the complex instability character. Two important zones are represented. The first one is a reaction dominated zone, where the matrix temperature is high and point defect and some precursors are highly mobile, thus the probability of reactions is rather limited. Within the diffusion zone, the point defect supersaturation increases as the matrix cools down, they tend to retrieve their equilibrium concentration, either by complex formation, annihilation, or out-diffusion. The second zone is a diffusion-reaction limited. In this zone, previously created species (surviving) are less mobile but enough to allow clustering. Since the temperature is lowered, the effectively contributing species (to O precipitates and voids) in addition to point defects and O_i , is limited to those species with higher diffusivities, e.g. $N_{2\text{ int}}$, while less mobile VO and NO would need a two stage diffusion and fixed VN_2O , V_2N_2 act as nuclei. The two stage diffusion is ensured by an exchange of an interstitial O atom (from the matrix) with the one bounded to the complex NO (or VO). Two levels of clustering appear in Fig. 40, which are the nucleation onsets for respectively voids and precipitates. These affect the defect growth mode during wafer annealing as sketched in the right hand side of the graphic.

Abe has proposed that the introduction of N in Si from the melt occurs by forming nitride [206]. It is conceivable that nitrogen is incorporated in Si crystals as single interstitials, which turn to pairs in a temperature range of few tens of degrees. As the Si matrix cools down and the stress increases, the N pairs preferentially capture V to compensate the strain created by $N_{2\text{ int}}$ and to lower the system free energy. This is favored by their high mobility at high temperature and by the fact that injected V in the crystal become supersaturated as the crystal cools down. Therefore, N incorporation is controlled by the equilibrium concentration of VN_2 close to the melting point.

VN_2 plays the role of active chemical complexes and can be for instance converted, at lower temperature (see Fig. 40), into a stable species (V_2N_2). V_2N_2 is a candidate for stable nuclei and react favorably and other impurities. We found a potential well of ~ -2.4 eV for the O adsorption at a V_2N_2 nuclei, this will be discussed in Chapter V.

The concentration of interstitial oxygen, the dominant specie, decreases significantly in the reaction and clustering dominated zone.

In N free CZ Si, VO is likely to form around 1150-1200°C, such a complex is suggested to be responsible for the formation of precipitates and voids [157, 185, 184]. In presence of N, if

the number of V bound to O is not affected by the N doping, then the temperature of formation will remain the same as in N free Si. On the other hand, the $[O_i]$ is not sensibly influenced by N doping, thus does not affect the VO temperature of formation. Ewels found that the IR absorption signature of VO complexes disappears below 350°C, which suggest that VO is totally transformed during precipitation.

Von Ammon proposed that NO, a dominant species in N-CZ, cancels the strong reduction of defects observed in N doped FZ [195]. The N defect control variation is seen in a change of one order of magnitude in density and size. We propose, based on the complex formation sequence and the limitation of N incorporation by the V, that VN_2O and alternatively N_2O , are rather the complexes controlling the extended defect formation. It is expected that VN_2O complex forms at a range between the VN_2 temperature of formation and the diffusion-reaction limited zone (this issue is being addressed by ab-initio calculations). In addition, the two nitrogen pair species (in interstitial and in substitutional positions) compete and form N_2O and VN_2O , by reacting with a close by O_i .

Chapter V

FIRST PRINCIPLES CALCULATIONS OF V-N-O COMPLEX FORMATION, THERMAL STABILITY, AND EQUILIBRIUM CONCENTRATION 91

1. Introduction 91
2. Atomic Structure, Formation Energy and Stability of N-Pairs and N-O-V complexes at the Ground State 94
 - 2.1. Atomic Structure 94
 - 2.2. Energy of Formation of N-Related Defects 96
 - 2.3. Results and Discussion 97
3. Thermal Stability of N-Pairs and Equilibrium Concentration of VN₂: Semi-Empirical and Statistical Thermodynamics Calculations 101
 - 3.1. Introduction 101
 - 3.2. Thermal Stability 102
4. Equilibrium concentration of VN₂ defects 102
5. Trapping of Oxygen and Vacancy by N-pairs 108
 - 5.1. Introduction 108
 - 5.2. Results and Discussion 109
6. Conclusion 113

Chapter V

FIRST PRINCIPLES CALCULATIONS OF V-N-O COMPLEX FORMATION, THERMAL STABILITY, AND EQUILIBRIUM CONCENTRATION

1. Introduction

In N-doped silicon, nitrogen exists at concentration much larger than the solid solubility limit, and is likely to control the formation and dissolution mechanisms of extended defects [189, 208, 209, 210]. Fourier Transform Infrared Spectroscopy (FTIR) has been used extensively in the past years to identify and characterize the atomic structure of nitrogen-related defects in N-FZ and N-CZ Si [207, 123, 124, 208, 209]. In N-doped Silicon, 80% of nitrogen is paired [38, 215] and bonded to silicon, leaving all silicon and nitrogen fully coordinated hence, removing any associated electrical activity [207, 210, 216]. Nitrogen-pairs might exist either in interstitial positions [192] forming N_2 complex, or in substitutional sites capturing a vacancy or divacancy forming nitrogen-vacancy (N-V) complexes (VN_2 or V_2N_2) [215], that subsequently impact the nucleation of oxygen precipitates and voids [3, 218, 219, 220]. Nitrogen indeed, exists at about the same concentration than vacancy and has a diffusion coefficient five times higher than oxygen interstitial. Vacancy concentration in N-CZ Si can vary from 2.5×10^{13} to 10^{15} cm^{-3} depending on the temperature [111 219, 222, 223, 75]. Furthermore, even in N-free CZ Si, Falster and Voronkov measured V concentration of $5 \times 10^{13} \text{ cm}^{-3}$ at the wafer surface by platinum diffusion in RTP heat treated wafer in N atmosphere, while V concentration was lower when using Argon atmosphere [38]. Direct evidences of V-N complexes in annealed N-FZ and N-CZ wafers have been reported based on, platinum diffusion [225], positron annihilation of N_2^+ implanted wafers [226], and DLTS measurements [133]. Nitrogen at a concentration of 10^{15} cm^{-3} induces a downward shift in the critical V/G ratio enabling N to trap vacancies at high temperatures and form V-N complexes [223]. Furthermore, the Si vacancy and interstitial nitrogen pairs can diffuse at high temperature at a moderate pace, see Fig. 41, allowing them to react.

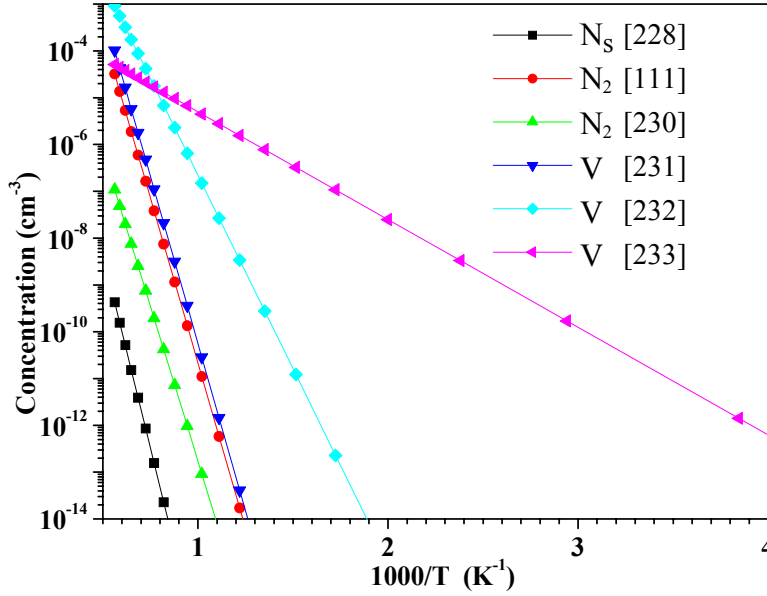


Fig. 41: Diffusivity of substitutional N [228] and N₂ interstitial [111, 230] compared to V [231, 232, 233].

In oxygen-rich silicon crystals, nitrogen interacts with oxygen forming N-O complexes [3, 212, 213, 38, 221, 234,]. The N and O coupling was attributed to the mobility of oxygen atoms around 400°C which become trapped by stable nitrogen defects. These complexes strongly control the formation and dissolution mechanisms of extended defects in N-CZ Si crystals [213, 212, 9]. The most dominant N-O defect are believed to be primary (N-N)O type of defects [3, 212, 237] but might also be (N-N)O₂ because the O₂ dimer can diffuse through Si with a lower barrier than single oxygen interstitial [238 and ref. therein]. Though, most of N-O complexes are electrically inactive in the as grown state, some of them might develop as shallow thermal donors (STDs) after annealing at 700°C [38, 239]. The STDs defects are reported to be a single nitrogen atom in interstitial position (N_i) associated to several oxygen atoms forming NO₂, NO₃, NO₄ resulting from the reaction [240, 241].



Only 20 % of nitrogen in silicon exist as N_i and quenching is required for nitrogen to be frozen as N_i [242].

The interaction between nitrogen, oxygen, and vacancies is a key issue for assessing the defect formation kinetics and to correctly measure nitrogen concentration in N-doped Si crystals. However, the mechanisms by which nitrogen affects the precipitation processes are still under

debate and direct experimental evidences are yet to be done. Little is known about the real atomic and electronic structure and thermal stability of N-related defects in silicon. Quantitative modeling of extended defects in N-CZ Si requires considering the nitrogen-vacancy-oxygen related complexes atomic structure, thermal stabilities and equilibrium concentrations. The dominance and atomic structure of V-N complexes is still under debate which is complicated by the temperature dependency. So far, nitrogen-vacancy complexes have been theoretically investigated at the ground state using first-principles calculations by few authors [243, 244] but limited data dealing with the interaction between nitrogen-pairs and oxygen atoms are available [237, 242].

In this chapter, a study of the atomic structure, energy of formation, vibrational spectra and thermal stability of dominant N-pairs, and N-O defects in silicon, using first-principles total energy calculations is presented. Results from molecular mechanics calculations on the capability of nitrogen-vacancy defects of trapping oxygen atoms and vacancies are also discussed. The equilibrium concentrations of VN_2 complexes, which is perceived as an important intermediary species, have been also studied for a range of temperatures. We use Density Functional Theory (DFT) in the Local Density Approximation (LDA) [245] for the electronic structure relaxation and vibrational spectra calculation; Semi-empirical Hartree-Fock quantum mechanical formalism for the thermal properties and equilibrium concentration. The calculations were performed on SGI Origin 2400, Cray T916 and IBM SP, using CASTEP [246], DMol³ [247] and Unichem [248] computational chemistry packages. We present the relaxed atomic structure geometry, the energy of formation for the ground state and vibrational spectra of V-N-O defects. The free energy change, enthalpy, vibrational and configurational entropy of the chemical reactions are used to predict the chemical complex thermal stability and the equilibrium concentration of VN_2 from 1650 K down to 500 K. The entropy of configuration/mixing of a defect is calculated using combinatory statistics. These results have been correlated in order to delineate the most likely atomic structures for N-related defects in N-CZ Si.

We focused our study on two sets of atomic complexes, the first set concerns N-V complexes i.e. N_2 , VN_2 and V_2N_2 (see Fig. 42); the second set results from reactions of the above V-N centers and one or two oxygen interstitials (O_i) resulting in N_2O , N_2O_2 , VN_2O , VN_2O_2 , V_2N_2O , and $V_2N_2O_2$ complexes (see Fig. 43). The potential wells or potential barriers induced by

N_2 , VN_2 or V_2N_2 complexes have been calculated for a single oxygen atom or a single vacancy approaching the defect from infinity.

2. Atomic Structure, Formation Energy and Stability of N-Pairs and N-O-V complexes at the Ground State

2.1. Atomic Structure

The geometry used to simulate the real space of the defects, either with periodic boundary supercells (crystal) or clusters, has an important impact on the minimum energy of the system. A periodic system introduces defect-defect interactions while a cluster has a surface array of dangling bonds that need to be filled with hydrogen atoms in order to remove induced energy levels from the gap. However, in this case defect-surface interactions still remain.

In order to simulate the crystal real structure and to preserve all symmetries of the diamond structure, we use periodic cubic systems for the atomic structure, consisting of supercells of 64 silicon atoms containing the defect in its center. All defects have been considered in their neutral state. To avoid defect interactions in neighboring supercells, we maintain immobile all atoms at the supercell boundaries during the relaxation of the system.

The neutral N_2 interstitial with C_{2h} symmetry, see Fig. 42 (a), is obtained by placing a N-N pair symmetrically in the center of a bond, within a $\langle 110 \rangle$ Si atomic chain, in an anti-parallel configuration, as proposed by Jones [192217]. The four Si-N bonds forming a diamond shape lying in a $\{110\}$ plane with the N-N diagonal along $[110]$. Based on Ion Channeling, IR absorption, and theoretical simulations the bond centered interstitial configuration of N pair is suggested to be energetically favorable compared to the interstitial “Humble structure” [192217]. Sawada [243] reported another stable structure made of single N in S interstitial site that is actually not dominant. As shown in see Fig. 42 (b), the neutral VN_2 complex is formed by placing a N pair in a vacancy in the center of a tetrahedron. The central bond N-N is aligned to $[001]$ and the four N-Si bonds point to the summits of the tetrahedron, and lie in two perpendicular $\{110\}$ planes. VN_2 pertains to the D_{2d} group of symmetry. The V_2N_2 complex is constructed by inserting two N atoms in two adjacent vacancy sites, see Fig. 42 (c). The divacancy was formed by removing two neighboring atoms and the bonds were reconfigured according to the defect symmetry and charge neutrality. V_2N_2 defect has the symmetry D_{3d} of the

ideal divacancy resulting in the ‘Breathing’ model [249]. During relaxation the divacancy is subject to Jahn-Teller distortion that lowers its symmetry to C_{2h} , resulting in the ‘pairing’ and ‘resonant-bond’ structures [249, 250, 251, 252].

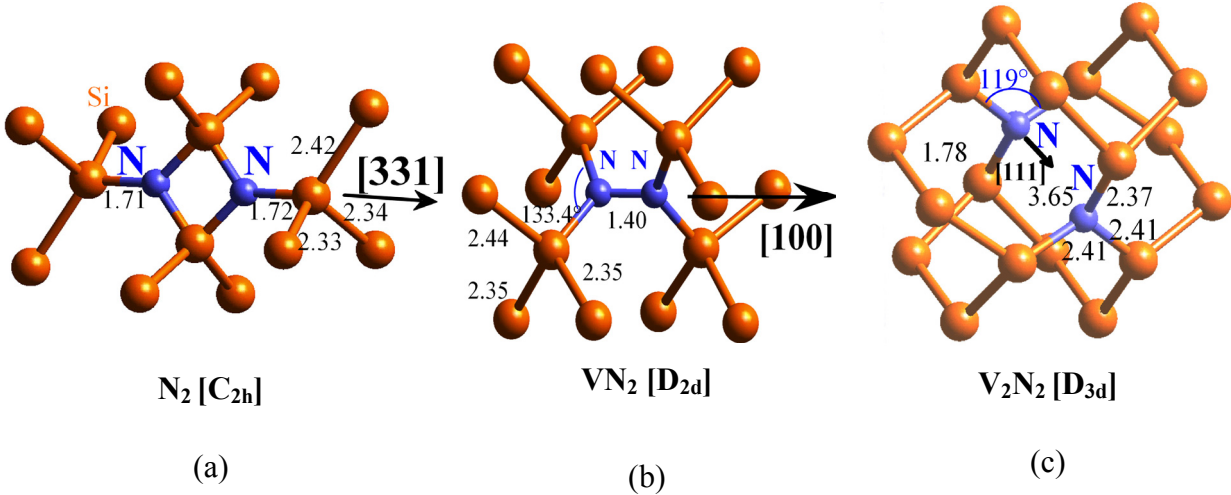


Fig. 42 : Relaxed geometries of neutral (a) N_2 , (b) VN_2 , and (c) V_2N_2 complexes in Si with DFT (LDA). Only the defect chemical complex and its immediate surroundings within a supercell are represented. Bond lengths are in Å.

The (N-N)O and (V-N)O complexes considered in this study i.e., N_2O , VN_2O and V_2N_2O , are formed by bonding an oxygen interstitial atom to the relaxed core defects (N-N) or (V-N). The oxygen atom is inserted within the most dilated Si-Si bond neighboring the N-Si bond (Fig. 43 (a), (c), and (e)). Indeed, previous investigations of interstitial oxygen in silicon showed a preference for bridging dilated Si bonds [253] along $\langle 111 \rangle$ directions resulting in the lowest energy configuration. (N-N) O_2 complexes i.e. N_2O_2 , VN_2O_2 and $V_2N_2O_2$ are built similarly by adding two bond centered oxygen interstitial atoms, one on each side of the pair as shown in Fig. 43 (b), (d), and (f). The most dilated bonds on each side of the defect are symmetric by inversion (around N-N mid-point).

The postulated defected supercells were relaxed progressively by minimizing the crystal total energy starting with the nearest-neighbors to the defect. The defected supercell was first relaxed by valence force field method using COMPASS potential [254] and then, using DFT. The ground state energy and forces were determined using Harris functional [255], an approximate scheme of the density-functional scheme of Kohn and Sham [245], and Vosko-Wilk-Nusair parameterization for the exchange-correlation terms [257].

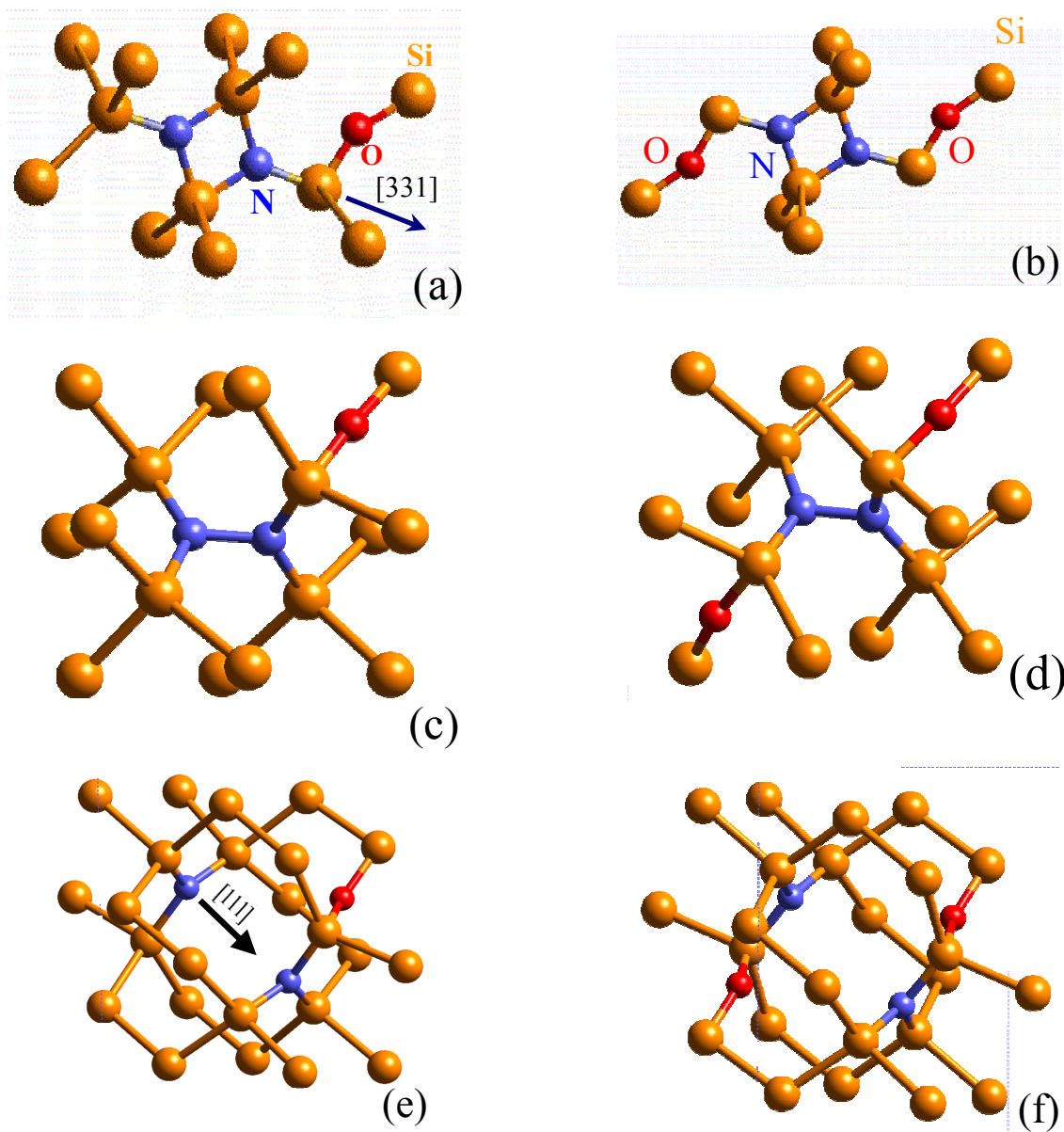


Fig. 43 : Atomic structure of the three classes of N-O complexes in (a) N_2O (b) N_2O_2 , (c) VN_2O , (d) VN_2O_2 , (e) V_2N_2O , and (f) $V_2N_2O_2$

2.2. Energy of Formation of N-Related Defects

To calculate the formation energy and study the stability, chemical reactions leading to the formation N pairs (the “core defects”), have been considered:





and the associated V-N-O complexes are produced by:



For these chemical reactions the formation energy $E_f(X_C)$ of the product X_C in the notation $X_A + X_B \rightarrow X_C$ is defined as [258]:

$$E_f(X_C) \equiv E(X_C) + E_{\text{bulk}} - E(X_A) - E(X_B) \quad (27)$$

where $E(X_i)$ is the total energy of a supercell containing either a reactant or a product, and E_{bulk} is the total energy of the same size pure silicon supercell.

In these solid-state reactions, the contribution of the surrounding matrix atoms (from the unperturbed bulk) has been removed. For instance the formation energies of the core defects are given by [258]:

$$E_f(\text{N}_2) = [E(\text{Si}_{64}\text{N}_2) + E(\text{Si}_{64})] - 2 E(\text{Si}_{64}\text{N}) \quad (28)$$

$$E_f(\text{VN}_2) = [E(\text{Si}_{63}\text{VN}_2) + E(\text{Si}_{64})] - [E(\text{Si}_{64}\text{N}_2) + E(\text{Si}_{63}\text{V})] \quad (29)$$

$$E_f(\text{V}_2\text{N}_2) = [E(\text{Si}_{62}\text{V}_2\text{N}_2) + E(\text{Si}_{64})] - [E(\text{Si}_{63}\text{VN}_2) + E(\text{Si}_{63}\text{V})] \quad (30)$$

$$E_f(\text{V}_2\text{N}_2) = [E(\text{Si}_{62}\text{V}_2\text{N}_2) + E(\text{Si}_{64})] - [E(\text{Si}_{64}\text{N}_2) + E(\text{Si}_{62}\text{V}_2)] \quad (31)$$

2.3. Results and Discussion

Quantum mechanics DFT-LDA calculations have provided detailed geometry parameters of the relaxed atomic structure as well as the energetic of the four complexes under consideration. The relaxed atomic structures of neutral N_2 , VN_2 , and V_2N_2 with their closest neighboring Si atoms are shown in Fig. 42. The calculated formation energies for the complexes considered in

this study are summarized in Table III. The calculated atomic structures as a function of bond length and bond angles are given in Table IV, Table V, and Table VI.

By examining the Si-Si bond length of the first neighboring Si atoms to the defect, one can see that N-N center strains the surrounding lattice. Indeed we observe:

- i) a dilation around N_2 of about 2.5% along the N-N axis ($\langle 331 \rangle$ oriented) and a compression of -2.5% along the perpendicular direction,
- ii) an asymmetric lattice dilation around VN_2 , for which one of the three bonds of the neighboring Si (to a N atom) is 4% longer than the two others. The bonds of the second N atom are produced with an inversion symmetry relative to those of the first N atom.
- iii) and a symmetric expansion of the lattice outward around the V_2N_2 defect.

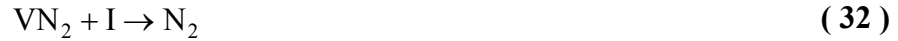
Calculated N-N bond lengths for N_2 , VN_2 , and V_2N_2 are 2.28, 1.35 and 3.65 Å, respectively. The large gap between N-N atoms in N_2 and V_2N_2 indicates that no covalent bond can exist between these atoms. The high stability of N_2 and V_2N_2 , as we will see later, is due to the strong Si-N bonds, as suggested by Kageshima et al [244]. Calculated Si-N bond lengths in N_2 , VN_2 and V_2N_2 are respectively, 1.70, 1.80, and 1.77 Å, which are much shorter than the defect-free Si-Si bond (2.35 Å). Note that these values are very close, within $\pm 3\%$. The Si-N characters are due in part to the small covalent radius of N atom (i.e., 0.75 Å versus 1.11 Å for Si) and the large electronegativity of nitrogen which pulls charges from its Si neighbors making the bond shorter and stronger.

The ground state formation energy of N_2 , VN_2 , and V_2N_2 obtained from chemical reactions in a solid matrix, given in (17), (18), (19), and (20) were found to be -4.1 eV, 2.0 eV, and -5.2 eV, or -1.0 eV, respectively (see Table III). The chemical reactions producing N_2 and V_2N_2 were found exothermic. Thus, these two complexes are formed spontaneously in contrast to VN_2 . These values show that N_2 and V_2N_2 are much more stable than VN_2 , which is in good agreement with prior work [243]. The positive value found for the formation energy of VN_2 complex in the ground state confirms its low stability. Nevertheless, the high stability of V_2N_2 when formed from reaction 3 (-5.2 eV) shows that VN_2 is an important species that participates in the formation of stable nuclei. The enthalpy change when V_2N_2 is formed from the coupling of N_2 with a divacancy is just -1 eV. The former is favored, because around temperature of defect formation (1100°C) divacancies cannot form.

Table III: Formation energy of N-pairs and V-N-O complexes as calculated by quantum mechanics DFT-LDA on 64 Si atom supercells.

	N ₂	VN ₂	V ₂ N ₂	N ₂ O	N ₂ O ₂	VN ₂ O	VN ₂ O ₂	V ₂ N ₂ O	V ₂ N ₂ O ₂
(eV)	-4.1	2.0	-5.2 (3) -1 (4)	-0.78	-1.52	0.08	0.33	-0.62	-1.31

Even though, the chemical reaction forming VN₂ is endothermic, hence requires a supply of energy, this complex is an important species around temperature of defect formation because it contributes to the formation of very stable complexes which effect the nucleation and growth of extended defects in N-CZ Si crystals. For example, VN₂ may recombine with a self-interstitial through the following reaction [222]:



forming stable N₂, or can associate with a vacancy through reaction



to form stable and immobile V₂N₂ complexes. The calculated formation energy for VN₂ of 2 eV is in agreement with the reported formation energy of VN complexes in Si [259]. The required energy to form VN₂ can be supplied near melting point to produce non-negligible amount of these species. As we will see in the next paragraph, statistical thermodynamics calculations [236] showed indeed, that the equilibrium concentration of VN₂ is maximum near melting point and at high nitrogen concentration ($\sim 10^{16} \text{ cm}^{-3}$) about 75% of vacancies are trapped by nitrogen. The calculated formation energies for N₂ and V₂N₂ are in agreement with reported values [243, 244].

The N-N bond length in VN₂ is about 1.40 Å. Nitrogen has the tendency to form strong bonds with silicon because of the small covalent radius of N atom compared to Si (0.75 Å versus 1.11 Å) and the large electronegativity of nitrogen which pulls charges from its Si neighbors making the bond shorter and stronger. Thus, the large spatial gap between the two N atoms in N₂ and V₂N₂ forbids N-N covalent bonding (see Table IV). Calculated Si-N bond lengths vary between 1.65°Å and 1.80°Å, much shorter than the defect-free Si-Si bond (2.35 Å). A tensile strain of N₂, VN₂ and V₂N₂ surrounding bonds appear after relaxation. The first neighboring Si-Si bonds are dilated to about 3% relatively to the Si-Si bond length in a perfect crystal (2.35 Å). The bond dilation and the tensile stress favor oxygen trapping. This is especially verified for

V_2N_2 which is stable and immobile, and has the 18 Si-Si first neighboring bonds (i.e., six three-fold symmetric bonds) under tensile stress.

Table IV: Geometry parameters of relaxed V-N core defects by DFT-LDA calculations on 64 atom supercells.

	N-N (Å)	Si-Si (Å) (1 st neighbor)	Si-N (Å)	∠ Si-N-Si	∠ N-Si -N	∠ Si-N-N
N_2	2.28	2.33, 2.34, 2.42	1.67, 1.70, 1.72	97.9	83.1	-
VN_2	1.40	2.35, 2.35, 2.44	1.79	133.2	-	113.4
V_2N_2	3.65	2.37, 2.41, 2.41	1.77	118.5	-	96.1

Nitrogen-oxygen complexes have been observed in as-grown and annealed CZ-Si wafers as well as in nitrogen/oxygen implanted FZ-Si [207, 215, 210]; their concentration is maximum around 600°C and they annealed out at 1000°C [3]. In the relaxed structures of N-V-O complexes (Table V), oxygen is forced in a position off the bond centered site, forming an Si-O-Si angle that varies from 137.3° to 174.6°, which is in the range of measured and calculated angles for oxygen interstitial [253, 260]. The extent of the Si-O-Si angle depends on the N-N center composition. This angle indeed, is more acute for N_2 and V_2N_2 core than for VN_2 and can be used as a fingerprint for the core defect. To accommodate the O atoms the Si-O bonds expand increasing Si-Si equilibrium distance up to 3.2 Å; this is in agreement with the reported 36 % Si-Si bond dilation [261]. The Si-O bond close to the N atom(s) is about 2% shorter than the other Si-O bond due to the high electronegativity of both nitrogen and oxygen.

The chemical reactions forming N_2O_n and $V_2N_2O_n$ ($n=1, 2$) are exothermic hence energetically favorable. The heat of formation in Table III shows that N_2O_2 and $V_2N_2O_2$ can form spontaneously, and so do N_2O and V_2N_2O to a lesser extent. In contrary, reactions (7) and (8) that produce VN_2O and VN_2O_2 are slightly endothermic, thus not energetically favorable. While our ab-initio calculations showed the ability of VN_2 to react spontaneously with a vacancy to form the very stable V_2N_2 complexes; it seems to not react with oxygen.

The formation energies of N_2O and V_2N_2O (−0.78 eV and −0.62 eV respectively) are not largely negative so they can dissociate easily. This agrees with the formation and the dissociation reversible behaviors observed by Qi and Wagner [3, 212] between (N-N)O and N-N defects, upon successive heating and cooling. When accumulating more oxygen these complexes

become more stable, -1.52 eV for N_2O_2 and -1.33 eV for $V_2N_2O_2$, and might act as nucleation center for oxygen precipitation.

Table V: Geometry parameters of relaxed N-V-O defects by DFT-LDA calculations.

	N-N (Å)	Si-N (Å)	Si-O (Å)	\angle Si-O-Si
N_2O	2.25	Diamond shape: 1.68, 1.66, 1.69, 1.71 1.66 (nearest to O atom), 1.70	1.61 (N), 1.64	137.3
VN_2O	1.40	1.75 (nearest to O), 1.79, 1.78, 1.79	1.58 (N), 1.59	174.6
V_2N_2O	3.81	1.71 (nearest to O), 1.74, 1.80	1.60 (N), 1.64	144.4

Table VI: Geometry parameters of relaxed N-V- O_2 defects by DFT-LDA calculations.

	N-N (Å)	Si-N (Å)	Si-O (Å)	\angle Si-O-Si
N_2O_2	2.22	Diamond shape: 1.68, 1.68, 1.68, 1.68, 1.65	1.61 (N), 1.63	137.9
VN_2O_2	1.41	1.74 (O), 1.80	1.58 (O), 1.60	162
$V_2N_2O_2$	3.90	1.72 (O), 1.74, 1.80	1.60 (N), 1.62	144.1

3. Thermal Stability of N-Pairs and Equilibrium Concentration of VN_2 : Semi-Empirical and Statistical Thermodynamic Calculations

3.1. Introduction

The existence of VN_2 complexes is crucial for the formation of more stable N-V complexes like V_2N_2 which are believed to impact the extended defects formation in N-CZ and N-FZ Si wafers [236, 262]. In addition to the study of thermal stability of VN_2 , and V_2N_2 , the equilibrium concentration of N pairs in substitutional positions (VN_2) is investigated. Although unstable, the VN_2 defect in Si is foreseen as an active complex at high temperature, which contributes to the formation of more stable complexes like V_2N_2 and N_2 as shown in reactions (32) and (33). The activity of VN_2 is caused by its atomic structure and the strength of the Si-N bond coexisting with the weak single N-N bond. When compared to N_2 , the latter has four identical symmetric strong Si-N bonds attached to two other Si-N bonds.

The temperature dependent complexes stability and formation/dissociation thermodynamics was approached using a semi-empirical quantum mechanical method, the modified neglect of diatomic overlap-parametric method (MNDO) [263] in the restricted Hartree-Fock approximation implemented within UniChem package [264]. A hydrogen

terminated large Si crystalline-macro-molecule (CMM), which encompasses the Si crystal symmetry, was used to properly simulate the silicon crystal. The CMM, which was cut from a larger supercell relaxed with DFT, is formed of 75 Si atoms, terminated with 76 H atoms, and imbeds the defect in its center. The defected CMM was then relaxed using the self-consistent Austin Model Hamiltonian (AM1) [263]. The thermodynamic quantities of the CMMs with and without the defects were calculated from the rigid-rotor harmonic oscillator approximation and evaluated via the partition function. The energy terms have been corrected by adding the zero point energy value, which corresponds to the minimum energy value of the system in the harmonic oscillator approximation. The enthalpy change, vibrational entropy and Gibbs free energy of the reactions were determined relative to their standard values given by MNDO at 298K.

3.2. Thermal Stability

As shown in Fig. 44, reactions 2, 3, and 4 appear to lower the system free-energy ($\Delta G < 0$), reaction 4 being dominant over the entire temperature range. Reaction 2 that produces VN_2 is the least stable, leading to a smaller free-energy change ($-0.5 < \Delta G < -1$ eV) than reactions 3 and 4, which produce V_2N_2 . The neutral divacancy (reaction 4) significantly lower the free-energy to ~ -7.4 eV whereas V_2N_2 produced from reaction 3 gave a free energy change between -5 and -4 eV close to the ground state results. It should be noted that the occurrence of reaction 3 during crystal growth is statistically low as indicated by the shaded area in Fig. 44, since divacancy cannot form above 600K [265]. Therefore, reaction 3 prevails while the crystal cools down. Nevertheless, based on DLTS and ESR measurements, Abe suggested recently [266] that divacancies coupled with N-pairs might exist in annealed wafers at a concentration as high as $3.5 \times 10^{15} \text{ cm}^{-3}$. In this case, one may expect that upon wafer heating both reactions 3 and 4 are responsible for producing the reported high concentration of V pairs/agglomerates coupled with N-pairs.

4. Equilibrium concentration of VN_2 defects

Quantum mechanics calculations showed that reaction (18) is endothermic at the ground state, hence some energy is needed to produce VN_2 . Semi-empirical calculations showed that at high temperature, the reaction is slightly exothermic. Therefore, we have investigated VN_2 defect

equilibrium concentration using statistical thermodynamics and assuming no interaction with other dopant impurities.

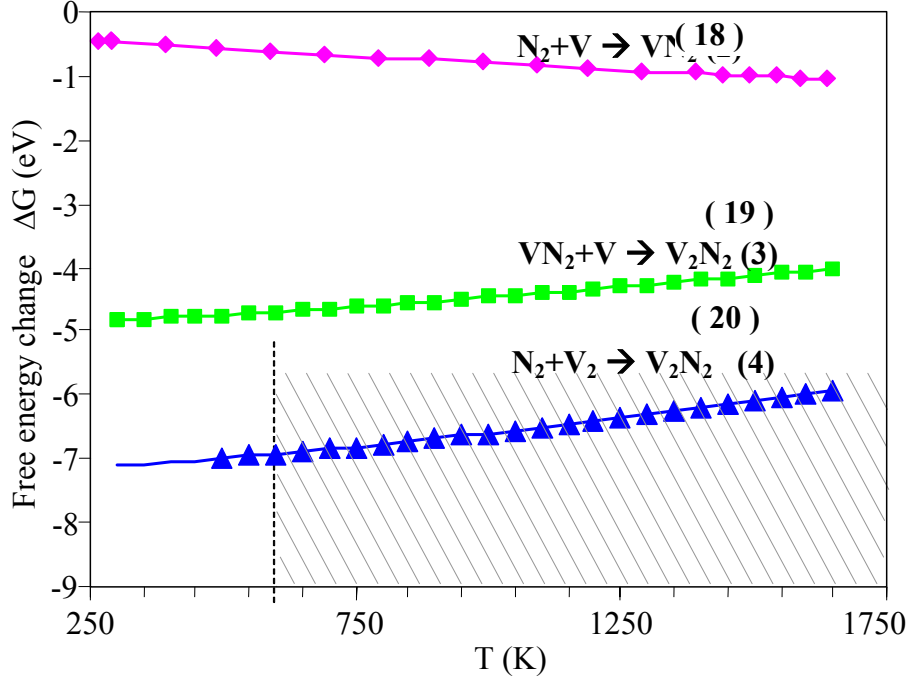


Fig. 44: Calculated Gibbs free-energy change versus temperature of chemical reactions described by equations (18), (19), (20) leading to N-V complexes in N-CZ Si (by MNDO-AM1 using standards at 298 K).

Over a wide range of temperature, starting from near the melting point, N atoms are paired and bonded to silicon [207] sitting in interstitial split positions forming N_2 [192]. In this configuration, they can be converted in VN_2 complexes via reaction (18). The system free energy change (per unit volume) subsequent to this reaction is then written as:

$$\Delta G = n_s E_f^{VN_2} - T n_s \Delta S_{vib}^{VN_2} - T \Delta S_{conf}^{VN_2} \quad (34)$$

where n_s , $E_f^{VN_2}$, $\Delta S_{vib}^{VN_2}$, and $\Delta S_{conf}^{VN_2}$ are the number of VN_2 complexes formed per unit volume, VN_2 formation energy, vibrational, and configuration entropies, respectively. The formation energy of VN_2 in the ground state as well as the thermal entropy change $\Delta S_{vib}^{VN_2}$ is obtained from DFT and MNDO-AM1 calculations. The vibrational entropy $\Delta S_{vib}^{VN_2}$ reflects the changes in vibrational spectrum as a result of the introduction of the defect. The configuration entropy

$\Delta S_{\text{conf}}^{\text{VN}_2}$ is calculated by combinatory statistics i.e. by enumerating the number of ways in which n_s interstitial nitrogen pairs can be arranged on n_v vacancy sites. For this, we considered N_2 located on bond centered interstitial sites; their number being $n_i = 2n_L$ for the diamond structure, where n_L is the number of silicon lattice sites per unit volume. The equilibrium concentration of VN_2 is obtained by minimizing the system free energy given in equation (19) with respect to n_s :

$$\left. \frac{\partial(\Delta S_{\text{conf}}^{\text{VN}_2})}{\partial n_s} \right|_{n_s=n_{\text{eq}}} - \left(\frac{E_f^{\text{VN}_2}}{T} - \Delta S_{\text{vib}}^{\text{VN}_2} \right) = 0 \quad (35)$$

The configuration entropy is calculated in terms of the concentration of the species involved in reaction R1 in the initial and final thermodynamics states [267]. For the initial thermodynamic state, Ω_i is the number of possible arrangements of n_{N_2} interstitial nitrogen pairs in n_i interstitial sites and n_v vacancies in n_L lattice sites, given by:

$$\Omega_i = C_{n_i}^{n_{\text{N}_2}} C_{n_L}^{n_v} \quad n_{\text{N}_2} \ll n_i, n_v \ll n_L \quad (36)$$

where $C_n^p = \frac{n!}{p!(n-p)!}$ is the number of combinations. For the final thermodynamic state, Ω_f is the number of ways to place n_s substitutional nitrogen pairs via chemical reaction given by equation (18).

$$\Omega_f = C_{n_{\text{N}_2}}^{n_s} C_{n_i}^{n_{\text{N}_2}} C_{n_v}^{n_s} C_{n_L}^{n_v} \quad (37)$$

The first two terms are the number of ways to select n_s pairs from n_{N_2} nitrogen pairs; these pairs can be configured in $C_{n_i}^{n_{\text{N}_2}}$ arrangements. The last two terms correspond to the number of ways of arranging the n_s pairs on n_v vacancies sites (having $C_{n_L}^{n_v}$ possible arrangements). The configuration entropy change involved in the reaction is then:

$$\begin{aligned} \Delta S_{\text{conf}}^{\text{VN}_2} &= k_B \ln\left(\frac{\Omega_f}{\Omega_i}\right) \quad (38) \\ &= k_b \log\left(\frac{n_{\text{N}_2}!}{n_s!(n_{\text{N}_2} - n_s)!} \cdot \frac{n_v!}{n_s!(n_v - n_s)!}\right) \end{aligned}$$

For large numbers one can approximate the derivative of $\Delta S_{\text{conf}}^{\text{VN}_2}$ with respect to n_s using Stirling's approximation . The equilibrium concentration of VN_2 becomes then:

$$n_s = [(n_{\text{N}_2} - n_s)(n_{\text{V}} - n_s)]^{1/2} \exp\left(\frac{\Delta S_{\text{vib}}^{\text{VN}_2}}{2k_b}\right) \left(\frac{-\Delta E_f^{\text{VN}_2}}{2k_b T}\right) \quad (39)$$

and for the case where $n_s \ll n_{\text{N}_2}, n_{\text{V}}$ we can write :

$$n_s = (n_{\text{N}_2} n_{\text{V}})^{1/2} \exp\left(\frac{\Delta S_{\text{vib}}^{\text{VN}_2}}{2k_b}\right) \left(\frac{-\Delta E_f^{\text{VN}_2}}{2k_b T}\right) \quad (40)$$

This equation is similar to the Frenkel pair equilibrium concentration expression [268]. We solved the general equation (18) for n_s as a function of temperature, and nitrogen and vacancy concentrations. The results are reported in Fig. 45 to Fig. 48.

A vibrational entropy of $5.2 k_b$ for VN_2 , was obtained using the local harmonic approximation which is higher than the $3.9 k_b$ calculated for a vacancy [269]. The anharmonic effect should normally be taken into account at high temperature where the defect induces phonon softening. We solved equation (18) for several values of $[\text{N}_2]$ and $[\text{V}]$. The results are presented in Fig. 45, which shows the calculated VN_2 equilibrium concentration versus temperature. As can be seen, the VN_2 equilibrium concentration depends strongly on the temperature, and increases when N_2 and vacancy concentrations increase. The equilibrium concentration reaches its maximum at temperatures close to the melting point then decreases abruptly during crystal cooling. Fig. 46 shows that not all V are trapped by nitrogen. At very low nitrogen concentration ($\sim 5 \times 10^{13} \text{ cm}^{-3}$), only about 10% of vacancy concentration is converted into VN_2 , while at high nitrogen concentration ($\sim 10^{16} \text{ cm}^{-3}$) about 75% of vacancies are trapped by nitrogen. This may explain the observed small size and high density of COPs in N-CZ Si [79], which is further supported by the small potential well for vacancy adsorption by V_2N_2 , as will be discussed later. The calculated equilibrium concentration for VN_2 is about $3.7 \times 10^{12} \text{ cm}^{-3}$ at 1000°C assuming a vacancy and nitrogen concentrations of $5 \times 10^{13} \text{ cm}^{-3}$ and 10^{15} cm^{-3} , respectively.

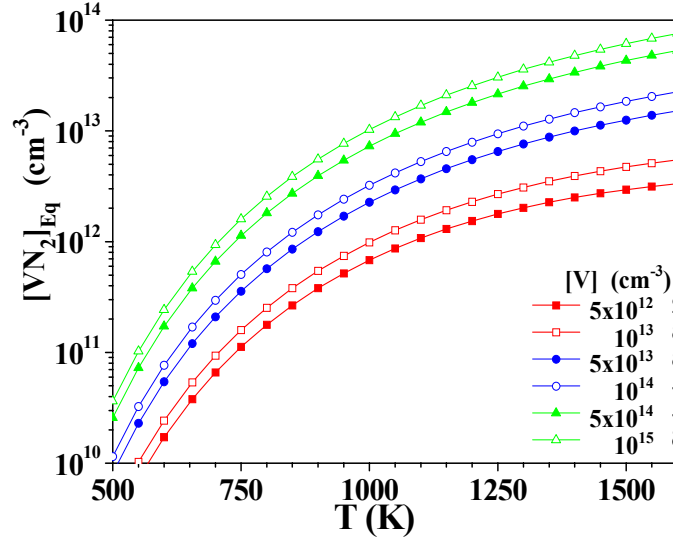


Fig. 45: Equilibrium concentration of VN_2 as a function of $[\text{V}]$ for $[\text{N}_2] = 1 \times 10^{15} \text{ cm}^{-3}$.

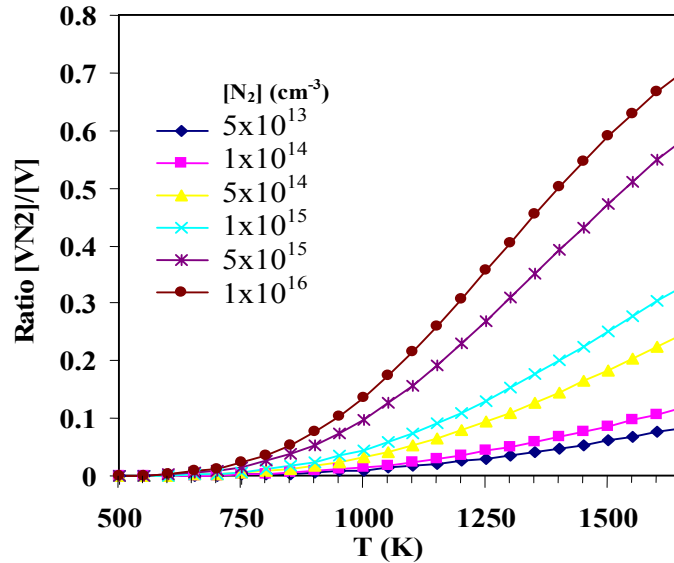


Fig. 46: Ratio of $[\text{VN}_2]$ over $[\text{V}]$ versus nitrogen pair concentration $[\text{N}_2]$.

Deviations from the calculated energy of formation of VN_2 show (see Fig. 47) that the higher the formation energy, the smaller the equilibrium concentration of VN_2 . An energy of formation lower than 1.5 eV would lead to the consumption of all vacancies by the formation of VN_2 defects, even at temperature as low as 750°C (nucleation temperature used during internal gettering process) thus, impeding the formation of V_2N_2 . This is in disagreement with the suggested nucleation by V-N complexes [111219, 220, 222, 262] of grown-in defects detected in N-CZ Si. Therefore, an energy of formation around 2 eV is a reasonable value, which is in agreement with the reported formation energy of VN complexes in Si [226, 259].

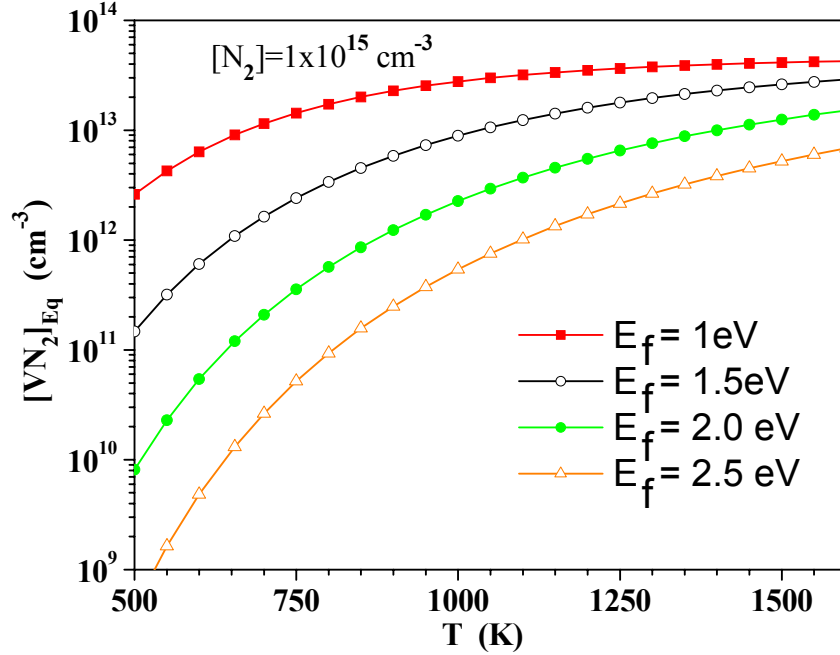


Fig. 47: Equilibrium concentration of VN_2 as a function of temperature when the formation energy of VN_2 deviates slightly from the calculated value of 2eV; $[\text{N}_2] = 1 \times 10^{15} \text{ cm}^{-3}$, $[\text{V}] = 5 \times 10^{13} \text{ cm}^{-3}$.

Figure 48 shows VN_2 formation temperature versus vacancy concentration (i.e., $[\text{V}]$) for several levels of VN_2 concentrations (i.e., $[\text{VN}_2]$), assuming a nitrogen concentration of $1 \times 10^{15} \text{ cm}^{-3}$. Experimentally measured [75] or suggested vacancy concentrations [222, 223] are reported on the graph. The hatched band shows the admitted grown-in defect formation temperatures in N-CZ Si crystals [272] ranging from 1100°C down to 900°C . The dashed box is the suggested zone of $[\text{V}]$ in equilibrium with $[\text{VN}_2]$, just prior to the onset of defect aggregation. It appears that high $[\text{V}]$ reduces the temperature of VN_2 formation via reaction (R1). Near the melting point, the VN_2 concentration will be higher than 10^{13} cm^{-3} for the reported vacancy concentration of 10^{15} cm^{-3} at that temperature [222, 223]. Based on the vacancy concentration reported in [222, 223, 75], it appears that before the onset of defect nucleation and growth, the concentration of the precursor VN_2 , hence V_2N_2 , would vary from 5×10^{11} to $5 \times 10^{12} \text{ cm}^{-3}$ (see the (a), (b), and (c) curve segments in Fig. 48). This range is compatible with the defect density of $10^{10} - 5 \times 10^{10} \text{ cm}^{-3}$ measured by OPP [236], and infrared laser scattering tomography [221]. Note, that this concentration includes only the detectable precipitates; we expect therefore, a much higher concentration of precipitates and hence higher concentration of V_2N_2 complexes.

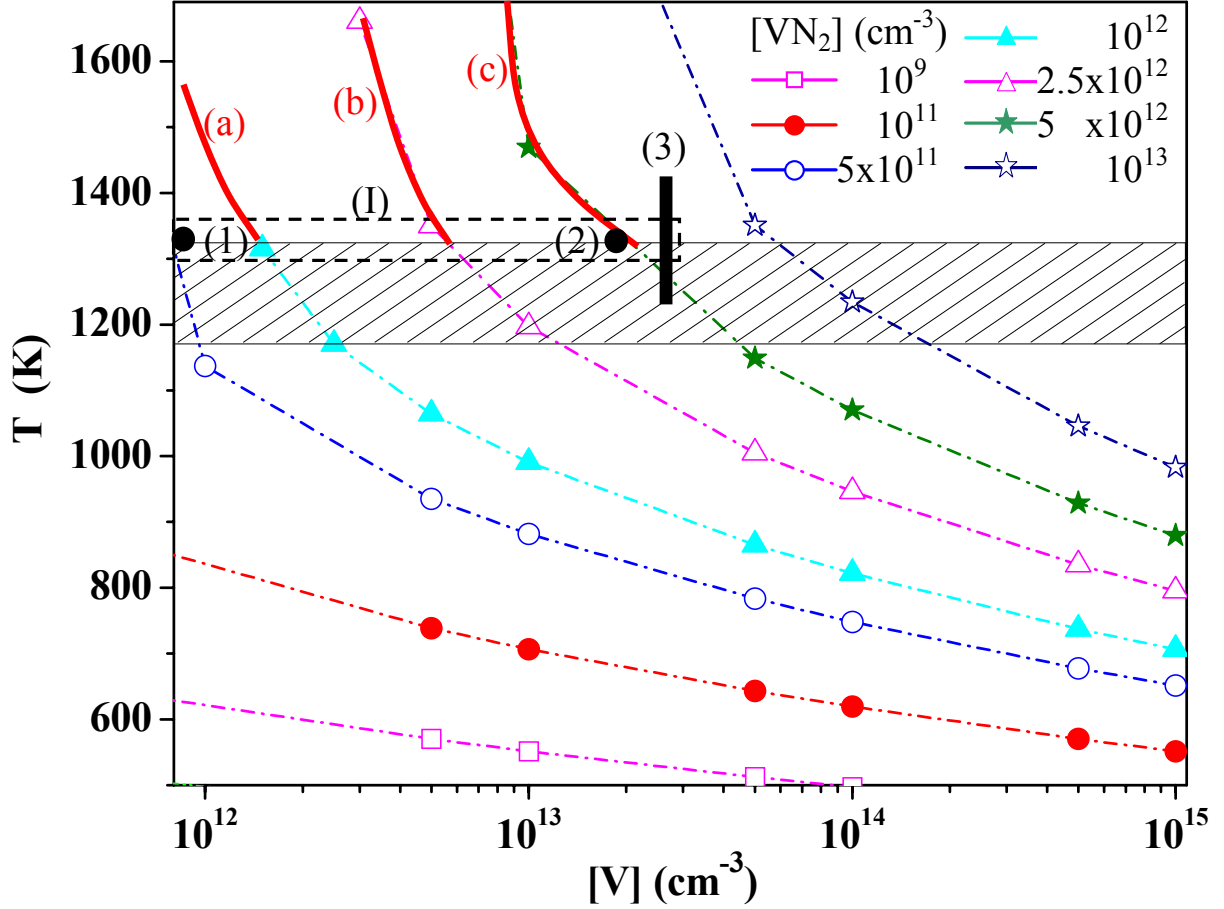


Fig. 48: VN₂ defect temperature of formation versus [V] for several levels of VN₂ concentration, [N₂] = 10¹⁵ cm⁻³. Dashed curves are computed based on the calculated $E_f^{VN_2} = 2 \text{ eV}$ and $\Delta S_{vib}^{VN_2}$ as a function of temperature.

- Hatched area: temperature range of extended defect nucleation and growth.
- (1), (2), and (3): [V] as predicted in [75, 222, 223].
- (I) dashed box: suggested zone of [V] in equilibrium with [VN₂] just prior to the onset of the precipitation.
- (a), (b), and (c): Expected concentrations of the precursor VN₂ before the onset of defect nucleation and growth.

5. Trapping of Oxygen and Vacancy by N-pairs

5.1. Introduction

In this section the ability of N₂, VN₂ and V₂N₂ to act as trapping centers for oxygen and Si vacancy is investigated. The interaction potential energy during the diffusion of an O atom and a vacancy from infinity to the vicinity of the defect is obtained. For this purpose, several

classical mechanics valence force field calculations have been performed using COMPASS potential [254]. A large Si crystalline supercell of about 4096 Si atoms was built with the defect (N_2 , VN_2 , V_2N_2) in its center and an oxygen atom or a vacancy 25 Å away. The diffusion path was chosen along a [110] lattice site chain, see Fig. 49. The point defect, O atom or V, was moved in [110] direction from a bond centered interstitial site (O atom) or a lattice site (V) to the next towards the defect. Note that the symmetric zigzag about the dashed line is due to the nature of the $\langle 110 \rangle$ atomic chain along which the diffusion occurs. At each step, the system is relaxed by minimizing its energy. The potential well is then calculated from the total energy change of the defected crystal during the diffusion of O atom or V. Two schemes of neutral V bond reconstruction were used for these calculations, which yield either reconstructed bonds perpendicular to [001] or perpendicular to [110]. Both gave the same interaction energy, in that no classical effect is seen, including when the V gets close to the highly strained surroundings of the core defect.

5.2. Results and Discussion

Interstitial nitrogen pair (i.e., N_2) appears a strong trap for oxygen with a potential well reaching ~ -2.8 eV when O sits on the Si-Si bond next to the N-pair, see Fig. 50 (a). As shown in Fig. 50 (b), N_2 seems unable to firmly trap vacancies since the potential well is only about -0.1 eV. This is in line with the instability of VN_2 complex established previously by DFT calculations. The repulsive interaction energy limits V- N_2 bonding. Therefore, N_2 appears not favorable for void growth while a good candidate for oxygen precipitate nucleation center.

On the contrary, VN_2 complexes repel oxygen atoms (Fig. 51 (a)); the potential energy reaches its maximum (+0.8 eV) when O atom approaches the core defect (i.e. O_i sits on the Si-Si bond next to VN_2). In fact, that position of O_i corresponds to that of oxygen in VN_2O . Therefore, the potential barrier of 0.8 eV for O adsorption by VN_2 is in agreement with the instability character of VN_2O and VN_2O_2 obtained at ground state by DFT and at high temperature by semi-empirical methods (see below). For the vacancy there is a very small potential of about -0.15 eV when the vacancy is located on the second neighboring lattice site to VN_2 , but when the vacancy sits close to VN_2 (lattice site next to N) the potential well jumps to -7.3 eV (Fig. 51 (b)), inferring that V and VN_2 can reconstruct easily into very stable V_2N_2 defect.

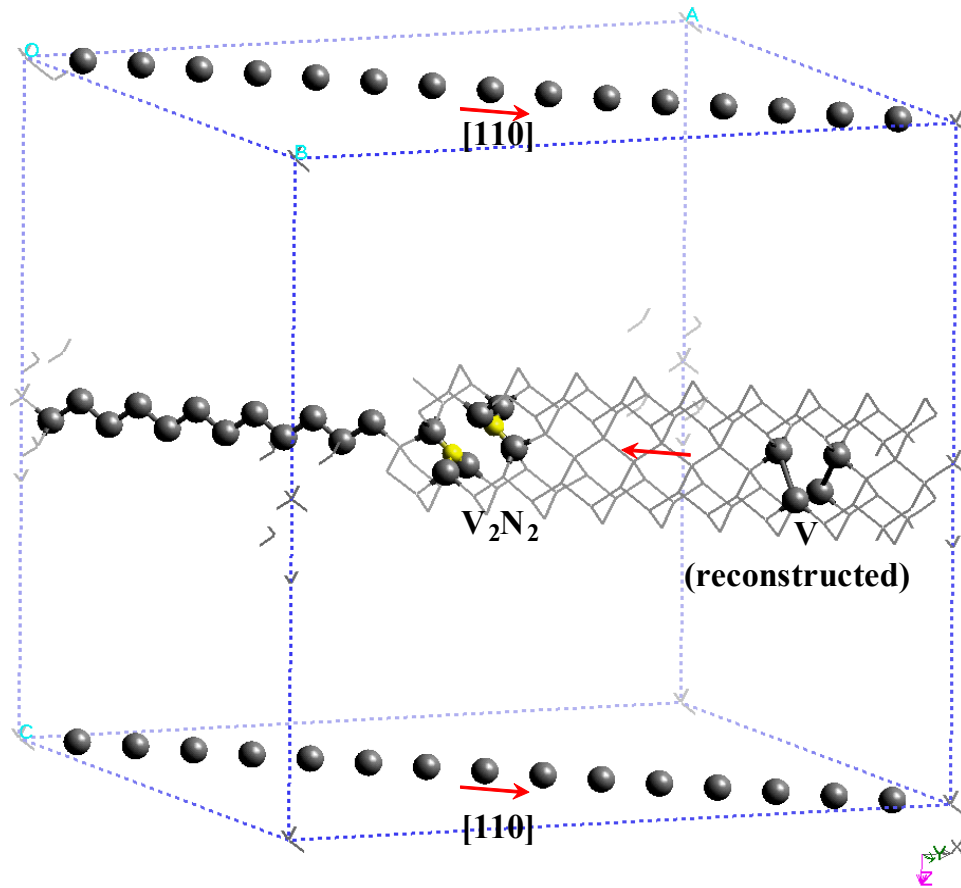


Fig. 49: Supercell used for the calculation of the potential well for vacancy adsorption by V_2N_2 defect. In this figure, most of the silicon atoms were removed to improve the visibility of the defects. The V (on the right) is moved along $[110]$ direction.

The interaction potential energies of V_2N_2 and a V or an O atom are shown in Fig. 52 (a), and Fig. 52 (b). When the oxygen interstitial atom is in the position for forming V_2N_2O (i.e. on the Si-Si bond next to the defect), the potential energy of the system decreases resulting in an adsorption well of -2.4 eV. The most favorable and stable O position is found at 5.9 Å from the defect center. When the O atom is located on the Si-N bond the energy of the system increases up to +0.4 eV, because of the shortness of the Si-N bond showing that O_i favor dilated Si-Si bonds. The potential well full width is about 9 Å; if one neglects additional strain effects induced by accumulated oxygen, the V_2N_2 complex surrounded by trapped interstitial O atoms may result in a nucleus of roughly 2 nm in diameter. Figure Fig. 52 (b) shows the variation of the potential energy during V migration towards V_2N_2 defect. In this case, a potential well of about -0.3 eV was found for the location of V at the second neighbor lattice site to the V_2N_2 defect. In contrary

to VN_2 , the energy change increases to -3.1 eV when the vacancy is localized on the first neighboring lattice site, i.e. directly connected to the N-N center. The significant difference (about one order of magnitude) between the potential well depth for V and that for O interstitial indicates that the V_2N_2 attracts preferentially oxygen. Although we found that V_2N_2 form by coupling a V with VN_2 during crystal cooling, further coupling with vacancies was found unlikely [243]. This supports the reduction of D-defects and the high density and stable grown-in oxygen precipitates found in N-CZ Si.

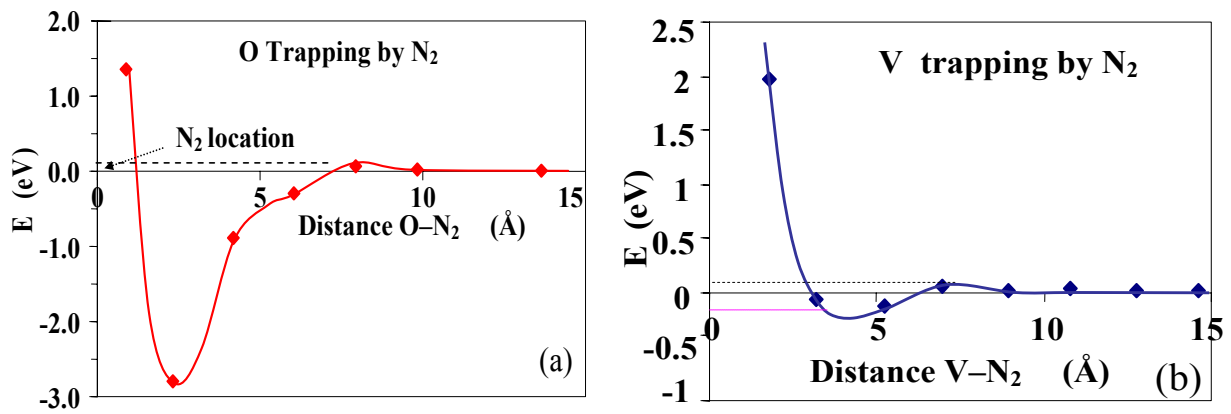


Fig. 50: Variation of the interaction potential energy of (a) O and (b) V and N_2 , as a function of the separation distance point defect-complex (i.e., V or O atom - N_2 center) which is along $[110]$. Note the small adsorption barrier for both O and V trapping by N_2 .

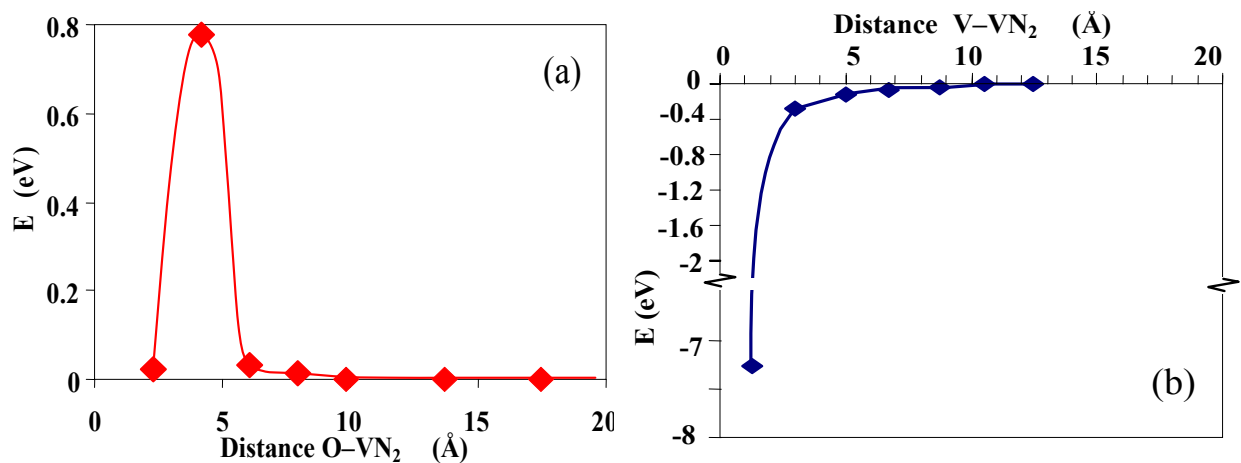


Fig. 51: Variation of the potential energy during (a) O and (b) V migration towards a VN_2 defect. Note that there is no potential well for V adsorption by VN_2 but a possible conversion of the latter to V_2N_2 .

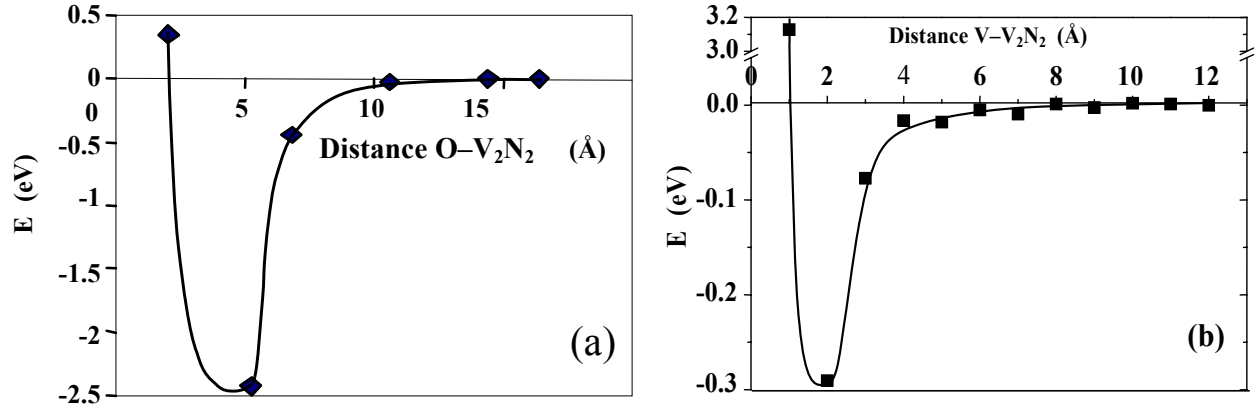


Fig. 52: Variation of the potential energy during (a) O and (b) V migration towards a V_2N_2 defect.

We propose that N_2 , and V_2N_2 chemical behavior can explain the significant change in the kinetic of extended defect formation in N-CZ Si as compared to N-free CZ-Si. We found that they are most stable nucleus, and strongly attract O atoms but not vacancies. These results corroborate indeed the formation of oxygen precipitates at the expense of voids in N-CZ Si, as well as the observed delay in void formation during crystal growth. Grown-in defects in N-CZ Si were identified to be small oxygen precipitates with a high content of nitrogen [275]. SIMS measurements on as grown and annealed N-CZ samples show (Chap. II and [273]) a strong correlation of N and O profiles, which provide evidences that N is totally coupled to O. These experimental facts together with our calculation results suggest that N_2O_x and $V_2N_2O_x$ are nucleation centers for oxygen precipitation. We have reported that grown-in nuclei and small precipitates do not dissolve at high temperature (i.e., during the first step of high-low-high thermal treatment, at a temperature of 1200°C) [235]; the reason is found in the behavior of the suggested complexes which do not easily loose the absorbed O atoms and have strong Si-N bonds.

Grown-in defects in N-CZ Si were identified to be oxygen precipitates with strong strain field around them [274,129]. Our calculations showed that N-related complexes strain the surrounding lattice, and this is particularly true for V_2N_2 where two of the three Si-Si bonds next to the N-N center are dilated. Therefore, the lattice strain induced by V_2N_2 suggests that oxygen precipitation occurs in N-CZ Si by cooperative growth of O precipitates rather than Oswald ripening mechanism, as observed in heat-treated N free CZ Si wafers [276, 277]. The suggested growth regime supports further the formation of small size and high density of oxygen

precipitates observed in N-CZ Si. During nucleation nitrogen indeed, uses up an appreciable amount of vacancies. The lack of vacancies results in stressed precipitates and reduces the oxygen precipitate size. This is compensated by a homogenization of the precipitation process where small precipitates now have chance to grow leading to a higher density and smaller oxygen precipitates compared to N-free CZ Si. The small size and high density of voids may also fall under this growth mode considering that vacancies are less mobile in the presence of nitrogen as suggested by Voronkov et al. [223].

6. Conclusion

The ground state and thermal stability, and atomic structure of N-related defects in Si have been investigated using first-principles quantum mechanics calculations and statistical thermodynamics. The calculated energies of formation in the ground state show that V_2N_2 when formed from VN_2 is the most stable followed by N_2 and V_2N_2 formed from a divacancy. VN_2 appeared to be not so stable while remaining an important intermediary species for the formation of very stable V_2N_2 complexes, which subsequently dominate the nucleation of oxygen precipitates. Consequently, the reaction forming V_2N_2 from VN_2 is favored during crystal growth, whereas upon wafer heating, this reaction might coexist with the reaction involving N_2 and a divacancy. Force Field calculations on a large periodic system where an O atom or a V moved in [110] direction towards N_2 and V_2N_2 defect displays a deep potential well for oxygen. This shows the ability of N_2 and V_2N_2 to preferentially act as nucleation center for oxygen precipitation. This is further supported by the reactions forming N_2O_n and $V_2N_2O_n$ ($n = 1, 2$) for the ground state which were found exothermic. In contrast, N_2 and V_2N_2 does not act as an effective trapping center for vacancies. Calculations of the equilibrium concentration of VN_2 complex shows that for low nitrogen concentration ($\sim 5 \times 10^{13} \text{ cm}^{-3}$), only about 10% of vacancy concentration is converted into VN_2 , while at high nitrogen concentration ($\sim 10^{16} \text{ cm}^{-3}$) about 75% of vacancies are trapped by N. A three way matching has been found between (i) the concentration of VN_2 as precursor for nuclei, (ii) the reported vacancy concentration, and (iii) the measured density of oxygen precipitates. Oxygen precipitation in N-CZ Si is suggested to occur by cooperative growth rather than Oswald ripening mechanism because of the lattice strain induced by the stable and immobile V_2N_2 complexes.

Chapter VI

FIRST PRINCIPLES CALCULATIONS OF THE VIBRATIONAL SPECTRA OF V-N-O
COMPLEXES AND EXPERIMENTAL IDENTIFICATION BY SYNCHROTRON FTIR

.....	115
1. Vibrational Spectra of N-V and N-V-O Defects in Nitrogen Doped Silicon Using Density Functional Theory	115
1.1. Introduction	115
1.2. Computational Method.....	115
1.3. Vibrational Spectra of N ₂ , VN ₂ and V ₂ N ₂ Complexes.....	116
1.4. Vibrational Spectra of N ₂ O _n , VN ₂ O _n , V ₂ N ₂ O _n Complexes (n=1,2)	117
2. Identification of Chemical Complexes in Subsurface of Annealed N-CZ Silicon Wafers Using Synchrotron FTIR	120
2.1. Introduction	120
2.2. Experimental Method.....	121
3. Results and Discussions	122
3.1. Nitrogen and Oxygen Segregation in N-CZ Heat Treated Wafers	122
3.2. Nitrogen Complexes in As-Grown N-FZ.....	124
4. Conclusion.....	126

Chapter VI

FIRST PRINCIPLES CALCULATIONS OF THE VIBRATIONAL SPECTRA OF V- N-O COMPLEXES AND EXPERIMENTAL IDENTIFICATION BY SYNCHROTRON FTIR

1. Vibrational Spectra of N-V and N-V-O Defects in Nitrogen Doped Silicon Using Density Functional Theory

1.1. Introduction

The absorption bands 771 cm^{-1} and 967 cm^{-1} measured by Fourier Transform IR spectroscopy (FTIR) at $T < 15\text{ K}$ [189, 124, 208, 123] have been associated with localized modes for N-pairs and are commonly used to measure nitrogen concentration in N-FZ/N-CZ Si wafers. The FTIR absorption lines of the N-O complexes occur at 806, 815, 1000, 1021, and 1031 cm^{-1} [279, 237]. In this chapter, we present results from Density Functional Theory (DFT) calculations of N_2 , VN_2 , V_2N_2 and $\text{V}_m\text{N}_2\text{O}_n$ vibrational properties (i.e. N_2O_n , VN_2O_n , $\text{V}_2\text{N}_2\text{O}_n$, $n=1, 2$). The calculated local vibrational modes (LVM(s)) are compared to FTIR measured data.

1.2. Computational Method

Computation of the vibrational spectra relies strongly on the accuracy of the Hessian matrix that can only be reached with a ‘good’ geometry. For this purpose we used at starting geometry the above periodic crystalline systems optimized using Harris functional. The local vibrational modes (LVMs) and their activity were evaluated by the eigenvalue method implemented within Accelrys’s DFT package DMol³ on periodic supercells. A double numerical with d orbital functions basis set, termed DND basis set, was used to ensure an accurate description of the bonding environment. We use Perdew-Wang approximation for the exchange correlation terms. Eight symmetry unique \mathbf{k} -points and 24 symmetric unique tetrahedra were used to sample the Brillouin zone. The Brillouin-zone integrations over all occupied orbitals are done with the tetrahedron method and equispaced Fourier meshes similar to the ones proposed by

Monkhorst and Pack [282]. The LVMs were determined within the Harmonic Oscillator Approximation from the energetic second derivatives with respect to displacement of the atoms. All calculations have been carried out on high performance computer, Origin 2400, and IBM SP.

1.3. Vibrational Spectra of N_2 , VN_2 and V_2N_2 Complexes

As shown in Fig. 55, N_2 interstitial exhibits four vibrational modes among them two are IR active asymmetric stretching modes, 779 cm^{-1} and 986 cm^{-1} , and two Raman active (dipole-forbidden) symmetric stretching modes, 743 cm^{-1} and 1084 cm^{-1} , in agreement with reported values by Goss et al. [283]. N_2 has a C_{2h} point group symmetry, that has normal modes belonging to the elements of symmetry $\{A_g, B_g, A_u, B_u\}$, two IR and two Raman bands. The calculated vibrational modes are in agreement with such symmetry for both methods. The selection rule for absorption in the IR spectrum is that the vibration must have the same symmetry as a p -orbital. A_u has the same symmetry as a p_z orbital while B_u has the same symmetry as the orbital p_x and p_y thus, are IR active. A_g and B_g vibrations are Raman active with the same symmetry as s - and d -orbitals. If we choose z as the principal axis of symmetry, 779 cm^{-1} belongs to B_u symmetry while 986 cm^{-1} line to A_u symmetry. In both modes the two N atoms are dynamically coupled and move as a whole against the Si lattice along $[\bar{1}10]$ and $[110]$ directions respectively, see Fig. 53 (a) and (b). The high vibration frequency can be explained as a strengthening of the six Si-N bonds and a weak N-N interaction.

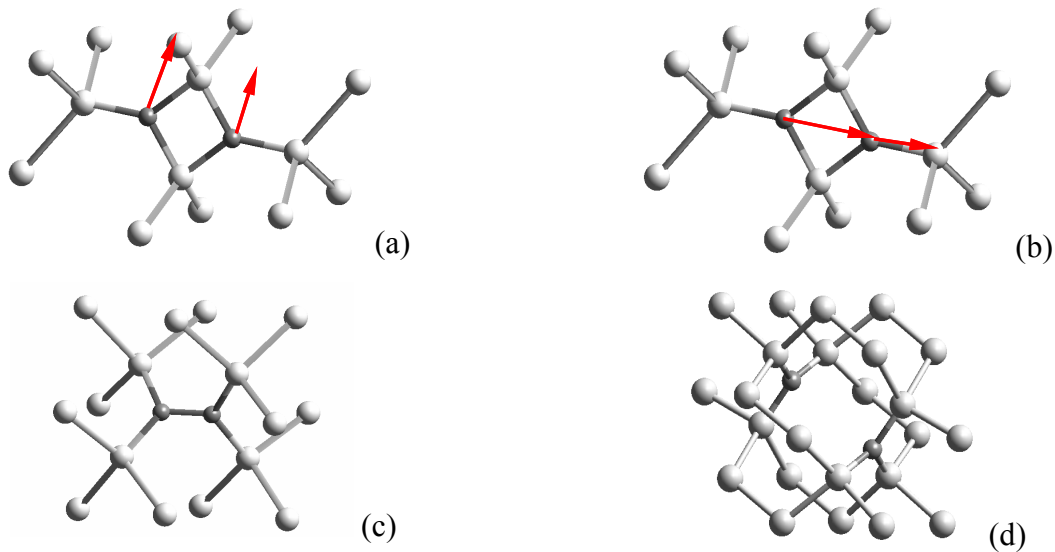


Fig. 53. (a) and (b) N_2 complex and its IR active frequencies (779 cm^{-1} and 986 cm^{-1}); (c) VN_2 defect ; (d) V_2N_2 defect.

Two IR active frequencies have been calculated for VN_2 (atomic structure of the defect cluster is shown in Fig. 53 (c), the cluster was cut from a supercell for visibility purpose), 585 cm^{-1} and 781 cm^{-1} , the latter being within 1% to the observed 771 cm^{-1} frequency. The 585 cm^{-1} frequency involves an in-phase asymmetric stretching of the two N atoms against the Si atoms while 781 cm^{-1} is doubly degenerate with the N atoms dynamically decoupled. After relaxation, VN_2 has a D_{2d} symmetry, which has normal modes belonging to the irreducible representation $\{A_1, A_2, B_1, B_2, E\}$. B_2 and E are IR and Raman active with E contribution doubly degenerate. The calculated LVMS agree with such representation. The 585 cm^{-1} and 781 cm^{-1} bands belong respectively to B_2 and E element of symmetry. The calculated 997 cm^{-1} frequency is Raman active, and involves a symmetric stretching of the N atoms. The calculated frequencies for VN_2 as well as their spectroscopy activity are in agreement with reported values for $\text{N}_i\text{-N}_s$ complex [283].

Two, doubly degenerate LVMS have been found for V_2N_2 , 621 cm^{-1} and 638 cm^{-1} . Each frequency corresponds to an asymmetric and a symmetric in phase vibrations of the N atoms. The point of symmetry of V_2N_2 is D_{3d} which has two Raman-active modes ($A_{1g} + E_g$) and two IR active modes ($A_{2u} + E_u$), E_u and E_g being doubly degenerate. The calculated modes are different of what is expected by the D_{3d} symmetry. During relaxation, divacancies are usually subject to Jahn-Teller distortion that lowers its symmetry to C_{2h} , resulting in the ‘pairing’ and ‘resonant-bond’ structures [249284, 285, 286, 287]. In a same way, the special point-group symmetry of V_2N_2 decreases from D_{3d} to C_{3v} leading to two doubly degenerate E orbitals, each one infrared and Raman active. Cunha et al. [288] found that substitutional N_2^+ (charged state) relaxed in C_{3v} while Goss et al. [283] found that a starting C_{3v} geometry relaxed in D_{3d} structure.

1.4. Vibrational Spectra of N_2O_n , VN_2O_n , $\text{V}_2\text{N}_2\text{O}_n$ Complexes ($n=1,2$)

Calculated vibrational spectra for N_2O display four IR active LVMS, 665 , 814 , 1003 , and 1029 cm^{-1} , as shown in Table VII. These frequencies shift to 658 , 825 , 945 and 1019 cm^{-1} for N_2O_2 . The 779 cm^{-1} frequency (N_2) is shifted to the blue by 35 and 46 cm^{-1} for N_2O and N_2O_2 respectively, because of O_i atoms in the vicinity which change the reduced mass. The 814 cm^{-1} (N_2O) and 825 cm^{-1} (N_2O_2) frequencies correspond to an N-N asymmetric stretching in $[1\bar{1}0]$ direction, with the highest strength on the N close to O in the case of N_2O . These frequencies were matched to the FTIR 806 cm^{-1} and 815 cm^{-1} absorption bands [279]. N_2O , 1003 cm^{-1}

frequency matches very well measured 1000 cm^{-1} and involves principally an in phase N-N asymmetric stretching along $[110]$ analog to the 986 cm^{-1} line for N_2 , a blue shift of 43 cm^{-1} . This normal mode shifts to 945 cm^{-1} for N_2O_2 defect. The 1029 cm^{-1} (N_2O) and 1019 cm^{-1} (N_2O_2) are predominantly ν_3 type Si-O stretch (Fig. 2). This is in agreement with FTIR experiment carried on FZ-Si implemented with mixed N and O isotopes [289]. Therefore, measured 1021 cm^{-1} and 1031 cm^{-1} frequencies are the FTIR signature for N_2O_2 and N_2O respectively. The two dipole forbidden transitions, shown in Table VII, found for N_2 are now allowed for N_2O but very weak due to reduced symmetry and unbalanced mass center. These transitions remain IR inactive for N_2O_2 . N_2O has one Si-O-Si ν_2 bending mode at 665 cm^{-1} , which split into two modes, 658 cm^{-1} , and 665 cm^{-1} for N_2O_2 . The 658 cm^{-1} line corresponds to an in phase asymmetric bending mode of both O atoms and the 665 cm^{-1} line involves a symmetric bending of the two O atoms hence is Raman active. The NNO defect has been previously theoretically investigated [237] using AIMPRO method on H-terminated clusters. Their calculated frequencies deviate significantly from our result concerning the vibration modes. The O mode was found between the two N modes in contrary to the observation. The authors had to displace the Si atom close to O in order to meet the experiment.

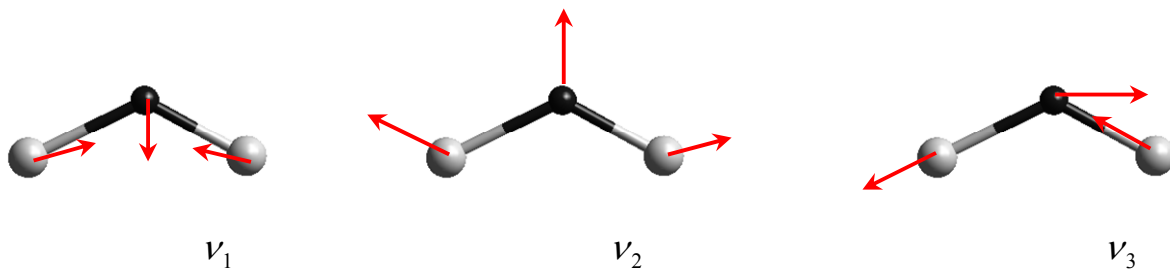


Fig. 54: ν_1 (symmetric stretching, 1203 cm^{-1}), ν_2 (symmetric bending, 517 cm^{-1}), ν_3 (asymmetric stretching, 1136 cm^{-1}) normal modes of Si_2O [291].

Complexes VN_2O and VN_2O_2 generate several IR active modes, see Table VII. VN_2O defect displays four IR active modes. One of them, 578 cm^{-1} involves an N-N stretching in the $[110]$ identical to the 585 cm^{-1} mode for VN_2 . This mode shifts to 567 cm^{-1} for VN_2O_2 . By adding one O atom, the degenerate frequency 781 cm^{-1} (VN_2) splits into two frequencies 797 cm^{-1} and 835 cm^{-1} . These modes shift for VN_2O_2 to 820 cm^{-1} (IR active), and to 828 cm^{-1} (Raman active) frequencies. Both modes involve respectively, asymmetric and symmetric stretching modes of nitrogen atoms and the nitrogen atoms are now dynamically coupled. The dipole forbidden

Table VII: Calculated vibrational spectra for N-pairs and N-O complexes. Infra-red and Raman active modes are labeled IR and RA, respectively.

	Symmetry	Calculated Frequency (cm ⁻¹)	Activity type		Symmetry	Calculated Frequency (cm ⁻¹)	Activity type	Measured by FTIR (cm ⁻¹)
N ₂	A _g	743	RA	VN ₂	B ₂ E A ₁	585	IR	N-N complexes 771 967 [278, 279, 281]
	B _u	779	IR			781	IR,RA	
	A _u	986	IR			997	RA	
	B _g	1084	RA					
N ₂ O		665	IR	VN ₂ O		578	IR	
		750	RA		642	IR		
		814	IR		797	IR		
		1003	IR		835	RA		
		1029	IR		985	IR		
		1137	RA		1049			
N ₂ O ₂		658	IR	VN ₂ O ₂		567	IR	N-O complexes 806 815 1000 1021 1031 [279, 237]
		780	RA		644	IR		
		825	IR		820	IR		
		945	IR		828	RA		
		1016	RA		976	RA		
		1019	IR		1103	IR		
		1027	RA		1113	RA		
V ₂ N ₂	E _u , E _g	615	IR,RA					
		627	IR, RA					
		638	IR, RA					
V ₂ N ₂ O		651	IR					
		709	IR					
		731	IR					
		819	IR					
		1068	IR					
V ₂ N ₂ O ₂		649	IR					
		729	IR, RA					
		810	IR, RA					
		1061	IR, RA					

997 cm⁻¹ shifts downward to 985 cm⁻¹ for VN₂O, and is now allowed but very weak because of the unbalanced mass center and the reduced symmetry. This mode shifts to 976 cm⁻¹ for VN₂O₂ and remains dipole forbidden in this case. New local vibration modes appear due to the oxygen atom(s). The 642 cm⁻¹ frequency (VN₂O) corresponds to ν_2 type bending mode (Fig. 2). This mode becomes doubly degenerate for VN₂O₂ and shifts to 644 cm⁻¹. The latter involves a symmetric and an asymmetric ν_2 bending of the O atoms. VN₂O exhibit a high frequency mode at 1049 cm⁻¹ involving ν_3 stretching of Si-O-Si. This mode shifts to 1103 cm⁻¹ for VN₂O₂, very

close to the oxygen interstitial 1107 cm^{-1} band. The VN_2O_2 defect has a Raman active high frequency mode at 1113 cm^{-1} involving ν_3 symmetric stretching of both Si-O-Si atoms.

The complex $\text{V}_2\text{N}_2\text{O}$ has five IR active LVMs and one Raman active, see Table VII. The degeneracy observed for V_2N_2 is removed and the LVMs shift to higher frequencies due to the effect of O atom(s), which lower the defect symmetry. Frequencies 695 and 709 cm^{-1} involve decoupled vibrations of the N atom that is away from O, while 731 and 819 cm^{-1} involve the N atom that is close to O. $\text{V}_2\text{N}_2\text{O}$ has one high frequency mode at 1069 cm^{-1} involving a ν_3 asymmetric stretching of oxygen. A ν_2 bending mode of the O atom at 651 cm^{-1} is also observed for this complex. All LVMs of $\text{V}_2\text{N}_2\text{O}_2$ remain degenerate as compared to V_2N_2 . The former exhibits four IR and Raman active modes that are 649 , 729 , 811 , and 1061 cm^{-1} . The 649 cm^{-1} frequency involves two modes; a symmetric and an asymmetric ν_2 bending mode of both O atoms while 1061 cm^{-1} frequency is due to ν_3 stretching of the O atoms. In both modes, the O atoms are dynamically coupled. The 729 and 811 cm^{-1} absorption lines are in-phase symmetric and asymmetric N-N stretching in $[111]$ and $[\bar{1}\bar{1}\bar{1}]$ direction, respectively. Calculated 811 and 819 cm^{-1} frequencies match 806 and 815 cm^{-1} measured lines. Calculated 729 cm^{-1} ($\text{V}_2\text{N}_2\text{O}_2$) and 731 cm^{-1} ($\text{V}_2\text{N}_2\text{O}$) may be assigned to the weak 739 cm^{-1} line observed in samples implanted with both N and O and presumably attributed to NNO complex. Indeed, implantation creates an excess of vacancies that can couple with nitrogen and oxygen forming V-N-O complexes. This mode anneals out above 700°C .

2. Identification of Chemical Complexes in Subsurface of Annealed N-CZ Silicon Wafers Using Synchrotron FTIR

2.1. Introduction

The large number of predicted IR absorption lines in N doped CZ silicon and the variations in experimental conditions (e.g. thermal history of the material) complicate the assignment of these lines to chemical complexes. However, high spatial resolution spectroscopic and analytical techniques, supported by quantum mechanics calculations, can be a powerful mean for analyzing complexes in special regions. The robustness of our complex identification method stems from detailed experimental data on extended defects combined with absorption line predictions by atomistic calculations. In Chapter II, we have investigated unique N and O related extended

defects in N-doped silicon by various techniques including Oxygen Precipitate Profiler (OPP)/etching, high-resolution transmission electron microscopy (HRTEM), Z-contrast imaging, as well as electron energy loss spectroscopy (EELS) and secondary ion mass spectroscopy (SIMS) simultaneous profiling to depict the mechanisms of defect formation [292, 293]. This identification approach was also used to verify the viability of the identified N-O-V species (in as-grown and annealed silicon) to their formation and stability thermodynamics. These interrelated studies on N-related complexes will benefit the continuum clustering modeling of extended defect growth in silicon [6, 40, 296].

The objective of this study is to employ synchrotron-based, High-Resolution Fourier Transform Infra-Red Spectroscopy (HR-FTIR) depth profiling to detect chemical complexes produced in the subsurface of annealed N-doped Czochralski (N-CZ) silicon wafers [297, 298, 299]. To consolidate this analysis, an N-doped Float Zone (N-FZ) Si wafer is examined along its radius, where N defects are known to vary. Detected IR optical lines are assigned to previously proposed operative chemical complexes determined from first principles calculations. Among other N-related issues, this study seeks to clarify the mechanisms causing N and O co-segregation.

2.2. Experimental Method

To perform HR-FTIR investigations, a state-of-the-art optical bench at the Advanced Light Source (ALS) of Lawrence Berkeley National Laboratory [300] was used. This comprises a Nicolet IR microscope that produces a 5 to 10 μm spot size, a liquid nitrogen-refrigerated detector and a mercury-cadmium-telluride (MCT) He-refrigerated bolometer. The IR light beam, produced by a bending magnet in the synchrotron storage ring, is highly collimated and is more than 3 orders of magnitude brighter than Globar source [301]. The high spatial resolution and accuracy of the HR-FTIR line scans are necessary to precisely map the distribution of N and O species in N-CZ subsurface defects [292] and in N induced native extended defects (the N-FZ ‘N-Skin’ [302]). Defect absorption lines are determined by subtracting a background spectrum from defect free zone of the same sample and acquired in the same conditions. The samples utilized are the one presented in chapter II.

3. Results and Discussions

3.1. Nitrogen and Oxygen Segregation in N-CZ Heat Treated Wafers

HR-FTIR data on the nature and distribution of N-O complex in N-CZ material annealed at 650°C for 8 Hrs and 1050°C for 16 Hrs (Lo-Hi anneal) are presented in this section. Based on OPP and SIMS depth profiling, we described in Chapter II, three defect regions as being controlled by the N distribution and the dynamics of vacancy exchange with the surface [303]. Typical OPP profile that clearly delineates these three regions is shown in Fig. 55(a). The first region spreads over 2 μm and is saturated with N and O. Due to thermal stresses, up to $1 \times 10^{18} \text{ cm}^{-3}$ out-diffused nitrogen and $2 \times 10^{21} \text{ cm}^{-3}$ oxygen accumulated at the subsurface, which results in an ultra shallow subsurface oxynitride layer. The latter is interesting for photovoltaic and optoelectronic devices [304, 305] but intriguing for IC technologies, because it contains a large density of small equilibrium precipitates [75293]. The second region, referred to as Low Density defect Zone (LDZ), is basically an “oxygen denuded zone” that was strongly modified by N [75293] and is left (after annealing) with a low density of very small precipitates and nuclei comparable to the N-CZ as grown defects. The third is characterized by high density of precipitates and stacking faults that are formed by a significantly different mechanism than in N free CZ Si [75293].

Figure 55 (b) shows a 2D representation of the differential reflectance spectra and Fig. 55 (c) the absorbance spectra as a function of depth. The intensity of some absorbance lines are shown in Fig. 56 (a); similar curves that are relevant to OPP profile features (in region III) are provided

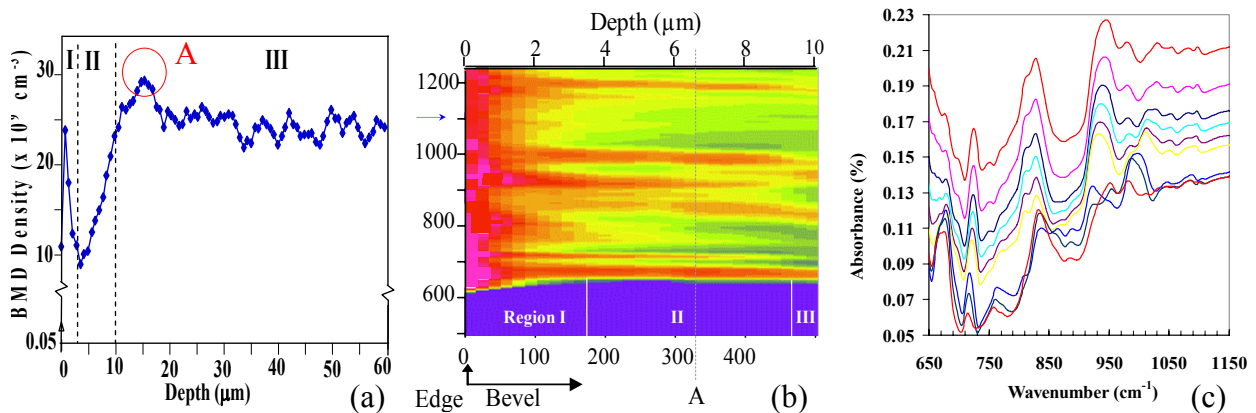


Fig. 55 : (a) Defect depth distribution by OPP in Lo-Hi cycled wafer.
(b) Differential reflectance spectra by HR-FTIR along bevel polished sample (magnification=50).
(c) Differential absorbance spectra calculated from measured reflectance.

separately in Fig. 56(b) gives an analysis of the absorption line positions in the three regions of the Lo-Hi beveled sample. These were obtained from the absorbance spectra given in Fig. 55 (c). Lines are compared between themselves (within each of the three regions) and assigned to chemical complexes in connection to previously calculated absorption [297].

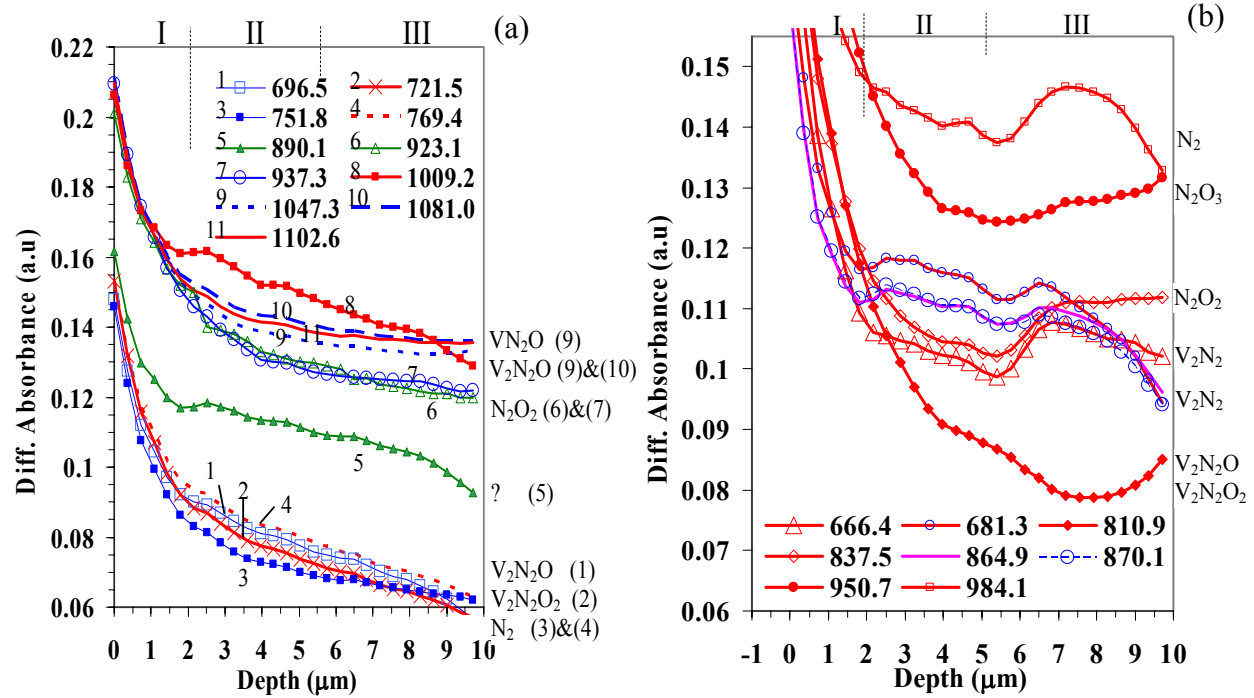


Fig. 56: Intensity of absorption lines (measured from the base) of annealed N-CZ Si wafer.

It is remarkable that in region I all lines show higher intensities and decay in the same fashion. More importantly, the decays have shape and the same depth range as the OPP defect density profile, in that region. Moreover, in all regions, one notices a correlation between the OPP profile and the shape of the 984.1, 666.4, and 837.5 cm^{-1} lines, representing the N_2 , V_2N_2 , $\text{N}_2\text{O}_2/\text{V}_2\text{N}_2\text{O}$ complexes respectively (see Table VIII), and to lesser extent 681.3 (representing the V_2N_2 complex), 864.9, 870.1, and 890.1 cm^{-1} lines. Certain peaks, however, demonstrate an anti-correlation with the OPP profile. This is especially visible on the peak at the beginning of region III, where the 810.9 ($\text{V}_2\text{N}_2\text{O}$, $\text{V}_2\text{N}_2\text{O}_2$, N_2O complexes) and 950.7 cm^{-1} (N_2 , N_2O_2) lines show an opposite behavior to the OPP depth profiles. This data indicates the close relation of the identified complexes to the extended defects (detected by OPP, see Fig. 55 (a)), as well as the interrelation between the complexes to which these IR lines belong. This represents a unique evidence of N-O species conversion into V-N, which occurs by loss of O from V-N-O complexes

(i.e., reduction of N_2O , V_2N_2O , and $V_2N_2O_2$ concentrations), which results in an increased concentration of V-N complexes (i.e., V_2N_2 and N_2). Note that the reflectance line at 1107 cm^{-1} (finger print of interstitial oxygen: O_i) varies smoothly, and increases in the subsurface towards the surface.

Table VIII: Analysis of the absorption line intensity and assignment to chemical complexes.

Line (cm^{-1})	Peak Position Variations	(I)	(II)	(III)	Proposed Chemical Complexes
666.4		VW	(-)	S	V_2N_2
681.3 (varies)	677 --> 678	W	(-)	S	V_2N_2
696.5		VW	(-)	N	V_2N_2O
721.5	716 --> 726	VS	(-)	M	$V_2N_2O_2$
751.8	No change	W	(-)	N	N_2
769.4	757 --> 768	VW	(-)	N	N_2
810.9	808 --> 814	VS	(-)	S	V_2N_2O , $V_2N_2O_2$
837.5 (2 lines)	829->839	VS	(-)	S	N_2O_2
864.9	No change	N	M	N	(-)
870.1	866-870	N	M	M	(-)
890.1	No change	N	(-)	M	
923.1	No change	N	M	M	N_2O_2
937.3	929 - 945	N	(-)	M	N_2O_2
950.7	Large & Broad Peak	VS	(-)	(-)	N_2 , N_2O_3
984.1	981 --> 986	M	(-)	S	N_2
1009.2	1005->1012	W	(-)	S	N_2O
1047.3	1047-->1055	W	(-)	W	VN_2O V_2N_2O
1081.0	No change	W	(-)	W	V_2N_2O
1102.6	1094-1100	W	(-)	W	O_i
The used acronyms are: - for regions: subsurface (I), LDZ (II), Bulk (III), - for line intensity: Null (N), Very Weak (VW), Weak (W), Medium (M), Strong (S), Very Strong (VS).					

3.2. Nitrogen Complexes in As-Grown N-FZ

We previously reported that the attempt of doping float zone silicon with high level of nitrogen using N_2 atmosphere gas during the zoning, leads to a non uniform distribution of the dopant [305]. As shown in the XRT image of a 32 mm in diameter N-FZ wafer, see Fig. 57(a), an external layer referred to as nitrogen-skin (N-Skin) is formed. In addition, there is a hallow of high density of pits (left in the central region after a long slurry polishing) that might be originated by voids in the central region, see micrograph in Fig. 57(a). Moreover, the XRT shows a series of co-centric rings (white contrast). The color coded map (see the strip

superimposed to the XRT image) shows the correlation of chemical complex IR absorption and structural defects (rings). Because of the nitrogen and oxygen saturation in the ingot rim, the stresses during the FZ Si zoning, and the cooling rate, we expect a variety of N-V species. Therefore the “N-Skin” wafer is an excellent test-bed for delineating N-V complexes with HR-FTIR.

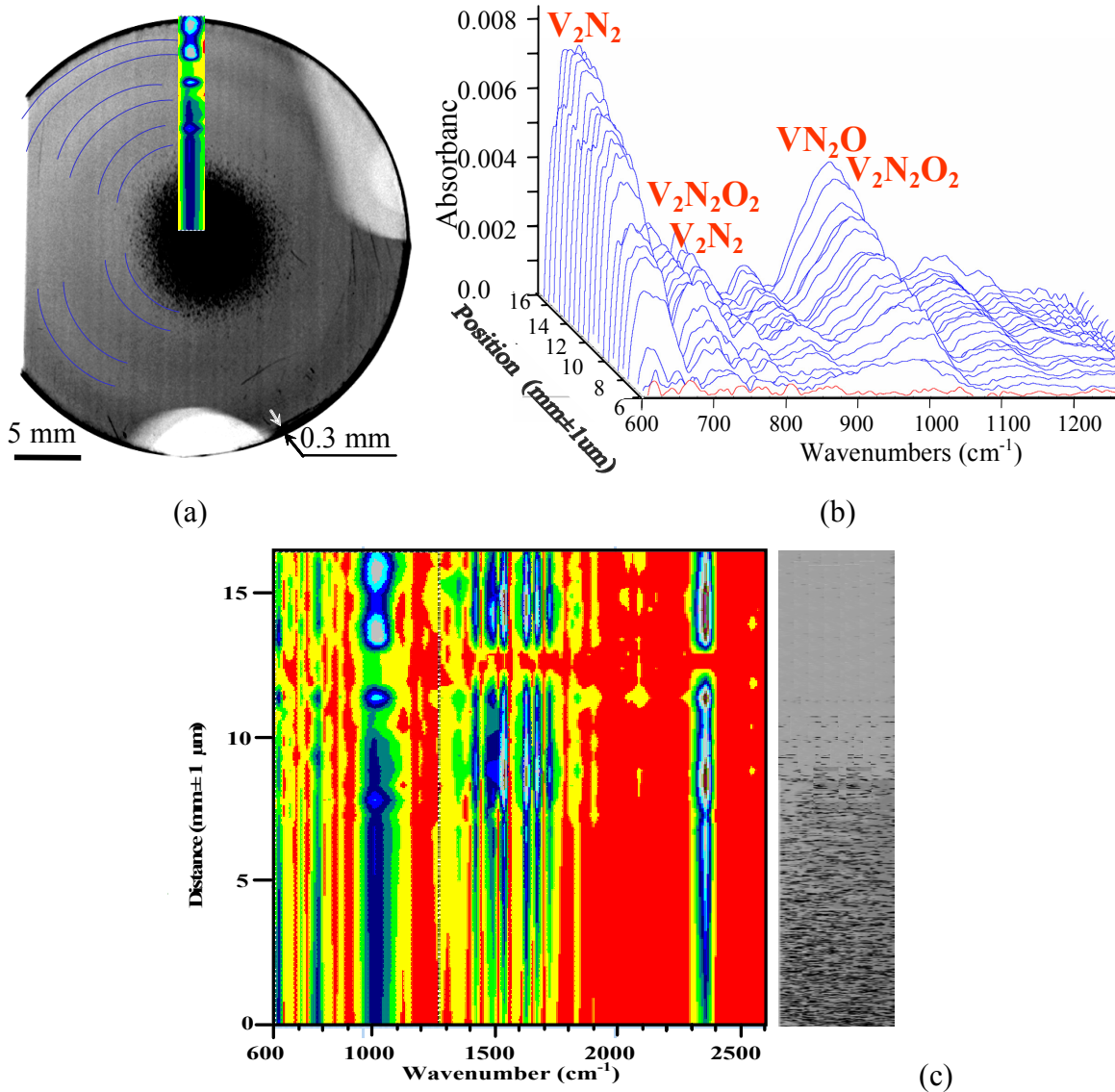


Fig. 57: (a) XRT of N-FZ wafer. Circles indicate defect rings. Color coded map shows variations of the intensity of IR absorption line (extracted from the FTIR spectra). (b) Differential absorbance spectra obtained along the radius of the same wafer, using HR-FTIR in transmission. (c) Space-wavenumber reflectance map acquired along the radius of wafer. Set of 24 micrographs taken by the video camera that is inline with the IR microscope used in the HR-FTIR system.

Figure 57 (b) shows the differential absorbance spectra acquired along the radius using a reference spectrum from the wafer center. One must first note that the O_i line (1106 cm^{-1}) is not detected. Secondly, the N related band (between 650 and 720 cm^{-1}) is the most dominant, its intensity increases as we go from the center to the wafer edge and fluctuates at the same spacing as the XRT rings of Fig. 57(a). In fact, this band is formed of four N-related lines, among which three are found in N-CZ (666.4 and 681 cm^{-1} both assigned to V_2N_2), the third is 696.5 cm^{-1} (attributed to V_2N_2O). However, line V_2N_2 must be dominant. The smaller bands appearing between 720 and 890 cm^{-1} like in NCZ, see Table VIII, are related to VNO and NO complexes. Although their intensity is limited, as expected from FZ material, to $\frac{1}{4}$ of similar ones in N-CZ, they show that N and O inevitably couple in float zone Si. This is in line with the very strong coupling of N and O found in N-CZ Si [75293]. The N and O interactions were discussed in Ref.75 293 based on O and N simultaneous profiling with HR-SIMS of the subsurface of N-CZ silicon. The stronger and broader band spreading from 920 to 1100 cm^{-1} is attributed to oxynitride phases within the silicon matrix. It denotes large variations in the concentrations of V-N species. It is remarkable that the V-N-O lines are detectable in this N-FZ wafer, and that their intensity increases as we go toward the wafer rim, where oxynitride skin is initiated. Moreover, the N appeared strong enough to drag a lot of oxygen and form oxynitride at the peripheral ring of the ingot as well as in the ring regions inside the wafer.

4. Conclusion

We have investigated, using DFT quantum mechanics calculations and large supercell, the vibrational spectra of several structures of N-pairs as well as N-O defects. Calculated local vibration modes correlate with the IR active energy levels foreseen by the symmetry of the defect. Calculated LVMs of N_2 deviate just about 1 to 3% from the observed 771 cm^{-1} and 967 cm^{-1} lines. This confirms that nitrogen atoms are paired and bonded to Si atoms. The calculated infrared spectra for N-O defects showed that low frequency N-O FTIR lines (806 , 815 cm^{-1}) are fingerprints for N_2O_n as well as $V_mN_2O_n$ ($m, n=1,2$) defects while high frequency N-O FTIR lines are solely fingerprints of N_2O_n . This suggests that both kinds of defects develop during both crystal growth and wafer annealing. When measuring N concentration in N-CZ Si, N-O FTIR lines should be taken into account.

Detailed information relevant to chemical complex generation in N doped silicon were obtained using the HR-FTIR setup at the Advanced Light Source. The differential FTIR spectra (using background spectrum from the same line scan) reveal the smallest possible lines and increases the high resolution capabilities. Using data from atomistic calculations, we have singled out the prominent FTIR lines. A variety of complexes in each of the three Lo-Hi annealed N-CZ wafer regions were identified. A strong correlation of the intensity depth profile of absorption lines with the OPP defect density were found for the three regions, in particular the subsurface region and at the LDZ-bulk interface. The surface affected the nature of these complexes by providing the necessary vacancies to form the most stable complexes at the surface and in the subsurface. In the N doped float zone we could detect the V-N species, as well as, N-O complexes.

Chapter VII:

Effect of O and N Doping on Mechanical Properties of Silicon Using Nano-Indentation

1. Introduction	129
2. Samples and Experimental Procedure	130
3. Results	133
1.1 Single Point Indentations.....	133
1.2 Indentation Arrays.....	134
1.3 Nano-scratch Tests	134
4. Discussion	137
5. Summary	143

Chapter VII

CHARACTERIZATION OF OXYGEN AND NITROGEN EFFECTS ON MECHANICAL PROPERTIES OF SILICON USING NANO-INDENTATION

1. Introduction

Float Zone (FZ) silicon offers the highest bulk lifetime and excellent electrical properties for high concentration solar cells. However, it is very fragile and needs to be strengthened. The options proposed to improve the material is based on using N doping in conjunction with O control. The objective of this chapter is to study the effects of O and N on silicon mechanical properties. This will allow understanding the hardening mechanisms and the phenomena underlying dislocation locking in N doped FZ silicon by means of point defects and N and O trapping, and stress induced phase transformation. This essential investigation is intended to help the design of FZ Si growth considering either or both N-, O- and C-doping. It is expected that these options will lead to optimal mechanical properties without hindering the benefits of FZ Si such as high lifetime, reduced precipitation,....

For undoped single crystal CZ silicon oriented [100], the hardness was measured by nano-indentation and found to be 13 GPa [306]. This value was obtained with a load of 0.2 mN with indentation depth at peak load equal to 24nm. For the same material and at a load of 15 mN with indentation depth at peak load equal to 267 nm, the same author reported a smaller value of 11.9 GPa. For P⁺ boron doped [100] oriented silicon a much lower hardness is reported, that is 5.1 GPa. This value was obtained by nano-indentation at a load of 0.2 mN with indentation depth at peak load equal to 44 nm; but with a larger load i.e., 15 mN and deeper indentation (depth at peak load is 318 nm) the hardness was found equal to 8.7 GPa [306].

For [111] oriented silicon the hardness was reported equal to 11.7 GPa; obtained by AFM nanotribology. This value is an average over an area of 500 nm x 500 nm with a 100 μ N load

[307]. Reported RMS roughness, microfriction coefficient, microscratching and microwear depths, and nano-indentation hardness data for various virgin, coated and treated silicon samples are given in Table IX [308].

Table IX: Published friction and hardness of silicon bulk and films.

Material	RMS Roughness scan 500x500 nm^2 (μm)	Coeff. of Friction	Scratch Depth Load: 40 μN (nm)	Wear Depth Load: 40 μN (nm)	Hardness at 100 μN (GPa)
Si (111)	0.11	0.03	20	27	11.7
Si (110)	0.09	0.04	20		
Si (100)	0.12	0.03	25		
Polysilicon	1.07	0.04	18		
Polysilicon (laped)	0.16	0.05	18	25	12.5
PECVD-oxide coated Si (111)	0.11	0.04	16	14	17.0
Wet-oxide coated Si (111)	0.25	0.04	17	18	14.4
C ⁺ implanted Si (111)	0.33	0.02	20	23	18.6

The elastic modulus (E) is obtained from the measured reduced modulus as indicated in the following equation:

$$\frac{1}{E_r} = \frac{1 - \nu_1^2}{E_1} + \frac{1 - \nu_2^2}{E_2} \quad (41)$$

where the subscript 1 corresponds to the indenter material and subscript 2 refers to the indented material, and ν is Poisson's ratio. For a diamond indenter tip, E_1 is 1140 GPa and ν_1 is 0.07.

To obtain the elastic modulus of the tested silicon material, published Poisson's Ratio value of 0.27 (for [111] undoped and polished silicon.[309]) was used. This value was measured by Surface Acoustic Waves [310]. A slightly higher value of 0.278 for Poisson's ratio usually used in finite element computations of both elastic and plastic regimes of ultra micro-hardness indentation of thin films, both thin films and substrates are assumed homogenous [311]. Much lower value of 0.22 was calculated assuming isotropic and linearly thermoelastic material [312].

2. Samples and Experimental Procedure

Nanoindentation tests were performed on nitrogen-doped samples i.e. N doped Float Zone (N-FZ) from NREL as well as Czochralski silicon (N-CZ) from Prof. D. Yang (*Zhejiang University, China*). The latter were heat treated with a denuded zone Lo-Hi annealing process, thus contain oxygen precipitates. The properties of these precipitates and their effect on the Si

matrix are of interest for material strengthening. Information on hardness and elastic modulus were attained from nano-indentation tests and controlled nano-scratches. Optical and *in-situ* Scanning Probe Microscopy (SPM) images were acquired and are presented for qualitative analysis.

Samples for nano-indentation were cut from the following set of wafers :

- 1) dislocated N free Float Zone Si (disl.-FZ), received from NREL
- 2) two N doped FZ Si wafers labeled N-FZ(1), and N-FZ(2) , also received from NREL. These two wafers were cut from different positions of the ingot.
- 3) N free CZ Si (labeled D1W2) and N doped CZ Si (N-CZ) (labeled D2W2) received from Prof. D. Yang (*Zhejiang University, China*). These wafers were cut from ingots grown simultaneously at the same rate in similar crystal pullers. The wafers were heat treated with two types of thermal annealing processes for DZ formation (i.e., Lo-Hi and Hi-Lo-Hi), as described in Chapter II with the same annealing parameters as for Set 1 wafers.

Samples cut from each of these wafers for the nano-indentation tests are listed in Table X. A single indent was performed on each of the samples disl.-FZ, N-FZ(1), N-FZ(2), and CZ using a peak load of 5000 μN and a Berkovich indenter tip (which has a 90° trihedral shape) as well as a series of individual indents was performed on the original surface of N-CZ sample. All indents were done using a trapezoidal load function, similar to that in Fig. 58, consisting of a 5 second loading segment, a 3 second holding segment, and a 5 second unloading segment.

In addition to single point indentations, indentation arrays were performed on the original surface and in the cross-section of N-CZ sample, from which average basic material parameters were deduced. However, it was not possible to locate precipitates using only the Triboindenter without *in-situ* coupling with another technique, such as nano-capacitance. The latter is expected to be sensitive to oxide or oxynitride precipitates embedded in the silicon matrix, via the difference in the dielectric constant. Correlation at the sub-micrometer level of the local properties of the shallow oxynitride near surface layer and the O and N depth profiles is anticipated. Even though we have used large grids with 49 indents, the mechanical properties of the Si matrix/O-precipitate system needed more clarification. Therefore, scratches were made in an attempt to intercept precipitates.

Table X: Description of the material tested by nanoindentation and load controlled nanoscratches.

Received from <i>NREL</i>			Grown at <i>Zhejiang University, China.</i>	
Pure FZ Si grown with dislocation. [O _i]= 7x10 ¹⁶ cm ⁻³ [N] < 1x10 ¹⁵ cm ⁻³ [111] As grown	N-doped FZ Si, (Ga doped). [O _i]=7x10 ¹⁶ cm ⁻³ [N]= [111] As grown	Wafer similar to N-FZ(1), cut from different positions of the ingot. [111] As grown	N-CZ Si 3" wafer [O _i]= 1.1x10 ¹⁸ cm ⁻³ [N]= 1x10 ¹⁵ cm ⁻³ [111] Hi-Lo-Hi 1250°C for 1 Hr 650°C for 8 Hr 1050°C for 16 Hr	CZ Si 3" wafer [O _i]= 1x10 ¹⁸ cm ⁻³ [111] Lo-Hi 650°C for 8 Hr 1050°C for 16 Hr
disl.-FZ	N-FZ(1)	N-FZ(2)	N-CZ (D2W2)	CZ (D1W2)

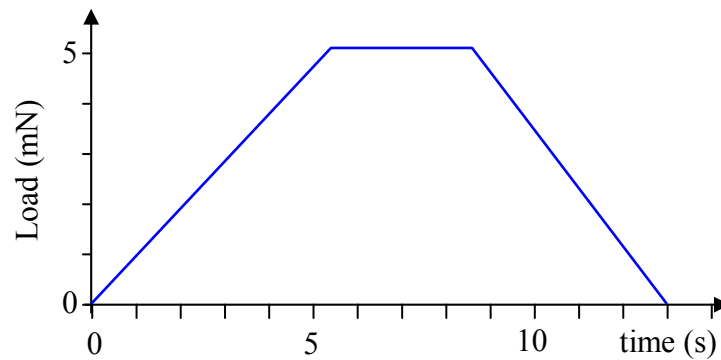


Fig. 58: Load vs. time during indentation tests used in single point and array indentations.

The tests in this work were performed using Hysitron Triboindenter¹. This apparatus is capable of performing both indentation and scratch testing with a high displacement resolution (0.8 nm in the z-direction and 50 nm lateral resolution) and a load resolution as small as 1 nN. In indentation mode, the instrument is a load-controlled displacement-sensing device. In controlled scratching mode, the indenter tip is driven into a sample and then withdrawn while controlling the applied force. The scratch tests have been made on the surface of N-CZ sample by ramping a load from 85 to 105 μ N using a 90 cube corner tip (Northstar indenter), the scratch time was programmed to be 60 seconds, since long material relaxation time is expected.

The Triboindenter can also provide *in-situ* images by operating the instrument in scanning probe microscopy mode (SPM). Images of the tested surface can be generated before and immediately after the indentation or scratch. These images with sub-micrometer resolution

¹ Hysitron Inc., Minneapolis, MN 55439

provide useful information on the test sample and surface morphology and heterogeneities (steps, voids, precipitates,...). Also roughness of the sample surfaces which influence the scratching can be visualized. Since the images are created *in-situ* (i.e., scanned with the same tip as the indenter tip) the combination of the imaging and indenting/scratching capability facilitates tip positioning and helps investigating particular features.

3. Results

3.1. Single Point Indentations

Images in Fig. 59 is a $5\ \mu\text{m} \times 5\ \mu\text{m}$ *in-situ* scan (in SPM mode) of a $5000\ \mu\text{N}$ indent with a Berkovich tip on the initial surface of N-CZ sample and on the cross-section in Fig. 59 (b). These figures illustrate the indent print. The bright side is from the illumination of an elevated ledge, whereas the dark areas are deep zones; cracks are initiated and propagate at the edges of the trihedral tip.

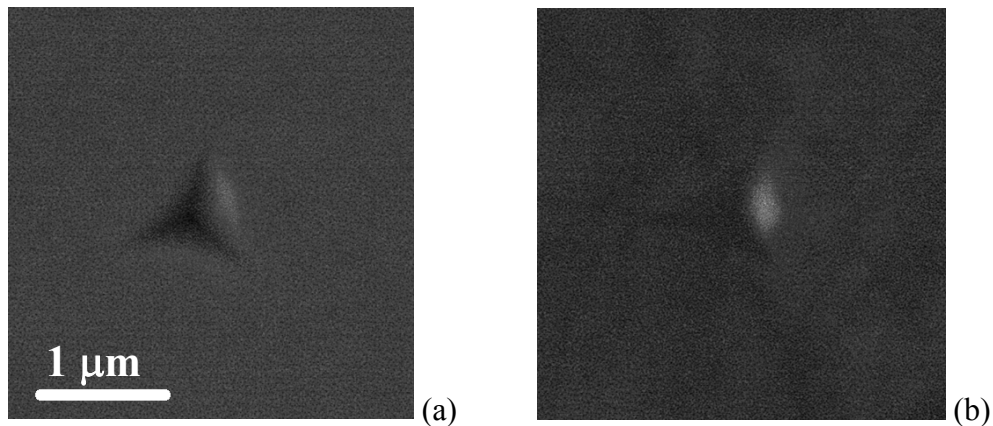


Fig. 59: (a) SPM of a $5\ \mu\text{m} \times 5\ \mu\text{m}$ area in which a $5000\ \mu\text{N}$ indent was performed with Berkovich tip on the initial surface of N-CZ sample.
(b) similar indentation on the cross-section of the same sample shows the differences between the imprints on the initial surface of the wafer from the interior of the bulk.

In Table XI, the elastic modulus, the hardness, and the average surface roughness obtained from individual indentation tests on the initial wafer surface of the five samples are summarized. Data for N-CZ sample are average over 14 indents; to these are associated standard deviations. Note that the roughness is much higher for the N-FZ samples than for N-CZ, which could affect the indentation measurement for these samples.

Table XI: Summary of results from single indentation tests made with Berkovich indenter on the five samples. All indents were done using a trapezoidal load function, see Fig. 58.

Sample Description	Indent #	Contact Depth (nm)	Reduced Modulus (GPa)	Elastic Modulus (GPa)	Hardness (GPa)	Average Roughness Ra (nm)
disl.-FZ	1	151.4	101.98	103.78	6.49	163.1
N-FZ(1)	1	135.2	164.13	177.61	8.00	110.8
N-FZ(2)	1	134.2	167.49	181.87	8.11	103.3
N-CZ (D2W2)	Average	114.4	173.2	189.2	10.8	10.5
(14 indents)	Std. Dev.	0.7	0.9	1.1	0.1	0.0
CZ (D1W2)	1	111.9	182.48	201.23	11.29	12.5

3.2. Indentation Arrays

A portion of N-CZ sample was mounted in epoxy in a cross-sectional orientation, and polished with a 1 μm diamond suspension. Four indentation grids were performed on the cross-section of N-CZ sample, Grid 1 was an array of 49 indents (7 by 7), spaced 2 μm , the grid center is at 150 μm from the sample surface. For Grid 1 peak loads of 5000 μN and Berkovich indenter tip were used. Grid 2 was an array of 20 indents (4 by 5) spaced 1.5 μm apart and centered 5 μm from the sample surface. For Grid 2, 400 μN peak loads and Berkovich indenter tip were used. Grid 3 was a 4 by 5 array of 20 indents spaced 1.5 μm apart and centered 150 μm from the sample surface. For Grid 3 400 μN peak load and a Berkovich indenter tip were used. Since Grid 4 was close to the surface edge, a sharper indenter tip “Northstar” and a lower load having a peak limited to 175 μN were used. Grid 4 is a 3 by 10 array of indents, spaced 50 nm apart, and its center is 2 μm away from the initial wafer surface.

3.3. Load controlled Nano-scratch Tests

The goal of this test is to examine the inhomogeneity of the mechanical properties resulting either from the discovered near surface oxynitride or from precipitates in heat treated N-CZ Si samples. Meaningful information on the surface morphological features, e.g., particle size, shape and distribution, can be extracted from this test. The contrast changes in the SPM images within a scratch can inform on the heterogeneities within the material namely oxynitride precipitates which have fairly contrasted hardness as compared to the silicon matrix.

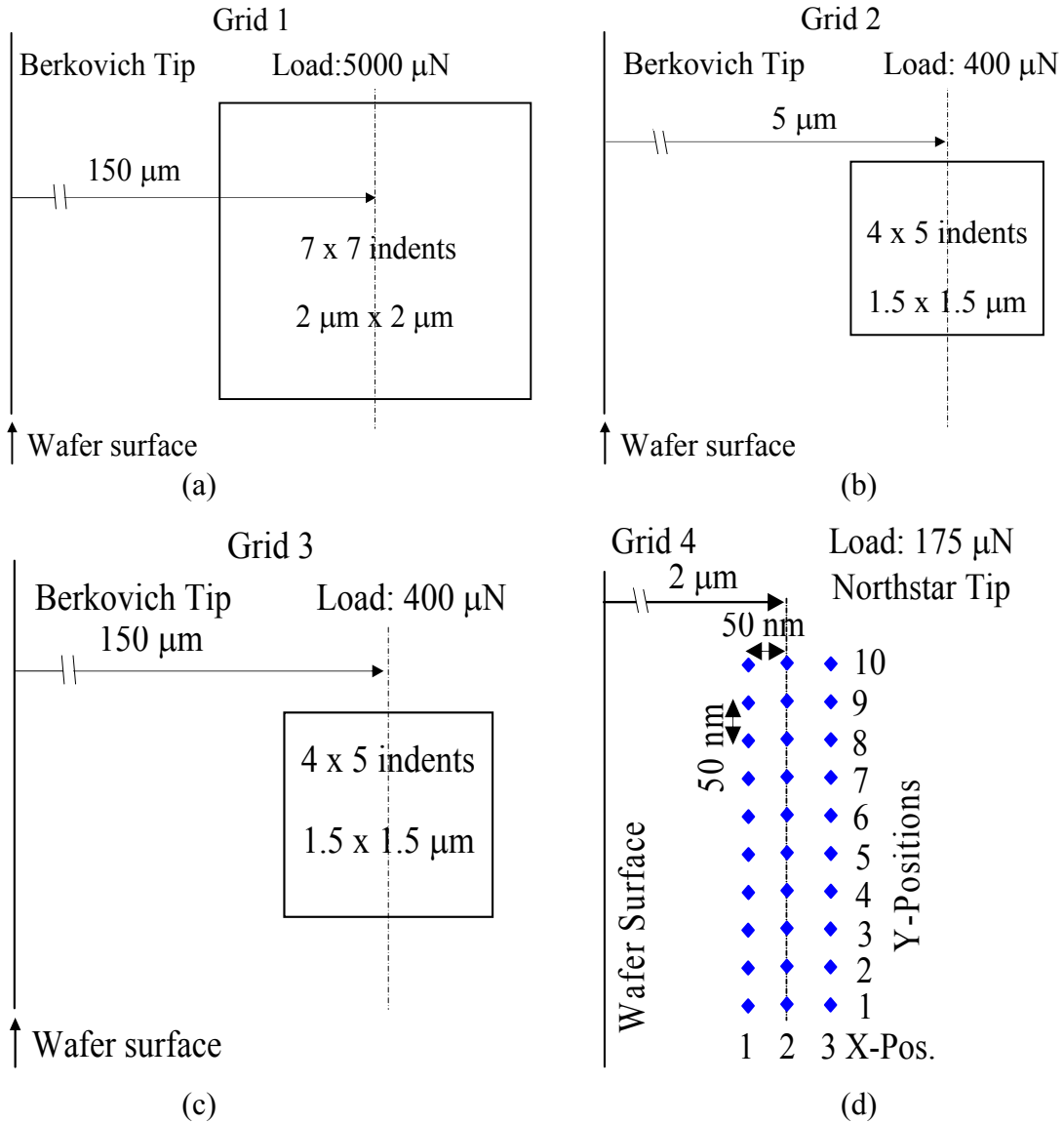


Fig. 60: Array of indents used in the analysis of N-CZ sample.

Figure 61 is a $15 \mu\text{m} \times 15 \mu\text{m}$ *in-situ* SPM image of scratch made with 2000 μN load on a conical indenter on the surface of the N-CZ Si Hi-Lo-Hi material (N-CZ sample). Fig. 62 (a) exhibits plots of normal force, applied during the scratch. Fig. 62 (b) shows the tip penetration. Note that due to the material stiffness the tip-material contact persists at the removal time for 8 secs resulting in a 45 nm compliance. Fig. 62 (c) gives the lateral force during the scratch. Fig. 62 (d) shows the lateral displacement cycle; the segment from 12 to 42 secs is due to tip pulling (represents the scratch itself). Fig. 63 is a plot of friction ratio.

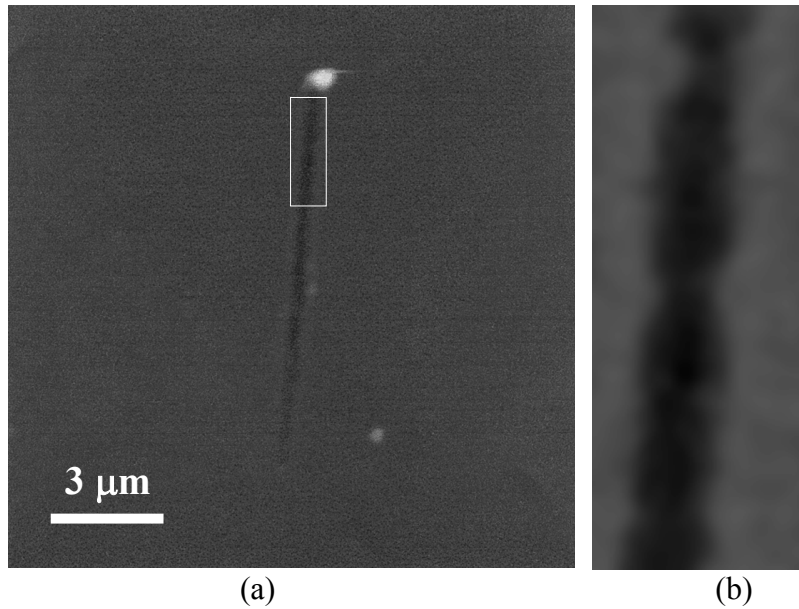


Fig. 61: A 15 μm scan of 2000 μN scratch made with a conical indenter on the surface of the N-CZ Si Hi-Lo-Hi material (N-CZ sample). Zoomed area is about 3 μm in length.

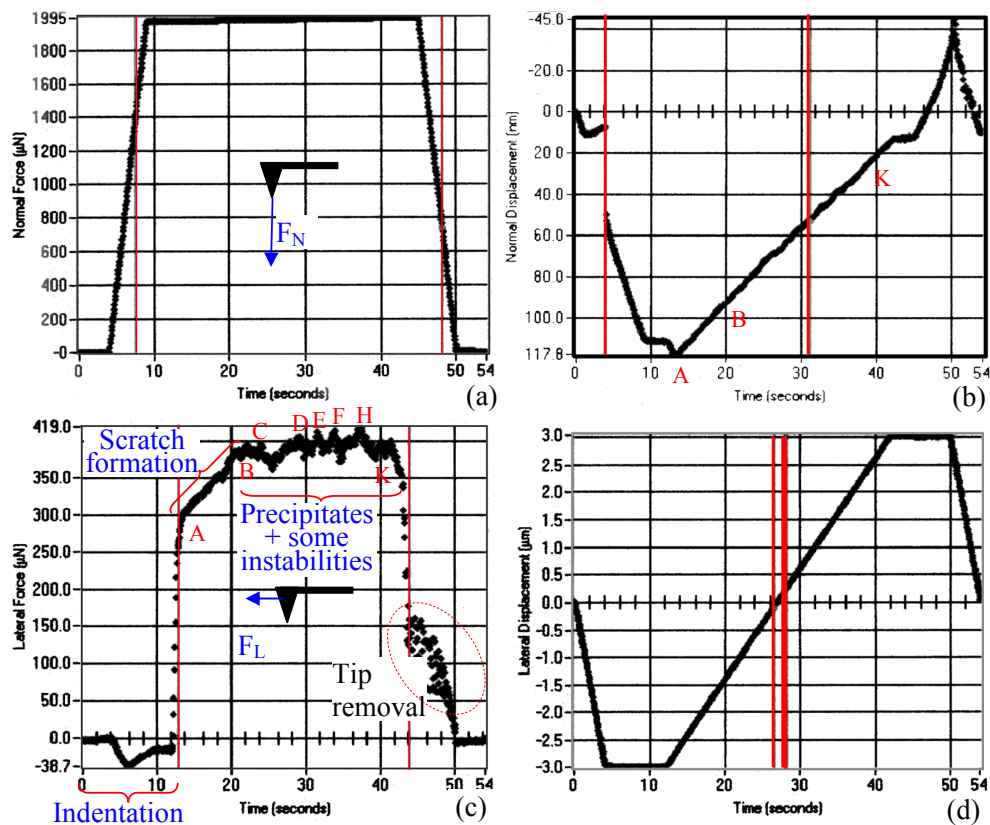


Fig. 62: Data from 2000 μN scratch on the initial surface of N-CZ sample with conical tip.
 (a) Normal force applied during the scratch.
 (b) Tip penetration.
 (c) Lateral force during the scratch.
 (d) Lateral displacement cycle.

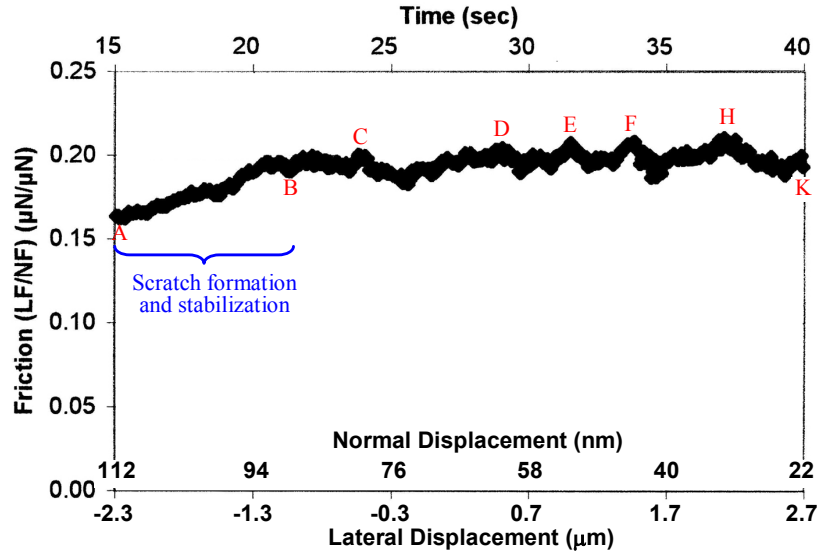


Fig. 63: Friction ratio for the load controlled scratch.

4. Discussion

The FZ samples disl.-FZ, N-FZ(1), and N-FZ(2) appeared softer and much rougher than the CZ and N-CZ samples. Note that N doping of float zone Si increased significantly the hardness (from 6.49 to 8.11 GPa) and reduced the surface roughness (from ~163 to 100 nm). Since this level of roughness is related to the material mechanical properties, it is worth mentioning that the FZ materials were polished with exactly the same conditions and similarly to the CZ wafers. Roughness analysis was done on SPM images of 10 μm x 10 μm obtained for each of the five samples.

Figure 64 and Fig. 65 are plots of hardness and reduced modulus versus contact depth for the individual indentations given in Table XI. The chart shows dispersion of the Hardness-depth data-points that is clearly related to the material type. Definitely the hardness decreases in the order CZ, N-CZ, N-FZ then FZ. Distinct softness of N free FZ is clear, while N-FZ is significantly made tougher by N doping. Note that N-CZ Si is only slightly softer than CZ. N doping readily increases the hardness of silicon to a comparable level as oxygen.

It is noticeable that the hardness decreases slightly with the contact depth (see the series of indents in Fig. 64 and Fig. 65) indicating a decrease in the hardness as the indenter goes deeper in the material (the effect of the tip shape is ruled out).

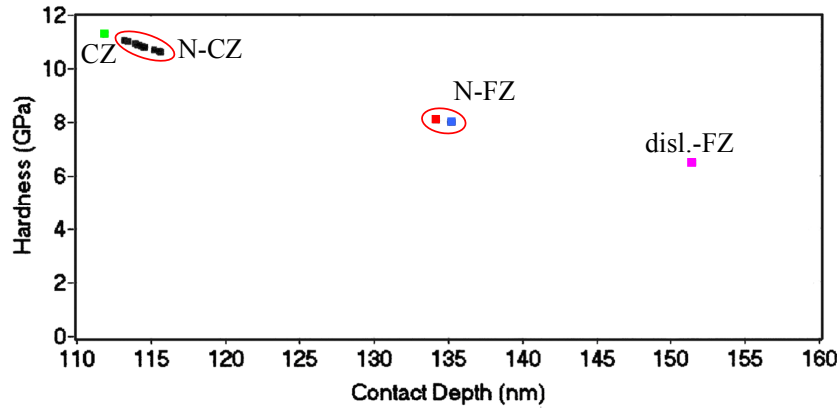


Fig. 64: Hardness vs. Contact Depth for the individual indents on each of the five samples; one indent each on the first four samples and fourteen indents on N-CZ sample.

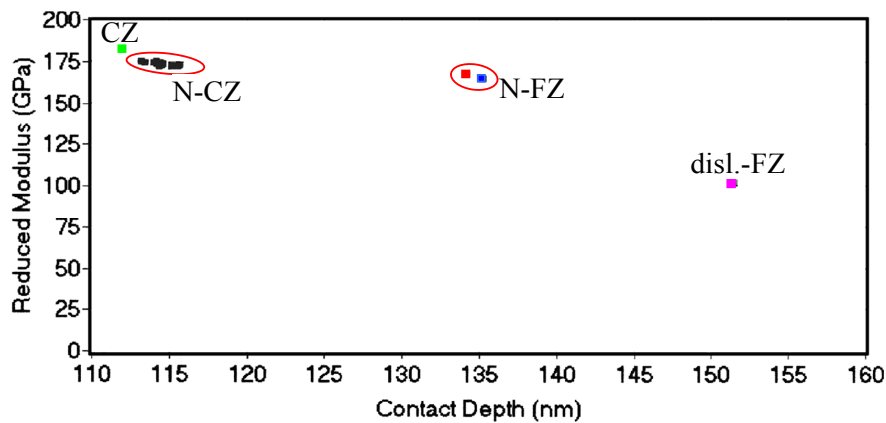


Fig. 65: Reduced Modulus versus Contact Depth for indents on each of the five samples; one indent each on the first four samples and fourteen indents on N-CZ sample.

Plots in Fig. 66 and Fig. 67 of hardness and reduced modulus versus contact depth respectively for indentation Grid 1 further support the linear decrease of the hardness of the shallow layer of N-CZ sample. Figure 68 and Fig. 69 are plots of hardness versus contact depth and reduced modulus versus contact depth respectively for indentation Grids 2, 3, and 4 made with 400, 400, and 175 μN load, respectively. The tests appear to be done in a linear regime Hardness-depth thanks to an adequate choice of the load. The finer Northstar indenter achieved a deeper contact (larger contact depth range). The Berkovich tip resulted in a more concentrated distribution of the data points. The observed dispersion could relate to heterogeneities and the amount of precipitates encountered in the material. The reduced modulus depends linearly on the Contact Depth when using a Berkovich Tip, while it is independent of the contact depth when using the Northstar tip.

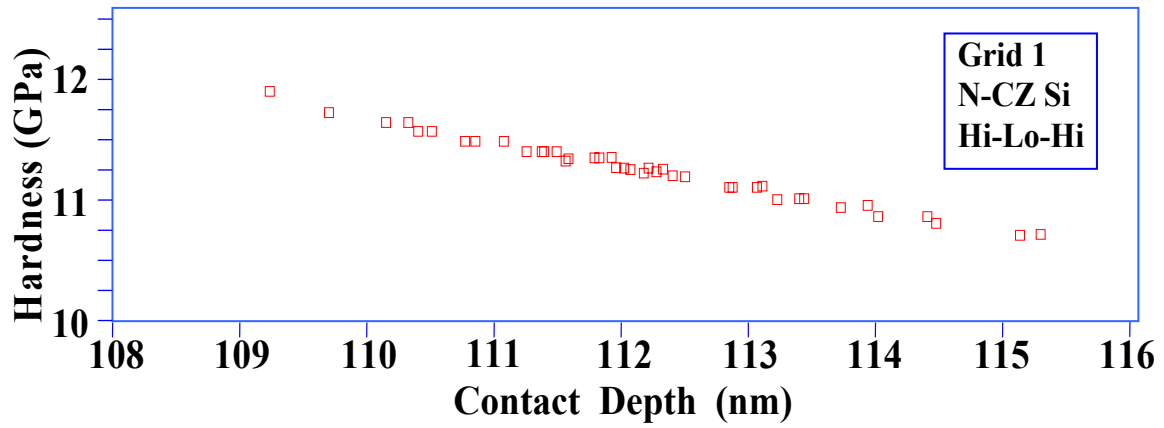


Fig. 66: Hardness vs. Contact Depth for the indentations from Grid 1 on N-CZ sample

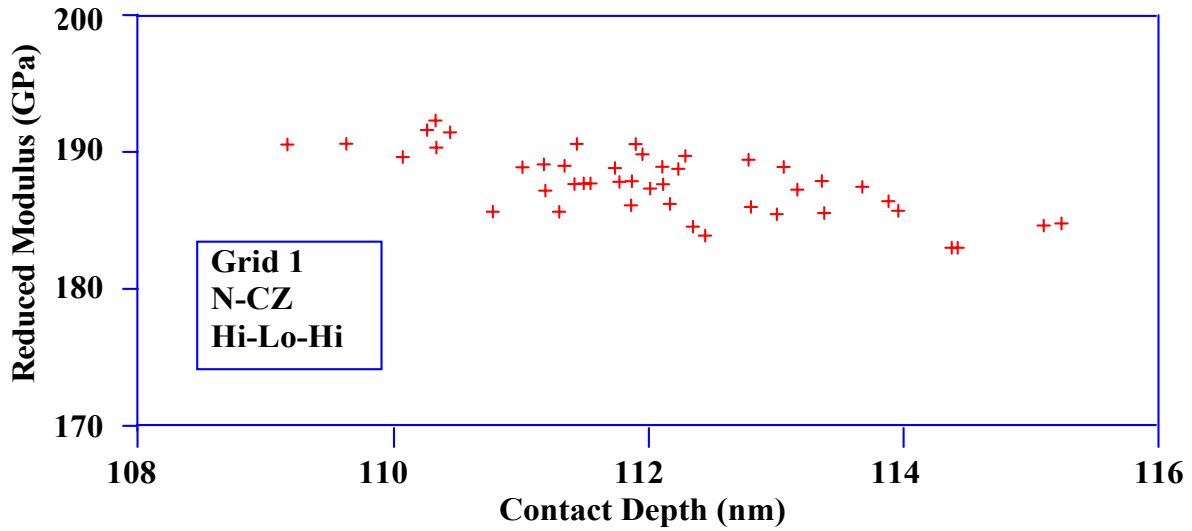


Fig. 67: Reduced Modulus vs. Contact Depth for the indentations from Grid 1 on N-CZ sample.

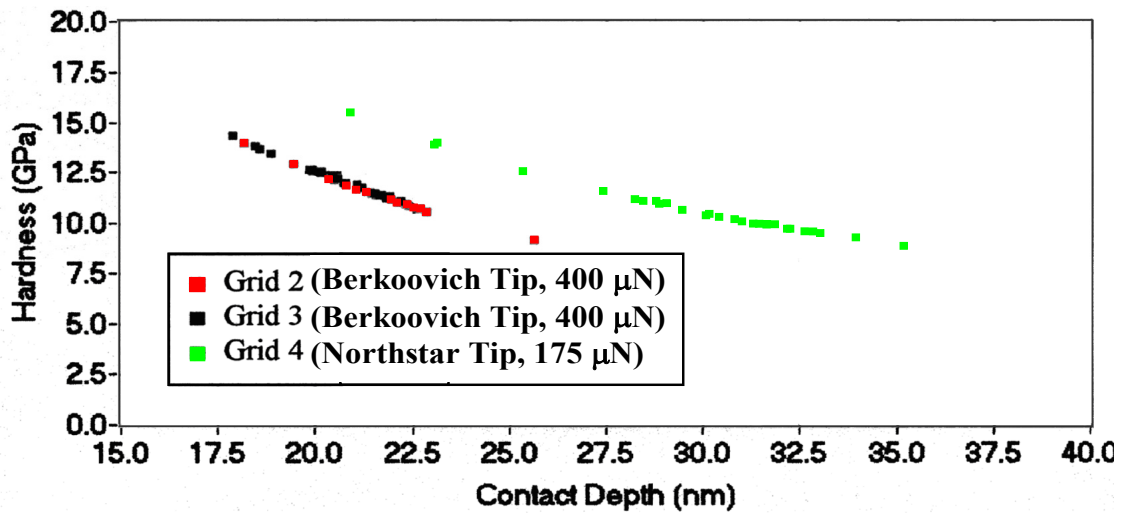


Fig. 68: Hardness vs. Contact Depth for the indentations in Grids 2, 3, and 4 on N-CZ sample.

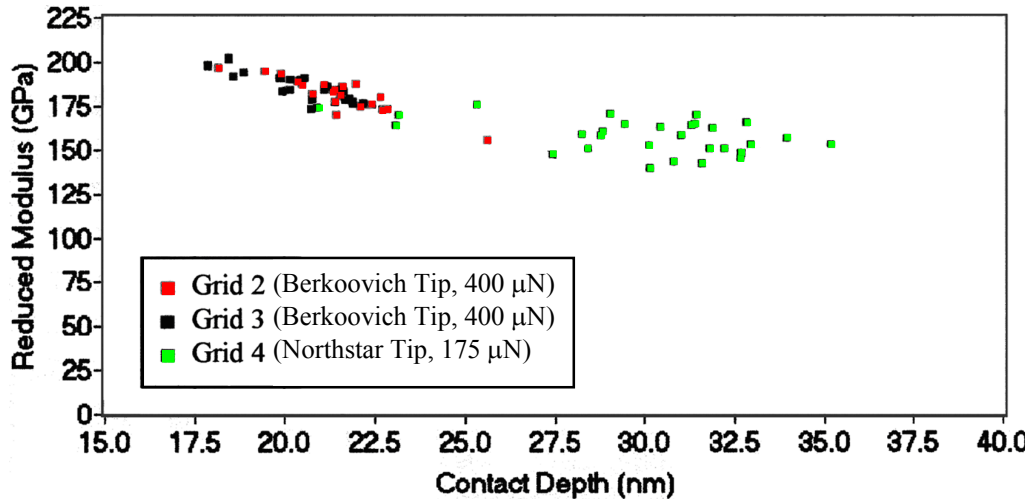


Fig. 69: Reduced Modulus vs. Contact Depth for the indentations in Grids 2, 3, and 4 on N-CZ sample.

Table XII contains a summary of the data obtained from each of the four indentation grids on N-CZ sample. The averages of The contact depth, reduced modulus, and hardness are given along with the standard deviation. Note the following:

1. Hardness of N-CZ sample made with both Berkovich indenter right at the wafer initial surface (Table XI) and with Northstar indenter (Table XII, Grid 4) at 2 μm from the wafer surface are similar. The former is the average of 14 data points and the latter is the average of 30 indents. Therefore one can consider, that the hardness at the surface of Hi-Lo-Hi treated N doped Si is: 10.8 ± 0.1 GPa, independent of the tip type and the applied load. However, the small deviation is caused by the lower hardness in the center of Region II where [O] and [N] are at their minimum. This will be discussed below in more details.
2. comparing the average hardness (Table XII, Grid 2 and Grid 3) made with the same tip and the same load indicate a smaller hardness in the near surface region (region II) than in the bulk region (region III). It has been shown in Chapter II that in region II of such a sample, there is a low O and N concentrations and the precipitate density is at its lowest, and might be the reason for the slight material softness in that region.
3. hardness obtained at the same load and tip (Grid 2 and Grid 3) show that Region II softer than region III, for which the hardness are 11.5 ± 1.0 , and 12.3 ± 0.9 GPa, respectively.
4. The high load used for Grid 1 provided the most homogeneous data with a standard deviation

equal to 0.25 (i.e., $\frac{1}{4}$ of the standard deviation obtained from Grid 2 and Grid 3). The high load resulted in a stabilization of the material response leading to a reduction in the sensitivity to heterogeneities within the Si matrix.

Table XII: Summary of the data obtained with various indentation grids on the cross-section of N-CZ silicon sample.

Grid	Region	Dist. from sample Edge	Tip Type	Load	Number of Indents	Indent Spacing	Average Contact Depth and St. Dev.	Average Reduced Modulus and St. Dev.	Elastic Modulus	Hardness and St. Dev.
#		(μm)		(μN)	#	(μm)	(GPa)	(GPa)	(GPa)	(GPa)
1	III	150	Berkovich	5000	49	2.00	112.0 \pm 1.4	188.0 \pm 2.5	208.5	11.3 \pm 0.25
2	II	5	Berkovich	400	20	1.50	21.5 \pm 1.5	181.3 \pm 9.7	199.7	11.5 \pm 1.0
3	III	150	Berkovich	400	20	1.50	20.5 \pm 1.2	185.9 \pm 7.6	205.7	12.3 \pm 0.9
4	II	2	Northstar	175	30	0.05	30.0 \pm 3.3	157.8 \pm 9.8	169.7	10.7 \pm 1.5

Table XIII: Main results obtained for different regions of Hi-Lo-Hi cycled N-CZ Si sample.

Region #	Characteristic	Distance to Edge (μm)	Load (μN)	Contact Depth (nm)	Reduced Modulus (GPa)	Hardness (GPa)
II	Low [O] Low [N]	2	175	30 \pm 3	158 \pm 9	10.7 \pm 1
III	High [O] High [N] High precipitate density	150	5000	112 \pm 1	188 \pm 2	11.3 \pm 0.2

Figure 70 is a series of four plots of hardness and reduced modulus values obtained from Grid 4 indents; the origin of X-axis is at the wafer initial edge. The data point distributions are compared along the respective X and Y axis as laid out in Fig. 60 (d). The values along X-axis represent depth positions of the indents from the wafer initial surface. In addition, one can see that hardness and reduced modulus decrease as a function of depth, while the variations are random along the lateral Y-direction (independent of depth) which depicts a harder phase towards Region I. The dispersion in the Y-direction delineates the fluctuations in the hardness, which is most likely due to the precipitates.

Figure 70 (a) shows a large deviation at the three lines of indentations. The deviation reaches 6 GPa at x-position 1950 nm from the wafer surface for an average hardness of

10.5 GPa. This deviation is due to oxynitride precipitates. This effect is seen more clearly in Fig. 70 (b), where a group of data points with high hardness is separated from the remaining points which are attributed to the matrix.

Concerning the scratch tests, bright lines in Fig. 61 appear in each side of the scratch. It is due to dislocation pile-ups and initiation of cracks. Zoomed areas show the heterogeneities of the scratch which may include instabilities that could be due to high velocity that leads the tip to jump during scratching or to probing harder phase (i.e. oxide precipitate).

As can be seen in Fig. 62 (a), the tip is first driven into the sample then withdrawn while controlling the applied force. Fifteen seconds were allowed for indentation and tip stabilization on the sample surface before the relevant segment of the scratch begins. The force is ramped by 40 μN (0.2% of the total load) during the displacement to insure a constant contact. The lateral force during scratching shows two stages, the first one extending from -3 μm to -0.6 μm is more relevant. During this stage the small variations are believed to be due to precipitations. The ellipsoidal like shape are deep and thus pertain to soft material of the matrix while the gray are due to deviation, thus are attributed to harder phases, most likely precipitates.

The friction ratio defined as the Lateral Force normalized with the Normal Force (about the sample surface). The more relevant part of the scratch corresponds to a constant average Lateral Force (or friction) to which fluctuations are superimposed (i.e., segment B-K in Fig. 63). The peaks C,D,...,H are peaks in the resultant lateral force are believed due to harder phase, most likely precipitates or N and O supersaturated zones. The average spacing is about 0.8 μm and the scratch average depth is 50 nm yield an average density of the hard phases equal to $3 \times 10^{13} \text{ cm}^{-3}$. This value matches very well the density of N related nuclei proposed in such N-CZ material, as discussed in section 4 of Chapter V.

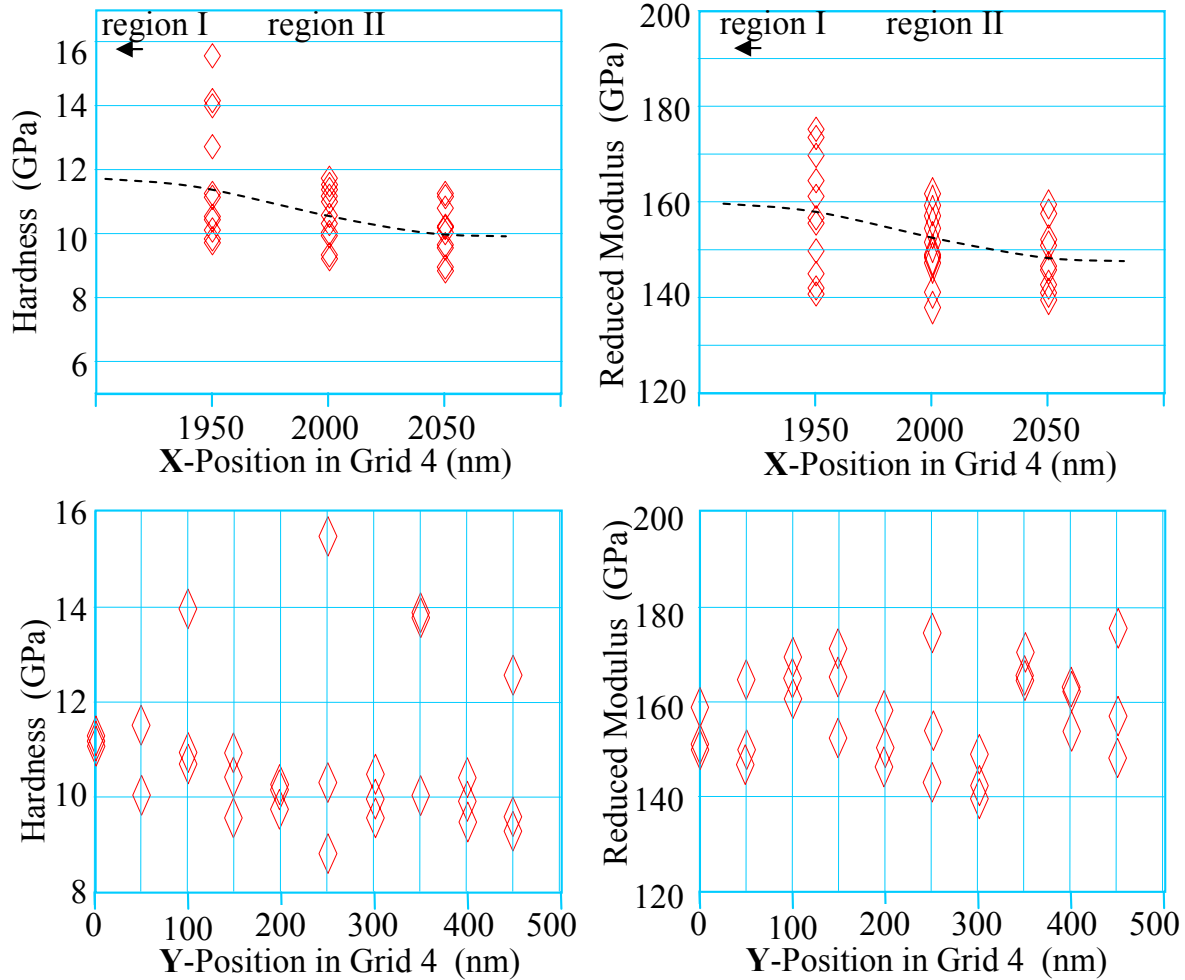


Fig. 70: Plots representing hardness and reduced modulus of Grid 4 indents compared along respective X and Y axes as laid out in Fig. 60; all indents in Grid 4 are 50 nm apart on both axes. X-origin is counted at the wafer surface (left hand-side of the cross sectional sample). Scattered points are attributed to heterogeneities, e.g. precipitates for the high hardness data points. Dashed lines are the expected hardness and reduced modulus.

5. Summary

The obtained hardness and modulus values for the three Float Zone silicon samples differ from those of CZ Si, both N free and N doped samples. Indentation grids and nano-scratches were employed to delineate dissolved N and O and precipitate effects on overall mechanical properties. A series of 14 indents performed on the surface of annealed N-CZ samples using Berkovich indenter and the Grid 4 of indentation done with Northstar indenter in a cross section close to the surface yielded similar data for hardness and reduced modulus. Grid 3 (150 μm deep in the bulk) and Grid 2 (5 μm away from the original surface of N-CZ sample) done with the

same load and indentation tip show that the bulk is slightly harder (12.3 versus 11.5 GPa). The hardness and reduced modulus values obtained with Grid 4 vary with respect to the indentation position from the wafer original as compared to the lateral direction (parallel to the wafer original surface) are due to non-uniform concentration of N and O. Distinctively high hardness is attributed to precipitates.

Hardness obtained at the surface of N-CZ Si is similar to that obtained in Region II of a cross sectional sample. Increased hardness in Region III 11.3 GPa. Region II (low O and N) appears softer than Region III. Nanoindentation showed some effects of precipitates (Precipitate density $< 3 \times 10^{10} \text{ cm}^{-3}$) as well as dissolved O and N accumulated in the near surface.

Scratch tests confirmed the existence of harder phases, which separation distance includes small precipitates not detectable by etching and OPP. An excellent matching of the density of hard phases in N-CZ with the N related nuclei density proposed for such a material.

Chapter VIII

INTERACTION OF LIGHT ELEMENTS WITH DISLOCATIONS IN SILICON	146
1. Introduction	146
2. Model Used for Dislocation-Impurity interactions	147
3. Calculation of dislocation-impurity Binding Energy	151
4. Simulation Results and Discussion:	152
4.1 Atomic Structure of the Used Specimen	152
4.2 Atomic Structure of the Core of an Edge Dislocation.....	152
4.3 Impurity Distributions Within The Dislocation Atmosphere.....	155
4.3.1. Oxygen.....	155
4.3.2. Nitrogen	156
4.3.3. Carbon.....	156
4.3.4. Germanium	157
4.4 Impurity-dislocation binding energy and shear stress for dislocation separation	158
4.4.1. Effect of the impurity Type.....	158
4.4.2. Effect of the Impurity Concentration.....	159
4.4.3. Temperature Effect on the dislocation atmosphere	161
5. Conclusion.....	162

Chapter VIII

INTERACTION OF LIGHT ELEMENTS WITH DISLOCATIONS IN SILICON

1. Introduction

The effects of nitrogen and oxygen (and other impurities) on mechanical properties can be connected to dislocation density and their motion and pinning. It is technologically relevant to know the doping levels that prevent slip dislocations. In this chapter, a theoretical study is presented on edge dislocation locking by various impurities including light elements (e.g., O, N, or C) in low oxygen content wafers. This is done by simulation of dislocation generation and locking by impurity atmosphere. Ultimately, the results of this study can be correlated to material strength, which is affected by the dislocation density and type and precipitate size distributions.

The used model is built upon the size-effect arising from the volume mismatch between the impurity and the host crystal atoms (i.e., silicon), which represents the primary contribution to the dislocation-impurity interactions. The major assumptions in the used model are (i) the added impurities occupy interstitial positions, the larger octahedral sites, and (ii) the shape has a secondary effect.

Three groups of impurities were considered: (i) light atoms N, O, C, (ii) dopants B, P, Al, and (iii) large atoms Ga, Ge, and As. The chosen specimen is an edge dislocation; it is constructed by inserting an extra-half plane in a silicon crystal with cylindrical boundaries taking into account the dislocation symmetry (i.e., its Burger and sense vectors). The system (a clean dislocation) is then relaxed by minimizing its total energy, which allows for the calculation of the residual strain distribution over the relaxed structure. Subsequently, an impurity atmosphere is created using Fermi-Dirac distribution.

In addition to studying different type of impurities, the atomic fraction within the atmosphere and the temperature (spanning from RT to wafer annealing range) have been varied. A wide range of impurity-dislocation interactions were observed and discussed.

2. Model Used for Dislocation-Impurity interactions

Early work on the interaction of point defects with a stress field was done by Cottrell and Bilby [313] allowed understanding phenomena such as material hardening, ageing,...[314, 315] and more recently gettering issues and electrical activities such as those explored by EBIC [316]. The prominent work done by Peirls and Nabarro [317] has been used mainly for alloys.

In addition to the self-energy barrier for migration of a dislocation, the binding energy of foreign atoms (including dopants) with dislocations make an important contribution to the activation energy for dislocation migration. The major part of this energy comes from the strain compensation by foreign atoms and is termed as "size interaction energy". The size difference between silicon atoms and gettered atoms relieves the stresses near the dislocations, thus reducing the overall energy of the system. This energy contribution is expressed as:

$$E = \int_{r>r_p} \int_{r>r_d} \sigma \varepsilon dV \quad (42)$$

where ε is the strain caused by the defect (i.e., displacement of atoms by a quantity \mathbf{u}) in the dislocation stress field σ . The bounds r_p and r_d are the point defect and dislocation core defect radii which avoid the severe computation singularities due to the subtle definition of the core. The Peirls-Nabarro leading model for dislocation assumes the energy of the dislocation core to be logarithmic. This allowed practical success in describing dislocation generation and the critical thickness in alloys and strained layers [318]. However, it is still not known how this empirical model relates to the atomic structure. Such understanding is becoming critical for nano-scale devices and layers. This justifies the current thrust for understanding the core contribution through atomistic first principle calculations [319], which do not refrain in considering elastic and non-elastic deformation or isotropic and non-isotropic medium. In fact these methods are overriding the empirical elastic models developed between 1950-1990; however, they require extensive computation.

For high purity crystals, the first order size can still provide significant information for the optimization of the doping and elimination of dislocation movement. The first order size effect elastic interaction between an edge dislocation and an impurity was first studied by Cottrell and Bilby [313] under the assumption that the point defect is a center of compression/dilatation in an isotropic continuum (size interaction). The energy commonly

referred to as the first order size effect elastic interaction was approximated by the following expression [314]:

$$E_{size} = \frac{\mu b(1+\nu)\Delta V \sin \theta}{3\pi(1-\nu)r} \quad (43)$$

with ΔV is the change in the lattice volume caused by the impurity, μ is the shear modulus of Si, ν Poisson's ratio, b the dislocation Burger's vector (e.g., 3.84 Å for an edge dislocation in silicon), and θ and r the cylindrical coordinates of the dopant in the dislocation referential [320].

Additional energy term was singled out by Koehler [321]; it relates to the local reduction of the crystal symmetry, as well as the symmetry change in the impurity migration saddle point as compared to the stable configuration; i.e., the migration energy is not isotropic in a stress field. A volume change occurs in the saddle point as discussed by Birnbaum et al [322]. These effects give rise to "Energy Shape Terms". It is very important to note that the interaction of non-spherical defects near dislocation can still be treated using elasticity theory. Elastic interaction energy of defects in system with tetragonal symmetry have been calculated by Cochardt et al [314] and by Huntington et al [324]. More recently, this model was further developed and discussed by Johnson [320]; the atomic description of the strain field was based on elastic theory (small deformation of the bonding; i.e., outer shell). Both the volume change and the distortion of the matrix symmetry are included. Johnson in his analytical formalism described the interactions of defects with dislocations by decomposition of the defect displacement field. This approach allowed investigation of the dislocation atmosphere and well enough the dislocation core. Johnson assumed in his formalism that the defect evolves in the strain field with an anisotropic displacement, see Fig. 71, its domain is decomposed in radial and non-radial components as follows:

$$u = u_1 + u_2 \quad (44)$$

$$u_1 = K_1 \frac{1}{r^2} \vec{e}_r \quad (\text{purely radial component}) \quad (45)$$

$$u_2 = K_2 \frac{1}{r^2} \left[(3A-1)(\vec{e}_r \cdot \vec{e}_d)^2 - A \right] \vec{e}_r + (\vec{e}_r \cdot \vec{e}_d) \vec{e}_d \quad (\text{bears asymmetric deformation}) \quad (46)$$

\vec{e}_r, \vec{e}_d unit vectors in the radial and "defect main axis" direction

$$A = \frac{1}{3} + \frac{1}{2}(2-\nu) \quad (47)$$

Equation (45) describes pure radial displacement, whereas equation (46) deals with the asymmetric deformation of the atoms (or fragments).

K1: “strength” of the displacement field

K2: if negative/positive a sphere changes in an oblate/prolate, respectively, see Fig. 71.

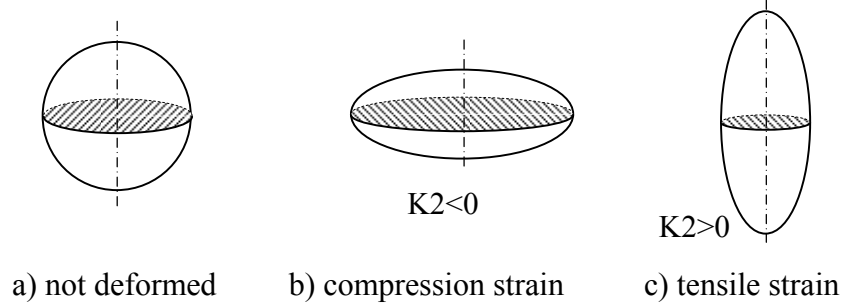


Fig. 71: Models for elastic shape deformation of atoms during interactions with dislocations.

The standard edge dislocation displacements components in the dislocation are:

$$u_x = \frac{b}{2\pi} \left[\tan^{-1}\left(\frac{y}{x}\right) + \frac{xy}{2(1-\nu)r^2} \right] \quad (48)$$

$$u_y = \frac{-b}{2\pi} \left[\frac{1-2\nu}{4(1-\nu)} \ln(r^2) + \frac{x^2 - y^2}{4(1-\nu)r^2} \right] \quad (49)$$

Johnson and co-authors³²⁰ evaluated efficiently the interaction energy of carbon atoms with an edge dislocation in α -iron. Carbon occupies octahedral sites in the BCC structure of iron as shown in Fig. 72 (a). Concerning the dopant atoms in silicon, within the dislocation atmosphere they most likely behave differently sitting in substitutional positions like in the defect free silicon crystal. In the dislocation stress field the majority of impurities is also expected to occupy the larger octahedral sites (because of the high concentration), which is likely to justify the first approximation for dopants as well.

For each displaced octahedral site the impurity-dislocation interaction energy was reported [325] to be:

$$E_x = A_1 \frac{y}{r^2} + A_2 \frac{y}{r^2} \left[-\left(\frac{1}{2} - \frac{\sqrt{6x}}{y}\right) \frac{(x^2 - y^2)}{r^2} - \nu \right] \quad (50)$$

$$E_y = A_1 \frac{y}{r^2} + A_2 \frac{y}{r^2} \left[-\left(\frac{1}{2} + \frac{\sqrt{6x}}{y}\right) \frac{(x^2 - y^2)}{r^2} - \nu \right] \quad (51)$$

$$E_z = A_1 \frac{y}{r^2} + A_2 \frac{y}{r^2} \left[\frac{(x^2 - y^2)}{r^2} - 2\nu \right] \quad (52)$$

with

$$A_1 = \frac{4(1+\nu)\mu b K_1}{3(1-\nu)} \quad (53)$$

$$A_2 = \frac{4(4-5\nu)\mu b K_2}{45(1-\nu)(1-2\nu)} \quad (54)$$

The subscripts in the energy expression indicate the orientation of the octahedral sites in the lattice coordinate system. Johnson has used for α -iron $\mu=550 \text{ eV/nm}^3$ for the bulk modulus, $\nu=0.317$ for the Poisson ratio, $b=0.25 \text{ nm}$ for the Burger's vector, $K_1=2.7 \times 10^{-4} \text{ nm}^{-3}$ and $K_2=4.1 \times 10^{-4} \text{ nm}^{-3}$

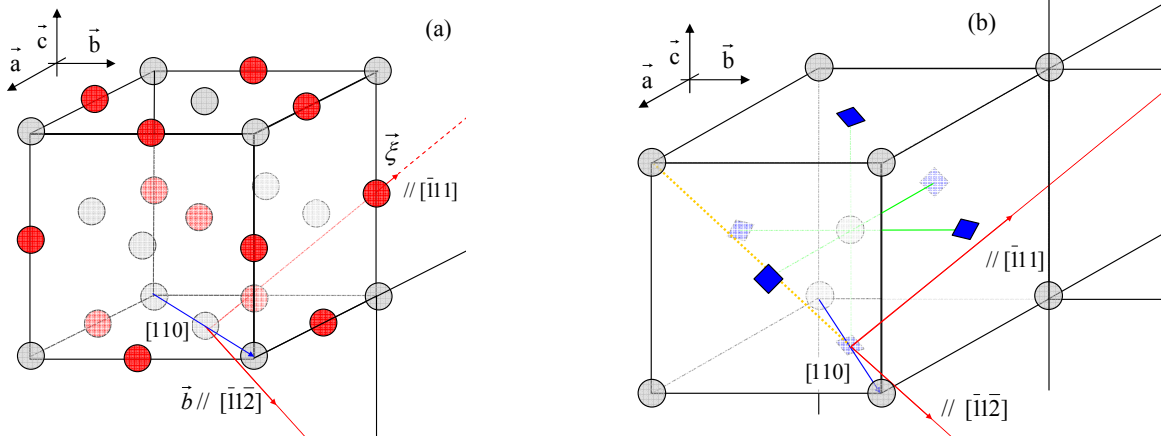


Fig. 72: Large interstitial octahedral sites in FCC and in BCC structures, and the used dislocation configuration.

The probability of occupancy of individual sites was computed using Fermi-Dirac distribution [10]. For the i^{th} site occupancy is:

$$R_i = \exp\left(-\frac{E_i}{kT}\right) \quad (55)$$

where E_i is the interaction energy of that site with the dislocation given by equation (9) to (11).

The probability of occupation of the i^{th} site by a given impurity atom is:

$$P_i = \frac{R_i}{F + R_i} \quad (56)$$

with F represents all free/excluded sites that the impurities are not occupying (do not contribute to the atmosphere, while within the dislocation field). The parameter F is therefore determined by the following continuity equation:

$$N = Na \sum_{i=1}^{Na} P_i + F(Ns - Na) \quad (57)$$

Ns : number of octahedral sites inside the sample. The sample is a cylinder slab with a radius equal to half distance between two dislocations.

Na : number of octahedral sites that are involved in making the dislocation atmosphere.

N : total number of impurities in the cylinder slab. This is determined by the atomic fraction (impurity atomic percentage in the atmosphere) and must not be paralleled to the concentration in the defect free Si matrix.

The total interaction energy of the dislocation with its atmosphere was then computed as:

$$E = \sum_{i=1}^{N_c} E_i P_i \quad (58)$$

The sensitive issue of the use of impurity Fermi-Dirac distribution first was discussed by Louat [327], while arguing the Maxwell Boltzmann distribution used by Cottrel et al [313]. The Fermi-Dirac distribution was debated by Beshers [328] and further clarified by Johnson [326].

3. Calculation of dislocation-impurity Binding Energy

The occupation probability attached to the impurity distribution around dislocation depends on the concentration of dopants and the dislocation density. The range for fraction sites involved in making the atmosphere was chosen between 10^{-5} to 10^{-1} . Using the spatial distribution of the occupation probability, an atmosphere of dopant atoms near the dislocation line was calculated. In order for the dislocation to migrate, it must separate from this 'atmosphere', naturally under external stress.

Practically, by holding the atmosphere fixed, and moving the dislocation in its plane, a separation stress can be calculated. This is made (in the simulation) by moving the extra-half plane in the glide plane. The step increments for energy calculation are subatomic distances. When a complete atomic jump is realized the atomic system is brought to equilibrium by minimizing its energy via readjustment of the atomic positions. The interaction energies were calculated at every step (of the movement). The total energy change is calculated by summing

the new energy state (that the impurity will acquire) multiplied by the occupation probabilities. A relation of dislocation-impurity “Interaction Energy” versus "Dislocation location" is obtained and a plot is constructed.

Table XIV: Basic parameters necessary for modeling the dislocation atmosphere (covalent radius, i.e, half bond length) for prominent impurities.

Element	O	N	C	B	P	Si	Al	Ga	Ge	As
Covalent bond radius (Å)	0.73	0.75	0.771	0.82	1.06	1.11	1.176	1.26	1.225	1.2

4. Simulation Results and Discussion:

4.1. Atomic Structure of the Used Specimen

The atomic sample is a cylinder whose axis is set along the dislocation sense vector. The sample radius is half of the distance between the two dislocations. The investigated material assumes that the dislocations are far enough from each other for not interacting.. The interactions are either directly by their stress fields or indirectly via inter-diffusion of impurities from their atmospheres. Thus the sample radius is determined by the dislocation density. This is taken equal to 70\AA , corresponding to a density of 100 cm/cm^3 . Three atomic planes are considered and which are reproduced identically by translation along the z-axis. The total number of atoms in such a sample is 2961. The silicon periodic blocks along the z-axis are 3.84\AA distant. The probability is normalized for the sample unit cell. The used bulk modulus is $\mu=0.48\text{ eV/nm}^3$, the Poisson ratio $\nu=0.27$, and the density $\rho=2.33$.

4.2. Atomic Structure of the Core of an Edge Dislocation

The imprecise use of the dislocation core in the empirical models and the limited number of atomic discrete positions lead to an imprecise evaluation of the shear at the peaks of the energy gradient (which is the most prominent information one seeks). Molecular Dynamics is used herein to find the exact atomic structure of the core and to evaluate the self-energy of the dislocation at equilibrium. The sample is basically a cylinder in accordance with the symmetry of the edge dislocation, which is placed in its center with sense vector $[\bar{1}10]$ along the cylinder axis (base perpendicular to the dislocation sense vector). The crystal orientation: $ox=[110]$, $oy=[001]$,

and $oz=[-110]$, see Fig. 73. The sample diameter is $\sim 144\text{\AA}$ and thickness is $\sim 35\text{\AA}$. The total number of Si atoms is 29610 and H terminating atoms is 4942 and there are 56759 bonds.

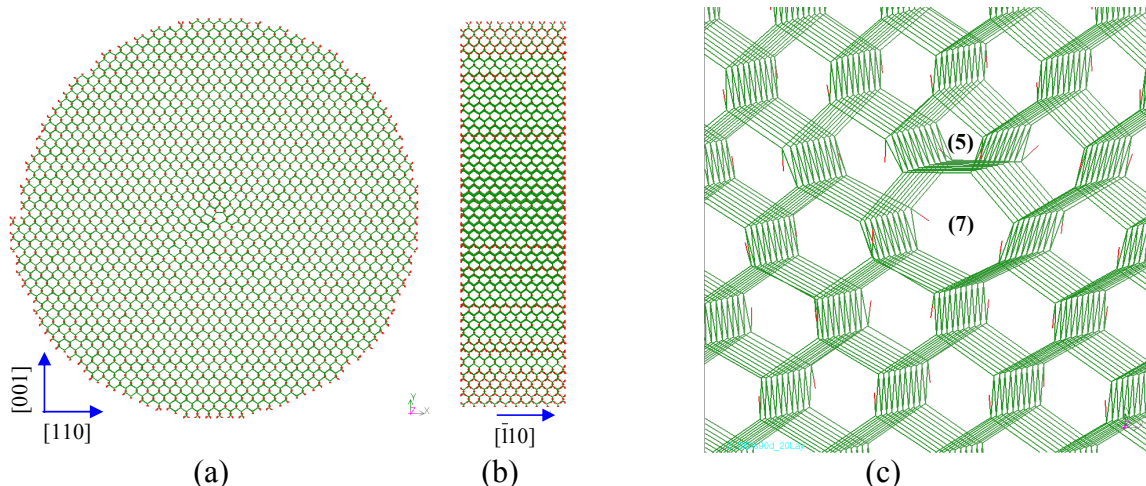


Fig. 73: Silicon sample that has an edge dislocation in its center. Crystal $\vec{o}z$ orientation is $[\bar{1}\bar{1}0]$, see (b). The red points and segments are immobile H atoms and the green ones are mobile silicon. The numbers (5) and (7) point to the penta- and septa-rings, respectively.

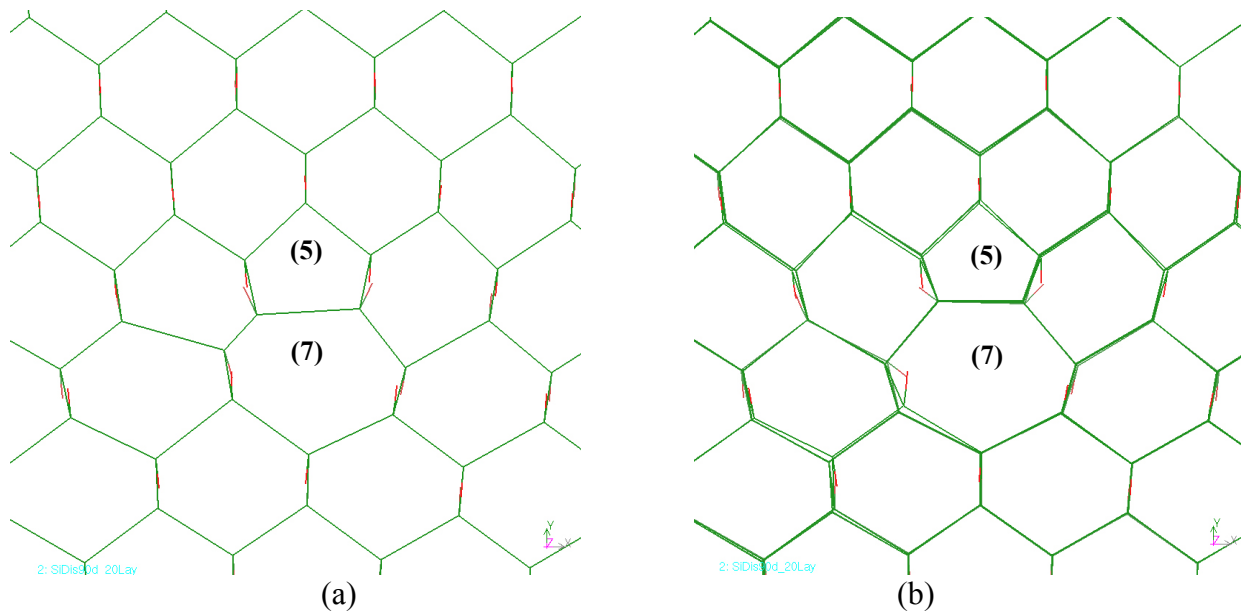


Fig. 74: Core of the edge dislocation visible with the penta-ring connected to a septa-ring, (a) guessed structure, and (b) relaxed structure. The relaxation was done by the atomistic classical mechanics (Force Field).

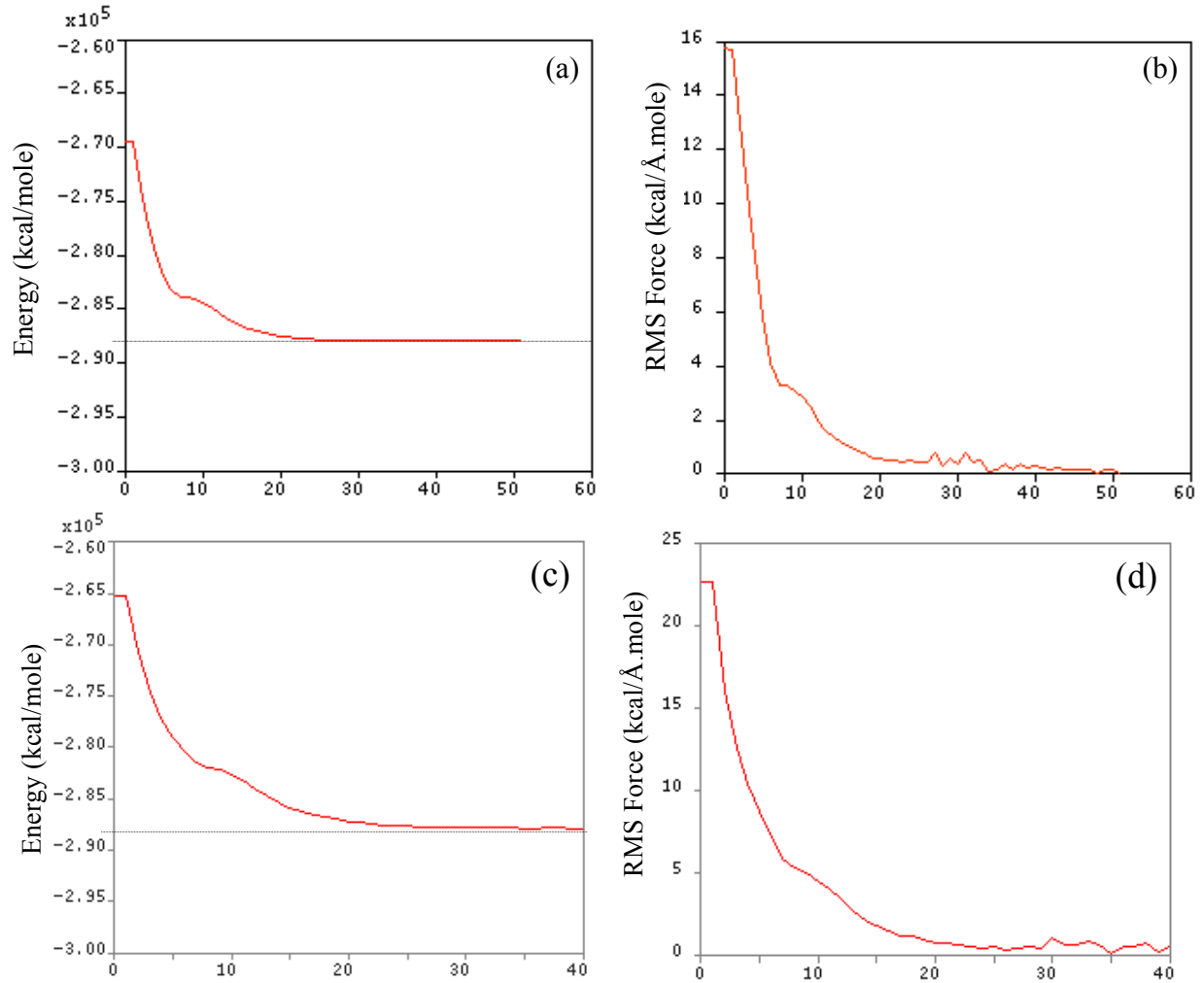


Fig. 75: Energy and stress force variations over time during a geometry optimization of a silicon sample without any dislocation in (a) and (b) and with an edge dislocation in its center in (c) and (d). The unit cell is shown in Fig. 73.

The total energy of the relaxed structure of the perfect silicon sample is -287989.5 kcal/mol. This includes the contribution of the residual stress. The same sample but with the edge dislocation has a total energy of -287863 kcal/mol, including stress related component. The various energy terms in the dislocation-free sample are presented in Table XV.

The difference in the total energy of a sample with dislocation and perfect sample with the same number of silicon atoms, (-287989 kcal/mol and -287863 kcal/mol, respectively) is a measure of the energy needed for dislocation formation. We found that the Energy of Formation of an edge dislocation of length 35 \AA in length is 5.46 eV . Thus the self-energy of an edge dislocation is 156 meV/\AA .

Table XV: Energy terms and the total energy of the cylindrical silicon sample (with 29610 Si atoms and terminated with 4942hydrogen atoms; the sample has 56759 bonds)

Valence Terms (kcal/mol)				Non-bond Terms (kcal/mol)			
Energy Terms	Perfect	Dislocated	Difference	Energy Terms	Perfect	Dislocated	Difference
Bonds	697.851	1427.98	730.129	Van der Waals	-96288.1	-96250.9	37.2
Angles	32081.7	33189.6	1107.9	Electrostatic	-160596	-162544.	-1948
Torsions	-66676.0	-66615.0	61				
Cross-Terms	2791.06	2929.64	138.58				

The main components of the total energy are the non-bond terms (i) electrostatic, (ii) Van der Waals terms, and (iii) the bond torsion. These terms make the system stable whereas the bond rotation, the bond stretching, and the cross-terms are positive thus tend to dissociation the system.

4.3. Impurity Distributions Within The Dislocation Atmosphere

Interactions of single atoms (N, O, C) and (Ge, P, B, Al) with edge dislocation have been calculated as a function of their concentration close to the dislocation as well as the sample temperature over a wide range including wafer annealing temperature. Although the probabilities of site occupancy were calculated for the octahedral interstitial sites (relevant to this study) they are displayed on the closest crystal sites in the $(\bar{1}10)$ plane. This is due to restrictions in the used graphical interface. Impurity distributions around an edge dislocation are given in the following for O, C, N, and Ge.

4.3.1. Oxygen

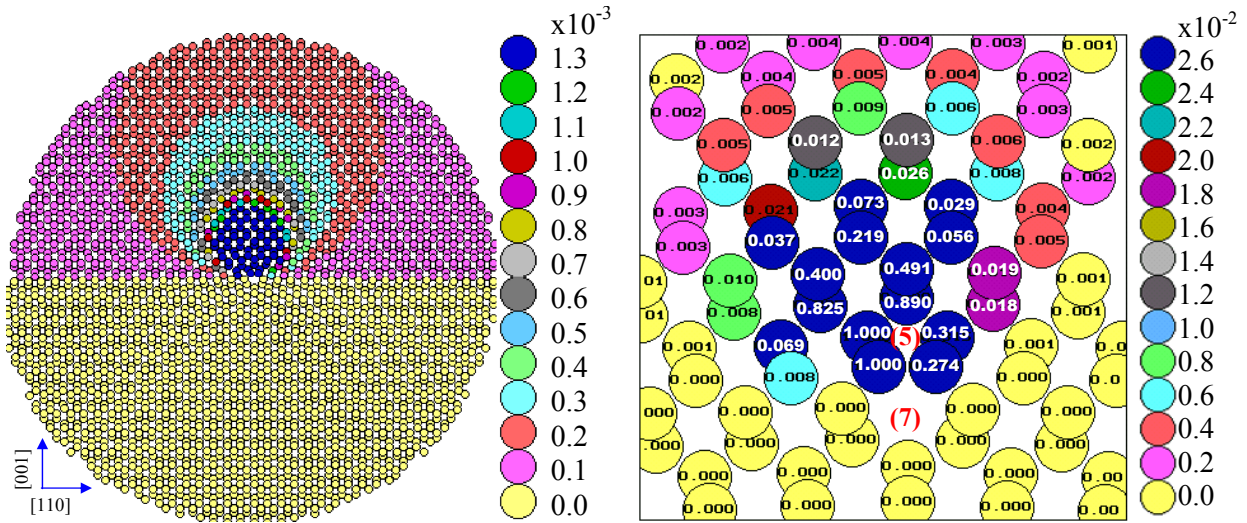


Fig. 76: Oxygen distribution in a 90° dislocation field at $T=300^\circ\text{K}$. In this case the O content around the dislocation is $x=10^{-4}$. The energy of the system after relaxation is

-2.403565 eV. The numbers (5) and (7) are labels for the penta- and septa-rings, respectively, located in the dislocation core.

4.3.2. Nitrogen

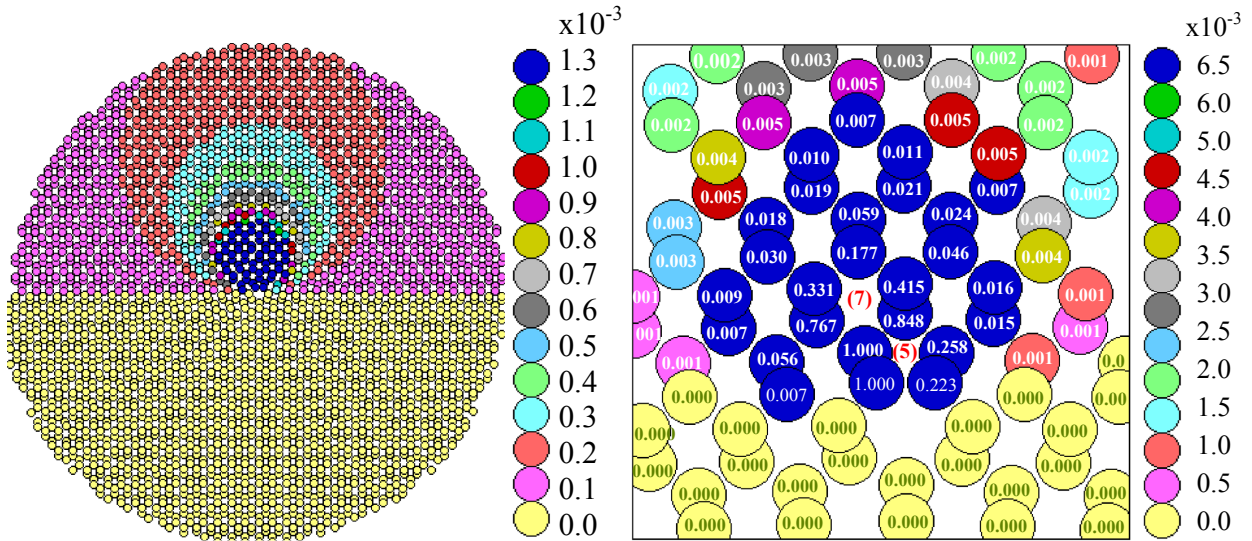


Fig. 77: Nitrogen distribution in 90° dislocation field at $T=300\text{K}$, shown in $(\bar{1}10)$ plane. Like oxygen in Fig. 76, the N content is taken $x=10^{-4}$. The energy of the system after relaxation is: -2.218454 eV.

4.3.3. Carbon

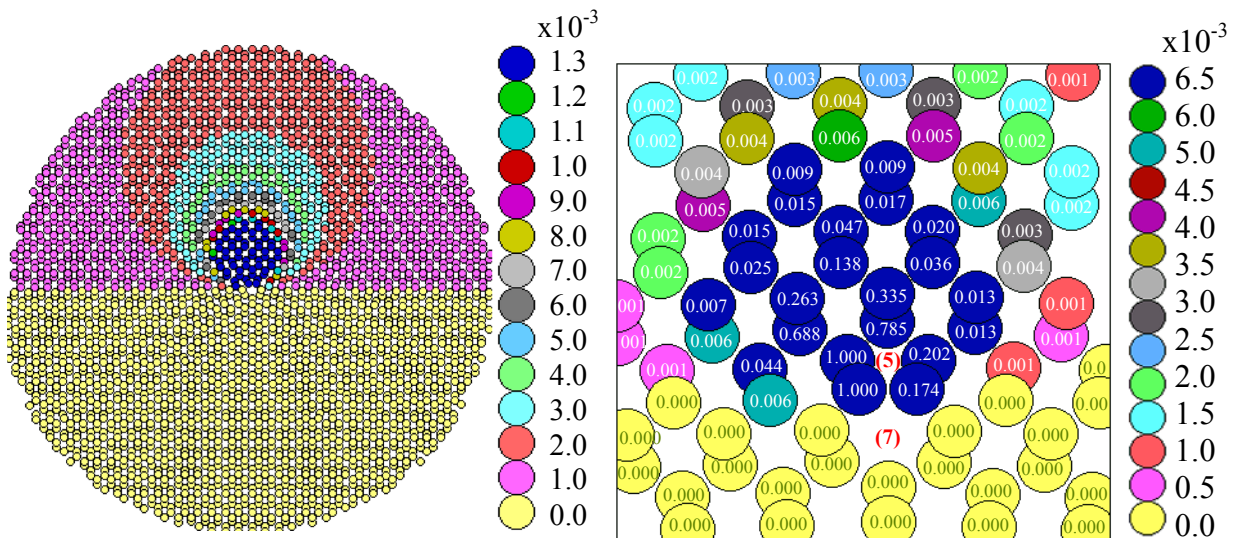


Fig. 78: Carbon distribution in a 90° dislocation field at $T=300\text{K}$, shown in $(\bar{1}10)$ plane. Again, the C content is taken $x=10^{-4}$. The energy of the system after relaxation is -2.023677 eV.

4.3.4. Germanium

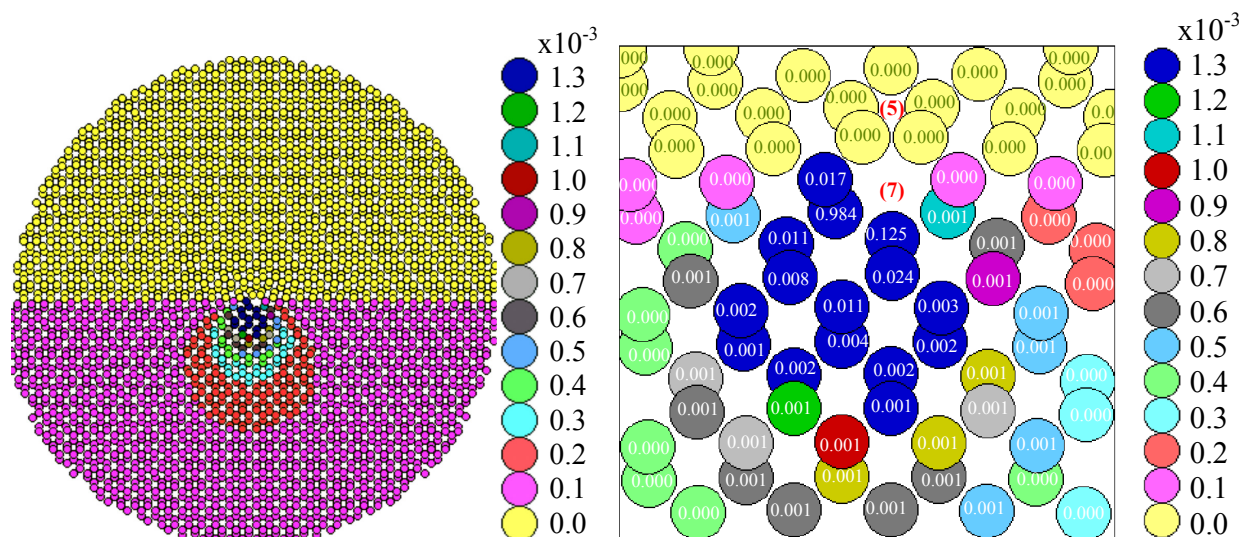


Fig. 79: Germanium distribution in a 90° dislocation field at $T=300^\circ\text{K}$, shown in $(\bar{1}10)$ plane. Like in previous cases, the Ge content is taken $x=10^{-4}$. The energy of the system after relaxation is: -0.377321 eV.

In Fig. 76 oxygen atoms appear to populate the dislocation core immediate surrounding with highest probability of site occupation as compared to other light elements. The penta-ring and one of the two upper hexa-rings, both in the compressive part of the dislocation domain, are the most likely zones for Oxygen atom localization. The lower part of the septa-ring is unlikely to hold O atoms. Likewise N and C in tetrahedral positions locate themselves in the top region (compressive side) of the dislocation, as shown in Fig. 77 and Fig. 78. These two light elements have a preference for the penta-ring as well. It is important to note that carbon is distributed in a more diffuse way than Nitrogen around the dislocation.

Germanium has no preference for the penta-ring but a little for the septa-ring. Even though germanium locates itself preferentially in the dilated half space by the dislocation (bottom region), see Fig. 79, it does not populate the near field of the edge dislocation. This shows that Ge is way less effective in locking an edge dislocation than O, N, and C.

It is important to note the differences in the distribution and the probability lead by O then N then C, while Ge is repelled.

Oxygen is very likely to locate itself in the very core of the edge dislocation and its distribution spans over a cylinder of 7 neighbors radius. This behavior is slightly attenuated for N and little more attenuated for C. This leads to the conclusion that the three impurities play almost the same role for the atmosphere composition with slight reduction for N then C. In contrast, Ge

scores only a full site and one tenth in a second site within the dislocation core, but absent otherwise.

4.4. Impurity-dislocation binding energy and shear stress for dislocation separation

The minimum shear stress required to separate the dislocation from its atmosphere is proportional to the maximum of the energy gradient given by [325]:

$$\tau = \frac{1}{2\sqrt{2} b^2} \left(\frac{dE}{dx} \Big|_{\max} \right) \quad (59)$$

In the following, the impurity-dislocation interaction energy and the separation shear stress are given for a number of impurities and other experimental conditions.

4.4.1. Effect of the impurity Type

For the isoelectronic substitutional impurities (C, Ge) the bonding occurs with four neighboring silicon atoms. For others like N, we have considered in this first step a rough approximation of VN complex, but the charge effect was omitted. In addition, we have considered that the trivalent atom sits in a four coordinated site, thus is bounded to its four neighboring atoms with an equally distributed charge of $\frac{3}{4}$ per neighboring silicon atom.

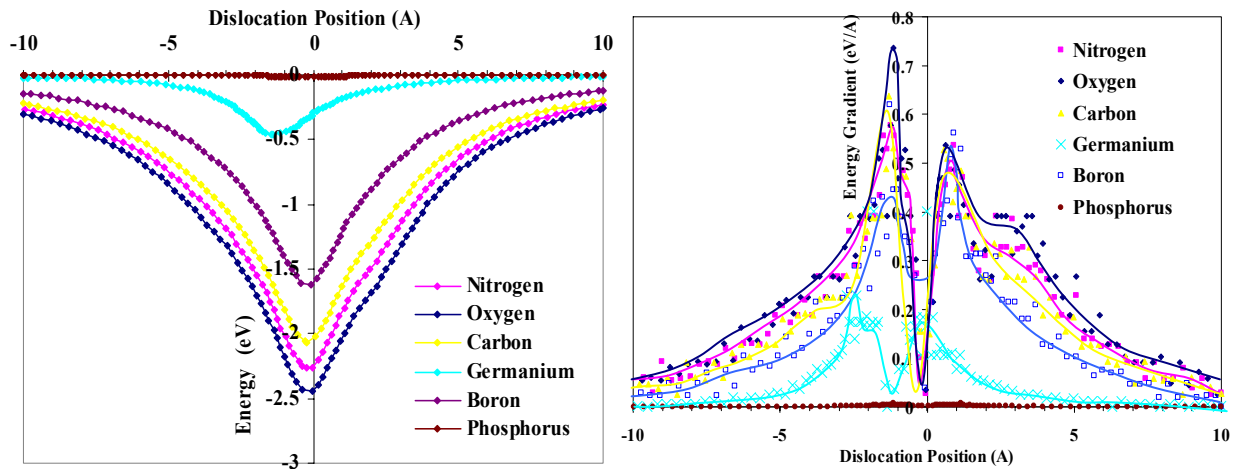


Fig. 80: (a) Distribution of various type of impurities in a 90° dislocation field at $T=300^\circ\text{K}$. The impurity content is taken $x=10^{-4}$. (b) Energy gradient (proportional to shear stress) versus separation distance dislocation-impurity atmosphere.

The size effect contribution to the edge dislocation-impurity interaction energy depends on the position. The maximum magnitude (i.e., at the dip) represents the binding energy, given in Table XVI per dislocation unit length for local impurity atomic fraction of 10^{-4} . Oxygen,

nitrogen then Carbon appear to be distinctively well bound to dislocation, whereas for instance P and B and to lesser extent Ge do not attach themselves to the dislocation.

On the other hand the shear stress which is proportional to the gradient of the impurity-dislocation interaction energy appears to be the highest for N then for O and C, but no shear stress could arise for instance from B and P impurities. Germanium exerts high shear stress only very close to the dislocation core, due to its narrow distribution around the dislocation core.

Table XVI: Dislocation-impurity binding energy due to size effect, for a number of prominent impurities in silicon at 10^{-4} . The type of the considered dislocation is edge.

	P	Ge	B	C	N	O
Binding Energy (eV/Å)	0.0077	0.338	1.19	1.54	1.66	1.80

4.4.2. Effect of the Impurity Concentration

The relationship of impurity concentration and atmosphere formation was investigated for Nitrogen only (for now). It is important to note that the impurity concentration to be considered must be an average value within the short range (several tens of Å) from the dislocation core. In the case of N, it must be much higher than the bulk concentration. It has been demonstrated that N locates itself along dislocations [330], scratches [331], and strained regions [332]. It is acceptable (for a first approximation) to use values in the range of N concentration measured close to the wafer surface (obtained by SIMS) and precipitate interfaces in N-CZ Si (estimated by EELS). We have demonstrated that N segregates to such boundaries, and we found a sharp concentration gradient at the surface of N-CZ wafers. In as grown N-CZ silicon $[N]=3.4 \times 10^{16} \text{ cm}^{-3}$ $[O]=4.7 \times 10^{18} \text{ cm}^{-3}$ and in a Lo-Hi cycled N-CZ wafers we found $[N]=8.6 \times 10^{17} \text{ cm}^{-3}$ and $[O]=1.7 \times 10^{20}$ annealed at 750° C for 64 hrs then 1050° C for 16 hrs.

Note that dislocation-impurity interactions are localized within a cylinder of 30 \AA in diameter. This implies that dislocations separated by more than 30 \AA will not interact through their atmosphere if less than 10% impurities were captured; this verifies that our initial hypothesis of using 70 \AA for non-interacting dislocation is largely fulfilled.

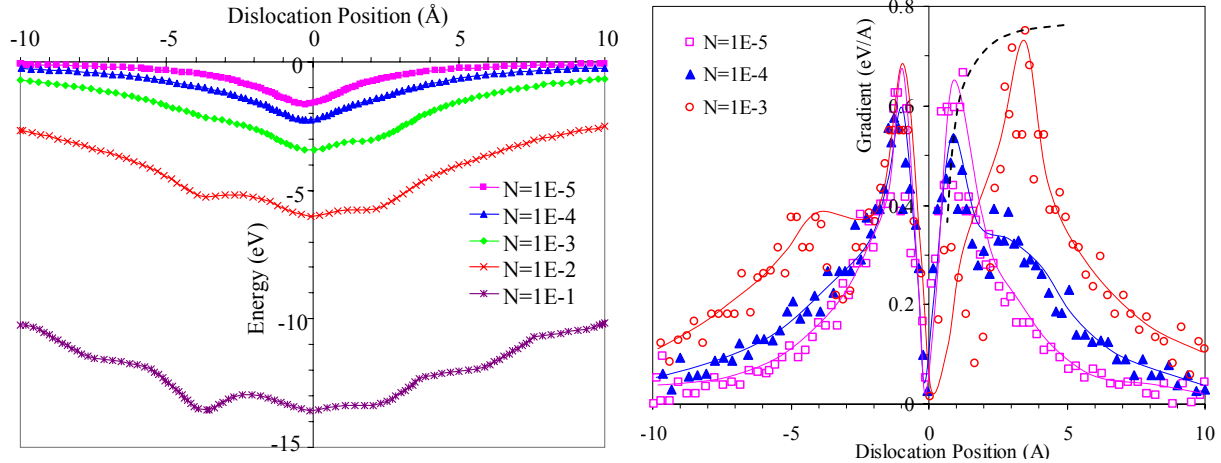


Fig. 81: (a) interaction energy of edge dislocation with nitrogen vs. N fraction (in the atmosphere), (b) and the shear stress. The dashed curve shows the maximum shear stress, that the dislocation has necessarily to overcome if it has to move away from its atmosphere.

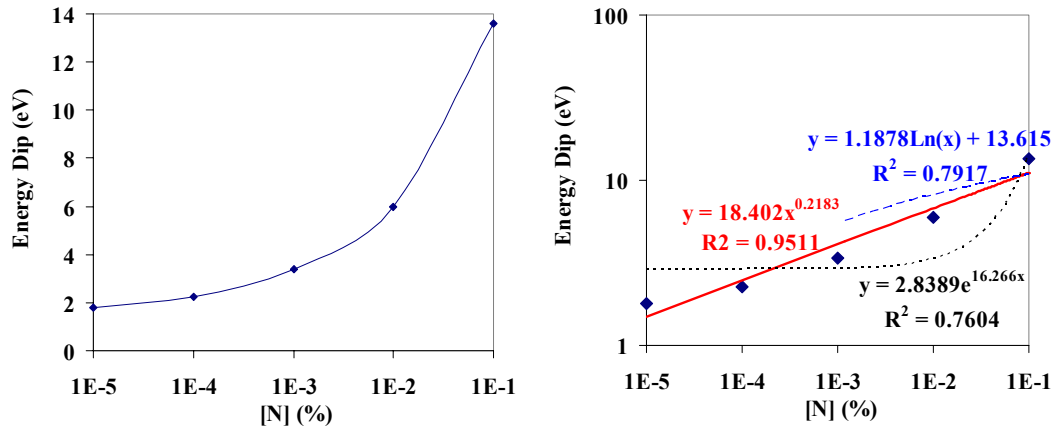


Fig. 82: (a) Binding energy versus N content, and (b) fitting curves of binding energy vs. [N].

The potential energy dip is increased with the concentration. At high concentrations (starting from 10^{-1}) the model does not well behave (undulations appear). To overcome this problem, certainly the bulk material property changes should be included. In addition, one has to address the crystal distortion by impurities at such high concentrations (these effects have been neglected in the model). Figure 9 shows the minimum of the nitrogen-dislocation interaction energy. The minimum represents the contribution of the size effect to the binding energy. The best trend found for the binding energy as a function of the N atomic fraction is a power function

$$E(\text{eV})=18.4 C_N^{0.22} \quad (60)$$

where E (eV) is the binding energy and C_N is the N atomic fraction in the dislocation atmosphere. This fitting does not account for the saturation beyond $x=10^{-2}$.

The interaction energy gradient of the edge dislocation with N atoms appears in Fig. 81 a. The energy gradient tend to flatten out at high concentration. The energy gradient as a function of N concentration is given in Fig. 83 (a); it instructs on the locking effect. This effect saturates at high N content, while it spills over a wider region, see FWHM curve in Fig. 83 (b).

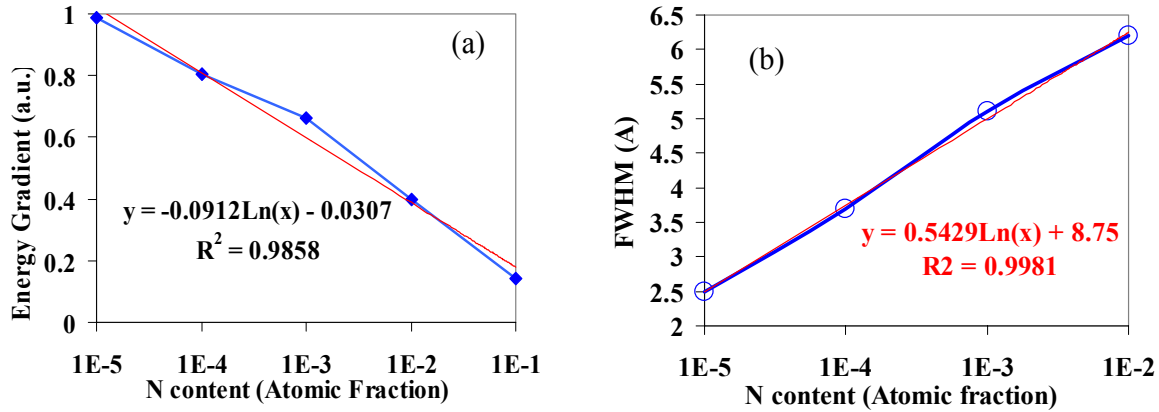


Fig. 83: (a) Interaction energy gradient calculated as $G = \frac{E_{\max} - E_{\min}}{E_{\max} + E_{\min}}$ (where E_{\min} is the energy dip and E_{\max} is the energy at 10 Å), (b) FWHM of the impurity distribution around edge dislocation as a function of N content (in atomic fraction). The best trend found for both curves is logarithmic.

For a nitrogen fraction of 10^{-3} , at 3.5 Å away from its equilibrium position, the dislocation must overcome a shear stress twice as high as for an atomic fraction of 10^{-5} , while it increases drastically (four times) for a concentration of 10^{-3} . The trend of these variations is given in Fig. 82. The shear stress increases significantly and seems to have higher effects at concentrations between 0.1% and 1% in the vicinity of the dislocation. At higher concentration the shear is reduced, apparently due to the change in the bulk material properties.

4.4.3. Temperature Effect on the dislocation atmosphere

The used model departs from a Fermi-Dirac distribution of the impurities in the bulk and accounts for the perturbation of this distribution around the dislocation. Such a perturbation is therefore affected by the sample temperature. In this study the temperature is varied from about RT to 950°C

The maximum shear stress occurs at the inflection point. The dislocation is able to oscillate a little around its equilibrium position within the interaction potential well (represented by the shear stress well).

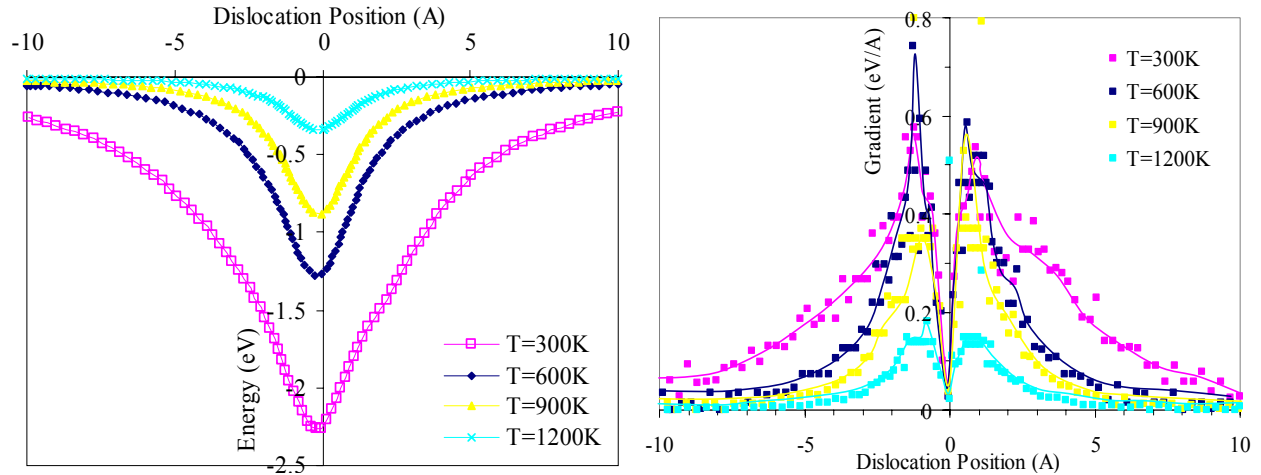


Fig. 84: Effect of the N concentration on (a) the interaction energy impurity-dislocation for an edge type (b) and the shear stress.

5. Conclusion

Among the impurities we have studied (O, N, C, Ge, B, P) oxygen locates itself at the core of an edge dislocation. O, N, and C distributions spread over a cylinder whose radius is about 7 neighbors in the plane normal to the dislocation line. The three impurities O, N, and C play slightly the same role for the atmosphere composition. In contrast Ge is not gettered by the edge dislocation in large number; almost only 1.2 sites are allowed for Ge.

The penta-ring and the upper hexa-ring, both in the compressive part of the dislocation domain, are the most likely zones for oxygen atom localization; whereas the septa-ring which is in the dilation side of the dislocation (lower part) repels O atoms. Likewise N and C in tetrahedral interstitial positions locate themselves in the compressive side of the dislocation. It is important to note that carbon is distributed in a slightly more diffuse way than Nitrogen around the dislocation.

The self-energy of an edge dislocation calculated by molecular mechanics is $156 \text{ meV}/\text{\AA}$.

It is suggested that the dislocation is free to fluctuate within a ring like stress, before it breaks away from its atmosphere.

Our calculations lead to an empirical expression for the binding energy of N with an edge dislocation as a function of the atomic fraction within the dislocation atmosphere.

Chapter IX
SUMMARY AND GENERAL CONCLUSIONS..... 164

Chapter IX

SUMMARY AND GENERAL CONCLUSIONS

Oxygen has been conventionally used for silicon wafer toughening and for impurity internal gettering away from devices zone. Integration and productivity increase lead to move toward large wafers (300mm) and reduction of oxygen precipitate size, which implies a reduction of the initial oxygen level. It appeared difficult to conciliate between the two technology requirements, and a new solution had to be found. On the other hand Float Zone (FZ) silicon has the highest minority carrier lifetime, thus is the ideal for high efficiency sliver and high concentration solar cells. However, FZ Si does not withstand handling during solar cell production. Nitrogen doping appeared the solution for these issues. Tailored growth and annealing conditions allow adjustment of point defect clustering and chemical reactions in solid state Si matrix, which effect the hardness. In this work we have investigated the structural, chemical, and mechanical properties of nitrogen doped silicon at different scales.

The importance of this work stems from the fact that IC technology demanded improvement of CZ silicon quality by reducing the oxygen content and use very light N doping level. Doping with a very low level of nitrogen effectively enhances the mechanical properties of low oxygen CZ silicon. However, nitrogen generates defects and creates segregation to the surface and pile up of both oxygen and nitrogen at the wafer sub-surface. Defect size distributions were studied in nitrogen-doped Czochralski (N-CZ) silicon wafers using an Oxygen Precipitate Profiler and Wright-Jenkins etching. These showed unique depth dependence in Low-High and High-Low-High cycled N-CZ wafers. New phenomena observed include a high defect density at the surface that decreases within the top 2 μm of the so-called denuded zone. In contrast to N-free CZ Si, for which the first High step annealing dissolves the grown-in defects, these appeared stable and or resilient in N-CZ Si in regard to the high temperature. As a result, the defect size distribution in the bulk was found to be independent of the annealing cycle. It was also found that the depth dependent defect density correlates well with the oxygen and strongly with the nitrogen concentration profile, suggesting that the N is the leading impurity in

the defect formation processes even though at very low concentration. Nitrogen appeared to effectively modify the nucleation regime by increasing the oxygen mobility, which results in a drastic increase of the nuclei density. At low temperature, under external stress, nitrogen and oxygen co-segregate to the surface where the stress is applied.

Nitrogen segregation and co-precipitation with oxygen in N-CZ silicon wafers are investigated based on extended defect structure and chemical composition as a function of depth. High resolution nitrogen and oxygen SIMS imaging revealed strong coupling of oxygen with nitrogen in annealed as well as in “as-grown” N-CZ Si wafers. In both cases, the near surface regions appeared highly supersaturated in N and O forming a continuum defect initiated by N-O complexes. The N and O stoichiometry depth profiles were found to depend on the material thermal history. The spatial variation of this ratio was also determined for precipitates using a combination of Scanning Transmission Electron Microscope (STEM) in Z-contrast mode with Electron Energy Loss Spectroscopy. The precipitate atomic and micro-structures, analyzed by High Resolution Transmission Electron Microscope and STEM, clearly demonstrate that second phase precipitate is precursor to a third phase, that is an outer oxynitride shell. The N and O co-segregation phenomenon clearly occurs at precipitate/matrix interface, in a similar fashion as in the near surface region. A new oxygen precipitation mechanism in N-CZ Si was then proposed. This mechanism involves (i) concurrent nucleation and growth, (ii) trapping of O inside the oxynitride shell, which cancels precipitate dissolution, and (iii) big precipitates do not grow at the expenses of small ones.

Nanoscale extended defects in N-CZ silicon annealed wafers were examined by high resolution TEM (HRTEM), Scanning TEM in the Z-contrast mode, and Electron Energy Loss Spectroscopy (EELS). Precipitate composition and strain at the interface are discussed in terms of point defect and local stress distributions. HRTEM combined with Z-contrast images and line-scans across precipitates show distinct regions within precipitates, and EELS provided a N to O concentration ratio between 2%, inside the precipitates, and 17 %, at the boundaries. Two-phase oxynitride precipitate formation mechanisms are suggested to be controlled by the interactions of nitrogen and point defects. The concerted effect of local stress and N segregation on oxygen precipitate morphology and on stacking fault formation is examined in connection to N-V species distribution. Precipitation and self-interstitial condensation mechanisms were found dependent on the depth. Precipitate growth appears to have two components, lateral and

transverse. The former depends largely on the depth, thus the point defect environment, particularly the interstitial flux and the stress at the interface that is modulated by vacancies and N-V complexes.

Point defect incorporation at the very moment of liquid-solid phase transform have been discussed in relation to the generation of the primary chemical complexes. The various stages of complex transformation were also overviewed in later stage of growth, based on published data and the theoretical results obtained in this work. A unified formation mechanism for void formation and oxygen precipitation based on V-O complex model, developed by Kiman Bae (former student of Prof. G. Rozgonyi) was reviewed as it represents the starting point of this work. This model was developed based on the analysis oxidation-induced stacking fault ring (OSF-Ring) structure. Its main features are the V-O complex and the dominance of vacancies lateral diffusion. For nitrogen doped CZ silicon, the model was extended to include the (i) competition of V-O and N-O complexes, (ii) the sequence of N pair transformation, (iii) the V_2N_2 nucleus, (iv) the intermediary defect VN_2 , and (v) the mobile N_2 .

These N related features were investigated by studying the electronic structure, formation energy, and thermal stability of nitrogen-vacancy complexes (as core defects) that can be bound to many more oxygen atoms. The atomic structure of a large variety of chemical complexes have been investigated using density functional theory and semi-empirical Hartree-Fock calculations. The calculated energies of formation in the ground state show that VN_2 is not stable, whereas V_2N_2 when formed from VN_2 is the most stable, followed by N_2 and V_2N_2 formed from a di-vacancy. The calculated free energy changes of the considered chemical reactions confirm the low stability of VN_2 compared to V_2N_2 . The latter can form during crystal growth from VN_2 , whereas reactions between N_2 and di-vacancy can also occur upon wafer heating. At low nitrogen concentration ($\sim 5 \times 10^{13} \text{ cm}^{-3}$), only about 10% of vacancy concentration is converted into VN_2 , while at high nitrogen concentration ($\sim 10^{16} \text{ cm}^{-3}$) about 75% of vacancies are trapped by N. V_2N_2 appeared to create a potential well of -2.4 eV for oxygen and about -0.3 eV for vacancies, suggesting that the stable V_2N_2 is a nucleus for oxygen precipitation while it is a weak trapping center for vacancies.

Extended defect nucleation and growth in N-CZ silicon crystals are investigated in terms of trapping vacancy and oxygen atoms by nitrogen-pairs using molecular mechanics. The results have been correlated to the formation energy and stability of nitrogen-vacancy-oxygen

complexes obtained by ab-initio density functional theory. On one hand N_2 in split interstitial position and V_2N_2 were found to have strong attraction to oxygen (the binding energy BE ~ -2.9 and -2.5 eV, respectively), whereas they bind weakly to vacancies (BE ~ -0.25 eV, one order of magnitude lower). On the other hand VN_2 can only be weakly coupled to remote vacancies (BE ~ -0.3 eV), though it reconstructs into stable V_2N_2 if the vacancy is trapped (BE ~ -7.9 eV), but more importantly VN_2 repels oxygen atoms (energy barrier 0.8 eV). This with the FTIR weak line confirm the proposed metastability character of VN_2 .

The interaction energy related results agree with the calculated formation energy and the degree of stability of nitrogen-vacancy-oxygen complex at ground state and by FTIR absorption line analysis, presented in this work. Combining the various results (complex energy of formation, thermal stability, and identification based on FTIR analysis) one can suggest that N_2 and V_2N_2 are nucleation centers for oxygen precipitation rather than void formation. The overall and most attracting result is the good agreement with the experimental data on defects in the “as-grown” N-CZ silicon, their nature and concentration ranges. We can see clearly why (i) nitrogen results in large concentration of precipitates, (ii) the absence of voids in contrary to N free CZ silicon, (iii) the strength of precipitate that grow on oxynitride nuclei, and (iv) the strong coupling of oxygen with nitrogen.

The N- and O- related chemical complex identification was validated using the HR-FTIR setup at the Advanced Light Source. Using data from atomistic calculations, we have singled out the prominent FTIR lines. A variety of complexes in each of the three Lo-Hi annealed N-CZ wafer regions were identified. A strong correlation of the intensity depth profile of absorption lines with the OPP defect density were found for the three defect regions, in particular the subsurface region and at the LDZ-bulk interface. The strong correlation between OPP depth profile and FTIR intensity lines demonstrate the validity of our complete chemical complex theoretical analysis (atomic structure of V-N-O complexes, energy of formation, thermal stability, and FTIR finger print).

Oxygen and nitrogen effects on dislocation motion have been studied in relation to mechanical properties of N-doped and N-free CZ and FZ silicon. Silicon hardness and elastic modulus were found to significantly vary with O and N contents. CZ Si appeared about twice as hard as pure FZ Si. Doping FZ Si with N significantly increases the hardness. Silicon is softened by heavily doping it with B, while this dopant reduces the O enhanced silicon hardness. This could

be explained by the B-O complex formation. It was found that the N and O denuded zone in annealed wafers is softer than the bulk region. The large hardness differences was investigated based on dislocation-impurity interactions. In close correlation with measured hardness, atomistic calculations showed that there are three groups of impurities that produce distinct dislocation locking effects in silicon. The model used, developed by R. A. Johnson, is based on impurity size effects and the continuum theory of elasticity. The distribution of O, N, and C appeared similarly localized at the core of edge dislocations, but totally different from other elements such as Ge. Light elements appear to strongly bind with edge dislocations, in line with the observed hardness enhancement by O and N doping. At local atomic fraction of 10^{-4} impurity-dislocation binding energy varies from 0.008 eV/Å for P to 1.7eV/Å and 1.8 eV/Å for N and O, respectively.

In conclusion, the effects of N and O on the hardness strongly correlates with their locking effects on edge dislocations. The BE of these impurities is 200 times higher than phosphor. Similarly, the dislocation-impurity separation shear stress is higher for O, N, then C than all other impurities.

To close this report, one can affirm that slightly doping CZ silicon with nitrogen offers a wide range of defect engineering. More importantly, a precise knowledge of point defect interactions allows creating options for nanoscale design of new materials and devices. As a matter of facts we are developing new techniques for directed self assembling structures by exploiting the nitrogen properties that are discussed along this report, particularly the segregation to the surface, local stresses induced by nitrogen clusters, and coupling of oxygen to nitrogen complexes.

LIST OF PUBLICATIONS RELATED TO THE THESIS

1. Structural Properties / Defect Size Distribution in N-CZ Si

1. A. Karoui, F. Sahtout Karoui, G. A. Rozgonyi, and D. Yang, Oxygen Precipitation in Nitrogen Doped Czochralski Silicon Wafers. I: Formation Mechanisms of Near-Surface and Bulk Defects, *J. Appl. Phys.*, **96**(6), 3255 (2004).
2. A. Karoui, and G. A. Rozgonyi, Oxygen Precipitation in Nitrogen Doped Czochralski Silicon Wafers. II: Effects of Nitrogen and Oxygen Coupling, *J. Appl. Phys.*, **96**(6), 3264 (2004).
3. A. Kvit, A. Karoui, G. Duscher, and G. A. Rozgonyi, Umbrella-like Precipitates in Nitrogen-Doped CZ Silicon Wafers, *Appl. Phys. Lett.* **84**(11), 1889 (2004).
4. G. A. Rozgonyi, A. Karoui, A. Kvit and G. Duscher, Nano-scale analysis of precipitates in nitrogen-doped Czochralski silicon, *Microelectronic Engineering*, **66**, Issues 1-4, 305-313 (2003).
5. A. Karoui, F. S. Karoui, D. Yang and G. A. Rozgonyi, *Solid State Phenomena*, 82-84, 69 (2002).
6. A. Karoui, F. Sahtout Karoui, A. Kvit, G. A. Rozgonyi, and D. Yang, Role of nitrogen related complexes in the formation of defects in silicon, *Appl. Phys. Lett.* , **80**(12), 2114 (2002).
7. A. Karoui, F. Sahtout Karoui and G. A. Rozgonyi, Nitrogen Related Complexes and Extended Defect Formation in N-CZ Silicon Wafers, *Solid State Phenomena*, **74**, 30 (2000).

2. Thermodynamics of chemical complexes in N-CZ Si

1. A. Karoui, Molecular Mechanics and Continuum Elasticity Theory Calculations of Dislocation Locking by Impurities in Silicon and Correlation with Mechanical Properties by Nanoindentation, Invited talk at the Eleventh International Conference On Composites/Nano Engineering (ICCE-11), Aug.8-14, 2004, Hilton-Head, SC.
2. F. Sahtout Karoui, A. Karoui, G. A. Rozgonyi, M. Hourai, and K. Sueoka, Characterization of Nucleation Sites in Nitrogen Doped Czochralski Silicon by Density Functional Theory and Molecular Mechanics, *Solid State Phenomena*, Vols. **95-96**, p. 99 (2004).
3. A. Karoui, F. Sahtout Karoui, G. A. Rozgonyi, M. Hourai, and K. Sueoka, Structure, Energetics and Thermal Stability of Nitrogen-Vacancy Related Defects in Nitrogen Doped Silicon, *J. Electrochem. Soc.*, **150** (12), G771-777 (2003).

4. A. Karoui, F. Sahtout Karoui, G. A. Rozgonyi, M. Hourai, and K. Sueoka, First Principle Calculations for Nitrogen-Vacancy Related Defects in Nitrogen Doped Silicon: Structure, Energetic and Thermal Stability, *Semiconductor Silicon 2002*, Vol. 2, Ed. H. Huff et al, p. 670. (2002).
3. Identification of Chemical complexes in N-CZ by Spectroscopy Methods
 1. A. Karoui, T. Buonassisi, M. Martin, F. Sahtout Karoui, G. A. Rozgonyi, E. R. Weber, Stress-Induced Nitrogen and Oxygen Segregation and Complex formation by High Resolution Synchrotron FTIR, Advanced Light Source, Berkeley, Oct.18-20, 2004.
 2. A. Karoui, T. Buonassisi, F. Sahtout Karoui, G. A. Rozgonyi, M. Martin, E. R. Weber, T. Ciszek, Stress-Induced Nitrogen and Oxygen Segregation and Complexing Investigated by Synchrotron FTIR, 14th Workshop On Crystalline Silicon Solar Cell, Materials and Processes, National Renewable Energy Laboratory, Aug. 10-13, 2004, Winter Park, CO, USA, pp. 77 (2004).
 3. F. Sahtout Karoui, A. Karoui, G. A. Rozgonyi, Vibrational Spectra of Nitrogen-Oxygen Defects in Nitrogen Doped Silicon Using Density Functional Theory, in *Silicon Front-End Junction Formation-Physics and Technology*, Eds. P. Pichler, A. Claverie, R. Lindsay, R. Orlovski, W. Windl, Mat. Res. Soc. Symp. Proc. Vol. **810**, C8.18 (2004).
 4. F. Sahtout Karoui, A. Karoui, G. A. Rozgonyi, N. Inoue, H. Harada, Ab-initio Vibrational Analysis of Nitrogen Defects in CZ Silicon, 201st Meeting of The Electrochemical Society, Abstracts, p 356 (2002).
 5. D. Funao, I. Ohkubo, N.Inoue, A. Karoui, F. Sahtout Karoui, and G.A.Rozgonyi, Theoretical Analysis of Nitrogen Complexes in CZ Si, Proceeding of the 202nd Meeting of the Electrochemical Society, Oct. 20-24, Salt Lake city, p. 133, (2002).
 6. F. Sahtout Karoui, A. Karoui, G. A. Rozgonyi, N. Inoue, Identification of Dominant Nitrogen-Oxygen Defects in Silicon using First Principles Calculations, 203rd Conference of The Electrochemical Society, April 27-May 2, Paris, 2003.
 7. N. Inoue, D. Funao, I. Ohkubo, A. Natsume, F. Sahtout Karoui, A. Karoui, G. A. Rozgonyi, Analysis on reaction process of nitrogen complexes in CZ silicon, submitted to DRIP X, Batz-sur-Mer, France, 29 September-October 2, 2003.
 4. On Aspects of Nucleation and Stimulated Defects in N-CZ
 1. N. Stoddard, A. Karoui, G. Duscher, A. Kvit, and G. Rozgonyi In-Situ Point Defect Generation and Agglomeration during Electron-Beam Irradiation of Nitrogen-Doped Czochralski Silicon, *Electrochem. and Solid-State Lett.* , **6**(11) pp. G134-G136 (2003).
 2. N. Stoddard, A. Karoui, G. Duscher, A. Kvit, and G. Rozgonyi, In-Situ Observations of Point Defect Generation and Complexing During Electron Beam Irradiation of Nitrogen Doped

Czochralski Silicon, PV 2002-20 High Purity Silicon VII -- C. L. Claeys, M. Watanabe, P. Rai-Choudhury, and P. Stallhofer; Salt Lake city, p. 347 (2002).

5. Point Defect Clustering in N-CZ

1. A. Karoui, Faouzia Sahtout Karoui, George A Rozgonyi, Molecular Dynamics and First-Principles Calculations of Defect Precursors Formation in N doped Silicon, MRS Spring Meeting 2004, Symposium Q: Nucleation Phenomena—Mechanisms, Dynamics, and Structure.
2. F. Sahtout Karoui, A. Karoui, and G. A. Rozgonyi, Simulation of Point Defect Clustering in CZ-Silicon Wafers On The Cray T3E Scalable Parallel Computer: Application to Oxygen Precipitation, MSM2000, San Diego, March 27-29, p. 98, (2000).

6. Mechanical Properties

1. A. Karoui, G.A.Rozgonyi, Effect of Grown-in Light Element Impurities on PV Silicon, DOE Solar Program Review Meeting, Denver, Oct.25-28, 2004.
2. A. Karoui, G. A. Rozgonyi, Molecular Mechanics and Continuum Elasticity Theory Calculations of Dislocation Locking by Impurities in Silicon and Correlation with Mechanical Properties by Nanoindentation, 14th Workshop On Crystalline Silicon Solar Cell, Materials and Processes, National Renewable Energy Laboratory, Aug. 10-13, 2004, Winter Park, CO, USA, pp. 127 (2004).
3. A. Karoui, Atomistic Modeling of Impurity Atmospheres in Silicon and Dislocation Locking Effects, in *Silicon Front-End Junction Formation-Physics and Technology*, Eds. P. Pichler, A. Claverie, R. Lindsay, R. Orłowski, W. Windl, Mat. Res. Soc. Symp. Proc. Vol. **810**, C8.19, (2004).
4. A. Karoui, G. A. Rozgonyi, Ted Cizek, Effect of Oxygen and Nitrogen Doping on Mechanical Properties of Silicon Using Nano-Indentation, in *Nanoscale Materials and Modeling Relations Among Processing Microstructure, and Mechanical Properties* Eds. P. M. Anderson, T. Foecke, A. Misra, R. E. Rudd, Mat. Res. Soc. Symp. Proc. Vol. **821**, P8.36 (2004).

7. Optical Properties

1. A. Karoui, R. Zhang, G. A. Rozgonyi, and, T. Cizek, Silicon Crystal Growth and Wafer Processing for High Efficiency Solar Cells and High Mechanical Yield, in Proceedings of NCPV, NREL/CP-520-31057, Lakewood, CO, 14-17 Oct. 2001.

8. Manuscripts Submitted (or to be submitted)

1. N. Stoddard, G. Dusher, A. Karoui, F. Stevie, G. Rozgonyi, Segregation and Enhanced Diffusion of Nitrogen in Silicon Induced by Low Energy Ion Bombardment, submit to J. Appl. Phys.
2. A. Karoui, T. Buonassisi, F. Sahtout Karoui, G. A. Rozgonyi, M. Martin, E. R. Weber, Nitrogen and Oxygen Segregation and Complexing Investigated by High Resolution Synchrotron Fourier Transform Infra Red, to Physica Status Solidi (a)
3. A. Karoui, G. A. Rozgonyi, Molecular Mechanics and Continuum Elasticity Theory Calculations of Dislocation Locking by Impurities in Silicon and Correlation with Mechanical Properties by Nanoindentation, to submit to Materials and Engineering: B
4. A. Karoui , and G. A. Rozgonyi, Nano-Scale Analysis of Precipitates and Stacking Faults in Nitrogen-Doped CZ Silicon Annealed Wafers.
5. F. Sahtout Karoui, A. Karoui, G. A. Rozgonyi, N. Inoue, ‘Nitrogen-pairs and Nitrogen-Oxygen Defects in N doped CZ Si by First-principles Calculations’, to submit to Physical Review B.

9. Patent Disclosures (based on our studies on nitrogen in silicon)

1. A. Karoui, F. Shatout Karoui, G. A. Rozgonyi, “Generation of Gradual Thin Oxynitride Layers at Near-Surface and Hetero-structure Interfaces of Nitrogen Doped Silicon Wafers by Pure Mechanical or Thermo-Mechanical Stresses for Electronic and Photovoltaic Technologies.”, filed on July 14, 2003 , File#04-004
2. N. Stoddard, A. Karoui, G. Dusher, G. A. Rozgonyi, “Ion Beam synthesis of oxynitride.”, filed on June 18, 2003, File#03-150
3. A. Karoui, F. Sahtout Karoui, G.A. Rozgonyi, T. Homma, “Directed self-organized nanoscale and quantum structures fabrication via development of stress risers on silicon on insulators”, Filed on Dec.20, 2004.

REFERENCES

- [1] G.A. Rozgonyi, *Electrochem. Soc. PV* **2002-1**, 149 (2002).
- [2] M. Tamatsuka, N. Kobayashi, S. Tobe and T. Masui, *Electrochem. Soc. PV* **99-1**, 456 (1999).
- [3] K. Nakai, Y. Inoue, H. Yokota, A. Ikari, J. Takahashi, A. Tachikawa, K. Kitahara, Y. Ohta and W. Ohashi, *J. Appl. Phys.*, **89-8**, 4301 (2001).
- [4] OPP: oxygen precipitate and defect profiler is an advanced IR interferometer microscope capable of profiling extended defects with a precipitate size resolution of 20nm and a mapping resolution of 0.7 μ m.
- [5] To be published
- [6] F. Sahtout Karoui, A. Karoui, and G. A. Rozgonyi, *Simulation of Point Defect Clustering in CZ-Silicon Wafers On The Cray T3E Scalable Parallel Computer: Application to Oxygen Precipitation*, MSM2000, San Diego, March 27-29, p. 98, (2000).
- [7] A. Karoui, F. Sahtout Karoui, G. A. Rozgonyi, M. Hourai, and K. Sueoka, *J. Electrochem. Soc.*, **150** (12), G771-777 (2003).
- [8] A. Karoui, F. Sahtout Karoui, G.A. Rozgonyi, Y. Inoue, *Electrochem. Soc. PV* **2002-2**, 670 (2002).
- [9] A. Karoui, F. Sahtout Karoui, D. Yang, G.A. Rozgonyi, *Solid State Phenom.ena*, **82-84**, 69 (2002).
- [10] R. A. Johnson, *Phys. Rev. B*, **24** (12), 7383 (1981).
- [11] A. Karoui, F. Sahtout Karoui, G.A. Rozgonyi, Patent filed on: July 14, 2003 , File#04-004.
- [12] N. Stoddard, A. Karoui, G. Dusher, and G.A. Rozgonyi, Patent filed on June 18, 2003, File#03-150.
- [13] A. Karoui, F. Sahtout Karoui, G.A. Rozgonyi, T. Homma, Filed on Dec.20, 2004.
- [14] Masaro Tamatsuka, *Correlation of Oxide Integrity with Crystalline Defects In Silicon*, Ph.D. Thesis, North Carolina State University, Raleigh, NC, 1997
- [15] J. Czochralski, *Z. Phys. Chem.* **92**, 219 (1918).
- [16] M. Hasebe, Y. Takeoka, S. Shinoyama, S. Naito, *Defect Control in Semiconductors Vol. 1* edited by K. Sumino, 157 (1990)
- [17] V.V. Voronkov, *J. of Crystal Growth*, **59**, 625 (1982)
- [18] T. Sinno, R. Brown, W. von Ammon, E. Dornberger, *Appl. Physics Let.*, **70**, 2250 (1997)
- [19] M. Suhren, D. Graf, U. Lambert, P. Wagner, *High Purity Silicon IV (ECS)* edited by C.L. Claeys et. al., 132 (1996)
- [20] A.J.R. de Kock, *Phillips Res. Report Suppl. No. 1* (1973)
- [21] P.M. Petroff, A.J.R. de Kock, *J. of Crystal Growth*, **30**, 117 (1975)
- [22] P.J. Rocksnoer, M.M.B. Van den Boom, *J. Cryst. Growth*, **53**, 563 (1981)
- [23]. J. Chikawa, *Defects and Properties of Semiconductors: Defect Engineering* edited by J. Chikawa, K. Sumino, K.Wada, 143 (1987).
- [24] N. Miyamoto, T. Sakai, J. Nishizawa, *Proc. Gakujutsushinkokai No.145 Comm. Meet.*, 49 (1978)
- [25] S. Sadamitsu, S. Umeno, Y. Koike, M. Hourai, S. Sumita and T. Shigematsu, *Japan J. Appl. Physics*, **32**, 3675 (1993)

- [26] K. Bae, A. Karoui, G. A. Rozgonyi, *OSF ring and D-defect Formation Mechanism in Czochralski-Grown Si crystals Based on Vacancy-Oxygen Interactive Precipitation Process*, Extended Abstract No 376, ECS Vol. **97-1**, Montreal, May '97.
- [27] J. Vanhellefont, C. Claeys, *J. of Appl. Physics*, **62**, 3961 (1987).
- [28] Ki-Man Bae, *Crown-in Defects in Silicon Wafer: Formation Mechanism And Surface Reactions*, Ph.D. thesis, North Carolina State University, Raleigh, NC, USA, 1998.
- [29] T. Sinno, R. A. Brown, *J. of the Electrochem. Soc.*, **146**, (6), 2300 (1999).
- [30] J. W. Corbett, G. D. Watkins, R. M. Chrenko, and R. S. McDonald, *Phys. Rev.*, **121**, 1015 (1961).
- [31] G. D. Watkins, and J. W. Corbett, *Phys. Rev.*, **121**, 1001 (1961).
- [32] A. Umerski and R. Jones, *Phil. Mag. A* **67**, 4, 905-915 (1993).
- [33] D. R. Bosomworth, W. Hayes, A. R. L. Spray, and G. D. Watkins, *Proc. Roy. Soc.*, **A 317**, 133 (1970).
- [34] B. Pajot, Chapter V in *Oxygen in Silicon*, ed. by F. Shimura, in the series: *Semiconductors and Semimetals*, ed. by R. K. Willardson and A. C. Beer, **42**, (Academic Press 1994), p. 191.
- [35] C. A. Londos, N. V. Sarlis, L. G. Fytros, NATO ARW, 'Oxygen'96', ASI Series Vol. 17, p. 477-484, ed. R. Jones, Kluwers Academic Press, (1996).
- [36] B. G. Svensson, J. L. Lindström, J. W. Corbett, *Appl. Phys. Lett.* **47** (8), p.841-843 (1985).
- [37] P. J. Grönberg, J. von Boehm, R. M. Nieminen, NATO ARW, 'Oxygen'96', ASI Series Vol. 17, p. 441-446, ed. R. Jones, Kluwers Academic Press, (1996).
- [38] R. Falster, and V. V. Voronkov, *Materials Science and Engineering*, **B73**, 87 (2000).
- [39] M. Schrems, in *Semiconductors and Semimetals*, Chap.10, R. K Willardson &al., ed. F. Shimura, **42**, 391(1994).
- [40] J.Esfandyari, C. Schmeiser, S. Senkader, G. Hobler, B. Murphy, *J. of the Electrochem. Soc.*, **143**, (3), p 995 (1996).
- [41] J. Esfandyari et al, *ECS. Proc.*,99-1, 437 (1999).
- [42] M. Schrems, *Oxygen in Silicon* in *Semiconductors and Semimetals*1994.
- [44] A. Karoui, Q. Zhang, A. Romanowski, G. A. Rozgonyi P. Rushbrook, and Jean F. Daviet, *Dislocation Control on Silicon Wafers in a Susceptor Based Rapid Thermal Processing Tool. 6th International Conference on Advanced Thermal Processing of Semiconductors, RTP'98, Kyoto, Japan Sep. 9-11, 1998.*
- [45] W. Ohashi, A. Ikari, Y. Ohta, H. Yokota, A. Tashikawa, K. Ishizaka, H. Deai, T. Fugati, J. Takahashi, Y. Inoue, and K. Nakai, *Proceedings of Silicon Materials Science and Technology Forum '99, Kazusa Academia Park*, p. 80 (1999).
- [47] T.Abe, K.Kikuchi, S.shira, and S.Muraoka, in "Semiconductor Silicon/1981", H.R.Huff, J.Kriegler and Y.Takeishi, eds., p.54, Softbound Symp. Serv. Electrochem. Soc., Pennington, New Jersey, 1981.
- [48] K.Sumino, I.Yonenaga, M.Imai and T.Abe, *J. Appl. Phys.* **54**, 5016 (1983).
- [49] W. Ohashi, A. Ikari, Y. Ohta, H. Yokota, A. Tachikawa, K. Ishizuka, H. Deai, F. Futagi, J. Takahashi, Y. Inoue, and N. Nakai, *Proceedings of The Kazusa Akademia Park Forum On The Science and Technology of Silicon Materials*, Ed. K.Sumino, Nov. 24-26 1999, p.80.
- [50] R. Falster, D. Gambaro, M. Olmo, M. Cornara, H. Korb, *Proceedings of the Fifth International Symposium on High Purity Silicon V*, 1998, p 135-46.
- [51] R. Falster, V. V. Voronkov, and F. Quast, *Phys. Stat. Sol. (b)*, **222**, 219 (2000).
- [52] R. Falster, *Diffusion and Defect Data Part B (Solid State Phenomena)*, **82-84**, p 9-16 (2002).

- [53] V. V. Voronkov, and R. Falster, *J. of Cryst. Growth*, **204**, 462 (1999).
- [54] T. Abe, K. Kikuchi, S. Shirai, and S. Muraoka, in “Semiconductor Silicon/1981”, H. R. Huff, J. Kriegler and Y. Takeishi, eds. , Softbound Symp. Serv. Electrochem. Soc., Pennington, New Jersey, p. 54 1981.
- [55] F. Shimura, and R. S. Hockett, *Appl. Phys. Letters*, **48**, 224 (1986).
- [56] Q. Sun, K. H. Yao, J. Lagowski, and H. C. Gatos, *J. Appl. Phys.*, **67** (9), 4313 (1990).
- [57] K. Nakai, H. Yokota, J. Takahashi, K. Kitahara, A. Ikari, Y. Ohta, M. Hasebe, and W. Ohashi, *Proceedings of Silicon Materials Science and Technology Forum '99*, Kazusa Akademia Park, p. 192 (1999).
- [58]. H. Lu, D. Yang, Li L, Z. Ye, and D. Que, *Phys. Stat. Sol. (a)*, **169** (2), 193 (1998).
- [59]. J. C. H. Spence, H. R. Kolar, and H. Alexander, *J. de Physique. III*, **7**, 2325 (1997).
- [60]. D. Maroudas, and R. A. Brown, *Appl. Phys. Lett.*, **58** (17), 1842 (1991).
- [61]. T. Abe, K. Kikuchi, S. Shirai, and S. Muraoka, in “Semiconductor Silicon/1981”, H. R. Huff, J. Kriegler and Y. Takeishi, eds. , Softbound Symp. Serv. Electrochem. Soc., Pennington, New Jersey, p. 54 (1981).
- [62]. K. Sumino, I. Yonenaga, M. Imai, and T. Abe, *J. Appl. Phys.*, **54**, 5016 (1983).
- [63]. A. Karoui, G. A. Rozgonyi, R. Zhang, and T. F. Cizek, in *Proceedings of NCPV, NREL/CP-520-31057*, Lakewood, CO, 14-17 Oct. 2001.
- [64]. T. F. Cizek, T. H. Wang, R. W. Burrows, T. Bekkedahl, M. I. Symko, and J. D. Webb. *Solar Energy Materials and Solar Cells*, **41/42**, 61 (1996).
- [65]. Q. Sun, K. H. Yao, H. C. Gatos, and J. Lagowski, *J. Appl. Phys.*, **71** (8), 3760 (1992).
- [66]. W. Ohashi, A. Ikari, Y. Ohta, H. Yokota, A. Tachikawa, K. Ishizaki, H. Deai, T. Futagi, J. Takahasi, Y. Inoue, and K. Nakai, *Proceedings of Silicon Materials Science and Technology Forum '99*, Kazusa Akademia Park, p. 80 (1999).
- [67]. A. Ikari, K. Nakai, Y. Tachikawa, H. Deal, Y. Hideki, Y. Ohta, N. Masahashi, S. Hayashi, T. Hoshino, and W. Ohashi. *Diffusion and Defect, Data Part B, Solid State Phenomena*, **69-70**, 161 (1999).
- [68]. X. Yu, D. Yang, X. Ma, J. Yang, L. Li, and D. Que, *J. of Appl. Phys.*, **92**, 188 (2002).
- [69] T. Abe, T. Masui, H. Harada, and J. Chikawa, *VLSI Science and Technology*, Eds. W. M. Bullis and S. Broydo, 543 (1985).
- [70]. H. D. Chiou, J. Moody, R. Sandford, and F. Shimura, *VLSI Science and Technology, Proceedings of the Second International Symposium on Very Large Scale Integration*, Eds., K. E. Bean and G. A. Rozgonyi, Electrochem. Soc, Pennington, NJ, p.59 (1984).
- [71]. M. Tamatsuka, N. Kobayashi, S. Tobe; and T. Masui, *ECS PV. 99-1*, p. 456 (1999).
- [72]. F. Shimura, R. S. Hockett, *Appl. Phys. Lett.*, **48**, 224 (1986).
- [73] W. v. Ammon, P. Dreier, W. Hensel, U. Lambert, and L. Koster, *Material Science and Engineering*, **B 36**, 33 (1996).
- [74]. D. Yang, X. Ma, R. Fan, J. Zhang, L. Li, and D. Que, *Physica B*, 273, 553 (1999).
- [75]. A. Karoui, F. Sahtout Karoui, A. Kvit, G. A. Rozgonyi, and D. Yang, *Appl. Phys. Lett.*, **80**(12), 2114 (2002).
- [76] W. von Ammon, R. Holzl, J. Virbulis, E. Dornberger, R. Schmolke, and D. Graf, *J. of Crystal Growth*, 226 (1), 19 (2001).
- [78]. B. Park, G. Seo, and G. Kim, *Journal of Crystal Growth*, 222 (1-2), 74 (2001).
- [79]. A. Ikari, K. Nakai, Y. Tachikawa, H. Deal, Y. Hideki, Y. Ohta, N. Masahashi, S. Hayashi, T. Hoshino, and W. Ohashi, *Solid State Phenomena*, 69-70, 161 (1999).

- [80] A. Karoui, F. Sahtout Karoui, G. A. Rozgonyi, and D. Yang, Part-I, *J. Appl. Phys* **96** (4), 2004.
- [82]. T. Kumar, and S. Singh, *Bulletin Of Electrochemistry*, 10 (11-12): 518 (1994).
- [83]. T. Abe, T. Masui, H. Harada, and J. Chikawa, *VLSI Science and Technology*, Eds., W. M. Bullis and S. Broydo, (The Electrochem. Soc. Proc. PV 85-5, Pennington, NJ, 1985) p543.
- [84]. H. D. Chiou, J. Moody, R. Sandford, and F. Shimura, *VLSI Science and Technology*, Eds., K. E. Bean, and G. A. Rozgonyi, (The Electrochem. Soc. Proc. PV 84-7, Pennington, NJ, 1984) p. 59.
- [85]. S. M. Hu, *Appl. Phys. Lett.*, 36 (7), 561 (1980).
- [86]. OPP is a non-contact diagnostic tool that offers a defect-size resolution of 20 nm, for an isolated defect. Defect separation is however limited by the used wavelength (1313 nm delivered by a YLF diode pumped laser) and the numerical aperture which yields better than 1 micron effective resolution.
- [87] D. Guidotti, J. S. Batchelder, and M. A. Taubenblatt, *Appl. Phys. A*, **55**, 139 (1992).
- [88]. K. Nakai, A. Matsumura, and H. Harada, *Rev. Sci. Instruments*, **69**(9), 3283 (1998).
- [89]. T. Sasaki, T. Ono, and G. A. Rozgonyi, *Electrochem. and Solid-State Letters*, 2, (1999).
- [90]. A. Borghesi, B. Pivac, A. Sassella, and A. Stella, *J. Appl. Phys.*, 77 (9), 4169 (1995).
- [91]. K. Marsden, T. Kanda, M. Okui, M. Hourai, and T. Shigematsu, *Materials Science and Eng.* **B36**(1-3), 16 (1996).
- [92]. M. L. Polignano, G. F. Cerofolini, H. Bender, C. Claeys, and J. Reffle, *Physica Status Solidi A*, **103**(1), 307 (1987).
- [93]. Ki-Man Bae, A. Karoui, and G. A. Rozgonyi, *Extended Abstract of ECS 191st Meeting*, Vol. **97-1**, 475 (1997).
- [95]. K. F. Kelton, R. Falster, D. Gambaro, M. Olmo, M. Cornara, and P. F. Wei, *J. Appl. Phys.*, **85**, 12, 8097 (1999).
- [97]. S. Senkader, G. Hobler, and C. Schmeiser, *Appl. Phys. Lett.*, **69**(15), 2202 (1996).
- [99] W. Ohashi, A. Ikari, Y. Ohta, H. Yokota, A. Tachikawa, K. Ishizaki, H. Deai, T. Futagi, J. Takahashi, Y. Inoue, and K. Nakai, *Proceedings of Silicon Materials Science and Technology Forum '99 at Kazusa Akademia Park*, edited by K. Sumino (Japan Technical Information ISBN-930825-12-1, Chiba, Japan, 1999) p.80.
- [101] F. Sahtout Karoui, A. Karoui, G. A. Rozgonyi, M. Hourai, and K. Sueoka, *Solid State Phenomena*, Vols. **95-96**, p. 99 (2004).
- [102]. A. Karoui, unpublished.
- [104]. D. Kashev, *Surface Science*, 14, 209 (1969).
- [105]. N. Inoue, K. Watanabe, K. Wada, and J. Osaka, *J. of Cryst. Growth*, **44**(1), 21 (1986).
- [106]. J. C. Mikkelsen, Jr., *Appl. Phys. Lett.*, **40**, 335 (1982).
- [107]. D. Huber, J. Reffle, *Solid State Technology*, 137 (1983).
- [108]. U. Ekhult, and T. Carlberg, *J. Electrochem. Soc.*, **136**, 551 (1989).
- [109]. Hirata, *J. Cryst. Growth*, **106**, 657 (1990).
- [110]. Y. Yatsurugi, N. Akiyama, and Y. Endo, *J. Electrochem. Soc.*, 120, 975 (1973).
- [111]. T. Itoh, and T. Abe, *Appl. Phys. Lett.*, **53**(1), 39 (1988).
- [112]. T. Abe, K. Kikuchi, S. Shirai, and S. Muraoka, in *Semiconductor Silicon 1981*, edited by H. Huff, R. J. Kriegler, and Y. Takeishi, *Electrochemical Society*, NJ, p. 54 (1981).
- [113] J. B. Mitchell, P. P. Pronko, and J. Shewchun, D. A. Thompson, and J. A. Daires, *J. Appl. Phys.*, 46, 332 (1975).

- [114]. V. I. Orlov, Yu. L. Iunin, M. V. Badylevich, O. Lysytskiy, and H. Richter, *Solid State Phenomena*, Vols. **95-96**, p. 465 (2004).
- [115]. R. Jones, C. Ewels, J. Goss, J. Miro, P. Deák, and S. Öberg, F. Berg Rasmussen, *Semicond. Sci. Technol.*, **9**, 2145 (1994).
- [116] T. Itoh, and T. Abe, *Appl. Phys. Lett.*, **53** (1), 39 (1988).
- [117] W. von Ammon, R. Holzl, J. Virbulis, E. Dornberger, R. Schmolke, and D. Graf, *J. of Crystal Growth*, **226** (1), 19 (2001).
- [118]. J. Esfandyari, J. Vanhellemont, and G. Obermeier, *Defects in Silicon III*, ECS PV 99-1, Eds. W.M. Bullis, W. Lin, P. Wagner, T. Abe, S. Kobayashi, (The Electrochemical Soc., Proc. 99-1, Seattle, WA, 1999) p.437.
- [119] E. van Dyke, A. Karoui, A. La Rosa, G. Rozgonyi, *Physica Status Solidi (c)* **1-6**, 848 (2004).
- [121] C. P. Ewels, *Density Functional Modelling of Point Defects in Semiconductor*, Ph.D. Thesis, University of Exeter, July 1997.
- [123]. M. W. Qi, S. S. Tan, B. Zhu, P. X. Zhu, P. X. Cai, W. F. Gu, X. M. Xu, T. S. Shi, D. L. Que, and L. B. Lim, *J. Appl. Phys.* **69** (6), 3775 (1991).]
- [124]. P. Wagner, R. Oeder, and W. Zulehner, *Appl. Phys. A*, **46**, 73 (1988).
- [125]. A. Karoui et al, unpublished
- [127] M. Tamatsuka, N. Kobayashi, S. Tobe, and T. Masui, *ECS Proc.* **99-1**, 456, (1999).
- [129] G. A. Rozgonyi, A. Karoui, A. Kvit, and G. Dusher, *Microelectronic Engineering*, **66**, 305 (2003).
- [130] A. Karoui, and G. A. Rozgonyi, unpublished
- [131] C. Frigeri, M. Ma, T. Irisawa, and T. Ogawa, *Materials Science and Engineering B Solid State Materials For Advanced Technology*, **91**, 170 (2002).
- [132] P. C. Kelires, and J. Tersoff, *Phys. Rev. Lett.*, **63**, 1164 (1989).
- [133] N. Fuma, K. Tashiro, K. Kakumoto, and Y. Takano, *Jpn. J. Appl. Phys.*, **35** Pt. 1, (4A), 1993 (1996).
- [134] W. R. Runyan, *Silicon Semiconductor Technology*, McGraw-Hill, New York, 1975.
- [135] H. Fujimori, *J. of the Electrochem. Soc.*, **144** (9), 3180 (1997).
- [136] R. J. Jaccodine, *J. Electrochem. Soc.*, **110**, 524, (1963).
- [137] R. R. Razouk, L. N. Lie, and B. E. Deal, *J. Electrochem. Soc.*, **128**, 2214, (1981).
- [138] E. A. Irene, H. Z. Massoud, and E. Tierney, *J. Electrochem. Soc.*, **133**, 1253 (1986).
- [139] W. A. Tilller, and S. Oh, *J. Appl. Phys.* **64** (1), 375 (1988).
- [140] J. Esfandyari, J. Vanhellemont, and G. Obermeier, *Defects in Silicon III*, ECS PV 99-1, Eds. W.M. Bullis, W. Lin, P. Wagner, T. Abe, S. Kobayashi, p.437 (1999).
- [141] F. Sahtout Karoui, A. Karoui, and G. A. Rozgonyi, *Proceedings of the 3rd International Conference on Modeling and Simulation of Microsystems*, San Diego, March 27-29, p. 98, (2000).
- [142] Dimo Kashchiev, *Nucleation basic theory with applications*, Butterworth Heinemann, Oxford, 2000.
- [143] F. R. N. Nabarro, *Proc. R. Soc. London Ser. A* **175**, 519 (1940).
- [146] T. Sekiguchi, K. Kimoto, T. Aoyama, and Y. Mitsui, *Jpn. J. Appl. Phys.*, **37**, (6B), L694 (1998).
- [148] This work, Chapter V
- [149] A. Karoui, F. S. Karoui, G. A. Rozgonyi, M. Hourai, and K. Sueoka, in *Semiconductor Silicon 2002*, Vol. 2, Ed. H. R. Huff et al, p. 670 (2002).

- [151] H.Kageshima and A.Taguchi, K.Wada, *App. Phys. Lett.*, **76**, 25, 3718 (2000).
- [152] A. Kvit, A. Karoui, G. Duscher, and G. A. Rozgonyi, *Appl. Phys. Lett.*, will appear on March 2004.
- [153] P. Gusev, H. C. Lu, E. L. Garfunkel, and T. Gustafsson, M. L. Green, *IBM J. Res. Develop.*, **43**, (3), 265 (1999).
- [154] P. M. Fahey, G. Barbuscia, and M. Moselhi, *Appl. Phys. Lett.* **46** (8), 784 (1985).
- [156] T. Sinno, R.A. Brown, *Semiconductor Silicon/1994 (ECS)* edited by H.R. Huff et al, 625 (1994)
- [158] K.A. Jackson, Theory of melt growth. In *Crystal Growth Characterization*, R.Ueda and J.B. Mullin eds. North Holland Publ., Amsterdam, (1975) , pp.21-32.
- [159] J.R.Carruthers and A.F. Witt, Transient segregation effects in Czochralski growth. In *Crystal Growth Characterization*, R.Ueda and J.B. Mullin eds. North Holland Publ., Amsterdam, (1975), pp.107-154.
- [160] K. Morizane, A. Witt, and H.C.Gatos, Impurity distribution in silicon single crystals. III. In impurity heterogeneities in single crystals rotated during pulling from melt. *J. Electrochem. Soc.* **114**, 738-742 (1967).
- [161] A. J. R. de Kock, P. J. Rocksnoer, and P. G. T. Boonen, Microdefects in swirl-free silicon crystals. In *Semiconductor Silicon 1973* (H.R. Huff and R.R.Burgess, eds.) pp. 83-94. Electrochem. Soc. Princeton, New Jersey, 1973.
- [162] H. Foll and B.O.Kolbesen, Formation and nature of swirl defects in silicon. *Appl. Pys.* **8**, 319-331 (1975).
- [163] S.N. Rea, "Czochralski silicon rate limits. *J. Cryst. Growth* **54**, 264-274 (1981).
- [164] J.W.Cahn, Theory of crystal growth and interface motion in crystal materials. *Acta metall.* **8**, 554-562 (1960).
- [165] R.H.Hopkins, R.G.Seidensticker, J.R.Davis, P.Rai-Choudhury, and P.D.Blais, Crystal growth considerations in the use of solar grade silicon. *J. Cryst. Growth*, **42** 493-498 (1977).
- [166] T. Abe, The growth of Si single crystals from the melt and impurity incorporation mechanisms. *J. Cryst. Growth*, **24/25**, 463-467 (1974).
- [167] J.C.Brice, Facet formation during crystal growth. *J. Cryst. Growth* **6**, 205-206 (1970).
- [168] W. Zulehner and D.Huber, Czchoralski-grown silicon. In *Crystal 8: Silicon*, Chemical Etching, J.Grabmaier, ed., pp. 1-143. Springer Verlag, Berlin and New York, 1981.
- [169] S. Umeno, S. Sadmitsu, H. Murakami, M. Hourai, Axial microscopic distribution of grown-in defects in Czochralski-grown silicon crystals, *Jpa. J. Appl. Phys.* **32**, Part 2, **5B**, pp. L699-702 (1993).
- [170] F.D.Rosi, Effect of crystal growth variables on electrical and structural properties of germanium. *RCA Rev.* **19**, 349-387 (1958).
- [171] J.A.M.Dikhoff, Cross-sectional resistivity variations in germanium single crystals. *Solid-State Electron.* **1**, 202-210 (1960).
- [172] M.G.Mil'Viskii, The crystallization front and the distribution of impurities across the transverse section of monocrystals grown from a melt. *Sov. Phys. Crystallogr. (Engl. Transl.)* **6**, 647-648 (1962).
- [173] E.Kuroda and H.Kozuka, Influence of temperature oscillations in silicon Czochralski growth. *J. Cryst. Growth* **63**, 276-284 (1983).

- [174] F. Shimura, Behavior and role of oxygen in silicon wafers for VLSI, in *VLSI Science and Technology/1982*, C.J.Dell'Oca and W.M.Bullis, eds., pp. 17-32. Electrochem. Soc., Princeton, New Jersey, 1982.
- [175] F.Shimura and H.R.Huff, VLSI silicon material criteria. In *VLSI Handbook*, N.G.Einspruch, ed., pp.191-269, Academic Press, New York, 1985.
- [176] T.Abe, Crystal fabrication. In *VLSI Electronics Microstructure Science*, N.G.Einspruch and H.R.Huff, eds., Vol. 12, pp. 3-61, Academic Press, New York, 1985.
- [177] C. Haas, The diffusion of oxygen in silicon and germanium, *J. Phys. Chem. Solids* **15**, 108-111 (1960).
- [178] U.Goesele and T.Y.Tan, The influence of point defects on diffusion and gettering in silicon. In *Impurity Diffusion and Gettering in Silicon*, R.B.Fair, C.W.Pearce, and J.Washburn, eds., pp.105-116, Mater. Res. Soc., 1985.
- [179] P. Gaworzewski and G.Ritter, On the out-diffusion of oxygen from silicon. *Phys. Status Solidi A* **67**, 511-516 (1981).
- [180] interstitial and vacancy influence on impurity diffusivity
- [181] R. Falster and V.V.Voronkov, *Mat. Res. Soc. Bulletin*, June 2000, p.28
- [183] V.V. Voronkov, G.I. Voronkova, N.V. Veselovskaya, M.G. Milvidski, and I.F. Chervonyi, *Sov. Phys. Crystallogr.* **29** (1984) p. 688.
- [184] V.V. Voronkov and R. Falster, *J. Cryst. Growth* **194** (1998) p. 76.
- [185] Ki-Man Bae, Crown-in Defects in Silicon Wafer: Formation Mechanism And Surface Reactions, Ph.D. thesis, North Carolina State University, Raleigh, NC, USA, 1998.
- [186] J. Crank, *The Mathematics in Diffusion*, Oxford University Press (1970)
- [187] T. Sinno, R.A. Brown, *Semiconductor Silicon/1994 (ECS)* edited by H.R. Huff et al, 625 (1994).
- [189] H.J.Stein, *Mat. Res. Soc. Symp. Proc.*, Vol. 59, p.523 (1986).
- [190] Y.Itoh, T.Nazaki, T.Masui, T.Abe, *Appl. Phys. Lett.*, **47** (5), 488 (1985).
- [191] Hara A, Masaki A, Koizuka M and Fukuda T 1994 *J. Appl. Phys.* **75** 2929.
- [192] R. Jones, S. Oberg, F. Berg Rasmussen and B. Bech Nielsen, *Phys. Rev. B*, **72** (12), 1882 (1994)
- [194] H. Sawada and K. Kawakami, *Physical Review B*, 62 (3),1851 (2000).
- [195] W. von Ammon, Proceedings of the Forum on the Science and Technology of Silicon Materials, H. Y. Kaneta, and K. Sumino, Eds, *Silicon Materials Science and Technology Forum*, Shonan, Kanagawa, Japan Nov. 26-28, 2001, (2001).
- [196] W. Ohashi, A. Ikari, Y. Ohta, H. Yokota, A. Tashikawa, K. Ishizaka, H. Deai, T. Fugati, J. Takahashi, Y. Inoue, and K. Nakai, Proceedings of Silicon Materials Science and Technology Forum '99, Kazusa Academia Park, p. 80 (1999).
- [198] W. v. Ammon, P. Dreier, W. Hensel, U. Lambert, L. Koster, *Mater. Sci. and Eng.*, **B36**, 33 (1996).
- [199] K. L. Brower, *Phys. Rev.*, **B26**, 6040 (1982).
- [200] H. J. Stein, in *Oxygen, Carbon, Hydrogen and Nitrogen in Crystalline Silicon*, *Mat. Res. Soc. Symp.*, Pittsburgh PA, ed J. C. Mikkelsen Jr., S. J. Pearton, J. W. Corbett, and S. J. Pennycook, **59**, 523 (1985).
- [201] Adam Gali, József Miro, Peter Deák, Chris P Ewels, Robert Jones, *J. Phys.: Condens. Matter*, **8**, 7711 (1996).
- [204] W. von Ammon, R. Holzl; J. Virbulis, E. Dornberger, R. Schmolke, D. Graf, *J. of Crystal Growth.*, **226**, 19, (2001).

- [205] Yang, R. Fan, L. Li, D. Que, Appl. Phys. Lett, **68** (4), 487 (1996).
- [206] T. Abe, Proceedings of the Forum on the Science and Technology of Silicon Materials, H. Y. Kaneta, and K. Sumino, Eds, Silicon Materials Science and Technology Forum, Shonan, Kanagawa, Japan Nov. 26-28, 2001, p. 19 (2001).
- [208] D. Yang, D. Que, K. Sumino, Stat. Sol. (B), **210**, 295 (1998).
- [209] M. Suezawa, K. Sumino, H. Harada, T. Abe, Jpn. J. Appl. Phys. Part-2, **25**, L859 (1986).
- [210] H. J. Stein, J. Electrochem. Soc., **134**, 2592 (1987).
- [215] H. J. Stein, Appl. Phys. Lett., **43** (3), 296 (1983).
- [216] K.L.Brower, Phys. Rev. B, **26**, 11, 6040 (1982).
- [218] W. v. Ammon, P. Dreier, W. Hensel, U. Lambert, L. Koster, Mater. Sci. and Eng., **B36**, 33 (1996).
- [219] W. von Ammon, R. Holzl; J. Virbulis, E. Dornberger, R. Schmolke, D. Graf, J. of Crystal Growth., **226**, 19, (2001).
- [220] K. Nakamura , T. Saishoji, S. Togawa, J. Tomioka, Proceedings of Silicon Materials Science and Technology Forum '99, Silicon Materials Science and Technology Forum, Kazusa Academia Park Ltd., Chiba, Japan, p. 116 (1999).
- [222] W. v. Ammon, R. Holtz, J. Virbulis, E. Dornberger, R. Schmolke, D. Graf, Solid State Phenomena, **Vols. 82-84**, pp 17-24 (2002).
- [223] V. V. Voronkov and R. Falster, J. Electrochem. Soc., **149** (3), G167-G174 (2002).
- [225] F. Quast, P. Pichler, H. Ryssel, R. Falster, ECS PV. **2000-17**, Eds., C. L. Claeys, P. Rai-Choudhury, M. Watnabe, P. Stallhofer, H. J. Dawson, p.156 (2000).
- [226] L. Shaik Adam, M. E. Law, S. Szpala, P.J.Simpson, D. Lawther, O. Dokumaci, S. Hegde, Appl. Phys. Lett., **79** (5), 623 (2001).
- [228] A. H. Clarke, J.D. MacDougall, K.E. Manchester, P. E. R Oughan, F. W. Anderson, Bull. Am. Phys. Soc., **13**, 376 (1968).
- [230] N. V. Deniseova, E. I. Zorin, P.V. Pavlov, D. J. Tetelbaum, A. F. Khokhlov, Izv. Akad. Nauk. SSSR Neorg. Mater., **11**, 2236 (1975).
- [231] H. Zimmerman, H. Ryssel, Appl. Phys., **A 55**,121 (1992).
- [232] K. Nakamura, T. Saishoji, T. Kubota, T. Iida, Y. Shimanuki, T. Kotooka, J. Tomioha, J. of Cryst. Growth, **180**, 61 (1997).
- [233] T. Sinno, R. A. Brown, W. von Ammon, E. Dornberger, Appl. Phys. Lett., **70**, 2250 (1997).
- [234] A.Hara, T.Myabo, L.Hirai, Appl. Phys. Lett., **54** (7), 626 (1989).
- [237] F. Berg Rasmussen, S. Öberg, R. Jones, C. Ewels, J. Goss, J. Miro, P. Deák, Mat. Sc. Eng., **B36**, 91 (1996).
- [238] J. Couhinto and R. Jones, P. R. Briddon, S. Öberg, Phys. Rev. B, **62** (16), 10824 (2000).
- [239] D. Yang, D. Que, K. Sumino, J. Appl. Phys., **77**(2), 943 (1995).
- [240] V. V. Voronkov, M. Porrini, P. Collareta, M. G. Pretto, and R. Scala, J. Appl. Phys., **89** (8), 4289 (2001).
- [241] Yang, R. Fan, L. Li, D. Que, Appl. Phys. Lett, **68** (4), 487 (1996).
- [242] C. Ewels, PhD. Thesis, University of Sussex, UK (1997).
- [243] H. Sawada and K. Kawakami, Physical Review B, **62** (3),1851 (2000).
- [244] H. Kageshima, A. Tauguchi, K. Wada, Appl. Phys. Lett., **76**, 3718 (2000).
- [245] W. Kohn and L. J. Sham, Phys. Rev. A, **140**, 1133 (1965).
- [246] Castep : Cambridge Sequential Total Energy Package, Ab-initio quantum mechanical package, Accelrys Inc.

- [247] DMol3 : DFT program which uses a numerical basis set, Accelrys Inc.
- [248] UniChem software has been developed by Cray Research Inc. and Oxford Molecular (UK).
- [249] B. J. Coomer, A. Resende, J. P. Goss, R. Jones, S. Oberg, P. R. Briddon, *Physica B*, **273-274**, 520 (1999).
- [250] G. D. Watkins and J. W. Corbett, *Phys. Rev.*, **138**, 2A, A543 (1965).
- [251] M. Saito and A. Oshiyama, *Phys. Rev. Let.*, **73**, 866 (1994).
- [252] H. Seong, L. J. Lewis, *Phys. Rev. B*, **53**, 9791 (1996).
- [253] A. Umerski and R. Jones, *Phil. Mag. A* **67**, 4, 905-915 (1993).
- [254] COMPASS force field potential developed by Accelrys Inc. (USA).
- [255] J. Harris, *Phys. Rev.* **B 31**, 1770 (1985).
- [257] S. H. Vosko, L. Wilk, M. Nusair, *Can. J. Phys.*, **58**, 1200 (1980).
- [258] C. S. Nichols, C. G. Van de Walle, and S. T. Pantelides, *Phys. Rev. B*, **40** (8), 5484 (1989).
- [259] J. S. Nelson, P. A. Schultz, A. F. Wright, *Appl. Phys. Lett.*, **73**, 247 (1998).
- [260] D.R. Bosomworth et al., *Proc. Roy. Soc. A*, 317 (1528), 133 (1970).
- [261] R. Jones and A. Umerski, *Physical Review B*, **45** (19), 11321 (1992).
- [262] Xuegong Yu, Deren Yang, Xiangyang Ma, Jiansong Yang, Liben Li, *J. Appl. Phys.*, **92** (1), 188 (2002).
- [263] M. J. S. Dewar and W. Thiel, *J. Am. Chem. Soc.*, **99**, 4899 (1977).
- [264] UniChem software has been developed by Cray Research Inc. and Oxford Molecular (UK).
- [265] A. Resende, ENDEASD report, 1 (1999).
- [266] T. Abe, Proceedings of the Forum on the Science and Technology of Silicon Materials, H. Y. Kaneta, and K. Sumino, Eds, *Silicon Materials Science and Technology Forum*, Shonan, Kanagawa, Japan Nov. 26-28, 2001, p. 19 (2001).
- [267] J. C. Anderson, K. D. Leaver, R. D. Rawling J. M. Alexander, in *Ch VIII, Materials Science* 3rd edition, Van Nostrand Reinhold, UK, (1922).
- [268] R. J. Borg, and G. J. Dienes, *The Physical Chemistry of Solids*, p.439, Academic Press Inc., San Diego, (1992).
- [269] Peter E. Blöchl, Enrico Smargiassi, R. Car, D. B. Laks, W. Andreoni and S. T. Pantelides, *Phys. Rev. Let.*, **70** (16), 2435 (1993).
- [272] W. Ohashi, A. Ikari, Y. Ohta, H. Yokota, A. Tashikawa, K. Ishizaka, H. Deai, T. Fugati, J. Takahashi, Y. Inoue, and K. Nakai, Proceedings of Silicon Materials Science and Technology Forum '99, Kazusa Academia Park, p. 80 (1999).
- [273] A. Karoui, F. Sahtout Karoui, G. A. Rozgonyi, submitted to *J. Appl. Phys.*
- [274] A. Karoui et al, to be published.
- [276] Dimo Kashchiev, *Nucleation basic theory with applications*, Butterworth Heinemann, Oxford, 2000.
- [277] A. Borghesi, B. Pivac, A. Sassela and A. Stella, *J. Appl. Phys.*, **77** (9), 4169 (1995).
- [282] H. J. Monkhorst and J. D. Pack, *Phys. Rev. B*, **13**, 5188 (1976).
- [283] J. P. Goss, I. Hahn, R. Jones, P. R. Briddon, and S. Oberg, *Phys. Rev. B*, **67**, 45206 (2003).
- [284] B. J. Coomer, A. Resende, J. P. Goss, R. Jones, S. Oberg, P. R. Briddon, *Physica B*, **273-274**, 520 (1999).
- [285] G. D. Watkins and J. W. Corbett, *Phys. Rev.*, **138**, 2A, A543 (1965).
- [286] Saito and A. Oshiyama, *Phys. Rev. Let.*, **73**, 866 (1994).
- [287] H. Seong, L. J. Lewis, *Phys. Rev. B*, **53**, 9791 (1996).
- [288] C. Cunha, S. Canuto, and A. Fazzio, *Phys. Rev. B*, **48(24)**, 17806 (1993).

- [289] F. Berg Rasmussen, S. Oberg, R. Jones, C. Ewels, J. Goss, J. Miro, and P. Deak, Mater. Sc. Forum, **196-201**, 791 (1995).
- [291] D. R. Bosomworth, W. Hayes, A. R. L. Spray, G. D. Watkins, Proc. Roy. Soc. Lond.A, **317**,133 (1970).
- [292] A. Karoui, F. Sahtout, G. A. Rozgonyi, and D. Yang, Oxygen Precipitation in Nitrogen Doped Czochralski Silicon Wafers. Part-I: Formation Mechanisms of Near-Surface and Bulk Defects, J. Appl. Phys., **96** (6), 3255 (2004).
- [293] A. Karoui, G. A. Rozgonyi, Oxygen Precipitation in Nitrogen Doped Czochralski Silicon Wafers, Part-II : Effects of nitrogen and oxygen coupling, J. Appl. Phys. , **96** (6), 3264 (2004).
- [296] M.Schrems, T.Bravec, M. Budil, H. W.Potzl, E. Guerrero, D.Huber, P. Pongratz, Mat. Sc. and Eng. ,B4, 393 (1989).
- [297] F. Sahtout Karoui, A. Karoui, G. A. Rozgonyi, M. Hourai, and K. Sueoka, *Characterization of Nucleation Sites in Nitrogen Doped Czochralski Silicon by Density Functional Theory and Molecular Mechanics*, Solid State Phenomena, Vols. 95-96, p. 99 (2004).
- [298] A. Karoui, Faouzia Sahtout Karoui, George A Rozgonyi, *Molecular Dynamics and First-Principles Calculations of Defect Precursors Formation in N-doped Silicon*, MRS Spring Meeting 2004, Symposium Q: Nucleation Phenomena—Mechanisms, Dynamics, and Structure.
- [299] N. Inoue, D. Funao, I. Ohkubo, A Natsume, F. Sahtout Karoui, A. Karoui, and G. A. Rozgonyi, *Analysis of nitrogen reactions in CZ silicon*, in Proceedings of the Forum on the Science and Technology of Silicon Materials 2003, Eds. H. Yamada-Kaneta, and K. Sumino, Shonan Village Center, Kanagawa, Japan, Nov. 25-27, 2003, p.242-246. and in DRIP X, 10th International Conference on Defects: Recognition, Imaging and Physics of Semiconductors in Batz-sur-Mer, France, Sep. 29 - Oct. 2, 2003.
- [300] The Advanced Light Source produces soft x-ray regions starting from 1Å, far ultraviolet up to 0.1 μm, and Vis-IR of at least 100 μm. ALS light is bright and Highly Collimated.
- [301] Value given for 2 cm⁻¹ spectral window, which is the typical bandwidth of a FTIR spectrometer.
- [302] A. Karoui, G.A.Rozgonyi, *Minority Carrier Lifetime in Nitrogen Doped FZ Si*, *Quarterly Report (QR2) of NREL-NCSU Project "Optimization of Silicon Crystal Growth and Wafer Processing for High Efficiency and High Mechanical Yield"* Project Number: AAT-2-31605-05, NCSU, June 30, 2002.
- [303] A. Karoui, F. Sahtout Karoui, A. Kvit, G. A. Rozgonyi, and D. Yang, Appl. Phys. Lett., **80** (12), 2114 (2002).
- [304] A. Karoui, R. Zhang, G. A. Rozgonyi, and, T. Cizek, *Silicon Crystal Growth and Wafer Processing for High Efficiency Solar Cells and High Mechanical Yield*, NCPV, NREL/CP-520-31057, Lakewood, CO, 14-17 Oct. 2001.
- [305] A. Karoui, F. Sahtout, and G. A. Rozgonyi, Patent filled with NCSU.
- [306] Bharat Bhushan, Xiaodong Li, Micromechanical and tribological characterization of doped single-crystal silicon and polysilicon films for microelectromechanical systems devices, J. Mater. Res., **12**(1), p. 54. (1997).
- [307] Bharat Bhushan, Nanotribology and Nanomechanics of MEMS Devices, IEEE Micro Electro Mechanical Systems Workshop, San Diego, California, Feb. 1996, p.91-p.97 (1996).

- [308] B. Bhushan and V.N.Koinkar, Tribology Studies of Silicon for Magnetic Recording Applications, J. Appl. Phys., 75, 5741 (1994).
- [309] P. Hess, Laser diagnostics of mechanical and elastic properties of silicon and carbon films, Applied Surface Science, **106**, 429 (1996)..
- [310] SAW, utilizes a nanosecond pulsed Nd:YAG at 355 nm for launching and the probe beam deflection arrangement.
- [311] L. Gan , B. Ben-Nissan, A. Ben-David, Modelling and finite element analysis of ultra-micro-hardness indentation, of thin films, Thin Solid Films, **290-291** , 362 (1996).
- [312] J. Dolbow, M. Gosz, Effect of out-of-plane properties of a polyimide film on the stress fields in microelectronic structures, Mechanics of Materials, **23**, 311 (1996).
- [313] A. H. Cottrel, and B.A.Bilby, Proc. Phys. Soc. A, **62**, 49 (1949).
- [314] A. W.Cochardt, G. Schoek, and H. Wiedersich, Acta Metall. **3**, 533 (1955).
- [315] D. M. Barnett and W. D. Nix, Acta Metall. **2**, (1955).
- [316] For instance Cavllani, Kittler, Alexander, C.Donolato, C.H.Leamy, Braga,
- [317] Pierls and Nabarro
- [318] G. E. Beltz and L. B. Freund, Philos. Mag. A, **69**, 171(1994).
- [319] L. B. Hansen, K. Stokbro, B. I. Lundqvist, K. W. Jacobsen, and Deaven, Phys. Rev. Lett., **75** (24), 4444 (1995).
- [320] R. A. Johnson, J. Appl. Phys., **50**, 1263 (1979).
- [321] J. Koehler, Phys. Rev. **181**, 1015 (1969).
- [322] H. K. Birnbaum, B. L. Eyre, and Drothing, Philos. Mag., **23**, 847 (1971).
- [324] H. B. Huntington and R.A.Johnson, Acta Metall. **10**, 281 (1962).
- [325] A. S. Nandekar, and R.A.Johnson, Acta Metall. **30**, 2055 (1982).
- [327] N. Louat, Proc. Phys. Soc. **50**, 1263 (1979).
- [328] D. N. Beshers, Acta Metall. **6**, 521 (1958).
- [330] K. Sumino, I. Yonenaga, M. Imai, T. Abe, J. Appl. Phys., **54**, 5016 (1983).
- [331] T.Abe, K. Kikuchi, S. Shirai, and S. Muraoka, in *Semiconductor Silicon 1981*, edited by H. Huff, R. J. Kriegler, and Y. Takeishi (Electrochemical Society, NJ, 1981), p.54.
- [332] T. Itoh, and T. Abe, Diffusion coefficient of a pair of nitrogen atoms in float-zone silicon. Appl. Phys. Lett., **53**, (1), (1988).